Winter 12-15-2021

Dissecting the Molecular Mechanism of Familial Cardiomyopathies

Sarah Ruth Clippinger Schulte
Washington University in St. Louis

WASHINGTON UNIVERSITY IN ST. LOUIS

Division of Biology and Biomedical Sciences
Biochemistry, Biophysics and Structural Biology

Dissertation Examination Committee:
Michael Greenberg, Chair
John Cooper
Eric Galburt
Moe Mahjoub
Jon Silva

Dissecting the Molecular Mechanism of Familial Cardiomyopathies

By

Sarah Ruth Clippinger Schulte

A dissertation presented to
The Graduate School
of Washington University in
partial fulfillment of the
requirements for the degree
of Doctor of Philosophy

December 2021
St. Louis, Missouri

Table of Contents

List of Figures ..... *v*

List of Tables ..... *vi*

Acknowledgments ..... *vii*

Abstract of the Dissertation ..... *ix*

Chapter 1: Introduction *1*

1.1 Overview of Molecular Motors **2**

1.2 Beta Cardiac Myosin and Power Generation in the Heart **3**

1.3 Regulatory Proteins Tropomyosin and Troponin **4**

1.4 iPSC-CMs as a tool for studying the early disease phenotype **6**

1.5 Conclusions **7**

1.6 References **7**

Chapter 2: Computational tool to study perturbations in muscle regulation and its application to heart disease *9*

2.1 Introduction **10**

2.2 Results and Discussion **12**

2.3 Conclusion **18**

2.4 Materials and Methods **19**

2.5 Figures **23**

2.6 References **27**

2.7 Supporting Materials **30**

Chapter 3: Disrupted Mechanobiology Links the Molecular and Cellular Phenotypes in Familial Dilated Cardiomyopathy *36*

3.1 Introduction **37**

3.2 Results **40**

3.3 Materials and Methods **58**

3.4 Figures **61**

3.5 References **68**

3.6 SI Methods **74**

Chapter 4: The variant R94C in TNNT2-encoded troponin T predisposes to pediatric restrictive cardiomyopathy and sudden death through impaired thin filament relaxation resulting in myocardial diastolic dysfunction *101*

4.1 Introduction **103**
4.2 Results **104**
4.3 Discussion **108**
4.4 Conclusions **111**
4.5 Methods **112**
4.6 Figures **117**
4.7 References **123**
4.8 Supplemental Material **128**
Chapter 5: Mechanical dysfunction of the sarcomere induced by a pathogenic mutation in troponin T drives cellular adaptation ***129***
5.1 Introduction **130**
5.2 Results **133**
5.3 Discussion **143**
5.4 Conclusions **152**
5.5 Methods **153**
5.6 Figures **166**
5.7 References **171**
5.8 Supplemental Materials **179**
Gene Symbol 185
Gene Name 185
Product Number 185
Chapter 6: Analysis of single-molecule data from optical trapping experiments ***189***
6.1 Introduction **189**
6.2 Overview of the three-bead assay and data analysis techniques **189**
6.3 Manipulation of Window Size, covariance smoothing, minimum event duration and minimum event separation in SPASM **191**
6.4 Conclusions **193**
6.5 References **193**
Chapter 7: Step size and kinetics of cardiac myosin crossbridges are not affected by troponin and tropomyosin (first draft) ***195***
7.1 Introduction **196**
7.2 Results **198**
7.3 Discussion **201**
7.4 Conclusions **203**
7.5 Material and Methods **203**

7.6 Figures 207
7.7 References 211
Chapter 8: Conclusions and Future Directions 214
8.1 Diversity of genetic cardiomyopathies and importance of studying molecular effects 214
8.2 Mechanosensing and adaptive/maladaptive changes in heart tissue 215
8.3 Future Directions for *in vivo* modeling of Tn-T mutations 216
8.4 Future Directions for optical trapping experiments 216
8.5 Summary 217
8.6 References 217

List of Figures

Chapter 1
Figure 1 1
Chapter 2
Figure 1. Schematic of the three-state model of muscle regulation. 23
Figure 2. Hypothesis testing. 24
Figure 3. Traditional vs. global fitting of the three-state model to fluorescence titration data 25
Figure 4. Effects of the ΔE160 mutation in troponin T on thin-filament regulation. 26
Chapter 3
Fig. 1. Structure of the troponin core complex and in vitro motility assay. 61
Fig. 2. Determination of equilibrium constants governing thin filament regulation for ΔK210 62
Fig. 3. Effects of ΔK210 on tropomyosin positioning along the thin filament 64
Fig. 4. Computational modeling of the steady-state and transient force per sarcomere. 65
Fig. 5. Immunofluorescence images of sarcomeres in hiPSC-CMs 65
Fig. 6. Quantification of immunofluorescence staining for sarcomeres in hiPSC-CMs on rectangular patterns on glass and 10 kPa hydrogels 66
Fig. 7. Traction force microscopy of single hiPSC-CMs patterned on 10 kPa polyacrylamide gels. 67
Fig. S1. ADP release rates from myosin bound to regulated thin filaments for WT and ΔK210 at 20°C 91
Fig. S2. Variants identified from whole exome sequencing of BJFF.6 cells. 93
Fig. S3. Sequence alignment of all expressed human TNNT2 splice isoforms and CRISPR/Cas9 constructs for introducing the mutation into stem cells 94
Fig. S4. Karyotyping of gene edited cells 95
Fig. S5. Staining of gene-edited cells with markers of pluripotency demonstrates that stem cells retain pluripotency after gene editing. 96
Fig. S6. Differentiation protocol used to derive hiPSC-CMs from hiPSCs. 97
Fig. S7. Occupancy of regulated thin filament states at different calcium concentrations. 98
Chapter 4
Figure 1. Clinical evaluation of TNNT2-R94C positive kindred 117
Figure 2. R94C localizes to a highly conserved region of TNNT2 118
Figure 3. Pedigree of TNNT-R94C kindred 119
Figure 4: Measurement of the biochemical steps involved in thin filament activation 120
Figure 5: Computational modeling of the effects of the variant on the force-calcium relationship. 121
Chapter 5
Figure 1. R92Q mutation in troponin T causes hypertrophic cardiomyopathy 166
Figure 2. R92Q does not change the rate of unloaded actomyosin dissociation or calcium binding affinity to troponin C. 167
Figure 3. R92Q alters the positioning of tropomyosin along the thin filament 168
Figure 4. Computational modeling reveals that altered tropomyosin positioning is sufficient to explain the hypercontractility seen with R92Q 169
Figure 5. R92Q causes cellular hypercontractility in hiPSC-CMs. 170
Figure 6. R92Q hiPSC-CMs show altered calcium transients and gene expression. 170

Figure 7. Spontaneous and evoked action potentials are altered in R92Q hiPSC-CMs and I_{Ca} densities are reduced..... 171
Fig. S1. The affinity of calcium binding to the troponin complex at 20 ℃ and 37 ℃. 179
Fig. S2. Generation of gene edited hiPSC-CMs 180
Fig. S3. Immunofluorescence images of stem cells and hiPSC-CMs..... 181
Fig. S4. The relative expression of fetal (slow skeletal) and adult (cardiac) troponin I isoforms in hiPSC-CMs 182
Fig. S5. Representative traces of hiPSC-CMs spontaneously beating on 10 kPa polyacrylamide gels measured by traction force microscopy 183
Fig. S6. Comparison of the two independently derived R92Q clones examined using traction force microscopy reveals no significant differences between the clones 184
Fig. S7. RT-qPCR gene names and primers. 185
Fig S8. RT-qPCR measurements of the expression of key calcium handling genes. 186
Fig. S9. Table of values from electrophysiological experiments..... 187
Chapter 7
Figure 1. Stopped-flow assays to compare regulated and unregulated thin filaments 208
Figure 2. In vitro motility and the three-bead optical trap assay. 208
Figure 3. Ensemble averages of all collected data and cumulative distributions. 209
Figure 4. Positional feedback optical clamp data 210

List of Tables

Chapter 3
Table 1..... **Error! Bookmark not defined.**
Chapter 4
Table 1: In silico variant prediction aggregate analysis of the TNNT2 Arg94Cys variant using variant prediction models. 122
Supplement Table 1: Clinical and genetic information for the multi-generational family..... 128

Acknowledgments

I would like to thank my advisor, Michael Greenberg, for being a fantastic mentor and supporting me through this process. I have become a better scientist and coworker because of your training.

I am grateful to all the members of the Greenberg Lab, especially Tom Stump and Lina Greenberg for your patience and guidance since the beginning.

I would like to thank the Division of Biology and Biomedical Sciences for providing an excellent PhD program.

Sarah Clippinger Schulte

Washington University in St. Louis

December 2021

Dedicated to my husband

and Titan and Chucho

ABSTRACT OF THE DISSERTATION

Dissecting the Molecular Mechanism of Familial Cardiomyopathies

By

Sarah Ruth Clippinger Schulte

Doctor of Philosophy in Biochemistry, Biophysics & Structural Biology

Washington University in St. Louis, 2021

Familial cardiomyopathies, including hypertrophic (HCM), restrictive (RCM) and dilated cardiomyopathy (DCM), are the leading cause of sudden cardiac death in young people. These diseases, which are characterized by altered cardiac contractility and remodeling of the heart, can lead to heart failure. These diseases are primarily caused by point mutations in sarcomeric proteins that generate or regulate heart contraction, such as troponin T. In the heart, the troponin complex together with tropomyosin lie along the actin filament and regulate myosin's ability to bind actin and produce force. Here I show how mutations in troponin T affect contractility at the molecular level leading to differing phenotypes at the cellular level and in patients. At the molecular level, I show that a model troponin-T HCM mutation and RCM mutation result in an increased population of force generating states while a troponin-T DCM mutation causes a decreased population of force generating states. Second, on a more basic science level, I show that the presence of troponin and tropomyosin on actin do not significantly affect the kinetics and mechanics of the cardiac myosin working stroke, which will serve as crucial parameters for accurate modeling of the heart's force velocity relationship. In total, this work has important implications for our understanding of the molecular mechanism of cardiac muscle contraction and for interpreting the effects of disease-causing mutations in sarcomeric proteins.

Chapter 1: Introduction

Familial Cardiomyopathies

As humans develop the heart must be able to efficiently pump blood to the entire body and adapt to changing demands including growth, exercise, stress, and many others. During pregnancy, the heart adapts in a physiological response to the increased cardiac output. The heart also adapts or maladapts as a pathophysiological response in the case of disease including familial cardiomyopathies (1). However, while physiological remodeling of the heart is reversible, the remodeling caused by disease is generally irreversible. One such disease, familial cardiomyopathies, have a prevalence of >1:500 people and are the leading cause of sudden cardiac death in people under the age of 30 (2). Familial cardiomyopathies are caused by single mutations in sarcomeric proteins that generate or regulate force production. How the heart responds to these mutations on the biophysical, cellular and tissue level determines where the disease phenotype will fall on the spectrum between hypertrophy or dilation and despite approximately 30 years of research the complexity of these diseases has made the development therapeutics challenging (3).

Figure 1

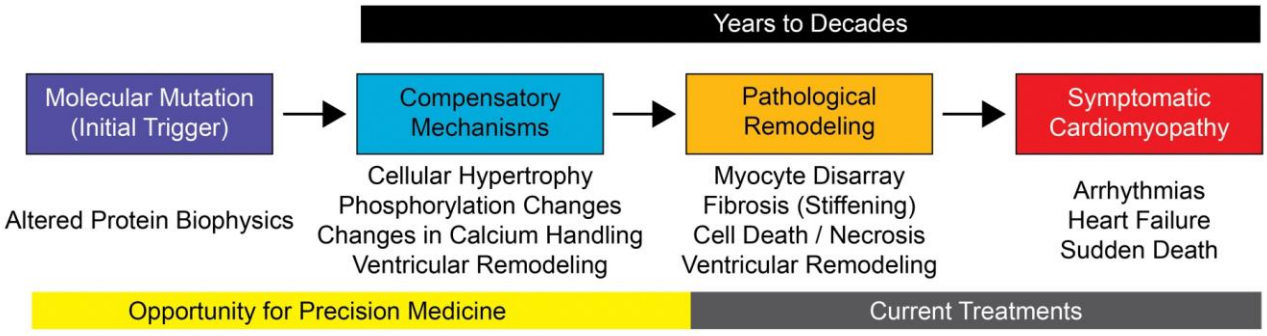

In hypertrophic cardiomyopathy (HCM), the heart undergoes hypertrophy of the left ventricular wall, myocyte disarray and fibrosis. HCM patients also experience diastolic dysfunction, in that the heart does not relax fast enough or incompletely following each beat. In dilated cardiomyopathy (DCM), the heart undergoes dilation of the ventricular chamber with thinning of the left ventricular wall, lengthening of individual myocytes, and fibrosis. This weakening of the heart's main pumping chamber results in reduced ejection fraction and systolic dysfunction. Sharing some of the same features as HCM, a third type of familial cardiomyopathy is restrictive cardiomyopathy (RCM) which results in diastolic dysfunction usually as a result of increased myocardial stiffness rather than thickening of the left ventricular wall (1). One of the challenges in treating these diseases is that similar mutations within the same protein can lead to any one of these three phenotypes. Another challenge is that while we know how the disease progresses during the late stages of the disease when the remodeling of the heart is very obvious, how these mutations affect force and power production during the early development of the disease is not well understood (Fig 1) (4). Increasing our understanding in these areas will greatly aid in the development of therapeutics to treat patients in a mutation-specific manner (precision medicine) and before the disease progression impacts quality of life.

1.1 Overview of Molecular Motors

Molecular motors are a diverse group of proteins that use chemical energy in the form of ATP (at least for all motors discussed here) to generate force and movement in the cell. This process is termed mechanochemical coupling and these motors function in a wide array of functions including but not limited to cell migration, mechanosensing, intracellular transport and muscle

contraction.(5) Molecular motors can be categorized in different ways, one of which is as processive or non-processive motors. Processivity refers to the number of steps a motor can take before it detaches from its track. Processive motors are those like kinesin or certain types of myosins (myosin V) for which a single motor molecule takes many steps as it "walks" along either microtubules or actin to transport cargo to specific locations of the cell. Non-processive motors or those that do not stay attached to their "track" after taking a step. In other words, the motors bind to their track, undergo their mechanochemical cycle and then detach. One important parameter of molecular motors is the "duty ratio" which is the fraction of the biochemical cycle spent attached to the track. Duty ratio is mostly determined by which step in the motor's ATPase cycle is rate-limiting (5). However, duty ratio and processivity are not synonymous. For example an anchoring myosin that stays attached to actin for long periods of time would have a high duty ratio but is still a non-processive motor (6).

1.2 Beta Cardiac Myosin and Power Generation in the Heart

β-cardiac myosin (βCM) is a non-processive motor responsible for muscle contraction in the heart, particularly in the ventricles where cardiomyopathies cause the most remodeling. βCM is a two-headed myosin, but it has a relatively low duty ratio, meaning that it is extremely unlikely that both heads would ever be bound to actin at the same time (7). βCM is also a mechanosensor in that it responds to force. In the heart, the main force resisting the powerstroke of βCM is referred to as the afterload. Using single-molecule techniques discussed in chapter 7, it was previously shown that force slows the rate of ADP release for βCM (8). While it is now possible to purify human βCM for use in biochemical experiments (9), the process is very difficult and the yield of

purified protein is relatively low. Therefore in this work we used βCM from porcine ventricles (MYH7) which is 97% identical to human βCM and has very similar biophysical properties. (8) Each myosin head serves as an independent force generator within a cell or muscle, therefore the ensemble force produced by multiple myosins multiplied by the velocity of contraction is equal to the power output (10). Mutations in βCM that cause familial cardiomyopathies are predicted to either affect the power output of the heart by altering the ensemble force or the velocity of contraction. However, while the general consensus is that HCM mutations cause hypercontractility/more power output and DCM mutations cause hypocontractility/less power output, the effect these mutations have on a molecular and even cellular level during the early stages of the disease progression is a current area of study.

1.3 Regulatory Proteins Tropomyosin and Troponin

While there are many mutations that have been identified in βCM that cause familial cardiomyopathies (11), this work focuses on mutations in regulatory proteins which control βCM's ability to bind to actin and produce force in a calcium dependent manner. These proteins are tropomyosin (Tm) and troponin (Tn), which decorate actin and combine to make up the thin filament. Upon calcium influx into the cytoplasm of the cell, the thin filament is activated by binding of calcium to one of the three subunits of Tn, troponin-T (Tn-T). However, instead of this being a merely "on" or "off" mechanism, activation is a multistep process described by a three-state model first identified by McKillop and Geeves (12). The first state is the blocked state where Tm completely occludes the myosin binding site on actin. Once calcium binds to Tn-T, this causes a conformational shift to the closed state where Tm slightly moves out of the way of the myosin

binding site but myosin can only weakly bind to actin. Tm can then either move spontaneously into the open position or it can be pushed there by myosin binding. Only in the open state can myosin bind and produce force. This three-state model has since been confirmed by structural techniques (13). The study of thin filament mutations that cause cardiomyopathies has been challenging because mutations in a similar region of a specific protein can lead to totally different phenotypes. Similar to mutations in βCM, the effect that Tn-T mutations have on a molecular level during the early disease progression is not well understood. This lack of understanding is reflected in the lack of translational therapeutics that have been employed for these patients despite approximately 30 years of research (3).

As mentioned previously, βCM is a mechanosensor that responds to force and while βCM interactions with actin have been studied in the presence of force, these experiments have not been performed in the presence of cardiac regulatory proteins. One study argued that the presence of Tm and Tn decreased the total step size by half; however, not all proteins used were from a cardiac source (14). In this work I present evidence that Tm and Tn do not affect the step size of βCM and the differences in kinetics are not necessarily biologically relevant. I also dissected the exact transition of the three-state model that each of three mutations (one for DCM, one for HCM and one for RCM) was affecting. At the molecular level it was determined that mutations in Tn-T do alter the population of thin filament in the open position, meaning these mutations directly affect the ability of myosin to bind to actin and produce force. With this knowledge of how exactly each mutation was affecting the ability of myosin to bind, we then connected this mechanism to the disease phenotype at the cellular or patient level.

1.4 iPSC-CMs as a tool for studying the early disease phenotype

In chapters 3 and 5 the Tn-T mutation being studied at the molecular level was also introduced into human induced pluripotent stem cell derived cardiomyocytes (iPSC-CMs). By manipulation of the Wnt signaling pathway using small molecules, methods have been developed for differentiation of stem cells into cardiomyocytes that beat spontaneously in a dish (15). Several models that have been developed for studying cardiomyopathies, and they each have disadvantages for the questions being asked in this work. For example, mouse models have been widely used to study heart disease and familial cardiomyopathies. However, mouse hearts beat much faster than human hearts and largely contain the α-cardiac myosin which differs from βCM by 83 amino acids in the motor domain alone (16). Another approach is studying human tissue collected from cardiomyopathy patients; however, human samples are relatively rare and are usually only collected from patients experiencing later stages of the disease. While iPSC-CMs are developmentally immature when compared to mature cardiomyocytes found in human tissue, the purpose of this work is again to study the effect of mutations during the early stages of the disease making this system ideal.

The findings in our work modeling Tn-T mutations in iPSC-CMs are consistent with previously proposed models that cellular tension is what distinguishes hypertrophic versus dilated cardiomyopathy (17). Our results showed that the initial insult of the Tn-T mutations was to alter force production in the cell and that other cellular affects such as mechanotransduction (Chapter 3) and changes in calcium handling (Chapter 5) are secondary. This mechanistic insight will be valuable in the application of a precision medicine approach for genetic cardiomyopathies (3).

1.5 Conclusions

Studies of βCM and the mechanism of thin filament regulation by Tm and Tn have broadly expanded our knowledge of how force production is regulated in the heart. First, in vitro experiments in the absence and presence of force have given us insight into the kinetics of βCM and well as that βCM is a mechanosensor and responds to force. Second, pioneering work by McKillop and Geeves demonstrated that the regulatory proteins Tm and Tn control βCM's ability to bind to actin and produce force as defined by the three-state model. Finally, the development of iPSC-CMs has provided a valuable model for studying the early disease phenotype of familial cardiomyopathies.

At a fundamental level this work has helped to answer the question of how a single mutation results in a complex clinical phenotype. Due to the complexity of familial cardiomyopathies, there is no one-size-fits all approach for treating patients, and it is therefore logical to instead treat patients in a mutation-specific manner. In order for this to be possible, in this thesis I showed how regulatory proteins affect force production by βCM in the presence of force, and I identified the initial molecular insult of three different mutations that cause either DCM, HCM or RCM. This work will contribute to the development of mechanism-based precision medicine.

1.6 References

1. J. G. Seidman, C. Seidman, The Genetic Basis for Cardiomyopathy: from Mutation Identification to Mechanistic Paradigms. *Cell* **104**, 557–567 (2001).
2. P. A. Harvey, L. A. Leinwand, Cellular mechanisms of cardiomyopathy. *J. Cell Biol.* **194**, 355–365 (2011).
3. M. J. Greenberg, J. C. Tardiff, Complexity in genetic cardiomyopathies and new approaches for mechanism-based precision medicine. *J. Gen. Physiol.* **153** (2021).
4. M. L. Lynn, S. J. Lehman, J. C. Tardiff, Biophysical Derangements in Genetic

Cardiomyopathies. *Heart Fail. Clin.* **14**, 147–159 (2018).
5. E. M. De La Cruz, E. M. Ostap, Relating biochemistry and function in the myosin superfamily. *Curr. Opin. Cell Biol.* **16**, 61–67 (2004).
6. M. J. Greenberg, G. Arpağ, E. Tüzel, E. M. Ostap, A Perspective on the Role of Myosins as Mechanosensors. *Biophys. J.* **110**, 2568–2576 (2016).
7. J. C. Deacon, M. J. Bloemink, H. Rezavandi, M. A. Geeves, L. A. Leinwand, Identification of functional differences between recombinant human α and β cardiac myosin motors. *Cell. Mol. Life Sci.* **69**, 2261–2277 (2012).
8. M. J. Greenberg, H. Shuman, E. M. Ostap, Inherent force-dependent properties of β-cardiac myosin contribute to the force-velocity relationship of cardiac muscle. *Biophys. J.* **107**, L41–L44 (2014).
9. R. Srikakulam, D. A. Winkelmann, Chaperone-mediated folding and assembly of myosin in striated muscle. *J. Cell Sci.* **117**, 641–652 (2004).
10. J. A. Spudich, Hypertrophic and Dilated Cardiomyopathy: Four Decades of Basic Research on Muscle Lead to Potential Therapeutic Approaches to These Devastating Genetic Diseases. *Biophys. J.* **106**, 1236–1249 (2014).
11. R. Walsh, C. Rutland, R. Thomas, S. Loughna, Cardiomyopathy: A systematic review of disease-causing mutations in myosin heavy chain 7 and their phenotypic manifestations. *Cardiology* **115**, 49–60 (2009).
12. D. F. McKillop, M. A. Geeves, Regulation of the interaction between actin and myosin subfragment 1: evidence for three states of the thin filament. *Biophys. J.* **65**, 693–701 (1993).
13. K. J. V. Poole, *et al.*, A comparison of muscle thin filament models obtained from electron microscopy reconstructions and low-angle X-ray fibre diagrams from non-overlap muscle. *J. Struct. Biol.* **155**, 273–284 (2006).
14. N. M. Kad, S. Kim, D. M. Warshaw, P. VanBuren, J. E. Baker, Single-myosin crossbridge interactions with actin filaments regulated by troponin-tropomyosin. *Proc. Natl. Acad. Sci. U. S. A.* **102**, 16990–16995 (2005).
15. X. Lian, *et al.*, Directed cardiomyocyte differentiation from human pluripotent stem cells by modulating Wnt/β-catenin signaling under fully defined conditions. *Nat. Protoc.* **8**, 162–175 (2013).
16. S. Lowey, *et al.*, Functional Effects of the Hypertrophic Cardiomyopathy R403Q Mutation Are Different in an α- or β-Myosin Heavy Chain Backbone*. *J. Biol. Chem.* **283**, 20579–20589 (2008).
17. J. Davis, *et al.*, A Tension-Based Model Distinguishes Hypertrophic versus Dilated Cardiomyopathy. *Cell* **165**, 1147–1159 (2016).

Chapter 2: Computational tool to study perturbations in muscle regulation and its application to heart disease

This chapter was published in Biophysical Journal as:

S. K. Barrick, S. R. Clippinger, L. Greenberg, M. J. Greenberg, Computational Tool to Study Perturbations in Muscle Regulation and Its Application to Heart Disease. *Biophys. J.* **116**, 2246–2252 (2019).

Author contributions: SB and SC contributed equally to this work. S.K.B. performed and analyzed the fluorescence experiments and developed code. S.R.C. helped with the early development and testing of the MATLAB code. L.G. generated mutant protein. M.J.G. oversaw the project and developed the early code for analyzing data. S.K.B. and M.J.G. wrote the first draft of the paper, and all authors contributed to the final draft.

Abstract

Striated muscle contraction occurs when myosin thick filaments bind to thin filaments in the sarcomere and generate pulling forces. This process is regulated by calcium, and it can be perturbed by pathological conditions (e.g., myopathies), physiological adaptations (e.g., β-adrenergic stimulation), and pharmacological interventions. Therefore, it is important to have a methodology to robustly determine the impact of these perturbations and statistically evaluate their effects. Here, we present an approach to measure the equilibrium constants that govern muscle activation, estimate uncertainty in these parameters, and statistically test the effects of perturbations. We provide a MATLAB-based computational tool for these analyses, along with easy-to-follow tutorials that make this approach accessible. The hypothesis testing and error estimation approaches described here are broadly applicable, and the provided tools work with other types of data, including cellular measurements. To demonstrate the utility of the approach, we apply it to elucidate the biophysical mechanism of a mutation that causes familial hypertrophic cardiomyopathy. This approach is generally useful for studying muscle diseases and therapeutic interventions that target muscle contraction.

2.1 Introduction

Force production in cardiac and skeletal muscle is tightly regulated to ensure that contraction occurs in a controlled and concerted manner. Dysfunction of this regulation can lead to a wide array of diseases, including cardiomyopathies, and there are currently several therapies in development that target this regulation (1-3). Given the role of perturbations of muscle regulation

in health and disease, there is an outstanding need for tools that can resolve statistically significant changes in this regulation.

At the molecular scale, force production in muscle is powered by the molecular motor myosin, which contracts the sarcomere by pulling thin filaments (i.e., actin filaments decorated with tropomyosin and the troponin complex) toward the M-line of the sarcomere. The interaction between myosin and the thin filament is regulated in a calcium-dependent manner, where calcium influx into the cytoplasm leads to activation of the thin filament and subsequent muscle contraction. In their landmark work, McKillop and Geeves (4) used a battery of biochemical and biophysical techniques to demonstrate that thin-filament activation is a multi-step process, requiring contributions from calcium binding to troponin as well as actomyosin binding. Their model is known as the "three-state model" (Fig. 1). In the absence of calcium, tropomyosin is in the blocked state, obscuring the myosin-binding site on the thin filament and inhibiting muscle contraction. Calcium binding to the troponin complex causes tropomyosin to shift to the closed state on the thin filament, exposing part of the myosin-binding site. Tropomyosin can either move to the open position spontaneously, where it permits myosin strong binding, or it can be pushed there by myosin binding. Myosin first binds weakly to the thin filament, then isomerizes to a strongly bound, force-generating state. The binding of one myosin to the thin filament pushes tropomyosin into the open position, exposing adjacent myosin-binding sites and leading to cooperative activation. The three states of tropomyosin positioning along the thin filament were subsequently confirmed using structural techniques (5).

The three-state model provides a useful framework to understand the mechanism of perturbations in skeletal and cardiac thin-filament regulation, such as drug treatments (1, 6),

protein isoform changes (7), disease-causing mutations (8), and post-translational modifications (9, 10). The formalism laid out by McKillop and Geeves enables the determination of the equilibrium constants that govern transitions between states, and thus the population of thin-filament regulatory units in each state (Fig. 1). However, it has been challenging to precisely define the values of these equilibrium constants, due in part to the number of free parameters in the model. Furthermore, the original McKillop and Geeves approach did not provide a methodology for assessment of uncertainty in parameter values or hypothesis testing. Such a methodology is necessary for the rigorous assessment of the effects of perturbations.

Here, we have modified the approach of McKillop and Geeves to better resolve the effects of perturbations in tropomyosin positioning along the thin filament. We provide a MATLAB-based computational tool and a user guide that enables users to measure the equilibrium constants that govern thin-filament activation, estimate uncertainty in these parameters, and statistically test the effects of perturbations. We demonstrate the utility of our approach by applying it to investigate the biophysical mechanism of a mutation in troponin T, ΔE160, that causes familial hypertrophic cardiomyopathy (HCM) (11). This approach allows for the robust determination of differences between wild-type and mutant proteins, which is an important step toward developing novel therapies to treat HCM and other devastating muscle diseases.

2.2 Results and Discussion

Here we present a methodology and MATLAB-based computational tool for analyzing biochemical measurements of thin-filament positioning. This procedure builds on the formalism developed by McKillop and Geeves (4), extending it to allow for improved precision of parameter

values, estimations of uncertainties, and statistical hypothesis testing. The basic workflow for the analysis follows:

1. Measure the value of the equilibrium constant between the blocked and closed states of the thin filament, K_B, using a stopped-flow kinetic technique (see Supporting Materials).
2. Perform steady-state fluorescence titrations measuring myosin binding to regulated thin filaments (RTFs; see Supporting Materials). The titrations should be carried out at three separate calcium concentrations (i.e., low (nocal), high (cal), and intermediate (midcal) calcium concentrations). These data will be used in step 4 to determine the following parameters: K_T (the equilibrium constant between the closed and open states of the thin filament) at each calcium concentration, K_W (the equilibrium constant describing weak myosin binding), and *nH* (the size of the cooperative unit).
3. Use the provided script (Script_normalization_replicate.m) to normalize the data from each technical replicate (typically three curves: nocal, midcal, cal) before pooling the data.
4. Use the provided script (Script_global_fitting.m) to globally fit the pooled titration data set to determine the best-fit values and calculate confidence intervals from bootstrapping simulations for each parameter ($K_{T\text{-}nocal}$, $K_{T\text{-}midcal}$, $K_{T\text{-}cal}$, K_W, *nH*).
5. For a given perturbation, statistically test for differences between individual parameters obtained from the fitting using the provided script (Script_hypothesis_testing.m).

A detailed user guide describing how to perform each of these steps, along with the data used to generate the figures in this manuscript, is provided with the computational tool.

Results obtained using the traditional fitting procedure and the estimation of uncertainties

The individual equilibrium constants that define the positioning of cardiac tropomyosin along the thin filament were determined using tissue-purified porcine cardiac myosin and actin and recombinant human troponin and tropomyosin (see Supporting Materials). The equilibrium constant for the transition between the blocked and closed states, K_B, was determined by performing stopped-flow kinetic measurements. We measured $K_B = 0.3 \pm 0.2$, in agreement with the previously determined value (4, 15). Although there is some variance between technical replicates for K_B, the values of parameters obtained from fitting of the titration data are relatively insensitive to small changes in the value of K_B.

The equilibrium constants for the transition between the closed and open states, K_T, and for myosin weak binding, K_W, were determined by performing titrations of RTFs with myosin at high (pCa 3) and low (2 mM EGTA) calcium. The titration curves were fit independently by Equation 1 (4). To ensure that the fitting was not biased by the initial guesses of parameter values, we modified the fitting procedure described in (4) to incorporate an annealing routine that iteratively fits the data with altered initial guesses. The values obtained from these fits are shown in Figure 3A, and they are consistent with values obtained previously with skeletal and cardiac muscle proteins (15-17). The original formulation of the McKillop and Geeves model did not include a methodology for determining uncertainty in fitted parameters. We developed a procedure to calculate 95% confidence intervals via bootstrapping of the original data set (12, 13), and we applied this procedure to calculate the confidence intervals of the parameters calculated using the classic approach. With this procedure, we saw that the classic approach gave considerable uncertainty in the values of the fitted parameters. For example, for the data collected at low calcium, we obtained

uncertainties much larger than the measured parameters for both K_W (0.13 (-0.03/ +1.26)) and *nH* (6 (-2/+6)).

Global fitting improves the resolution of fitted parameters

To improve the resolution of parameters derived from the fitting of the data, we adopted two modifications from the traditional approach. First, we performed an additional titration at an intermediate calcium concentration (pCa 6.25). The inclusion of an additional titration curve at an intermediate calcium concentration is advantageous because some perturbations shift the calcium sensitivity at intermediate calcium concentrations but not under fully activating or deactivating conditions (18). Second, titration curves collected at the three different calcium concentrations were fit globally rather than individually. In the global fitting, the values of K_W, K_S, and *nH* were shared between the fits of all curves. Global fitting of the three curves (Fig. 3A) yielded tighter 95% confidence intervals for both K_W and *nH* (Fig. 3). The confidence interval for K_W was 0.13 (-0.02/+0.03), compared to 0.13 (-0.03/+1.26) for the individually fit curve at low calcium. Similarly, the confidence interval for *nH* for the individually fit data was 6 (-2/+6), while the confidence interval for the globally fit data was 6 (-2/+4). These data demonstrate the improved resolution of this approach.

Hypothesis testing and its application to determining the biochemical mechanism of a mutation that causes hypertrophic cardiomyopathy

To demonstrate the utility of our approach for resolving the effects of molecular-based changes in cardiac thin-filament regulation, we examined a point mutation that causes familial hypertrophic cardiomyopathy (HCM), ΔE160 in troponin T (11). Clinical studies have shown that this

mutation causes pronounced ventricular hypertrophy and sudden cardiac death, with half of the patients not surviving past age 40 (11). Previous studies of the ΔE160 mutation in muscle fibers (19, 20), transfected myotubes (21), and purified proteins (22) have shown that the ΔE160 mutation causes increased activation of contractility. However, the biochemical mechanism of this activation is not well understood.

We applied our methodology to determine which transitions involved in thin-filament regulation (Fig. 1) are affected by the ΔE160 mutation. The goal of this analysis is not an exhaustive characterization of the mutant; rather, it is to demonstrate the utility of this approach for statistically assessing the effects of perturbations on thin-filament regulation. From stopped-flow kinetic measurements (Fig. 4A), we obtained a K_B of 0.2 ± 0.1 for ΔE160, which is indistinguishable from the value obtained for wild-type (WT) troponin (0.3 ± 0.2; p=0.41). We also performed fluorescence titrations (Fig. 4B) to measure steady-state actomyosin binding and determine K_W, K_T, and nH. We used the computational tool to calculate parameter values and their corresponding uncertainties from global fitting of the titration curves (Fig. 4C).

To determine whether there are statistically significant differences between the parameters for WT troponin and the ΔE160 mutant, we applied the hypothesis testing methodology described in the Materials and Methods. We found that the mutant showed a threefold increase in K_T at high calcium (0.17 (-0.12/+0.18) for WT versus 0.52 (-0.16/+0.28) for ΔE160; p=0.014). This threefold increase in K_T would result in an increased population of force-generating cross bridges at high calcium. We also found a slight, but statistically significant, decrease in K_W (0.13 (-0.02/+0.03) for WT versus 0.08 (-0.01/+0.01) for ΔE160; p=0.002). We saw that at low calcium, K_T was 3-fold larger for the mutant (p=0.076); however, this difference was not significant at the 95% confidence level.

We did not detect statistically significant differences in the values of *nH* (p=0.89), K_B (p=0.41), or $K_{T\text{-}midcal}$ (p=0.95). The net effect of these changes would be to increase activation, which is consistent with the hypercontractility associated with HCM. Taken together, these data demonstrate the power of this approach for hypothesis testing and for determining the biochemical mechanism of perturbations of thin-filament regulation. Moreover, determination of the specific steps of thin-filament activation affected by a perturbation provides a useful framework for interpreting results obtained from complementary methods (e.g., structural biology, muscle fiber mechanics), enhancing our understanding of muscle physiology and disease.

Relationship to other models of thin-filament regulation

Our method is based on the McKillop and Geeves approach, which significantly advanced our understanding of thin-filament regulation. The goal of this paper is not to distinguish between this and other proposed models (23, 24); rather, it is to provide an improved framework for interpreting results obtained using the McKillop and Geeves formalism. In recent years, there have been additional modeling efforts to better refine the McKillop and Geeves model (25-29) and to extend its applicability to larger systems with more states. These efforts have enhanced our understanding of muscle contraction and have led to the development of systems that can recapitulate many of the salient features of muscle contraction in silico (28). However, these models are also significantly more complicated than the McKillop and Geeves model. The ability to assess the effect of perturbations on thin-filament regulation using the relatively simple three-state model is a major advantage of the approach and computational tool presented here.

Application of the hypothesis testing and uncertainty estimation to other systems

The computational tool for hypothesis testing and confidence interval estimation from bootstrapping simulations is not limited to analysis of fluorescence titrations, but it can be broadly applied to other data sets as well. We have supplied a stand-alone version of this section of the code for examining the mean and median values (i.e., data frequently used for single cell measurements) so that others can apply it to their experimental system. This methodology is useful for data sets for which the form of the underlying distribution is either unknown or not normal, such as single-molecule data (30) and single-cell studies, as demonstrated in (18).

2.3 Conclusion

Here, we have demonstrated a method for extending the utility of the McKillop and Geeves (4) approach to understanding thin-filament regulation, and we have provided a well-documented, accessible computational tool to implement this methodology. Our approach extends the McKillop and Geeves approach to include a method for calculating confidence intervals and performing statistical tests. This methodology allowed us to resolve the molecular effects of a mutation that causes hypertrophic cardiomyopathy. This tool should be useful for studying physiological and pathological changes in muscle, as well as for testing new therapies that target muscle regulation.

Code Availability

The computational tool can be downloaded from GitHub at:

https://github.com/GreenbergLab/Thin_Filament_Fitting

The computational tool consists of a series of scripts that are executable in MATLAB. The software is compatible with at least versions of MATLAB 2017b to 2019a. Where we are aware of potential compatibility issues with previous versions of MATLAB, we provide suggestions for resolving these issues in the scripts. The scripts require the following MATLAB toolboxes: Global Optimization, Statistics and Machine Learning. The Parallel Computing toolbox is recommended for the purposes of decreasing the time required to perform the fitting, but it is not strictly required to run the scripts. We also provide an in-depth user guide, along with the raw data used in the examples presented here. The MATLAB code is provided as an appendix to the user guide for users wanting to adapt the code to a different language.

Acknowledgements:

Funding for this project was provided by the National Institutes of Health (R00HL123623, R01HL141086 to M.J.G., T32EB018266 to S.R.C.), and the March of Dimes Foundation (FY18-BOC-430198 to M.J.G.). We thank Tommy Blackwell and Tom Stump for critical evaluation of the code.

Conflict of interest statement:

All experiments were conducted in the absence of any commercial or financial relationships that could be construed as a potential conflict of interest.

2.4 Materials and Methods

Determination of equilibrium constants using the McKillop and Geeves analysis

In the classic McKillop and Geeves analysis, the values of the equilibrium constants that govern muscle activation (Fig. 1) were determined from biochemical measurements. K_B was calculated based on stopped-flow measurements of the rates of myosin binding to regulated thin

filaments (RTFs) at low (pCa 9) and high (pCa 4) calcium (see Supporting Materials for details). K_W, K_T, and *nH* (i.e., the size of the cooperative unit) were calculated from titrations of pyrene-labeled RTFs with myosin performed at saturating calcium (pCa 3; cal) and in the absence of calcium (2 mM EGTA; nocal) (see Supporting Materials for details). The relationship between the fraction of myosin-bound subunits, *f*([m]), and the fractional change in pyrene fluorescence upon myosin binding is given by the following equation (4):

$$\mathrm{f([m])} = \frac{\mathrm{F_0 - F}}{\mathrm{F_0 - F_\infty}} = \frac{\mathrm{K_W[m]P^{(nH-1)}(K_T(1+K_S)^{(nH)}+1)}}{\left(\mathrm{K_T P^{(nH)} + Q^{(nH)} + \frac{1}{K_B}}\right)\mathrm{(1+K_S)^{(nH-1)}}} \qquad \text{Equation 1}$$

where *F* is the measured pyrene fluorescence; F_0 and F_∞ are the pyrene fluorescence in the absence of myosin and at saturating myosin, respectively; [m] is the concentration of myosin; $P = 1 + [m]*K_W(1 + K_S)$; and $Q = 1 + [m]*K_W$. K_B at high calcium and K_S were set to 20 and 18, respectively, based on (4). *nH*, K_W, and K_T were determined in the presence and absence of calcium by fitting each titration curve independently.

Modified fitting approach

To improve the resolution of the parameters extracted from fitting of the data, we modified the classic McKillop and Geeves approach:

(1) For the calculations of K_T, K_W, and *nH* using steady-state fluorescence titrations, McKillop and Geeves examined two calcium concentrations (pCa 3 and 2 mM EGTA). Here, we perform an additional steady-state fluorescence titration at an intermediate calcium concentration (pCa 6.25; midcal) to improve our ability to resolve these parameters.

(2) The data for curves collected at three different calcium concentrations are globally fit using least squares optimization, and the parameters that minimized the aggregate error in all three data sets are determined. In global fitting, individual parameters can be shared between data sets, reducing the number of free variables and increasing the power to precisely measure parameter values. Here, K_W and *nH* are shared parameters among all three curves; however, this approach does not require sharing these parameters. K_T depends on calcium, thus three distinct K_T values ($K_{T\text{-}nocal}$, $K_{T\text{-}midcal}$, $K_{T\text{-}cal}$) are determined using this approach, one for each of the calcium concentrations used in the titrations (2 mM EGTA, pCa 6.25, and pCa 3, respectively).

(3) We use a simulated annealing algorithm (simulannealbnd, included in the Global Optimization Toolbox of MATLAB) in our fitting procedure to avoid biasing the fit toward the initial guesses used in the fitting. The annealing routine ensures that the best-fit parameters are obtained from a global rather than local minimum.

Hypothesis testing and statistics

One limitation of the original formulation of the three-state model is that it lacks procedures for calculating uncertainties and statistical hypothesis testing. Here, we use the well-established technique of bootstrapping simulations to calculate 95% confidence intervals (12, 13) for the parameter values determined by fitting Equation 1 to the fluorescence titration data (see Figure 4B-D). This data set consists of the titration data collected at three calcium concentrations: no calcium (2 mM EGTA; nocal), intermediate calcium (pCa 6.25; midcal), and saturating calcium (pCa 3; cal). In the bootstrapping method, the original data set is randomly resampled to generate synthetic

data sets, each containing the same number of points as the original data set. Each synthetic data set is then fit to determine the best-fit values of the parameters for that data set. 95% confidence intervals are defined as the interval over which 95% of the simulated parameter values are found. Note that the number of bootstrapping simulations required will depend on the noise in the data as well as the number of sampled points. As such, one should empirically determine the number of simulations required for stable convergence of the confidence intervals. We find that for the experiments described here, 1000 rounds of bootstrapping simulations are sufficient (Fig. 2A).

For statistical hypothesis testing, we define a test statistic as the difference between parameter values in the perturbed and unperturbed systems (14). For example, to determine whether there is a statistically significant difference in the value of K_W for a mutant protein relative to wild-type (WT), the test statistic is H = K_W(WT) – K_W(mutant). The value of the test statistic is calculated for the real data and for pairs of K_W values drawn from the bootstrapping simulations of the data. The interval within which 95% of the test statistic values from the bootstrapped simulations fall is defined as the 95% confidence interval. If the null hypothesis (i.e., H_0=0) is not contained within the 95% confidence interval, then the null hypothesis is rejected, and K_W(WT) ≠ K_W(mutant) with a p-value < 0.05 (Fig. 2B-C). The p-value can be calculated from a cumulative distribution of the test statistic by finding the largest interval that does not contain the null hypothesis (Fig. 2D). This value is multiplied by two to make the test equivalent to a two-tailed test.

2.5 Figures

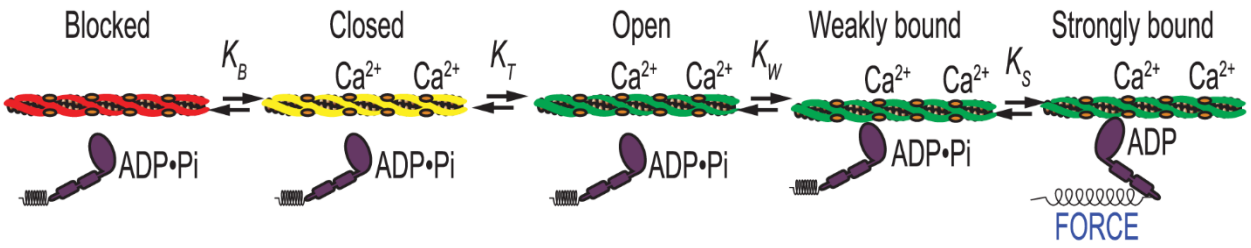

Figure 1. Schematic of the three-state model of muscle regulation. Red, yellow, and green represent the blocked, closed, and open states of tropomyosin, respectively. The equilibrium constants K_B and K_T describe transitions between states of tropomyosin on the thin filament, whereas K_W and K_S describe weak and strong myosin binding, respectively.

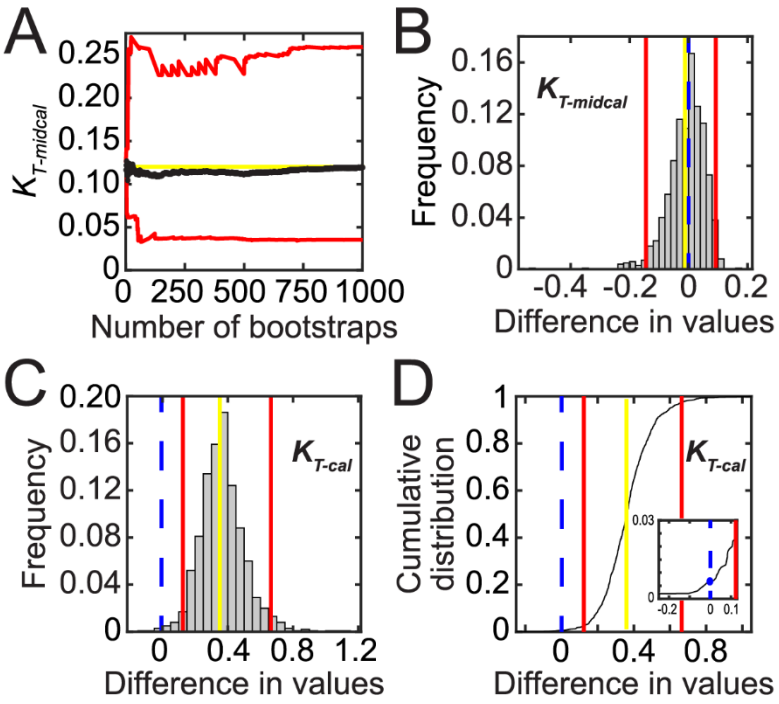

Figure 2. Hypothesis testing. **A.** Values of the average (black) and upper and lower bounds (red) of the 95% confidence interval for $K_{T\text{-}midcal}$ for WT troponin as a function of the number of bootstraps performed during error estimation. The yellow line marks the measured best-fit value. **B-C.** Histograms of the test statistic (i.e., the difference in values between parameters determined for WT and ΔE160) for $K_{T\text{-}midcal}$ (B) and $K_{T\text{-}cal}$ (C). Vertical lines represent the measured difference in values (yellow), the bounds of the 95% confidence interval (red), and the null hypothesis (blue dashed). The difference in parameter values is statistically significant at the 95% confidence level if the null hypothesis falls outside the 95% confidence interval, as in C. **D.** Cumulative distribution of the difference in values between WT and ΔE160 calculated from the bootstrapping simulations for $K_{T\text{-}cal}$. Vertical lines are the same as in C. Inset highlights the determination of the p-value from the value of the cumulative distribution at x = 0. This value is multiplied by two to make the test equivalent to a two-tailed test.

A

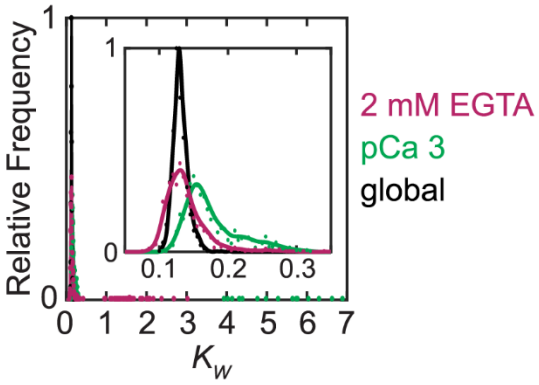

B

	2 mM EGTA Individual fit	pCa 3 Individual fit	Global fit
K_W	0.13 (-0.03/+1.26)	0.16 (-0.03/+0.13)	0.13 (-0.02/+0.03)
$K_{T\text{-}nocal}$	0.03 (-0.03/+0.07)	--	0.05 (-0.05/+0.09)
$K_{T\text{-}midcal}$	--	--	0.12 (-0.09/+0.13)
$K_{T\text{-}cal}$	--	0.22 (-0.21/+0.21)	0.17 (-0.12/+0.18)
nH	6 (-2/+6)	4 (-1/+6)	6 (-2/+4)

Figure 3. Traditional vs. global fitting of the three-state model to fluorescence titration data. **A.** Histograms showing the frequency of K_W values determined from 1000 bootstrapping simulations. Points are the values from the global fitting (black) and from the individual fits of data collected at 2 mM EGTA (magenta) and pCa 3 (green). Lines are inserted to guide the eye. The inset shows the distributions near the mean values of K_W. These data demonstrate that global fitting reduces the uncertainty in the measurement. **B.** Table of parameter values obtained from individual fits of data collected at 2 mM EGTA (nocal) or pCa 3 (cal) compared to those obtained from our global fitting method, which includes pCa 6.25 (midcal). Values in parentheses indicate the 95% confidence intervals.

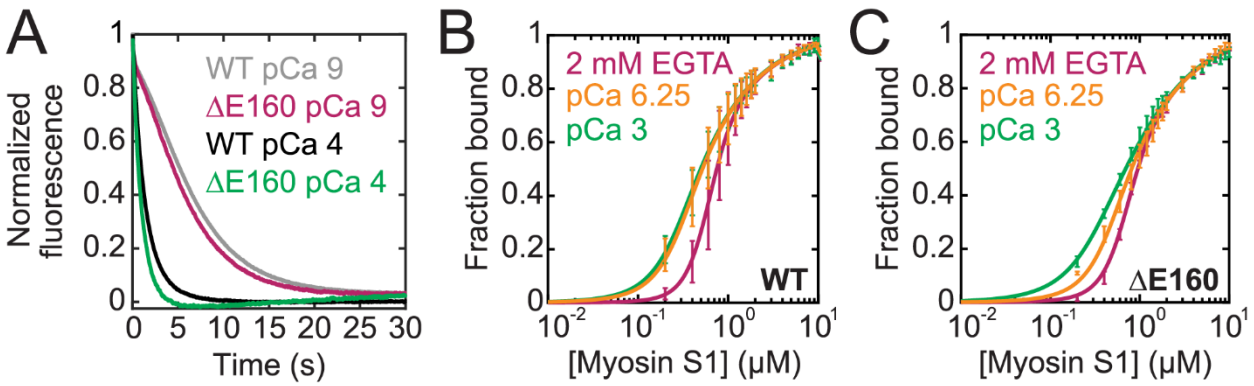

D

	WT	ΔE160	p
K_B	0.3 (+/- 0.2)	0.2 (+/- 0.1)	0.407
K_W	0.13 (-0.02/+0.03)	0.08 (-0.01/+0.01)	0.002*
$K_{T\text{-}nocal}$	0.05 (-0.05/+0.09)	0.15 (-0.07/+0.16)	0.076
$K_{T\text{-}midcal}$	0.12 (-0.09/+0.13)	0.11 (-0.04/+0.04)	0.950
$K_{T\text{-}cal}$	0.17 (-0.12/+0.18)	0.52 (-0.16/+0.28)	0.014*
nH	6 (-2/+4)	6 (-1/+1)	0.888

Figure 4. Effects of the ΔE160 mutation in troponin T on thin-filament regulation. **A.** Normalized stopped-flow fluorescence traces of regulated thin filaments binding to myosin. The pyrene fluorescence is quenched at a higher rate at saturating calcium (pCa 4, green/black) than at low calcium (pCa 9, magenta/gray). The traces for WT (black/gray; average of n=6 curves each) and the ΔE160 mutant (magenta/green; average of n=4 curves each) are similar at each calcium concentration. **B-C.** Steady-state titrations of regulated thin filaments with myosin for the WT (B) or mutant (C) protein conducted at three distinct calcium concentrations: saturating calcium (cal, pCa 3, green), intermediate calcium (midcal, pCa 6.25, orange), and low calcium (nocal, 2 mM EGTA, magenta). Curves are fits to the data. Error bars show the standard deviation of five technical replicates. **D.** Table of parameter values obtained for WT and ΔE160 troponin complexes from stopped-flow measurements (for K_B) and using the computational tool (for all others). Values in parentheses indicate the standard deviation of four replicates for K_B and 95% confidence intervals determined using the computational tool for all other parameters. Asterisks indicate statistical significance at the 95% confidence level.

2.6 References

1. Malik, F. I., J. J. Hartman, K. A. Elias, B. P. Morgan, H. Rodriguez, K. Brejc, R. L. Anderson, S. H. Sueoka, K. H. Lee, J. T. Finer, R. Sakowicz, R. Baliga, D. R. Cox, M. Garard, G. Godinez, R. Kawas, E. Kraynack, D. Lenzi, P. P. Lu, A. Muci, C. Niu, X. Qian, D. W. Pierce, M. Pokrovskii, I. Suehiro, S. Sylvester, T. Tochimoto, C. Valdez, W. Wang, T. Katori, D. A. Kass, Y. T. Shen, S. F. Vatner, and D. J. Morgans. 2011. Cardiac myosin activation: a potential therapeutic approach for systolic heart failure. Science 331(6023):1439-1443.
2. Green, E. M., H. Wakimoto, R. L. Anderson, M. J. Evanchik, J. M. Gorham, B. C. Harrison, M. Henze, R. Kawas, J. D. Oslob, H. M. Rodriguez, Y. Song, W. Wan, L. A. Leinwand, J. A. Spudich, R. S. McDowell, J. G. Seidman, and C. E. Seidman. 2016. A small-molecule inhibitor of sarcomere contractility suppresses hypertrophic cardiomyopathy in mice. Science 351(6273):617-621.
3. Messer, A. E., and S. B. Marston. 2014. Investigating the role of uncoupling of troponin I phosphorylation from changes in myofibrillar Ca(2+)-sensitivity in the pathogenesis of cardiomyopathy. Front Physiol 5:315.
4. McKillop, D. F., and M. A. Geeves. 1993. Regulation of the interaction between actin and myosin subfragment 1: evidence for three states of the thin filament. Biophysical Journal 65(2):693-701.
5. Lehman, W., R. Craig, and P. Vibert. 1994. Ca(2+)-induced tropomyosin movement in Limulus thin filaments revealed by three-dimensional reconstruction. Nature 368(6466):65-67.
6. Woody, M. S., M. J. Greenberg, B. Barua, D. A. Winkelmann, Y. E. Goldman, and E. M. Ostap. 2018. Positive cardiac inotrope omecamtiv mecarbil activates muscle despite suppressing the myosin working stroke. Nat Commun 9(1):3838.
7. Gupta, M. P. 2007. Factors controlling cardiac myosin-isoform shift during hypertrophy and heart failure. Journal of molecular and cellular cardiology 43(4):388-403.
8. Garfinkel, A. C., J. G. Seidman, and C. E. Seidman. 2018. Genetic Pathogenesis of Hypertrophic and Dilated Cardiomyopathy. Heart Fail Clin 14(2):139-146.
9. Muthu, P., K. Kazmierczak, M. Jones, and D. Szczesna-Cordary. 2011. The effect of myosin RLC phosphorylation in normal and cardiomyopathic mouse hearts. Journal of cellular and molecular medicine.
10. Levine, R. J., Z. Yang, N. D. Epstein, L. Fananapazir, J. T. Stull, and H. L. Sweeney. 1998. Structural and functional responses of mammalian thick filaments to alterations in myosin regulatory light chains. Journal of Structural Biology 122(1-2):149-161.
11. Watkins, H., W. J. McKenna, L. Thierfelder, H. J. Suk, R. Anan, A. O'Donoghue, P. Spirito, A. Matsumori, C. S. Moravec, J. G. Seidman, and et al. 1995. Mutations in the genes for cardiac troponin T and alpha-tropomyosin in

hypertrophic cardiomyopathy. The New England Journal of Medicine 332(16):1058-1064.
12. Efron, B. 1979. Bootstrap Methods: Another Look at the Jackknife. The Annals of Statistics 7(1):1-26.

13. Press, W. H. 1992. Numerical recipes in C : the art of scientific computing. Cambridge University Press, Cambridge England ; New York.
14. Martin, M. A. 2007. Bootstrap hypothesis testing for some common statistical problems: A critical evaluation of size and power properties. Comput Stat Data An 51(12):6321-6342.
15. Maytum, R., F. Bathe, M. Konrad, and M. A. Geeves. 2004. Tropomyosin exon 6b is troponin-specific and required for correct acto-myosin regulation. The Journal of biological chemistry 279(18):18203-18209.
16. Boussouf, S. E., R. Maytum, K. Jaquet, and M. A. Geeves. 2007. Role of tropomyosin isoforms in the calcium sensitivity of striated muscle thin filaments. Journal of muscle research and cell motility 28(1):49-58.
17. Maytum, R., B. Westerdorf, K. Jaquet, and M. A. Geeves. 2003. Differential regulation of the actomyosin interaction by skeletal and cardiac troponin isoforms. The Journal of Biological Chemistry 278(9):6696-6701.
18. Clippinger, S. R., P. E. Cloonan, L. Greenberg, M. Ernst, W. T. Stump, and M. J. Greenberg. 2019. Disrupted mechanobiology links the molecular and cellular phenotypes in familial dilated cardiomyopathy. Biorxiv.
19. Morimoto, S., Q. W. Lu, K. Harada, F. Takahashi-Yanaga, R. Minakami, M. Ohta, T. Sasaguri, and I. Ohtsuki. 2002. Ca(2+)-desensitizing effect of a deletion mutation Delta K210 in cardiac troponin T that causes familial dilated cardiomyopathy. Proceedings of the National Academy of Sciences of the United States of America 99(2):913-918.
20. Harada, K., F. Takahashi-Yanaga, R. Minakami, S. Morimoto, and I. Ohtsuki. 2000. Functional consequences of the deletion mutation deltaGlu160 in human cardiac troponin T. J Biochem 127(2):263-268.
21. Sweeney, H. L., H. S. Feng, Z. Yang, and H. Watkins. 1998. Functional analyses of troponin T mutations that cause hypertrophic cardiomyopathy: insights into disease pathogenesis and troponin function. Proceedings of the National Academy of Sciences of the United States of America 95(24):14406-14410.
22. Tobacman, L. S., D. Lin, C. Butters, C. Landis, N. Back, D. Pavlov, and E. Homsher. 1999. Functional consequences of troponin T mutations found in hypertrophic cardiomyopathy. The Journal of Biological Chemistry 274(40):28363-28370.
23. Houmeida, A., D. H. Heeley, B. Belknap, and H. D. White. 2010. Mechanism of regulation of native cardiac muscle thin filaments by rigor cardiac myosin-S1 and calcium. The Journal of Biological Chemistry 285:32760-32769.
24. Hill, T. L., E. Eisenberg, and L. Greene. 1980. Theoretical model for the cooperative equilibrium binding of myosin subfragment 1 to the actin-troponin-tropomyosin complex. Proceedings of the National Academy of Sciences of the United States of America 77:3186-3190.
25. Mijailovich, S. M., O. Kayser-Herold, X. Li, H. Griffiths, and M. A. Geeves. 2012. Cooperative regulation of myosin-S1 binding to actin filaments by a continuous flexible Tm-Tn chain. Eur Biophys J 41(12):1015-1032.
26. Mijailovich, S. M., O. Kayser-Herold, B. Stojanovic, D. Nedic, T. C. Irving, and M. A. Geeves. 2016. Three-dimensional stochastic model of actin-myosin binding in the sarcomere lattice. J Gen Physiol 148(6):459-488.

27. Mijailovich, S. M., X. Li, J. C. del Alamo, R. H. Griffiths, V. Kecman, and M. A. Geeves. 2010. Resolution and uniqueness of estimated parameters of a model of thin filament regulation in solution. Comput Biol Chem 34(1):19-33.
28. Mijailovich, S. M., D. Nedic, M. Svicevic, B. Stojanovic, J. Walklate, Z. Ujfalusi, and M. A. Geeves. 2017. Modeling the Actin.myosin ATPase Cross-Bridge Cycle for Skeletal and Cardiac Muscle Myosin Isoforms. Biophysical Journal 112(5):984-996.
29. Smith, D. A., M. A. Geeves, J. Sleep, and S. M. Mijailovich. 2008. Towards a unified theory of muscle contraction. I: foundations. Ann Biomed Eng 36(10):1624-1640.
30. Woody, M. S., J. H. Lewis, M. J. Greenberg, Y. E. Goldman, and E. M. Ostap. 2016. MEMLET: An Easy-to-Use Tool for Data Fitting and Model Comparison Using Maximum-Likelihood Estimation. Biophysical Journal 111(2):273-282.

2.7 Supporting Materials

Protein expression and purification

Cardiac ventricular myosin and actin were prepared from cryoground porcine ventricles (Pelfreez) as previously described (1). Cardiac actin was labeled with N-(1-pyrenyl)iodoacetamide (pyrene-actin) as described in (2, 3). The concentration of pyrene-actin was determined by measuring the absorbances at 290 nm and 344 nm. Myosin subfragment-1 (S1) was prepared from full-length myosin by chymotrypsin digestion (4), and its purity was assessed using SDS-PAGE.

Recombinant human tropomyosin was expressed in BL21-CodonPlus cells (Agilent) and purified using established protocols (5). The concentration of tropomyosin was determined by measuring the absorbance at 280 nm.

Human recombinant troponin I, troponin C, and troponin T were expressed in BL21-CodonPlus cells (Agilent), complexed, and purified using established protocols (6), with the modification that the final complexed protein was purified using a MonoQ column. Troponin complex concentration was measured spectroscopically using the Bradford reagent (Coomassie Plus Assay kit, Thermo Scientific). The □E160 mutation in troponin T was introduced using the QuikChange Site-Directed Mutagenesis Kit (Agilent) and verified by sequencing (GENEWIZ). The □E160 protein was expressed, purified, and complexed into functional troponin units using the same procedure as the WT protein.

Stopped-flow kinetic measurements

Stopped-flow transient kinetic measurements were carried out in buffer containing 60 mM MOPS, 200 mM KCl, 5 mM $MgCl_2$, 1 mM DTT, 2 mM EGTA, and either 5.2 µM $CaCl_2$ (pCa 9) or 2.15 mM $CaCl_2$ (pCa 4). Total concentrations of calcium, magnesium, ATP, and EGTA added were calculated using MaxChelator (7). Prior to measurements, tropomyosin was reduced by addition of 50 mM DTT, heated at 56 °C for 5 min, and allowed to cool to room temperature before centrifuging 30 min at 436000 x g at 4 °C in an Optima MAX-TL Ultracentrifuge (Beckman Coulter) equipped with a TLA 120.2 rotor (Beckman Coulter). Phalloidin-stabilized, pyrene-labeled actin filaments were prepared by incubating 50 µM pyrene-actin with 55 µM phalloidin in low-calcium buffer at least 10 min at room temperature. Pyrene was excited at 365 nm, and the fluorescence emission was detected using a 395-nm cutoff filter. Apyrase (0.02 units/mL) was added to each protein solution before mixing to ensure the absence of nucleotide (i.e., ATP and ADP).

Measurement of K_B using stopped-flow kinetics

K_B, the equilibrium constant between the blocked and closed states, was calculated by measuring the rates of myosin strong binding to pyrene-labeled regulated thin filaments (RTFs) in the presence and absence of calcium, as previously described (8). Fluorescent RTFs (2.5 µM phalloidin-stabilized pyrene-actin and 1 µM troponin and tropomyosin) were rapidly mixed with 0.25 µM myosin subfragment-1 (S1) using an SX20 stopped-flow mixer (Applied Photophysics). All concentrations refer to the final concentrations after mixing. The pyrene fluorescence of the actin in the thin filaments was quenched by myosin strong binding, yielding an exponential decrease in

fluorescence. K_B was calculated by taking the ratio of the rate constants of myosin binding at low ($k(-Ca^{2+})$; pCa 9) and high ($k(+Ca^{2+})$; pCa 4) calcium, as described by

McKillop and Geeves (8):

$$\frac{k(-Ca^{2+})}{k(+Ca^{2+})} = \frac{K_B}{1+K_B} \qquad \text{Equation S1}$$

A single experiment consisted of recording at least three kinetic time traces at each calcium concentration followed by fitting of a single exponential function to the averaged traces. The reported K_B values (see Figure 4D) are the average of at least four independent experiments, and reported errors are the standard deviations of these values. Statistical significance between K_B values was evaluated using a Student's two-tailed t-test.

Measurement of steady-state myosin binding to regulated thin filaments to determine *K_T*, *K_W*, and *nH*

The parameters K_T, K_W, and *nH* were calculated from equilibrium titrations measuring the concentration-dependent binding of myosin to pyrene-labeled RTFs (8). Myosin strong binding to the pyrene-labeled RTFs quenches the fluorescence, thus the fractional change in fluorescence was measured as a function of myosin added. Fluorescence titrations were performed in buffer containing 60 mM MOPS, 200 mM KCl, 5 mM $MgCl_2$, 1 mM DTT, and either 2 mM EGTA (low Ca^{2+}), 2 mM EGTA and 1.19 mM $CaCl_2$ (pCa 6.25), or 1 mM $CaCl_2$ (pCa 3). Reduced tropomyosin and phalloidin-stabilized pyrene-actin were each prepared as described above. RTFs (0.5 µM phalloidin-stabilized pyrene-actin and 0.27 µM troponin and tropomyosin) were continuously stirred and myosin S1 was added in the presence of 2 mM ADP, as well as 50 µM P^1,P^5-di(adenosine-5′) pentaphosphate (Ap5a), 1 µM hexokinase, and 2 mM glucose to maintain the nucleotide in the ADP state. Myosin S1 was added at 1-minute

intervals in increments of 0.2 µM up to 2 µM, then at 1-µM increments up to 10 µM. The steady-state pyrene fluorescence was measured at 1-minute intervals. Five technical replicates per condition were collected.

Supporting References

1. Greenberg, M. J., H. Shuman, and E. M. Ostap. 2014. Inherent force-dependent properties of beta-cardiac myosin contribute to the force-velocity relationship of cardiac muscle. Biophysical Journal 107:L41-44.
2. Pollard, T. D. 1984. Purification of a high molecular weight actin filament gelation protein from Acanthamoeba that shares antigenic determinants with vertebrate spectrins. The Journal of Cell Biology 99:1970-1980.
3. Greenberg, M. J., T. Lin, Y. E. Goldman, H. Shuman, and E. M. Ostap. 2012. Myosin IC generates power over a range of loads via a new tension-sensing mechanism. Proceedings of the National Academy of Sciences of the United States of America 109:E2433-2440.
4. Eads, T. M., D. D. Thomas, and R. H. Austin. 1984. Microsecond rotational motions of eosin-labeled myosin measured by time-resolved anisotropy of absorption and phosphorescence. Journal of Molecular Biology 179:55-81.
5. Hitchcock-DeGregori, S. E., and R. W. Heald. 1987. Altered actin and troponin binding of amino-terminal variants of chicken striated muscle alpha-tropomyosin expressed in Escherichia coli. The Journal of Biological Chemistry 262:9730- 9735.
6. Kozaili, J. M., D. Leek, and L. S. Tobacman. 2010. Dual regulatory functions of the thin filament revealed by replacement of the troponin I inhibitory peptide with a linker. The Journal of Biological Chemistry 285:38034-38041.
7. Bers, D. M., C. W. Patton, and R. Nuccitelli. 2010. A practical guide to the preparation of Ca(2+) buffers. Methods in Cell Biology 99:1-26.
8. McKillop, D. F., and M. A. Geeves. 1993. Regulation of the interaction between actin and myosin subfragment 1: evidence for three states of the thin filament. Biophysical Journal 65:693-701.

Chapter 3: Disrupted Mechanobiology Links the Molecular and Cellular Phenotypes in Familial Dilated Cardiomyopathy

This chapter was published in Proceedings of the National Academy of Sciences of the United States of America as:

S. R. Clippinger, P.E. Cloonan, L. Greenberg, M. Ernst, W.T. Stump, MJ Greenberg, Disrupted mechanobiology links the molecular and cellular phenotypes in familial dilated cardiomyopathy. *Proc. Natl. Acad. Sci. U. S. A.* **116**, 17831–17840 (2019).

Authors contributions: SC and PC contributed equally to this work. S.R.C. purified proteins, performed and analyzed the stopped flow and fluorescence experiments, and drafted the manuscript. P.E.C. performed and analyzed the fluorescence and traction force microscopy experiments with the stem-cell-derived cardiomyocytes. L.G. purified proteins, performed *in vitro* motility assays, implemented the cell-based assays, and performed and analyzed experiments with stem-cell-derived cardiomyocytes. M.E. performed and analyzed fluorescence microscopy experiments. W.T.S. designed tools for microcontact printing. M.J.G. oversaw the project, generated mutant proteins, implemented biochemical assays, analyzed data, and drafted the manuscript. All authors contributed to the editing of the final manuscript.

Abstract

Familial dilated cardiomyopathy (DCM) is a leading cause of sudden cardiac death and a major indicator for heart transplant. The disease is frequently caused by mutations of sarcomeric proteins; however, it is not well understood how these molecular mutations lead to alterations in cellular organization and contractility. To address this critical gap in our knowledge, we studied the molecular and cellular consequences of a DCM mutation in troponin-T, ΔK210. We determined the molecular mechanism of ΔK210 and used computational modeling to predict that the mutation should reduce the force per sarcomere. In mutant cardiomyocytes, we found that ΔK210 not only reduces contractility, but also causes cellular hypertrophy and impairs cardiomyocytes' ability to adapt to changes in substrate stiffness (e.g., heart tissue fibrosis that occurs with aging and disease). These results help link the molecular and cellular phenotypes and implicate alterations in mechanosensing as an important factor in the development of DCM.

3.1 Introduction

DCM is a major cause of sudden cardiac death in young people, and it is a significant cause of heart failure (1). DCM is phenotypically characterized by dilation of the left ventricular chamber, and it is often accompanied by changes in cellular and tissue organization, including lengthening of individual myocytes and fibrosis-induced stiffening of the myocardial tissue. Genetic studies have demonstrated that familial DCM can be caused by single point mutations, many of which are in sarcomeric proteins responsible for regulating cardiac contractility (1); however, the connection between the initial insult

of molecular-based changes in contractile proteins and the development of the cellular disease phenotype is not thoroughly understood. This lack of understanding has hampered efforts to develop novel therapeutics, and there is currently no cure for DCM, with heart transplantation being the only long-term treatment. The goal of this study was to better understand the connection between mutation-induced changes in contractility and the cellular phenotype in DCM.

Understanding the link between point mutations in sarcomeric proteins and the development of the disease phenotype in cells has been challenging for several reasons. One challenge stems from the fact that the clinical presentation and prognosis appear to depend on the specific mutation. In fact, different point mutations within the same molecule, and even different substitutions at the same amino acid site can lead to different forms of cardiomyopathy (e.g., hypertrophic, dilated, restrictive) with different ages of onset (2-5). Another challenge stems from selecting appropriate model systems of the human disease for the specific question being posed. *In vitro* biochemical studies are excellent for deciphering the molecular consequences of the initial insult (4); however, they are not clearly predictive of how the disease will manifest itself in cells (6). Studies using transgenic mice have significantly advanced our understanding of the disease; however, these mice do not always recapitulate the human disease phenotype due to differences in cardiac physiology between humans and mice (7-13). Patient tissue is excellent for studying the disease phenotype in humans (14); however, tissue from patients is difficult to obtain and usually only available from patients in the advanced stages of the disease or post mortem, when compensatory mechanisms can mask the initial insult.

Recent advances in stem cell (15, 16) and gene editing technologies (17) have provided a new avenue for modeling DCM in human induced pluripotent stem cell derived cardiomyocytes (hiPSC-CMs) (18, 19). These hiPSC-CMs can faithfully recapitulate many aspects of the early human disease (20), making them an excellent tool for deciphering how the initial molecular insult leads to the development of the early disease phenotype. Moreover, these cells can be examined in simplified *in vitro* systems that mimic various aspects of the environment in the heart to dissect how the local environment influences the development of the disease phenotype. It has been shown that cardiomyocytes can adapt their structural organization and contractility in response to their local mechanical and geometric environment (21-23). It is possible aberrant responses of cardiomyocytes to disease-related alterations in the local environment such as fibrosis-induced stiffening of the heart tissue could contribute to the development of the disease phenotype.

To uncover the connection between molecular changes and the development of the cellular disease phenotype, we determined the molecular and cellular mechanisms of a DCM-causing point mutation in troponin-T (TNNT2), deletion of lysine 210 (ΔK210) (24) (Fig. 1A). The ΔK210 mutation has been identified in patients as young as 2 years old in at least four unrelated families (25-27). Troponin-T is a subunit of the troponin complex, which, together with tropomyosin, regulates the calcium-dependent interactions between the force-generating molecular motor myosin and the thin filament. TNNT2 is one of the most frequently mutated genes in DCM (28, 29). There have been several excellent model systems developed to better understand aspects of the disease caused by this

mutation (30-34); however, the connection between the molecular mutation and the cellular phenotype seen in humans remains unclear.

Our results demonstrate that ΔK210 causes a reduction in myosin-based force generation at the molecular and cellular levels, and we used computational modeling to help link the contractile phenotypes seen at these scales. Surprisingly, we found that this disease-causing mutation of a sarcomeric protein not only impairs cardiomyocyte contraction, but it also causes cellular hypertrophy and impairs the ability of cardiomyocytes to sense and respond to changes in their mechanical environment. Our results suggest a central role for defects in cardiomyocyte mechanosensing in the disease pathogenesis of DCM.

3.2 Results

ΔK210 decreases calcium sensitivity in an *in vitro* motility assay

We set out to decipher the molecular mechanism of the ΔK210 mutation *in vitro*. The molecular effects of cardiomyopathy mutations depend on the myosin heavy chain isoform (7-9, 35-37) and therefore, we used porcine cardiac ventricular myosin (38). Porcine ventricular cardiac myosin (MYH7) is 97% identical to human, while murine cardiac myosin (MYH6) is only 92% identical. Unlike murine cardiac myosin, porcine cardiac myosin has very similar biophysical properties to human cardiac myosin, including the kinetics of the ATPase cycle, step size, and sensitivity to load (38-41), making it an ideal myosin for biophysical studies.

Given the role of troponin-T in thin filament regulation, we first determined whether the ΔK210 mutation affects calcium-based regulation of myosin's interactions with thin

filaments using an *in vitro* motility assay (42). Reconstituted thin filaments, consisting of porcine cardiac actin and recombinantly expressed human troponin complex and tropomyosin, were added to a flow cell coated with porcine cardiac myosin in the presence of ATP. The speed of filament translocation was measured as a function of added calcium. As has been reported previously, the speed of regulated thin filament translocation increased sigmoidally with increasing calcium concentration (43), (Fig. 1B). Data were fit with the Hill equation to obtain the pCa50 (i.e., the concentration of calcium necessary for half-maximal activation). Consistent with previous studies using mouse cardiac, rabbit cardiac, and rabbit skeletal muscle fibers (31, 33, 44), ΔK210 shows a right-shifted curve (pCa50 = 5.7 ± 0.1) compared to the WT (pCa50 = 6.1 ± 0.1; $p < 0.0001$), meaning more calcium is needed for the same level of activation. This suggests that the mutant could show impaired force production during a calcium transient.

Molecular mechanism of ΔK210-induced changes in thin filament regulation

The changes in calcium sensitivity seen in the *in vitro* motility assay could be due to changes in the kinetics of myosin attachment and/or detachment from the thin filament. To test whether the mutation affects the kinetics of myosin detachment from thin filaments, we measured the rate of ADP release from myosin, the transition that limits actomyosin dissociation at saturating ATP in the absence of load (45). Consistent with previous studies of other DCM troponin mutations (46), ΔK210 does not change the kinetics of ADP release from myosin (SI Appendix, Fig. S1). Therefore, the primary effects of the mutation are likely due to alterations in the kinetics of myosin attachment to the thin filament.

The kinetics of myosin attachment to the thin filament are regulated by myosin and the thin filament proteins troponin and tropomyosin. Biochemical (47) and structural biological (48, 49) experiments have shown that thin filament regulation is a complicated process where tropomyosin can lie along the thin filament in three positions (blocked, closed, and open), and that this positioning is determined by both calcium and myosin binding (Fig. 2A). To determine the molecular mechanism of the observed changes in the calcium sensitivity of myosin-based motility, we determined the equilibrium constants for the transitions between these states using an approach pioneered by McKillop and Geeves (47).

The equilibrium constant for the transition between the blocked and closed states, K_B, was measured using stopped-flow kinetic techniques (47), where the rate of myosin binding to pyrene-labeled regulated thin filaments was measured at high (pCa 4) and low (pCa 9) calcium concentrations. Myosin strong-binding to labeled thin filaments quenches the pyrene fluorescence, leading to a roughly exponential decrease in fluorescence (Fig. 2B-C). The ratio of the rate constants for myosin binding to the thin filament at high and low calcium can be used to calculate the equilibrium constant, K_B (47):

$$\frac{k_{obs}(-Ca^{2+})}{k_{obs}(+Ca^{2+})} \approx \frac{K_B}{1+K_B} \ (Eq.1)$$

The values of K_B obtained were 0.36 ± 0.15 for WT (n=3) and 0.36 ± 0.10 for ΔK210 (n=3), indicating that ΔK210 does not significantly affect the equilibrium constant for the transition between the blocked and closed states ($p = 0.99$).

To determine the equilibrium constant for the transition between the closed and open states, K_T, we measured the steady-state binding of myosin to pyrene-labeled regulated thin filaments over a range of myosin concentrations (Fig. 2D-E). Titration

relationships obtained for WT and ΔK210 at high (pCa 3) and low (2 mM EGTA) calcium concentrations show two-state (i.e., no calcium-based blocking) and three-state processes, respectively, as has been observed previously (47). Five technical replicates were used to define each curve. As described in the SI Appendix, Materials and Methods, we modified the fitting and analysis procedure used by McKillop and Geeves to better define the values of the fitted variables (50). We performed an additional titration at an intermediate calcium concentration (pCa 6.25) and used an annealing algorithm to globally fit the binding curves of the fractional change in pyrene fluorescence (a) as a function of myosin concentration for all three calcium concentrations (Fig. 2D-E). The fractional change in the pyrene fluorescence is given by (47):

$$a = \frac{F_0 - F}{F_0 - F_\infty} = \frac{K_W[M]P^{n-1}(K_T(1+K_S)^n + 1)}{(K_T P^n + Q^n + \frac{1}{K_B})(1+K_S)^{n-1}} \quad (Eq. 2)$$

where [M] is the concentration of myosin, F is the measured fluorescence, F_0 is the fluorescence in the absence of myosin, F_∞ is the fluorescence at saturating myosin concentrations, n is the size of the cooperative unit, P=1+K_W[M](1+K_S), and Q=1+K_W[M] (Fig. 2D-E). For the fitting, K_T, K_W (i.e., the equilibrium constant between the open and myosin weakly bound states, sometimes denoted K_1), and n were fit parameters. K_B and K_S (the equilibrium constant between the myosin weakly and strongly bound states, sometimes denoted K_2) were fixed based on the calculated values for K_B (Fig. 2B-C) and previously measured values of K_S (51). For the fitting at pCa 6.25 and 4, K_B was fixed at 20, since the fit is insensitive to the exact value of K_B at those calcium concentrations, as long as K_B is greater than 5. 95% confidence intervals were calculated from 1000 rounds of bootstrapping simulations (see SI Appendix, Materials and Methods).

We found that while the measured values of K_T for ΔK210 were consistently lower compared to the WT at all calcium concentrations (Fig. 3A), only the difference in K_T at pCa 6.25 was statistically significant (p=0.028). From the measured equilibrium constants, it is straightforward to calculate the fraction of regulatory units in each state from the partition function (47). At all calcium concentrations, ΔK210 shows a decrease in the fraction of thin filaments in the open, weakly-bound, and strongly-bound states compared to the WT (Fig. 3B, S7), and an increase in the fraction of thin filaments in the blocked and closed states. These data give the biochemical mechanism of the reduced activation at sub-saturating calcium seen in the *in vitro* motility assays (Fig. 1B) and would predict a reduction in the force per sarcomere in mutant muscle due to a reduction in the fraction of myosin crossbridges in the strongly-bound state.

Computational modeling recapitulates the shift in calcium sensitivity and predicts a lower force per sarcomere for ΔK210

To predict how the observed changes in the equilibrium populations of thin filament regulatory units correspond with contractility in a sarcomere, we used a computational model developed by Campbell et al. (52). This model was chosen since it has many similarities to the McKillop and Geeves biochemical model of muscle regulation used to analyze the biochemical experiments (47), although it should be noted that the there are some important differences (see Discussion and the SI Appendix, Materials and Methods). The Campbell et al. model simulates an ensemble of sarcomeric regulatory units that can transition between the blocked, closed, open, and myosin bound states based on the equilibrium constants between these states and a constant describing the coupling between adjacent regulatory units. This model enables the calculation of both

the expected steady-state force as a function of calcium and the expected force produced per sarcomere in response to a calcium transient. The details of the implementation of the model are described in the Materials and Methods. Using our measured equilibrium constants, the steady-state normalized force was simulated for both WT and ΔK210 over a range of calcium concentrations (Fig. 4A). Simulation of ΔK210 shows a rightward shift towards supermaximal calcium activation, consistent with the shift seen in the *in vitro* motility assay (Fig. 1B). Therefore, the observed set of changes in the equilibrium constants in the mutant are consistent with the observed changes seen in the *in vitro* motility assay, validating the approach taken here.

To predict the effects of the ΔK210 mutation on the force per sarcomere, we used the same computational model to simulate the force per sarcomere in response to a calcium transient. In the modeling, we assumed that the primary effects of the mutation are on thin filament positioning, and that to a first order approximation, the calcium transient is not significantly changed by the mutation. The consequences of these assumptions are explored in the Discussion. The simulation predicts a smaller maximal twitch force per sarcomere in response to a calcium transient for ΔK210 compared to the WT (Fig. 4B). Taken together, these simulations predict that ΔK210 should decrease the force per sarcomere in cardiomyocytes.

Generation of ΔK210 induced stem cell-derived cardiomyocytes

To examine the effects of the ΔK210 mutation in human cells, we generated human induced pluripotent stem cell (hiPSC)-derived cardiomyocytes (hiPSC-CMs). The hiPSC lines were derived from the BJ foreskin fibroblast line by the Washington University

Genome Engineering core (see SI Appendix, Materials and Methods). Whole exome sequencing of the stem cell line demonstrated that these cells do not have any genetic variants associated with familial cardiomyopathies (SI Appendix, Fig. S2). Cell lines homozygous for the ΔK210 mutation were generated using the CRISPR/Cas9 system (17) (SI Appendix, Fig. S3, and Materials and Methods). ΔK210 mutant stem cells have normal karyotypes (SI Appendix, Fig. S4) and are pluripotent, as assessed by immunofluorescence staining for pluripotency markers (SI Appendix, Fig. S5). For all experiments with the mutant hiPSC-CMs, two separate stem cell lines were used to ensure that the observations are not due to potential off-target cuts introduced during the CRISPR/Cas9 editing. We also used hiPSC-CMs from at least two separate differentiations per cell line for both WT and ΔK210. hiPSCs were differentiated to hiPSC-CMs using established protocols (15, 53) involving temporal modulation of WNT signaling using small molecules (SI Appendix, Fig. S5) and aged at least 30 days before use. Using this procedure, >90% cardiomyocytes were obtained, as determined by immunofluorescence staining for cardiac troponin-T (SI Appendix, Fig. S5).

To examine the sarcomeric organization of hiPSC-CMs, cells cultured on glass were fixed and stained for troponin-I and α-actinin to visualize the thin filament and z-discs, respectively (Figure 5). Unlike adult human tissue derived cardiomyocytes, which are rectangular with sarcomeres that align with the long axis of the cell, WT hiPSC-CMs cultured on glass orient randomly and display robust sarcomeric staining that is typically not aligned along a single axis (Fig. 5A). Compared to the WT hiPSC-CMs, ΔK210 hiPSC-CMs display more disorganized sarcomeres with patches of punctate staining (Fig. 5B). Similar disorganization and punctate sarcomere structure has been seen with other

hiPSC-CM models of DCM cultured on stiff substrates (6, 18, 54), suggesting that it might be a common feature of some forms of DCM.

ΔK210 hiPSC-CMs show a pronounced increase in size and mechanosensitive alterations in sarcomeric structure

Cardiomyocytes are sensitive to their local physical environment, and it has been shown that providing physical cues that mimic the environment of the heart can improve cardiomyocyte structure and contractility (21, 55). During aging and DCM disease progression, the heart becomes stiffer, and the myocytes become disordered. We hypothesized that ΔK210 hiPSC-CMs would show aberrant responses to changes in their physical environment. To test this hypothesis, we examined the size and structure of cells on glass, which has a high stiffness (~GPa) and on hydrogel substrates with a stiffness matched to healthy heart tissue (10 kPa).

To examine the role of geometric cues in cellular organization, we micropatterned extracellular matrix for cellular adhesion in rectangular patterns with a 7:1 aspect ratio. It was previously shown that micropatterning of hiPSC-CMs improves cell maturity and the 7:1 aspect ratio optimizes force production (21). We examined live cells using bright field microscopy, and fixed cells stained for the z-disc marker α-actinin and troponin-I using confocal microscopy (Fig. 5C-F). Interestingly, the ΔK210 hiPSC-CMs are significantly larger than the WT in fixed cells on glass (Fig. 5 and 6), fixed cells on 10 kPa hydrogels (Fig. 5 and 6), and in live cells on 10 kPa hydrogels (Fig. 5 and 7). We analyzed a large number of cells and generated cumulative distributions of cell sizes for single cells, since this methodology does not assume a form for the underlying distribution (Fig. 6 and 7).

The cumulative distribution shows the fraction of cells with an area less than or equal to the value of the x-axis. The increase in size in the mutant is due to increases in both cell width and length (Table 1, Fig. 6). These data demonstrate that ΔK210 hiPSC-CMs are larger than the WT cells, and that this increase in size is not dependent on the mechanical environment.

Next, we examined the influence of substrate stiffness on the sarcomeric organization of ΔK210 hiPSC-CMs. We fixed and stained micropatterned hiPSC-CMs for the sarcomeric marker α-actinin on both glass and 10 kPa substrates. Both WT and ΔK210 hiPSC-CM sarcomeres orient preferentially along the long axis of the cells patterned on glass and on 10 kPa hydrogels (Fig. 5). To quantify the degree of sarcomeric organization, we used a program developed by Pasquilini et al. (55). The program analyzes fluorescence images with periodic structure, and it calculates the orientational order parameter, OOP (i.e., the fraction of z-discs that are oriented along a single axis). For cells with z-discs all oriented along a single axis, OOP=1, and for cells with z-discs with no preferred axis, OOP=0.

When patterned on glass (GPa stiffness), the ΔK210 mutant hiPSC-CMs show a reduction in the fraction of z-discs aligned along the long axis compared to the WT ($p = 0.008$) (Fig. 6A, Table 1). This is consistent with what we saw with unpatterned cells on glass (Fig. 5A-B). Strikingly, when patterned on hydrogels that mimic the stiffness of healthy heart tissue, the ΔK210 cells show significantly improved z-disc organization (Fig. 6B, Table 1). As quantified using the OOP, the organization of the ΔK210 z-discs are indistinguishable from the WT on 10 kPa substrates ($p = 0.5$). Taken together, these results demonstrate that the ΔK210 mutation affects how the hiPSC-CMs respond to their

mechanical environment, with ΔK210 cells showing normal z-disc organization on physiologically stiff substrates, but reduced sarcomeric organization on stiff substrates.

ΔK210 cells show altered contractility and features of hypertrophy on substrates of physiological stiffness

Our biochemical measurements (Fig. 3B) and computational modeling predict that ΔK210 cells should show a lower force per sarcomere (Fig. 4B); and therefore, we examined whether the ΔK210 mutation affects force production of single hiPSC-CMs. To measure force production of single hiPSC-CMs, we used traction force microscopy. Spontaneously beating cells were micropatterned onto 10 kPa hydrogels prepared with embedded fluorescent microbeads to monitor beating. Spinning disk confocal imaging was used to monitor the bead displacement as a function of time, and the total force of contraction for each cell was calculated using a MATLAB routine developed by Ribeiro et al. (56) (Fig. 7B-C). For each cell, the force per sarcomere was approximated by calculating the force per area.

The average total force per cell measured by traction force microscopy is the same for both WT (0.27 (-0.03/+0.04) μN) and ΔK210 hiPSC-CMs (0.27 (-0.04/+0.05) μN; $p = 0.98$) (Fig. 7C). These forces are consistent with previous measurements (21). For each cell analyzed by traction force microscopy, we measured its area from bright-field illumination images (Fig. 7A). Bright-field images of live cells lack the resolution of the immunofluorescence images, making it challenging to accurately measure the cross-sectional area of the live cells; however, ΔK210 hiPSC-CMs are significantly larger than the WT cells (Fig. 7A). Moreover, fixed ΔK210 hiPSC-CMs on 10 kPa hydrogels have a

z-disc organization that is indistinguishable from the WT (Fig. 6B). We calculated the force per area for each cell (Fig. 7B). The ΔK210 cells have a lower force per area (0.25 (-0.04/+0.05) $\mu N/\mu m^2$) compared to the WT (0.32 (-0.04/+0.04) $\mu N/\mu m^2$; p = 0.01). The lower force per area for ΔK210 is consistent with our biochemical measurements and the computational modeling, which predicted a lower force per sarcomere (Fig. 4B). These data help link the molecular and cellular phenotypes. Moreover, they demonstrate that although the force per sarcomere is reduced in the mutant, the ΔK210 hiPSC-CMs can compensate through an increase in size that results in a total force per cell that is indistinguishable from the WT.

Discussion

Here, we determined the molecular mechanism of a mutation in troponin-T that causes DCM in humans, ΔK210. We found that this mutation affects not only molecular and cellular contractility, but also the ability of the cardiomyocytes to respond to changes in the mechanical environment like stiffening of heart tissue associated with aging and disease in patients. These results implicate defective mechanosensing by cardiomyocytes as an important factor in the pathogenesis of DCM caused by mutations in sarcomeric proteins, and they highlight the importance of multiscale studies in understanding heart disease.

Proposed molecular mechanism for ΔK210 and its relationship to previous studies

The disease presentation of familial cardiomyopathies and their biophysical manifestation (i.e., contractile and force-dependent properties) can depend on the myosin isoform (7, 8, 57-60). Our *in vitro* motility results (Fig. 1B) using porcine cardiac actin and

ventricular β-cardiac muscle myosin (MYH7), which closely mimics the biophysical and biochemical properties of human ventricular β-cardiac muscle myosin (38, 39), demonstrate a shift towards supermaximal calcium activation, consistent with previous experiments studying the ΔK210 mutation using different myosin isoforms (31, 44).

We determined that this shift is due to alterations in the equilibrium constants that govern the positioning of tropomyosin along the thin filament, leading to a reduction in the population of force-generating cross bridges at submaximal calcium concentrations (Fig. 3 and 4A). The structural basis of these mutation-induced shifts is not well understood; however, it is possible that the mutation affects the interaction between the troponin complex and tropomyosin (61) and/or the allosteric coupling between subunits of the troponin complex (2, 5, 62, 63). These non-exclusive mechanisms could contribute to the observed decrease in force-producing states seen in ΔK210 thin filaments, and future studies should be able to shed light on the structural basis of these changes.

Our biochemical data were analyzed using the formalism developed by McKillop and Geeves (47). These data clearly demonstrate a decrease in the population of strongly-bound myosin crossbridges in the mutant (Figs. 3B, S7), suggesting that the mutant would show reduced force production. We predicted the effects of the mutations on sarcomeric contractility using a computational model developed by Campbell et al. (52) that is similar, but not identical to the McKillop and Geeves model (47). For example, the McKillop and Geeves model has a calcium dependence for K_T, while this term is calcium independent in the Campbell et al. model. Although these models are not exactly equivalent, the computational modelling was are able to recapitulate the shift in calcium sensitivity seen in the motility assay (Fig. 1B and 4A). Other models of thin filament

regulation exist (64-68), but the McKillop and Geeves model is one of the most frequently used. Regardless of the model used to interpret the results, our biochemical data clearly show molecular hypocontractility in the mutant at micromolar calcium concentrations.

The computational modeling based on our biochemical studies predicts a larger reduction in the force per sarcomere than we observed in hiPSC-CMs (Figure 7). This is likely due to several necessary simplifying assumptions made in the modeling: 1) We assumed that the mutation does not change the magnitude or time course of the calcium transient, which is not necessarily true given that the knock-in ΔK210 mouse shows altered calcium transients (31). 2) We assumed that the troponin in hiPSC-CMs has the same biochemical properties as the adult cardiac troponin complex that we examined in our biochemical experiments. This is not necessarily the case, since four troponin-T isoforms can be detected in the human heart at different developmental stages (69, 70), and hiPSC-CMs primarily express a slow skeletal muscle isoform of troponin-I (71), rather than the cardiac isoform used in the biochemical studies. While all isoforms of troponin expressed in hiPSC-CMs would have the ΔK210 mutation (SI Appendix, Fig. S3), different isoforms have different calcium sensitivities (69). That said, even with these simplifying assumptions, the simulations were able to predict the reduction in the force per sarcomere seen in the ΔK210 cardiomyocytes.

Linking the molecular and cellular contractile phenotypes for ΔK210

Patients with the ΔK210 mutation show early onset of the disease phenotype and a high incidence of sudden death (26). Aspects of the disease have been replicated in knock-in mouse models (31), which have significantly advanced our understanding of the

disease phenotype. However, the ΔK210 mouse model shows significant differences with respect to the human phenotype, due to inherent physiological differences between mouse and human hearts, including differences in gene expression, calcium-handling machinery, and ion channel composition (34).

We used human hiPSC-CMs to study how the initial insult of a molecular-based change leads to the early disease pathogenesis in human cells. For these studies, hiPSC-CMs are excellent models, since they can capture cellular changes that occur before major compensatory mechanisms (e.g., fibrosis, activation of neurohormonal pathways, changes in gene expression) mask the initial molecular phenotype (18-20, 54, 72). Contractile changes associated with the disease have been observed in cardiomyopathy patients before adverse remodeling of the heart (73-75). That being said, hiPSC-CMs are developmentally immature, meaning that they do not necessarily recapitulate all the aspects of the phenotype in adults or the later stages of the disease progression. All of our molecular and cellular studies modeled the homozygous ΔK210 mutation, so care should be used when extrapolating the results here to the phenotype seen in patients.

ΔK210 hiPSC-CMs on patterned hydrogels show a reduced force per area compared to WT cells (Fig. 7B) without any significant differences in the z-disc organization (Fig. 6B). These data are consistent with the reduced force per sarcomere predicted from our biochemical experiments (Fig. 3B) and computational modeling (Fig. 4B), linking the molecular phenotype with cellular contractility. It should be noted that our studies only examined the z-disc organization, and that it is possible that the mutations could affect the expression of other sarcomeric proteins.

Interestingly, while the force per sarcomere is reduced in the mutant, the total force per cell is not different from the WT (Fig. 7C). This can be explained by the fact that the mutant cells are larger (Fig. 6, 7), a result that would not have been predicted from the molecular studies alone. This increase in size occurs in single cells, independent of endocrine or cell-cell signaling. One possible explanation for this increase in size is that the cells are undergoing compensatory hypertrophy, which allows the cells to counteract the reduced force per sarcomere. While we have not investigated whether the increase in size seen in our cells is due to activation of hypertrophic signaling pathways, future studies should elucidate the mechanism of the increase in cell size seen here. Recent work from the Molkentin lab has shown that reduced total tension developed by cardiomyocytes is strongly correlated with the development of dilated cardiomyopathy in both hiPSC-CMs and mice (76); however, it is also possible that the increase in cell size could be due to alterations in calcium handling.

Defects in ΔK210 mechanosensing contribute to the disease phenotype

Fundamentally, troponin serves as a gate that regulates myosin-based tension. As such, one would expect that the primary effects of the mutation would be to reduce force production; however, the ΔK210 cells show several changes beyond altered contractility. While healthy cardiomyocytes adapt their contractility and structure to changes in their mechanical environment, such as age or disease-related stiffening of the heart tissue (21), ΔK210 cells do not adapt in the same way as the WT cells. Similar to other hiPSC-CM models of DCM grown on stiff substrates, ΔK210 hiPSC-CMs cultured on glass show impaired sarcomeric organization (18, 54, 77); however, ΔK210 hiPSC-CMs z-discs can

organize normally when given mechanobiological cues that mimic the healthy heart (Fig. 5 and 6). Therefore, the ΔK210 mutation affects not only contractility, but also the ability of the hiPSC-CMs to sense and respond to their environment.

The connection between the reduction in myosin-generated tension in the mutant cells and an impaired ability to respond to mechanical forces warrants further investigation; however, a possible link between cellular tension and sarcomeric organization in DCM was revealed by live-cell imaging of sarcomerogenesis in hiPSC-CMs (54). It was shown that pharmacological inhibition of myosin contractility or genetic disruption of titin leads to an impaired ability of cells to generate well-organized sarcomeres. Chopra et al. proposed that the transduction of myosin-driven tension is necessary for the proper assembly of sarcomeres in hiPSC-CMs. We propose that a similar mechanism could be relevant in ΔK210 hiPSC-CMs, which show reductions in myosin-based contractility and z-disc disorganization when patterned on glass. Consistent with this idea, treatment of hiPSC-CMs containing a different DCM mutation with Omecamtiv mecarbil, a myosin-based thin filament activator (41, 78, 79), leads to an improvement in sarcomeric organization (77). We speculate that some of the salutary effects of the drug are due to the restoration of tension necessary for proper mechanosensing.

The result that ΔK210 hiPSC-CMs show altered responses to changes in their mechanical environment has important implications for the mechanism of the disease pathogenesis. Previous studies of cardiomyocytes have shown that the organization of sarcomeres varies depending on substrate stiffness (21, 77), with peak contractility occurring on substrates of physiological stiffness. ΔK210 hiPSC-CMs can organize

properly and they have normal force production on substrates that match the stiffness of the healthy heart (Fig. 6 and 7); however, heart tissue becomes stiffer with the disease progression and aging. We propose that as the heart tissue becomes stiffer, ΔK210 cells would become more disordered, effectively causing a progressive loss of function, and potentially contributing to myocyte disarray. Thus, the inability of the mutant cells to adapt to changes in their mechanical environment may contribute to the disease pathogenesis and progression.

The potential importance of mechanosensing in DCM pathogenesis

Our results suggest that reduced force at the molecular scale due to a mutation in a sarcomeric protein can lead to impaired mechanosensing in cardiomyocytes. While the disease presentation in DCM depends on the exact mutation (80), we propose that disruption of mechanosensing in cardiomyocytes could be a common mechanism in the disease pathogenesis of other sarcomeric and non-sarcomeric DCM mutations. It has been proposed that DCM can be caused by molecular hypocontractility (4, 76, 81); however, there are also many DCM-causing mutations in non-sarcomeric genes with no known roles in contractility; suggesting that other mechanisms might be involved (1, 3, 82). Most of these genes are located along proposed mechanosensing pathways (83, 84) used to sense and transduce mechanical forces. For example, some of these genes link the cytoskeleton to the extracellular matrix (e.g., dystrophin (DMD), vinculin (VCL)), others link the cytoskeleton to the nucleus (e.g., nesprin-1 (SYNE1), lamin-A (LMNA), centromere protein F (CENP-F)), and others are mechanosensitive transcription factors (e.g., TAZ). Consistent with this idea, altered mechanobiology has been identified in DCM

cells with mutations in the non-sarcomeric protein lamin A/C (82). Moreover, patients with mutations in these genes, such as those with Duchenne muscular dystrophy and Emery-Dreifuss muscular dystrophy, often develop DCM. It is intriguing to speculate that impaired mechanosensing by cardiomyocytes in the heart could link some of these seemingly different diseases and provide a common pathway that could be targeted by therapeutic interventions.

Conclusions

Using a combination of biochemical, computational, and cell biological techniques, we reveal several features of the early disease pathogenesis of a DCM mutation that would have been missed by studying the molecular or cellular phenotypes alone. We demonstrate that the ΔK210 mutation in human cardiac troponin-T causes a change in the equilibrium positioning of tropomyosin, leading to alterations in the calcium sensitivity of thin filament activation and a reduction in the number of strongly-bound myosin crossbridges at all calcium concentrations. Computational modeling predicts that these changes should lead to a reduction in the force generated per sarcomere in mutant cells, and we demonstrate that this is indeed the case in hiPSC-CMs. We demonstrate that the ΔK210 hiPSC-CMs can increase in size to normalize their force production. Moreover, our results demonstrate that the ΔK210 mutation affects the structural organization of hiPSC-CMs and alters how they respond to their mechanical environment. This impaired mechanosensing likely contributes to the DCM disease progression and the development of myocyte disarray as the heart stiffens. Taken together, these results demonstrate that disease-causing mutations of sarcomeric proteins affect not only contraction, but also

how cardiomyocytes sense and respond to changes in their mechanical environment associated with aging and disease. These data also suggest that disrupting mechanosensing pathways can contribute to the disease phenotype in DCM.

3.3 Materials and Methods

Investigation of the Molecular Mechanism Using Recombinant Proteins

Human troponin and tropomyosin were expressed recombinantly in *E. coli,* and cardiac actin and myosin were purified from porcine ventricles. *In vitro* motility assays were conducted as previously described (36). The equilibrium constants that govern thin filament activation were determined using stopped-flow and steady-state fluorescence techniques (47, 50). Full details are provided in the SI Appendix, Materials and Methods.

Computational Simulations

Simulations of force production by sarcomeres were conducted using the model developed by Campbell et al. (52). Full details are provided in the SI Appendix, Materials and Methods.

Differentiation of hiPSCs to hiPSC-CMs

The parent stem cell line, BJFF.6, was generated from the human BJ fibroblast line (CRL-2522, ATCC) by the Genome Engineering and iPSC Center at Washington University in St. Louis. Two independent stem cell lines homozygous for the ΔK210 deletion were generated using the CRISPR/Cas9 system (17, 85). Differentiation to hiPSC-CMs was accomplished using the method of Lian et al. (53). Full details are provided in SI Appendix, Materials and Methods.

Analysis of Sarcomeric Structure in Cardiomyocytes

hiPSC-CMs were fixed in 4% paraformaldehyde (Electron Microscopy Sciences) and sarcomeric structure was visualized via immunofluorescence using confocal microscopy (Washington University Center for Cellular Imaging). Analysis of the organization of the sarcomeres was analyzed using software developed by the Parker lab (55). Full details are provided in SI Appendix, Materials and Methods.

Analysis of single cardiomyocyte contractility

Single hiPSC-CMs were seeded onto rectangular patterns on hydrogels for traction force microscopy according to the protocol of Ribeiro et al., (21). All traction force microscopy measurements were performed on patterned polyacrylamide hydrogels with a stiffness of 10 kPa with hiPSC-CMs that were at least 30 days post-differentiation. Single, spontaneously-beating cells were imaged in an environmentally controlled chamber (Tokai Hit) on a Nikon spinning disk confocal microscope (Washington University Center for Cellular Imaging). Traction force movies were analyzed by generating displacement maps of the fluorescent beads using a MATLAB program developed by the Pruitt lab (56). Full details are provided in SI Appendix, Materials and Methods.

Acknowledgements:

We would like to thank Stuart Campbell and Francesco Pasqualini for sharing their code for the simulations and sarcomeric structure analysis, respectively. We acknowledge Mike Ostap and Ken Margulies for extremely helpful discussions during the early planning phases of this project. We would also like to acknowledge Drew Braet for technical assistance and Samantha Barrick for assistance with biochemical experiments. The authors acknowledge the Washington University Institute of Materials Science and Engineering for the use of microfabrication instruments and staff assistance, and we thank the Alvin J. Siteman Cancer Center at Washington University School of Medicine and Barnes-Jewish Hospital in St. Louis, MO., for the Genome Engineering and Induced Pluripotent Stem Cell Center, which provided the genome editing service (NCI Cancer Center Support Grant #P30 CA091842). Confocal microscopy was performed through the Washington University Center for Cellular Imaging supported by Washington University School of Medicine, The Children's Discovery Institute of Washington University and St. Louis Children's Hospital (CDI-CORE-2015-505) and the Foundation for Barnes-Jewish Hospital (3770). Exome sequencing was performed by the McDonnell Genome Institute. Funding for this project was provided by a pilot grant from the Children's Discovery Institute of Washington University and St. Louis Children's Hospital, the Washington University Center for Cellular Imaging (CDI-CORE-2015-505), the National Institutes of Health (R00HL123623, R01HL141086 to M.J.G., T32EB018266 to S.R.C.), and the March of Dimes Foundation (FY18-BOC-430198 to M.J.G.).

3.4 Figures

Fig. 1.

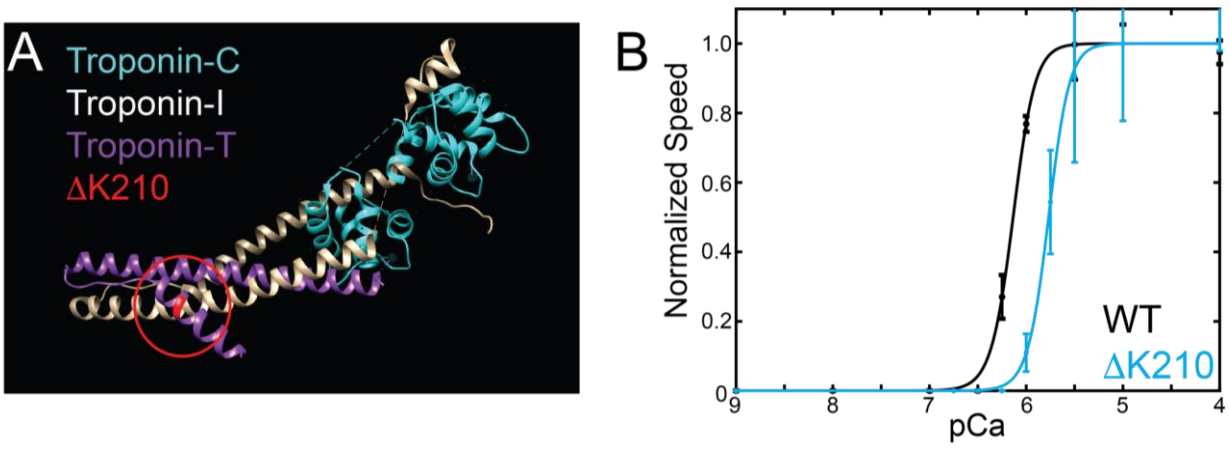

Fig. 1. (A) Structure of the troponin core complex (PDB: 4Y99), showing troponin-C (cyan), troponin-I (white), troponin-T (purple), and K210 of troponin-T (red). (B) Speed of thin filament translocation as a function of calcium measured in the in vitro motility assay. Error bars show the standard deviation of n=3 experiments. Data show a significant shift in the pCa50 towards submaximal calcium activation for ΔK210 ($p<0.0001$). The Hill coefficient is not changed between the WT and ΔK210 ($p = 0.45$).

Fig. 2.

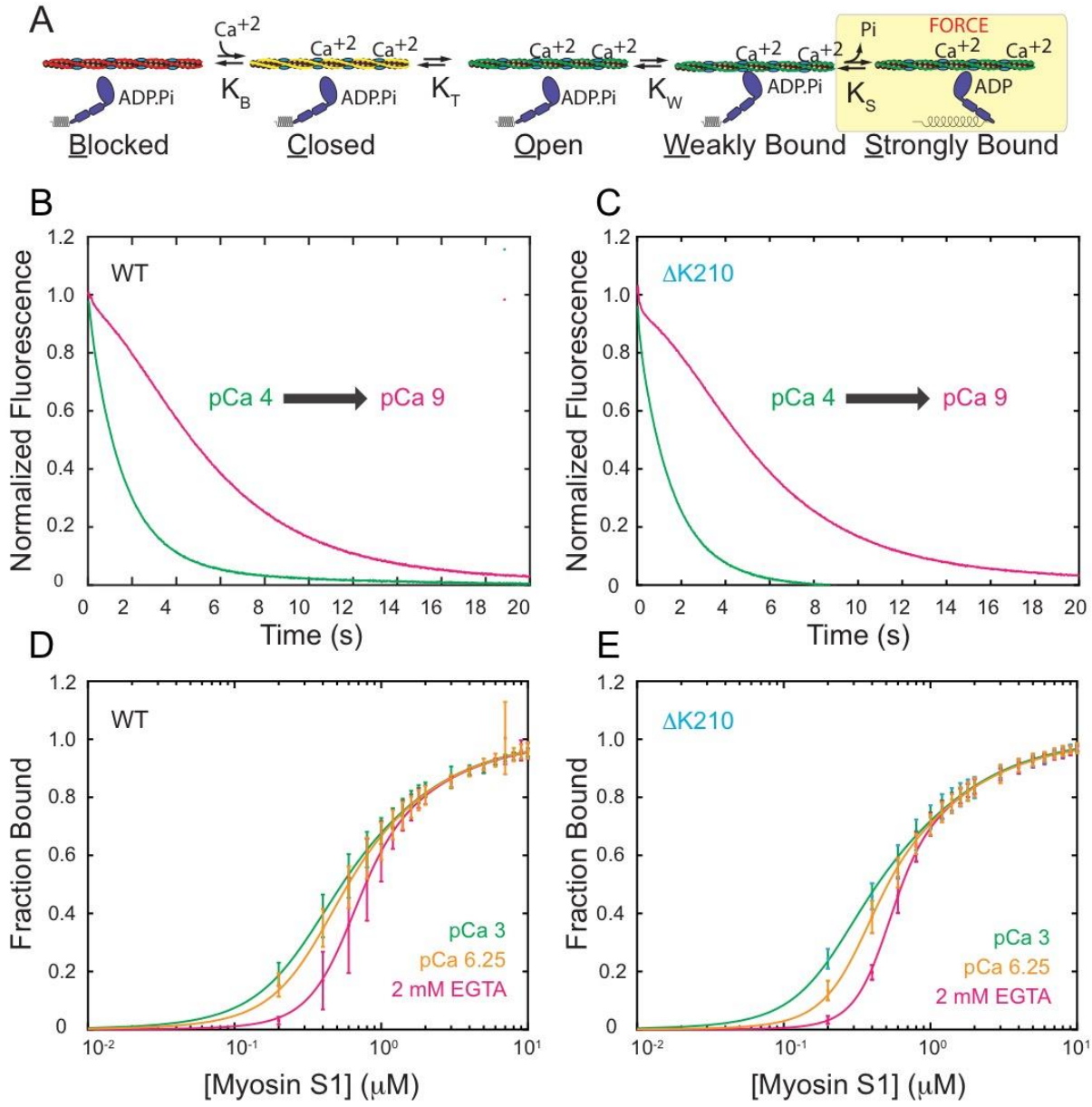

Fig. 2. *Determination of equilibrium constants governing thin filament regulation for ΔK210. (A) The three-state model for tropomyosin positioning along the thin filament (47). Activation of the thin filament and subsequent force generation requires both calcium and myosin binding. The equilibrium constant for the blocked to closed transition is K_B and the equilibrium constant for the closed to open transition is K_T. K_W and K_S are the equilibrium constants for myosin weak- and strong-binding to the thin filament, respectively. (B-C) Normalized stopped-flow fluorescence traces of myosin binding to regulated pyrene-actin. The quenching of pyrene-actin upon binding of S1 occurs at a faster rate at pCa 4 (green) compared to pCa 9 (pink) due to the activating effect of calcium. Traces for (A) WT and (B) ΔK210 are very similar and the calculated values of K_B are not statistically different (p=0.998). (D-E) Fluorescence titrations in*

which increasing amounts of S1 myosin were gradually added to regulated thin filaments to a final concentration of 10 μM S1 in the presence of ADP. Titration curves at three different calcium concentrations are shown for both (C) WT and (D) ΔK210. 5 repeats were performed for each condition and error bars show the standard deviation. At low concentrations of myosin, more myosin is bound to the thin filament at higher calcium concentrations (pCa 6.25 (orange) and pCa 3 (green)) than at low calcium (2 mM EGTA, pink).

Fig. 3

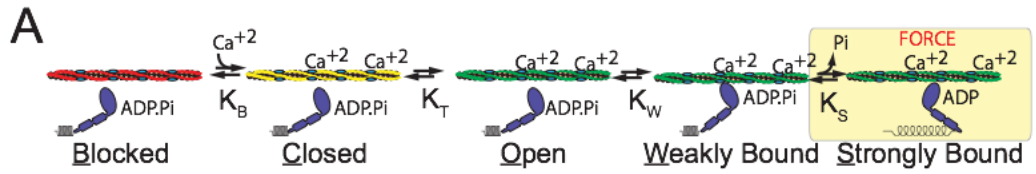

	WT	ΔK210	p
K_B	0.36 (-0.15/+0.15)	0.36 (-0.10/+0.10)	0.99
K_w	0.12 (-0.01/+0.02)	0.13 (-0.01/+0.01)	0.09
K_T pCa >9	0.09 (-0.08/+0.12)	0.02 (-0.02/+0.03)	0.20
K_T pCa 6.25	0.14 (-0.09/+0.09)	0.04 (-0.02/+0.03)	0.03
K_T pCa 3	0.28 (-0.18/+0.23)	0.17 (-0.09/+0.12)	0.40
n	5.23 (-1.50/+3.12)	6.88 (-1.13/+1.54)	0.26

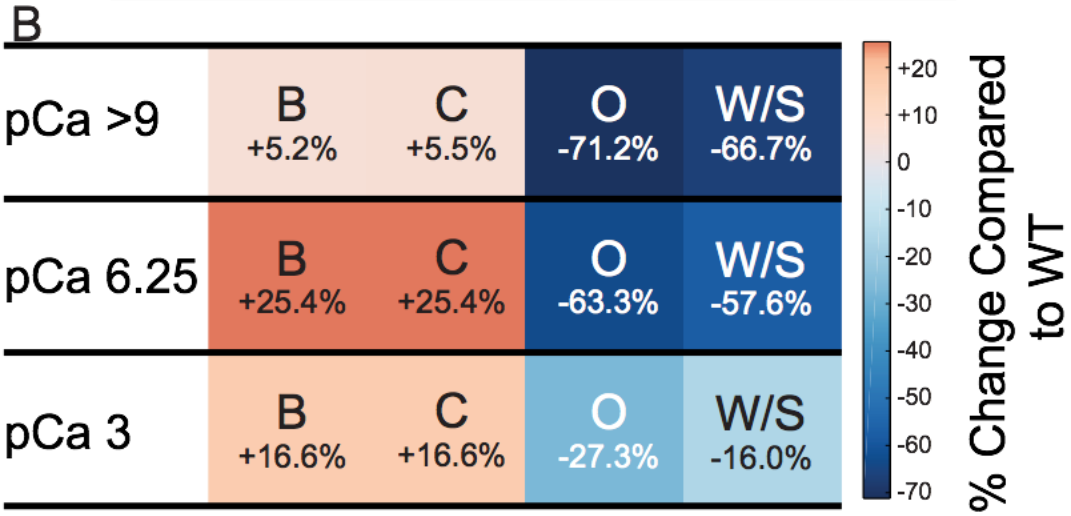

Fig. 3. Effects of ΔK210 on tropomyosin positioning along the thin filament. (A) The three-state model for tropomyosin positioning along the thin filament (47) and parameter values obtained from the stopped-flow and fluorescence titration experiments. Reported uncertainties are 95% confidence intervals. K_T for ΔK210 at pCa 6.25 is statistically different from WT (p=0.028). Error bars are the 95% confidence intervals. (B) Percent change in the occupancy of each state for the mutant compared to the WT. Reds denote increased population of a state, while blues denote decreased population. ΔK210 causes a decrease in the population of the states where myosin is bound to the thin filament and an increase in the population of the inhibited (i.e., blocked and closed) states. Note that the fraction of thin filaments in the blocked and closed states is does not change, since K_B does not change between the WT and the mutant.

Fig. 4.

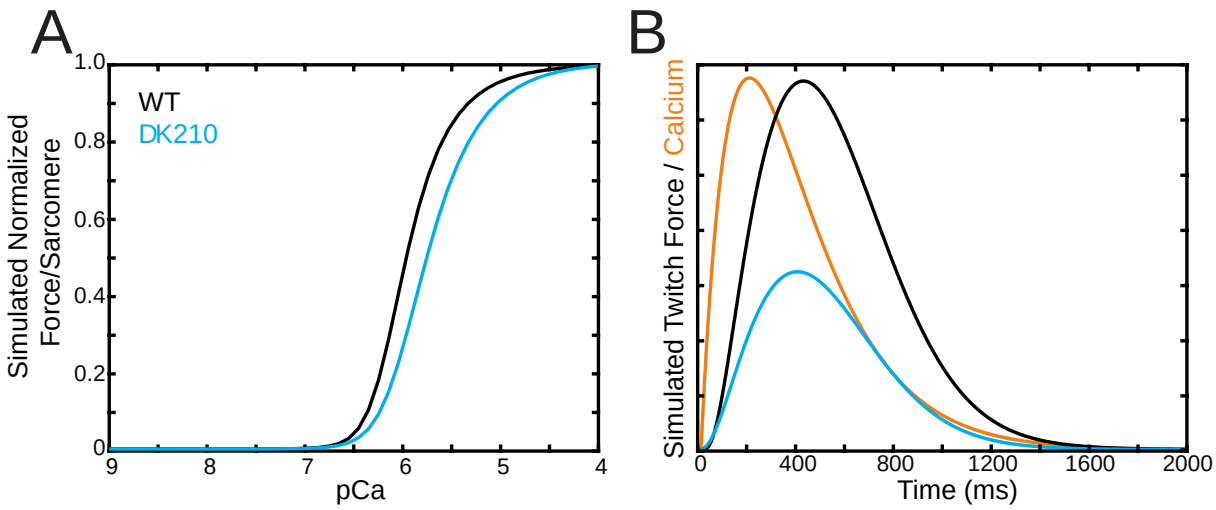

Fig. 4. Computational modeling of the steady-state and transient force per sarcomere. (A) Using the model developed by Campbell et al. (52), the steady-state normalized force per sarcomere as a function of calcium can be simulated for both ΔK210 and WT. The simulation shows a shift in the pCa50 towards supermaximal calcium activation in the mutant. (B) Simulated twitch forces per sarcomere in response to a calcium transient. The model predicts that ΔK210 should show a lower twitch force per sarcomere.

Fig. 5.

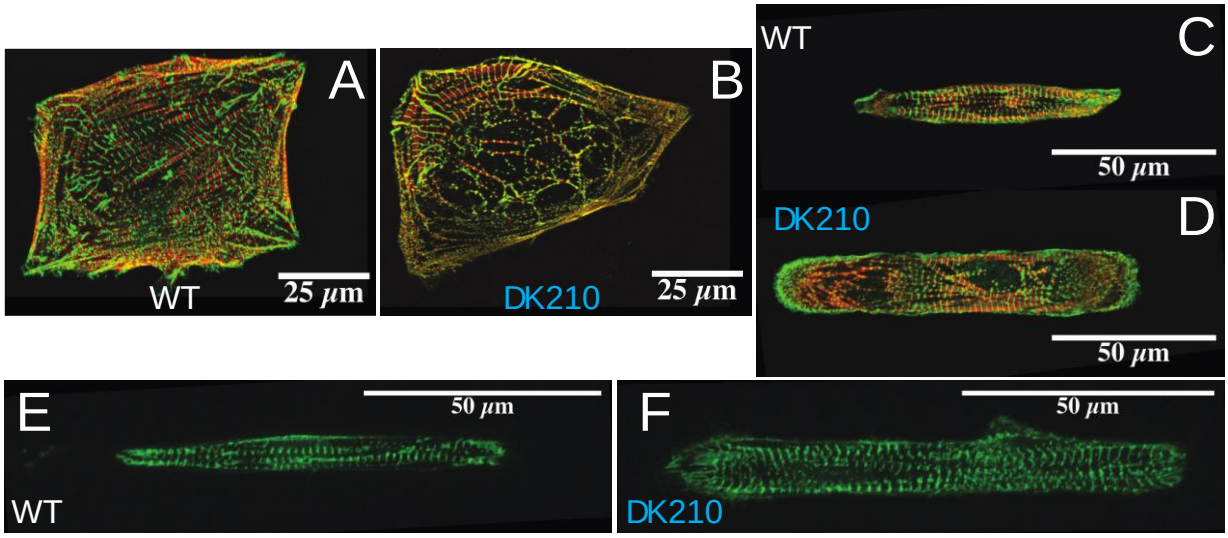

Fig. 5. Immunofluorescence images of sarcomeres in hiPSC-CMs. Troponin-I is red and α-actinin is green. All images are z-projections. (A) WT hiPSC-CM on glass. (B) ΔK210 hiPSC-CM on glass,

showing sarcomeric disorganization. (C) WT cell on a rectangular pattern on glass. (D) ΔK210 cell on a rectangular pattern on glass. (E) WT cell on a rectangular pattern on a 10 kPa hydrogel. (F) ΔK210 cell on a rectangular pattern on a 10 kPa hydrogel. The sarcomeric organization is significantly improved on the hydrogel with a physiologically relevant stiffness.

Fig. 6.

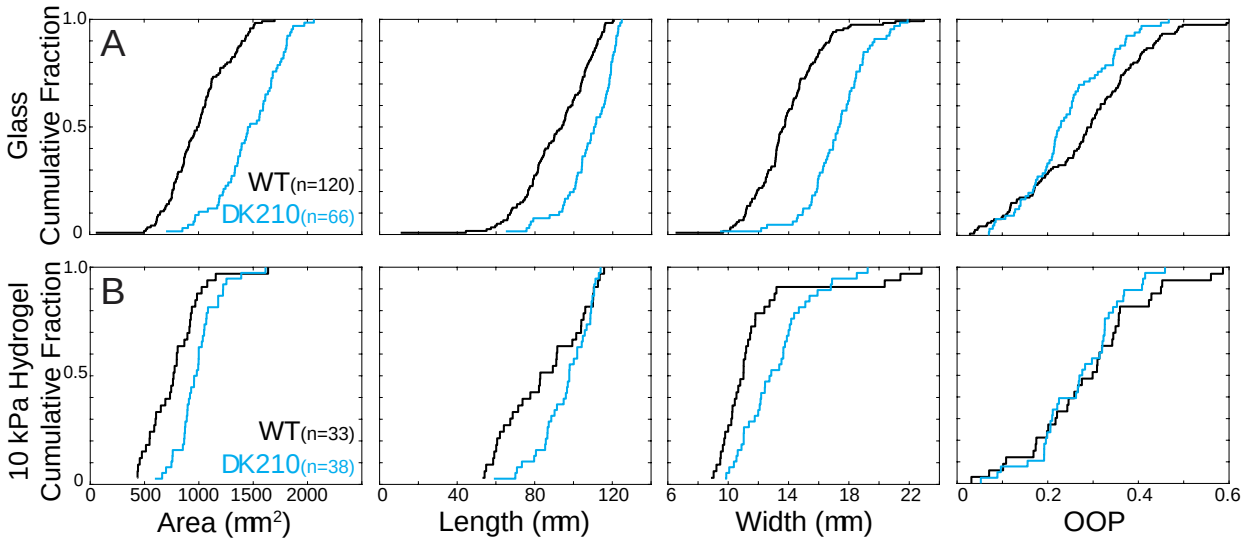

Fig. 6. Quantification of immunofluorescence staining for sarcomeres in hiPSC-CMs on rectangular patterns on (A) glass and (B) 10 kPa hydrogels. Data are plotted as cumulative distributions and parameter values can be found in Table 1. ΔK210 cells are significantly larger on both glass and 10 kPa hydrogels ($p = 0.00002$), due to increases in both length and width. The orientation order parameter (OOP) is a measurement of sarcomeric organization. For a hiPSC-CM in which all of the sarcomeres are aligned along a single axis the OOP=1 and for a hiPSC-CM with no preferred axis, the OOP = 0. On glass, ΔK210 cells have lower OOP values than the WT ($p = 0.008$). On physiologically stiff hydrogels, there is no significant difference between the OOP of the WT and mutant cells ($p = 0.5$).

Fig. 7.

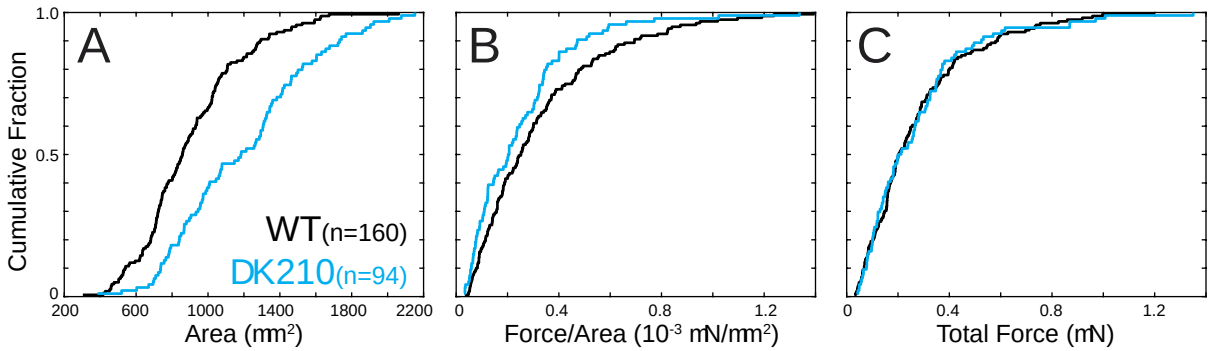

	WT (n=160)	ΔK210 (n=94)	p
Area (μm^2)	900 (-40/+50)	1200 (-80/+80)	<0.00002
Force / area (10^{-3} $\mu N/\mu m^2$)	0.32 (-0.04/+0.04)	0.25 (-0.04/+0.05)	0.01
Total force (μN)	0.27 (-0.03/+0.04)	0.27 (-0.04/+0.05)	0.98

Fig. 7. Traction force microscopy of single hiPSC-CMs patterned on 10 kPa polyacrylamide gels. (A) Live ΔK210 hiPSC-CMs on hydrogels are significantly larger than WT cells. (B) ΔK210 cells have a lower force per area (i.e., lower force per sarcomere), consistent with the molecular studies; however, since they are larger, (C) their total force production is not significantly different from the WT cells. Reported uncertainties are 95% confidence intervals.

Table 1: Analysis of Fixed Cell Sizes on Rectangular Patterns (reported uncertainties are 95% confidence intervals)

Patterned on glass

	WT (n=120)	ΔK210 (n=66)	p
Area (μm²)	1000 (-50/+50)	1470 (-70/+70)	0.00002
Length (μm)	91 (-3/+3)	108 (-3/+3)	0.00002
Width (μm)	13 (-0.4/+0.4)	17 (-0.5/+0.5)	0.00002
Length : width ratio	6.7 (-0.3/+0.3)	6.4 (-0.2/+0.3)	0.1
OOP	0.28 (-0.02/+0.02)	0.24 (-0.02/+0.02)	0.008

Patterned on 10 kPa hydrogels

	WT (n=33)	ΔK210 (n=38)	p
Area (μm²)	770 (-80/+90)	990 (-60/+60)	0.0002
Length (μm)	85 (-7/+7)	96 (-4/+4)	0.007
Width (μm)	11 (-1/+1)	13 (-0.7/+0.8)	0.06
Length : width ratio	7.6 (-0.9/+0.9)	7.6 (-0.6/+0.6)	0.9
OOP	0.28 (-0.04/+0.04)	0.27 (-0.03/+0.03)	0.5

3.5 References

1. McNally EM & Mestroni L (2017) Dilated Cardiomyopathy: Genetic Determinants and Mechanisms. *Circulation research* 121(7):731-748.
2. Lynn ML, Lehman SJ, & Tardiff JC (2018) Biophysical Derangements in Genetic Cardiomyopathies. *Heart Fail Clin* 14(2):147-159.
3. McNally EM, Golbus JR, & Puckelwartz MJ (2013) Genetic mutations and mechanisms in dilated cardiomyopathy. *The Journal of clinical investigation* 123(1):19-26.
4. Spudich JA (2014) Hypertrophic and dilated cardiomyopathy: four decades of basic research on muscle lead to potential therapeutic approaches to these devastating genetic diseases. *Biophysical journal* 106(6):1236-1249.
5. Williams MR, Lehman SJ, Tardiff JC, & Schwartz SD (2016) Atomic resolution probe for allostery in the regulatory thin filament. *Proceedings of the National Academy of Sciences of the United States of America* 113(12):3257-3262.
6. Hinson JT*, et al.* (2015) HEART DISEASE. Titin mutations in iPS cells define sarcomere insufficiency as a cause of dilated cardiomyopathy. *Science* 349(6251):982-986.
7. Lowey S, Bretton V, Gulick J, Robbins J, & Trybus KM (2013) Transgenic mouse alpha- and beta-cardiac myosins containing the R403Q mutation show isoform-dependent transient kinetic differences. *The Journal of biological chemistry* 288(21):14780-14787.

8. Ford SJ, Mamidi R, Jimenez J, Tardiff JC, & Chandra M (2012) Effects of R92 mutations in mouse cardiac troponin T are influenced by changes in myosin heavy chain isoform. *Journal of molecular and cellular cardiology* 53(4):542-551.
9. Lowey S*, et al.* (2008) Functional effects of the hypertrophic cardiomyopathy R403Q mutation are different in an alpha- or beta-myosin heavy chain backbone. *The Journal of biological chemistry* 283(29):20579-20589.
10. He H, Javadpour MM, Latif F, Tardiff JC, & Ingwall JS (2007) R-92L and R-92W mutations in cardiac troponin T lead to distinct energetic phenotypes in intact mouse hearts. *Biophysical journal* 93(5):1834-1844.
11. Roh J, Houstis N, & Rosenzweig A (2017) Why Don't We Have Proven Treatments for HFpEF? *Circulation Research* 120(8):1243.
12. Conceição G, Heinonen I, Lourenço AP, Duncker DJ, & Falcão-Pires I (2016) Animal models of heart failure with preserved ejection fraction. *Netherlands Heart Journal* 24(4):275-286.
13. Sacco A*, et al.* (2010) Short telomeres and stem cell exhaustion model Duchenne muscular dystrophy in mdx/mTR mice. *Cell* 143(7):1059-1071.
14. Fananapazir L, Dalakas MC, Cyran F, Cohn G, & Epstein ND (1993) Missense mutations in the beta-myosin heavy-chain gene cause central core disease in hypertrophic cardiomyopathy. *Proceedings of the National Academy of Sciences of the United States of America* 90(9):3993-3997.
15. Lian X*, et al.* (2012) Robust cardiomyocyte differentiation from human pluripotent stem cells via temporal modulation of canonical Wnt signaling. *Proceedings of the National Academy of Sciences of the United States of America* 109(27):E1848-1857.
16. Kehat I*, et al.* (2001) Human embryonic stem cells can differentiate into myocytes with structural and functional properties of cardiomyocytes. *The Journal of clinical investigation* 108(3):407-414.
17. Jinek M*, et al.* (2012) A programmable dual-RNA-guided DNA endonuclease in adaptive bacterial immunity. *Science* 337(6096):816-821.
18. Sun N*, et al.* (2012) Patient-specific induced pluripotent stem cells as a model for familial dilated cardiomyopathy. *Science translational medicine* 4(130):130ra147.
19. Lam CK & Wu JC (2018) Disease modelling and drug discovery for hypertrophic cardiomyopathy using pluripotent stem cells: how far have we come? *Eur Heart J* 39(43):3893-3895.
20. Musunuru K*, et al.* (2018) Induced Pluripotent Stem Cells for Cardiovascular Disease Modeling and Precision Medicine: A Scientific Statement From the American Heart Association. *Circ Genom Precis Med* 11(1):e000043.
21. Ribeiro AJ*, et al.* (2015) Contractility of single cardiomyocytes differentiated from pluripotent stem cells depends on physiological shape and substrate stiffness. *Proceedings of the National Academy of Sciences of the United States of America* 112(41):12705-12710.
22. Feaster TK*, et al.* (2015) Matrigel Mattress: A Method for the Generation of Single Contracting Human-Induced Pluripotent Stem Cell-Derived Cardiomyocytes. *Circulation research* 117(12):995-1000.

23. Jiang Y, Park P, Hong SM, & Ban K (2018) Maturation of Cardiomyocytes Derived from Human Pluripotent Stem Cells: Current Strategies and Limitations. *Mol Cells* 41(7):613-621.
24. Hershberger RE*, et al.* (2009) Clinical and functional characterization of TNNT2 mutations identified in patients with dilated cardiomyopathy. *Circ Cardiovasc Genet* 2(4):306-313.
25. Mogensen J*, et al.* (2004) Severe disease expression of cardiac troponin C and T mutations in patients with idiopathic dilated cardiomyopathy. *Journal of the American College of Cardiology* 44(10):2033-2040.
26. Kamisago M*, et al.* (2000) Mutations in sarcomere protein genes as a cause of dilated cardiomyopathy. *The New England journal of medicine* 343(23):1688-1696.
27. Hanson EL*, et al.* (2002) Cardiac troponin T lysine 210 deletion in a family with dilated cardiomyopathy. *J Card Fail* 8(1):28-32.
28. Dewan S, McCabe KJ, Regnier M, & McCulloch AD (2017) Insights and Challenges of Multi-Scale Modeling of Sarcomere Mechanics in cTn and Tm DCM Mutants-Genotype to Cellular Phenotype. *Front Physiol* 8:151.
29. Garfinkel AC, Seidman JG, & Seidman CE (2018) Genetic Pathogenesis of Hypertrophic and Dilated Cardiomyopathy. *Heart Fail Clin* 14(2):139-146.
30. Memo M*, et al.* (2013) Familial dilated cardiomyopathy mutations uncouple troponin I phosphorylation from changes in myofibrillar Ca(2)(+) sensitivity. *Cardiovascular research* 99(1):65-73.
31. Du CK*, et al.* (2007) Knock-in mouse model of dilated cardiomyopathy caused by troponin mutation. *Circulation research* 101(2):185-194.
32. Lu QW*, et al.* (2003) Cardiac troponin T mutation R141W found in dilated cardiomyopathy stabilizes the troponin T-tropomyosin interaction and causes a Ca2+ desensitization. *Journal of molecular and cellular cardiology* 35(12):1421-1427.
33. Morimoto S*, et al.* (2002) Ca(2+)-desensitizing effect of a deletion mutation Delta K210 in cardiac troponin T that causes familial dilated cardiomyopathy. *Proceedings of the National Academy of Sciences of the United States of America* 99(2):913-918.
34. Ahmad F*, et al.* (2008) The role of cardiac troponin T quantity and function in cardiac development and dilated cardiomyopathy. *PloS one* 3(7):e2642.
35. Chandra M, Tschirgi ML, Ford SJ, Slinker BK, & Campbell KB (2007) Interaction between myosin heavy chain and troponin isoforms modulate cardiac myofiber contractile dynamics. *American journal of physiology. Regulatory, integrative and comparative physiology* 293(4):R1595-1607.
36. Greenberg MJ, Kazmierczak K, Szczesna-Cordary D, & Moore JR (2010) Cardiomyopathy-linked myosin regulatory light chain mutations disrupt myosin strain-dependent biochemistry. *Proceedings of the National Academy of Sciences of the United States of America* 107(40):17403-17408.
37. Greenberg MJ*, et al.* (2009) Regulatory light chain mutations associated with cardiomyopathy affect myosin mechanics and kinetics. *Journal of molecular and cellular cardiology* 46(1):108-115.

38. Greenberg MJ, Shuman H, & Ostap EM (2014) Inherent force-dependent properties of beta-cardiac myosin contribute to the force-velocity relationship of cardiac muscle. *Biophysical journal* 107(12):L41-L44.
39. Sung J*, et al.* (2015) Harmonic force spectroscopy measures load-dependent kinetics of individual human beta-cardiac myosin molecules. *Nat Commun* 6:7931.
40. Deacon JC, Bloemink MJ, Rezavandi H, Geeves MA, & Leinwand LA (2012) Identification of functional differences between recombinant human alpha and beta cardiac myosin motors. *Cellular and molecular life sciences : CMLS* 69(13):2261-2277.
41. Woody MS*, et al.* (2018) Positive cardiac inotrope omecamtiv mecarbil activates muscle despite suppressing the myosin working stroke. *Nat Commun* 9(1):3838.
42. Kron SJ & Spudich JA (1986) Fluorescent actin filaments move on myosin fixed to a glass surface. *Proceedings of the National Academy of Sciences of the United States of America* 83(17):6272-6276.
43. Homsher E, Kim B, Bobkova A, & Tobacman LS (1996) Calcium regulation of thin filament movement in an in vitro motility assay. *Biophysical journal* 70(4):1881-1892.
44. Robinson P*, et al.* (2002) Alterations in thin filament regulation induced by a human cardiac troponin T mutant that causes dilated cardiomyopathy are distinct from those induced by troponin T mutants that cause hypertrophic cardiomyopathy. *The Journal of biological chemistry* 277(43):40710-40716.
45. Barany M (1967) ATPase activity of myosin correlated with speed of muscle shortening. *The Journal of general physiology* 50(6):Suppl:197-218.
46. Sommese RF*, et al.* (2013) Effects of troponin T cardiomyopathy mutations on the calcium sensitivity of the regulated thin filament and the actomyosin cross-bridge kinetics of human beta-cardiac myosin. *PloS one* 8(12):e83403.
47. McKillop DF & Geeves MA (1993) Regulation of the interaction between actin and myosin subfragment 1: evidence for three states of the thin filament. *Biophysical journal* 65(2):693-701.
48. Lehman W, Craig R, & Vibert P (1994) Ca(2+)-induced tropomyosin movement in Limulus thin filaments revealed by three-dimensional reconstruction. *Nature* 368(6466):65-67.
49. Vibert P, Craig R, & Lehman W (1997) Steric-model for activation of muscle thin filaments. *Journal of molecular biology* 266(1):8-14.
50. Barrick SK, Clippinger SR, Greenberg L, & Greenberg MJ (2019) Computational Tool to Study Perturbations in Muscle Regulation and Its Application to Heart Disease. *Biophysical journal* 116(12):2246-2252.
51. Maytum R, Westerdorf B, Jaquet K, & Geeves MA (2003) Differential regulation of the actomyosin interaction by skeletal and cardiac troponin isoforms. *The Journal of biological chemistry* 278(9):6696-6701.
52. Campbell SG, Lionetti FV, Campbell KS, & McCulloch AD (2010) Coupling of adjacent tropomyosins enhances cross-bridge-mediated cooperative activation in a markov model of the cardiac thin filament. *Biophysical journal* 98(10):2254-2264.

53. Lian X*, et al.* (2013) Directed cardiomyocyte differentiation from human pluripotent stem cells by modulating Wnt/beta-catenin signaling under fully defined conditions. *Nature protocols* 8(1):162-175.
54. Chopra A*, et al.* (2018) Force Generation via beta-Cardiac Myosin, Titin, and alpha-Actinin Drives Cardiac Sarcomere Assembly from Cell-Matrix Adhesions. *Developmental cell* 44(1):87-96 e85.
55. Pasqualini FS, Sheehy SP, Agarwal A, Aratyn-Schaus Y, & Parker KK (2015) Structural phenotyping of stem cell-derived cardiomyocytes. *Stem Cell Reports* 4(3):340-347.
56. Ribeiro AJS*, et al.* (2017) Multi-Imaging Method to Assay the Contractile Mechanical Output of Micropatterned Human iPSC-Derived Cardiac Myocytes. *Circulation research* 120(10):1572-1583.
57. Nag S*, et al.* (2015) Contractility parameters of human beta-cardiac myosin with the hypertrophic cardiomyopathy mutation R403Q show loss of motor function. *Sci Adv* 1(9):e1500511.
58. Tyska MJ*, et al.* (2000) Single-molecule mechanics of R403Q cardiac myosin isolated from the mouse model of familial hypertrophic cardiomyopathy. *Circulation research* 86(7):737-744.
59. Palmiter KA*, et al.* (2000) R403Q and L908V mutant beta-cardiac myosin from patients with familial hypertrophic cardiomyopathy exhibit enhanced mechanical performance at the single molecule level. *Journal of muscle research and cell motility* 21(7):609-620.
60. Greenberg MJ, Arpag G, Tuzel E, & Ostap EM (2016) A Perspective on the Role of Myosins as Mechanosensors. *Biophysical journal* 110(12):2568-2576.
61. Jin JP & Chong SM (2010) Localization of the two tropomyosin-binding sites of troponin T. *Arch Biochem Biophys* 500(2):144-150.
62. Sfichi-Duke L*, et al.* (2010) Cardiomyopathy-causing deletion K210 in cardiac troponin T alters phosphorylation propensity of sarcomeric proteins. *Journal of molecular and cellular cardiology* 48(5):934-942.
63. Liu B, Tikunova SB, Kline KP, Siddiqui JK, & Davis JP (2012) Disease-related cardiac troponins alter thin filament Ca2+ association and dissociation rates. *PloS one* 7(6):e38259.
64. Houmeida A, Heeley DH, Belknap B, & White HD (2010) Mechanism of regulation of native cardiac muscle thin filaments by rigor cardiac myosin-S1 and calcium. *The Journal of biological chemistry* 285(43):32760-32769.
65. Mijailovich SM*, et al.* (2010) Resolution and uniqueness of estimated parameters of a model of thin filament regulation in solution. *Computational biology and chemistry* 34(1):19-33.
66. Smith DA, Geeves MA, Sleep J, & Mijailovich SM (2008) Towards a unified theory of muscle contraction. I: foundations. *Ann Biomed Eng* 36(10):1624-1640.
67. Longyear T, Walcott S, & Debold EP (2017) The molecular basis of thin filament activation: from single molecule to muscle. *Sci Rep* 7(1):1822.
68. Hill TL, Eisenberg E, & Greene L (1980) Theoretical model for the cooperative equilibrium binding of myosin subfragment 1 to the actin-troponin-tropomyosin complex. *Proceedings of the National Academy of Sciences of the United States of America* 77(6):3186-3190.

69. Gomes AV, Guzman G, Zhao J, & Potter JD (2002) Cardiac troponin T isoforms affect the Ca2+ sensitivity and inhibition of force development. Insights into the role of troponin T isoforms in the heart. *The Journal of biological chemistry* 277(38):35341-35349.
70. Iorga B*, et al.* (2017) Differences in Contractile Function of Myofibrils within Human Embryonic Stem Cell-Derived Cardiomyocytes vs. Adult Ventricular Myofibrils Are Related to Distinct Sarcomeric Protein Isoforms. *Front Physiol* 8:1111.
71. Kadota S, Pabon L, Reinecke H, & Murry CE (2017) In Vivo Maturation of Human Induced Pluripotent Stem Cell-Derived Cardiomyocytes in Neonatal and Adult Rat Hearts. *Stem Cell Reports* 8(2):278-289.
72. Birket MJ*, et al.* (2015) Contractile Defect Caused by Mutation in MYBPC3 Revealed under Conditions Optimized for Human PSC-Cardiomyocyte Function. *Cell Rep* 13(4):733-745.
73. Forsey J, Benson L, Rozenblyum E, Friedberg MK, & Mertens L (2014) Early changes in apical rotation in genotype positive children with hypertrophic cardiomyopathy mutations without hypertrophic changes on two-dimensional imaging. *J Am Soc Echocardiogr* 27(2):215-221.
74. Ho CY*, et al.* (2002) Assessment of diastolic function with Doppler tissue imaging to predict genotype in preclinical hypertrophic cardiomyopathy. *Circulation* 105(25):2992-2997.
75. Rüssel IK*, et al.* (2011) Increased left ventricular torsion in hypertrophic cardiomyopathy mutation carriers with normal wall thickness. *J Cardiovasc Magn Reson* 13:3.
76. Davis J*, et al.* (2016) A Tension-Based Model Distinguishes Hypertrophic versus Dilated Cardiomyopathy. *Cell* 165(5):1147-1159.
77. Broughton KM*, et al.* (2016) A myosin activator improves actin assembly and sarcomere function of human-induced pluripotent stem cell-derived cardiomyocytes with a troponin T point mutation. *American journal of physiology. Heart and circulatory physiology* 311(1):H107-117.
78. Nagy L*, et al.* (2015) The novel cardiac myosin activator omecamtiv mecarbil increases the calcium sensitivity of force production in isolated cardiomyocytes and skeletal muscle fibres of the rat. *Br J Pharmacol* 172(18):4506-4518.
79. Malik FI*, et al.* (2011) Cardiac myosin activation: a potential therapeutic approach for systolic heart failure. *Science* 331(6023):1439-1443.
80. Burke MA, Cook SA, Seidman JG, & Seidman CE (2016) Clinical and Mechanistic Insights Into the Genetics of Cardiomyopathy. *Journal of the American College of Cardiology* 68(25):2871-2886.
81. Moore JR, Leinwand L, & Warshaw DM (2012) Understanding cardiomyopathy phenotypes based on the functional impact of mutations in the myosin motor. *Circulation research* 111(3):375-385.
82. Bhattacharjee P, Dasgupta D, & Sengupta K (2017) DCM associated LMNA mutations cause distortions in lamina structure and assembly. *Biochim Biophys Acta Gen Subj* 1861(11 Pt A):2598-2608.

83. Uhler C & Shivashankar GV (2017) Regulation of genome organization and gene expression by nuclear mechanotransduction. *Nat Rev Mol Cell Biol* 18(12):717-727.
84. Iskratsch T, Wolfenson H, & Sheetz MP (2014) Appreciating force and shape-the rise of mechanotransduction in cell biology. *Nat Rev Mol Cell Biol* 15(12):825-833.
85. Hsu PD*, et al.* (2013) DNA targeting specificity of RNA-guided Cas9 nucleases. *Nature biotechnology* 31(9):827-832.

3.6 SI Methods

Tissue purification of proteins for *in vitro* biochemical experiments

Porcine cardiac myosin and actin were simultaneously purified from cryoground porcine ventricles (Pelfreez) as previously described (1). Myosin subfragment-1 (S1) was prepared by chymotrypsin digestion of myosin using the method of Margossian and Lowey (2) with the modifications of Eads et al. (3). Purity of S1 was assessed by SDS-PAGE, and the protein concentration was determined spectroscopically. Porcine cardiac actin was purified from acetone powder (4) and labeled with N-(1-pyrenyl)iodoacetamide (pyrene) as described previously (5, 6). Actin concentrations were determined by absorbance at 290 nm (and 344 nm for pyrene-labeled actin).

Preparation of recombinant human cardiac tropomyosin and troponin

pET3d vectors containing human cardiac tropomyosin, troponin-I, troponin-T, and troponin-C were a generous gift from L. Tobacmann (University of Illinois at Chicago). The ΔK210 mutation was introduced into troponin-T using a QuickChange Site-Directed Mutagenesis Kit (Agilent) and verified by sequencing. Human cardiac troponin complex subunits were expressed in *E. coli* and purified from BL21-CodonPlus cells (Agilent) using

established protocols (7), with the modification that the final protein was purified over a MonoQ column (GE Healthcare) instead of a ResourceQ column. Troponin complex concentration was measured using the Bradford reagent. Recombinant human tropomyosin was purified from BL21-CodonPlus cells (Agilent) using established protocols (8) with the modifications of McIntosh et al. (9). Tropomyosin concentration was determined using absorbance at 280 nm. Before use in biochemical assays, tropomyosin was reduced in 50 mM DTT at 56 °C for 5 minutes, and then aggregates were removed by ultracentrifugation (9).

In vitro motility assay

Phalloidin-stabilized F-actin and rhodamine-phalloidin-stabilized F-actin were each prepared in KMg25 buffer (25 mM KCl, 2 mM EGTA, 60 mM MOPS, 1 mM DTT, and 4 mM free $MgCl_2$). To remove myosin dead-heads, full-length cardiac myosin in high salt buffer (KMg25 with 300 mM KCl) with 2.17 μM phalloidin-stabilized F-actin and 1 mM ATP was sedimented at 355040 x g for 30 minutes at 4°C. A Bradford assay was used to determine the concentration of functional myosin heads following sedimentation. Flow cells were assembled with two glass coverslips (one coated with nitrocellulose) using double stick tape and vacuum grease. One volume of myosin (200 nM) was added to the flow cell followed by 1 volume of 1 mg/mL BSA, 1 volume unlabeled actin, 2 volumes of KMg25 + 1 mM ATP, 4 volumes of KMg25, and then 1 volume of reconstituted thin filaments (40 nM rhodamine-phalloidin-labeled actin with 2 μM troponin and tropomyosin). One volume equals 50 μL, which is slightly larger than the flow cell volume. Activation of motility was initiated by adding 2 volumes of activation buffer (KMg25 with 4 mM ATP, 1

mg/mL glucose, 192 U/mL glucose oxidase, 48 µg/mL catalase, 2 µM troponin and tropomyosin, 0.5% methyl cellulose). The speed of thin filament translocation was recorded at room temperature (~20 °C) over 20 frames. 25 consistently moving filaments from each video were manually tracked and analyzed using the MTrackJ plugin on Fiji ImageJ (10). Data were collected from 3 separate experiments.

Stopped-flow transient kinetics to determine K_B and the rate of ADP release

To determine K_B, the rate of myosin binding to regulated thin filaments was measured at 20 °C using stopped-flow techniques (11) in an SX-20 apparatus (Applied Photophysics). Pyrene-actin was excited at 365 nm, and fluorescence emission was detected using a 395 nm long-pass filter. 5 µM phalloidin-stabilized pyrene actin, 2 µM tropomyosin, 2 µM troponin, and 0.04 U/mL apyrase were rapidly mixed with 0.5 µM S1 myosin and 0.04 U/mL apyrase. The high calcium (pCa 4) buffer contained 200 mM KCl, 5mM free $MgCl_2$, 60 mM MOPS, 2 mM EGTA, 1mM DTT, and 2.15 mM $CaCl_2$. The low calcium (pCa 9) buffer contained 200 mM KCl, 5mM free $MgCl_2$, 60 mM MOPS, 2 mM EGTA, 1 mM DTT and 5.2 µM $CaCl_2$. Each experiment was the average of at least 3 separate mixes, and the data were fit by a single exponential curve. K_B was calculated by using Equation 1. The average K_B was calculated from three different experiments and the p-value was calculated using a 2-tailed Student's t-test.

The rate of ADP release from myosin bound to regulated thin filaments at 20 °C was determined using stopped-flow techniques (12). 1 µM phalloidin-stabilized pyrene-actin, 1 µM S1 myosin, 100 µM ADP, 100 µM $MgCl_2$, 2 µM tropomyosin, and 2 µM troponin were rapidly mixed with 5 mM ATP and 5 mM $MgCl_2$. The experiment was performed in

high calcium (pCa 4) buffer containing 25 mM KCl, 5mM $MgCl_2$, 60 mM MOPS, 2 mM EGTA, 1 mM DTT, and 2.15 mM $CaCl_2$. The rate of ADP release was calculated by fitting a single exponential function to the data, as we have previously done (6) (SI Appendix, Fig. S1). The average of three experiments was calculated, and statistical testing was done using a two-tailed Student's t-test.

Fluorescence titrations to determine the values of K_W, K_T, and n

Fluorescence titrations were carried out at 20 °C as described in (11) to determine the values of K_W, K_T, and n. S1 myosin (up to a final concentration of 10 µM) was added at 1-minute intervals to a stirred cuvette containing 0.5 µM pyrene-actin and 0.27 µM troponin and tropomyosin. Titrations were performed at low (2 mM EGTA), intermediate (pCa 6.25), and high (pCa 3) calcium concentrations. The buffers contained 200 mM KCl, 5 mM $MgCl_2$, 60 mM MOPS, 2 mM EGTA, 1 mM DTT, 2 mM ADP, and the desired free concentration of calcium from $CaCl_2$. The buffer also contained 50 µM P1,P5-di(adenosine-5')pentaphosphate (Ap5A), 2 mM glucose, and 1 µM hexokinase to eliminate any contaminating ATP. Five repeats were performed for each condition. Titration curves were globally fit using an annealing algorithm in MATLAB (MathWorks) (13). 95% confidence intervals were determined by fitting 1000 bootstrap simulations. A test statistic was defined by calculating the difference in fit parameters between bootstrap simulations of the WT and mutant data, and the p-value was determined from the fraction of test statistic simulations that did not include the null hypothesis (i.e., that the parameters for the WT are the same as the mutant). The fraction of thin filament in each equilibrium state (Fig. 3B) was calculated using the partition function.

Simulations

To predict the effects of the observed changes in the equilibrium constants for thin filament activation on force production by sarcomeres, we performed computational simulations using the model developed by Campbell et al. (14). This model is loosely based on the McKillop and Geeves formalism that was used to analyze the *in vitro* biochemical measurements (11). The Campbell et al. model simulates 9 sarcomeric regulatory units that can exist in blocked, closed, open, or force generating states, where the transition between states depends on the equilibrium constants between the states and a coupling term that was empirically determined by Campbell et al.

The Campbell et al. model differs from McKillop and Geeves in several important ways. Importantly, K_T is calcium dependent in the McKillop and Geeves formalism, but calcium independent in the Campbell et al. model. For the modeling here, we used a single value of K_T (the value at pCa 6.25) for the whole simulation, since this value was closest to the maximal calcium concentration experienced in a cardiomyocyte during contraction (~pCa 6) (15). Moreover, the Campbell et al. model uses empirically determined values for coupling between subunits to account for cooperativity, but this cooperativity is not the same as that measured in McKillop and Geeves. Finally, the equilibrium constants for the transitions into and out of the myosin-bound states were empirically determined by Campbell et al. and measured using the McKillop and Geeves approach. As such, it is not possible to directly use our measured equilibrium constants in the Campbell et al. model. Rather, we examined the effects of the relative changes in

the equilibrium constants. For example, we observed a ~3-fold decrease in K_T at pCa 6.25, and therefore we decreased the forward rate constant 3-fold to mimic the effects of the mutant. For simulation of the WT protein, the default parameters were used, except the value of the forward rate constant out of the blocked state was adjusted to capture the measured value of K_B. This same K_B value was used for the mutant simulation, since K_B was unchanged in the mutant.

Using this model, we calculated the normalized force-pCa curve and the twitch force in response to a calcium transient for a given set of equilibrium constants. The calcium transient used for the modeling of the twitch force was the default calcium transient employed by the model. This transient approximates the calcium in a cardiomyocyte (for example, see (15)), where the maximal calcium reached during activation was set to 1 μM calcium (pCa 6) and the minimal calcium was set to 0.1 μM (pCa 7). Code for the simulation was kindly provided by Stuart Campbell.

Stem cell line derivation

The parent stem cell line, BJFF.6, was generated from the human BJ fibroblast line (CRL-2522, ATCC) by the Genome Engineering and iPSC Center (GEiC) at Washington University in St. Louis. hiPSC reprogramming was done using the CytoTune-iPS 2.0 Sendai reprogramming kit (A16517, ThermoFisher) following the manufacturer's recommended protocol.

Whole exome sequencing

Whole exome sequencing of the BJFF.6 stem cell line was performed by the McDonnell Genome Institute (Washington University in St. Louis). DNA was isolated from a frozen cell pellet using the QiaAMP DNA Mini Kit (Qiagen) according to the manufacturer's recommendations. DNA was quantified fluorometrically using the Qubit and dsDNA HS Assay kit (Invitrogen). The DNA yield was 22 µg / 5 million cells.

An automated dual-indexed library was constructed with 250 ng of genomic DNA utilizing the KAPA HTP Library Kit (KAPA Biosystems) on the SciClone NGS instrument (Perkin Elmer) targeting 250 bp inserts. 1 µg of library was hybridized with the xGen Exome Research Panel v1.0 reagent (IDT Technologies) that spans 39 Mb target regions (19,396 genes) of the human genome. The concentration of the captured library pool was accurately determined through qPCR (Kapa Biosystems) to produce cluster counts appropriate for the S2 flow cell on the NovaSeq platform (Illumina). A 2 x 151 base pair end sequence data generated approximately 15 Gb per sample which led to greater than 90% of the targets covered at a minimum of 20x depth of coverage. The mean depth of coverage was approximately 200x. Variants were identified using the Variant Effect Predictor. Variants in genes that have been associated with cardiomyopathies (ABCC9, ACTC1, ACTN2, ALMS1, ALPK3, ANKRD1, BAG3, BRAF, CAV3, CHRM2, CRYAB, CSRP3, DES, DMD, DOLK, DSC2, DSG2, DSP, DTNA, EMD, FHL1, FKRP, FKTN, FLNC, GATAD1, GLA, HCN4, HRAS, ILK, JPH2, JUP, KRAS, LAMA4, LAMP2, LDB3, LMNA, MAP2K1, MAP2K2, MIB1, MTND1, MTND5, MTND6, MTTD, MTTG, MTTH, MTTI, MTTK, MTTL1, MTTL2, MTTM, MTTQ, MTTS1, MTTS2, MURC, MYBPC3, MYH6, MYH7, MYL2, MYL3, MYLK2, MYOZ2, MYPN, NEBL, NEXN, NKX2-5, NRAS, PDLIM3, PKP2, PLN, PRDM16, PRKAG2, PTPN11, RAF1, RBM20, RIT1, RYR2, SCN5A, SGCD,

SOS1, TAZ, TCAP, TGFB3, TMEM43, TMPO, TNNC1, TNNI3, TNNT2, TPM1, TTN, TTR, TXNRD2, VCL) were cross referenced with the ClinVar database. None of the variants identified in the BJFF.6 cell line have been characterized as pathogenic or likely pathogenic in patients (SI Appendix, Fig. S2).

Derivation of the ΔK210 stem cell lines

Two independent stem cell lines homozygous for the ΔK210 deletion, AN184.2-hTNNT2, were generated from the BJFF.6 human hiPSC line by the Genome Engineering and iPSC Center (GEiC) at Washington University in St. Louis using the CRISPR/Cas9 system (16, 17). The oligo used to generate the gRNA was ACACCGAGAAGATTCTGGCTGAGAGGG (SI Appendox, Fig. S3). This gRNA was selected to minimize potential off-target effects based on an analysis of similar sequences. The mutation was introduced using homology-directed repair to a single-stranded oligodeoxynucleotide template (ssODN) with the deletion. Approximately 1 to 1.5×10^6 hPSCs were washed in DPBS and resuspended in P3 primary buffer (Lonza) with 1 µg gRNA, 1.5 µg Cas9 vectors, and 1 µL ssODN (4µg, IDT) and then electroporated with a 4D-Nucleofector (Lonza) using the CA-137 program. Following nucleofection, cells were single-cell sorted (18) and screened with targeted deep sequencing analysis (19) using primer sets specific to target regions. The ΔK210 deletion was found in ~10% of the clones. Two clones with the ΔK210 mutation were then used for all cellular experiments.

After gene editing, karyotype (G-banding) analysis was performed by Cell Line Genetics. Cytogenetic analysis was performed on 20 G-banded metaphase cells (Cell

Line Genetics) and these cells had normal karyotypes (SI Appendix, Fig. S4). Cells were tested for myoplasma infections by the Genome Engineering core. Pluripotency of gene-edited hPSCs was characterized by staining for SSEA4, OCT4, SOX2, and TRA-1-61 using the Pluripotent Stem Cell 4-Marker Immunocytochemistry kit (A25526, ThermoFisher) following the manufacturer's recommended protocol. Immunofluorescent images of the stained cells were captured using a Nikon fluorescence microscope and CCD camera. Cells showed robust staining for pluripotency markers (SI Appendix, Fig. S5).

Stem cell culture and differentiation to hiPSC-CMs

All culture media contained 10 U/mL penicillin and 10 µg/mL streptomycin. hiPSCs were maintained at 37 °C and 5% CO_2 in feeder-free culture on Matrigel (Corning) coated plates in Essential 8 Flex or StemFlex media (ThermoFisher). Cells were passaged using 0.02% EDTA (Sigma). After passaging, the E8 media was supplemented with 5 µM of the ROCK inhibitor Y-27632 (Selleck Chem).

Differentiation to cardiomyocytes was accomplished using the method of Lian et al. (20) (SI Appendix, Fig. S6). Briefly, hiPSC colonies were dissociated to single cells using Accutase (Gibco) and seeded into monolayers on 12-well Matrigel coated plates at a density of 0.5-1 million cells per well. Cells were maintained in StemFlex media supplemented with 5 µM Y-27632 for the first 24 hours. Two days after seeding (day 0), the media was changed to RPMI/B27-I (RPMI-1640 media (Sigma) containing B-27 supplement without insulin (ThermoFisher). 6-8 µM of the WNT agonist CHIR-99021 (Selleck Chem) was added to initiate differentiation for 24 hours along with 1 µg/mL insulin

to improve cell survival. On day 1, the WNT agonist was removed and cells were cultured in RPMI/B27-I. On day 3, the media was collected and centrifuged to remove debris. The conditioned media was combined with fresh RPMI/B27-I media in a 1:1 ratio and was supplemented with 5 μM of the WNT inhibitor IWP-2. On day 5, the IWP2 was removed and the cells were cultured in RPMI/B27-I. On day 7, the media was changed to RPMI/B27+I (RPMI-1640 media containing B-27 supplement with insulin) and changed every 3 days. Spontaneous beating began on days 9-12.

To enrich the population of cardiomyocytes, metabolic selection was used (21). On days 12-17, the cells were cultured in glucose-free media (glucose-free RPMI-1640 supplemented with B-27 supplement with insulin). On day 19, the cells were dissociated using 0.25% trypsin and then passaged to gelatin coated culture dishes in RPMI-20 (RPMI-1640 + 20% FBS) with the addition of 10 μM Y-27632. Starting on day 21, cells were cultured in RPMI/B27+I and the media was changed every 3 days. Metabolic selection gave populations of >90% cardiomyocytes (SI Appendix, Fig. S6). Cells were aged at least 30 days after differentiation before being used for assays.

Fabrication of stamps for microcontact patterning

Stamps for microcontact printing were generated using standard microfabrication techniques, based on the procedure in Ribeiro et al. (22). A photomask containing an array of 17 x 118 μm (total area of 2000 μm^2) rectangles was generated (CAD/Art Services). SU-8-3010 (Microchem) was spin coated on to a 3” silicon wafer (University Wafer) using a Brewer Science CEE 200X instrument (Washington University Institute of Material Sciences and Engineering) to generate a 15 μm thick layer. The wafer was then

soft baked at 65 °C for 90 seconds followed by 6 minutes at 95 °C. The mask exposure was done using a Karl Suss MJB 3UV 400 Mask Aligner for a total exposure energy of 200 mJ/cm^2. Post exposure, the wafer was baked at 65 °C for 1 minute followed by 3 minutes at 95 °C. The un-polymerized SU-8-3010 was then removed from the master by washing in SU-8 developer (Y020100, Microchem).

Polydimethylsiloxane (PDMS) stamps for microcontact printing were prepared from the SU-8 master. The SU-8 master was silanized using vapor deposition of Trichloro(1H,1H,2H,2H-perfluoro-octyl) silane (Sigma) under vacuum. PDMS (Sylgard 184, Dow Corning) was prepared using a 10:1 w/w mixture of elastomer base:curing agent. PDMS was degassed under vacuum, poured on the master, and cured overnight under vacuum. The following day, the PDMS stamps were hard cured at 80 °C for 1 hour, peeled from the master, and then cut into 18 x 18 mm squares using a razor blade.

Microcontact patterning of cardiomyocytes on glass

For patterning of cardiomyocytes on glass, glass coverslips were first cleaned by sonication in isopropanol. The glass was washed twice with water and dried using compressed nitrogen gas. The glass was then plasma cleaned under vacuum for 1 minute. The glass surface was passivated for 30 minutes in 0.1 mg/mL PLL-g-PEG (SuSoS AG), then washed with water, and dried with nitrogen gas. PDMS stamps were sterilized under UV light before use for at least 10 minutes. Geltrex (ThermoFisher) was diluted 1:10 in DMEM-F12 and then 40 µL was added to the surface of the PDMS stamp for 20 minutes. The Geltrex-coated PDMS stamp was dried with nitrogen gas and then placed Geltrex side down on the PLL-g-PEG treated coverslip. A 50 or 100 g weight was

placed on top of the PDMS stamp for 2-3 minutes to transfer the Geltrex pattern onto the coverslip. The stamped glass coverslips were then transferred to the bottom of a 6-well tissue culture plate.

Cardiomyocytes were dissociated and singularized using 0.25% trypsin (Gibco). Cells were resuspended in RPMI-20 with 10 µM Y-27632 at a density of 500 cells/µL and then incubated on the patterned glass for 45 minutes. 18 mm coverslips required 300 µL volume per coverslip. The patterned cardiomyocytes were cultured in RPMI-20 with ROCK inhibitor (10 µM Y-27632) for 48 hours and were subsequently cultured in RPMI/B27+I with media changes every 3 days.

Immunostaining and fluorescence microscopy

Cardiomyocytes were fixed for 15 minutes in 4% paraformaldehyde (Electron Microscopy Sciences) in phosphate-buffered saline (PBS) and permeabilized with 0.1% Triton X-100 (Sigma) for 20 minutes. The cells were blocked for 1 hour using a blocking solution containing 3% bovine serum albumin (Gold Bio), 5% donkey serum (Sigma), 0.1% Triton X-100, and 0.02% sodium azide in PBS. Primary antibodies (see table below) were added for 1 hour at room temperature or overnight at 4 °C. Cells were then washed thoroughly in PBS before incubating for 1 hour in secondary antibody. Cells were again thoroughly washed in PBS. For experiments with 4′,6-diamidino-2-phenylindole (DAPI), the stain was used at a 1:50,000 dilution. For experiments using tetramethylrhodamine B isothiocyanate labeled phalloidin, the phalloidin was added using a 1:1000 dilution. Cells were visualized using a Nikon A1Rsi confocal microscope or a Nikon spinning disk confocal microscope equipped with a Yokagawa CSU-X1 variable speed Nipkow spinning

disk scan head and an Andor Zyla 4.2 Megapixel sCMOS camera (Washington University Center for Cellular Imaging). Z-stacks of cells with 60x magnification were recorded in sequential scanning mode.

Antibodies used

Antibody	Product Number	Working Dilution	Host species	Vendor
Alpha-actinin	A7811/EA-53	1:500	mouse	Sigma
Troponin-I	SC-15368	1:300	rabbit	Santa Cruz
Cy3 anti-rabbit	711165152	1:300	donkey	Jackson Immuno.
Cy2 anti-mouse	715225150	1:300	donkey	Jackson Immuno.
OCT4	A25532	1:400	Rabbit	Invitrogen
SSEA4	A25530	1:100	Mouse	Invitrogen
SOX2	A24759	1:100	Rat	Invitrogen
TRA-1-60	A24868	1:100	Mouse	Invitrogen

Analysis of immunofluorescence images

Analysis of the organization of the sarcomeres was done using software developed by the Parker lab (23). Standard deviation projections were generated from Z-stacks of hiPSC-CMs stained for α-actinin. Data were pre-processed in FIJI/ImageJ (10) using an ImageJ plugin (23). Data were then analyzed using the Parker lab's software to extract the orientational order parameter (OOP, a measure of sarcomeric alignment along a single axis) (23). The cellular area, length, and width were calculated from thresholded images of cardiomyocytes in ImageJ. Cumulative distributions of parameters were generated in MATLAB (MathWorks). A Kruskal–Wallis one-way analysis of variance test

was used to compare the distributions. To compare individual parameters, 95% confidence intervals were determined by calculating the mean parameter value from 1000 bootstrap simulations. A test statistic was defined by calculating the difference in fit parameters between bootstrap simulations of the WT and mutant data, and the p-value was determined from the fraction of test statistic simulations that did not include the null hypothesis (i.e., that the parameters for the WT are the same as the mutant).

Device fabrication for traction force microscopy

Hydrogels for traction force microscopy were generated in 35 mm dishes according to the protocol of Ribeiro et al., (22). The 14 mm glass-bottom of the 35 mm tissue culture dishes (MatTek) were silanized with 0.4% 3-trimethoxylyl-propylmethacrylate (Sigma) for 1 hour and then washed with water and dried with nitrogen gas. To make 10 kPa polyacrylamide hydrogels, a prepolymer solution containing 0.1% bisacrylamide was used (24). 0.2 µm diameter fluorescent beads were added to the prepolymer solution (FSSY002, Bangs Beads) as markers for the traction force.

Patterned coverslips were prepared using PDMS stamps and microcontact printing. 12mm round coverslips were cleaned by plasma cleaning under vacuum for 5 minutes. 1:10 dilution of Geltrex was prepared in DMEM-F12. 40 µL of Geltrex was added to the surface of the PDMS stamp and allowed to incubate for 20 minutes. Then the stamp was dried with nitrogen gas and placed on the 12 mm round coverglass for 2-3 minutes under a 50 g or 100 g weight, transferring the pattern to the coverglass. Unpatterned coverslips were prepared by coating the entire surface of a 12 mm coverglass with Geltrex.

To assemble the hydrogels, 15 µL of prepolymer solution was added to the silanized glass tissue culture dishes and then the 12 mm Geltrex-patterned coverglass was placed pattern side down. Hydrogels were allowed to polymerize for 15 minutes and then PBS was added for at least 1 hour to hydrate the hydrogels. Hydrogels could be stored in PBS at 4°C until cell seeding. Before cell seeding, the 12 mm coverglass was removed using forceps.

Traction force microscopy

All traction force microscopy measurements were performed on patterned polyacrylamide hydrogels with a stiffness of 10 kPa with hiPSC-CMs that were at least 30 days post-differentiation (22). Cardiomyocytes were singularized using 0.25% trypsin and then resuspended in RPMI-20 with 10 µM Y-27632. PBS from the hydrogels was aspirated and 100 µL of media containing 50,000 cells was added to the hydrogel surface. After 45 minutes, 2 mL of RPMI-20 with 10 µM Y-27632 was added to the well. Cells were placed in the incubator for 48 hours, and then the media was changed to RPMI/B27+I and changed every 3 days until imaging.

On the day of imaging, fresh RPMI/B27+I was added 1 hour before imaging. Single, spontaneously-beating cells were imaged in an environmentally controlled chamber (Tokai Hit) on a Nikon spinning disk confocal microscope equipped with a Yokagawa CSU-X1 variable speed Nipkow spinning disk scan head and Andor Zyla 4.2 Megapixel sCMOS camera (Washington University Center for Cellular Imaging). Cells were imaged over an 800x400 pixel region of interest using a 40x objective. 20 seconds

of data were collected at 33 frames per second. Both bright-field and fluorescence images were recorded.

Analysis of traction force microscopy data

Traction force movies were analyzed by generating displacement maps of the fluorescent beads using a MATLAB program developed by the Pruitt lab (25). The program enables the measurement of several parameters, including the force and power output of single cells. Cumulative distributions of parameters were generated in MATLAB. A Kruskal–Wallis one-way analysis of variance test was used to compare the distributions. To compare individual parameters, 95% confidence intervals were determined by calculating the mean parameter value from 1000 bootstrapped simulations (13). A test statistic was defined by calculating the difference in fit parameters between bootstrapping simulations of the WT and mutant data, and the p-value was determined from the fraction of test statistic simulations that did not include the null hypothesis (i.e., that the parameters for the WT are the same as the mutant).

Hydrogel fabrication for immunofluorescence microscopy

Hydrogels for immunofluorescence microscopy were generated on 12 mm glass coverslips according to the protocol of Ribeiro et al., (22). 12 mm glass coverslips were silanized with 0.4% 3-trimethoxylyl-propylmethacrylate (Sigma) for 1 hour and then washed with water and dried with nitrogen gas. To make 10 kPa polyacrylamide hydrogels, a prepolymer solution containing 0.1% bisacrylamide was used (24).

Patterned coverslips were prepared using PDMS stamps and microcontact printing. 12 mm round coverslips were cleaned by plasma cleaning under vacuum for 5 minutes. 1:10 dilution of Geltrex was prepared in DMEM-F12. 40 µL of Geltrex was added to the surface of the PDMS stamp and allowed to incubate for 20 minutes. Then the stamp was dried with nitrogen gas and placed on the 12 mm round coverglass for 2-3 minutes under a 50 g or 100 g weight, transferring the pattern to the coverglass.

To assemble the hydrogels, 15 µL of prepolymer solution was added to the silanized 12 mm coverglass and then the 12 mm Geltrex patterned coverglass was placed pattern side down to create a sandwich between the two coverglasses. Hydrogels were allowed to polymerize for 15 minutes and the sandwiches were transferred into a 24-well tissue culture plate. PBS was added for at least 1 hour to hydrate the hydrogels. Hydrogels could also be stored in PBS at 4 °C until cell seeding. Before cell seeding, the top coverglass was removed using a razor blade, leaving behind the 12 mm coverglass with the patterned hydrogel. Cell seeding and immunofluorescence preparation and imaging were carried out in the same manner as described in the traction force microscopy and immunofluorescence sections above.

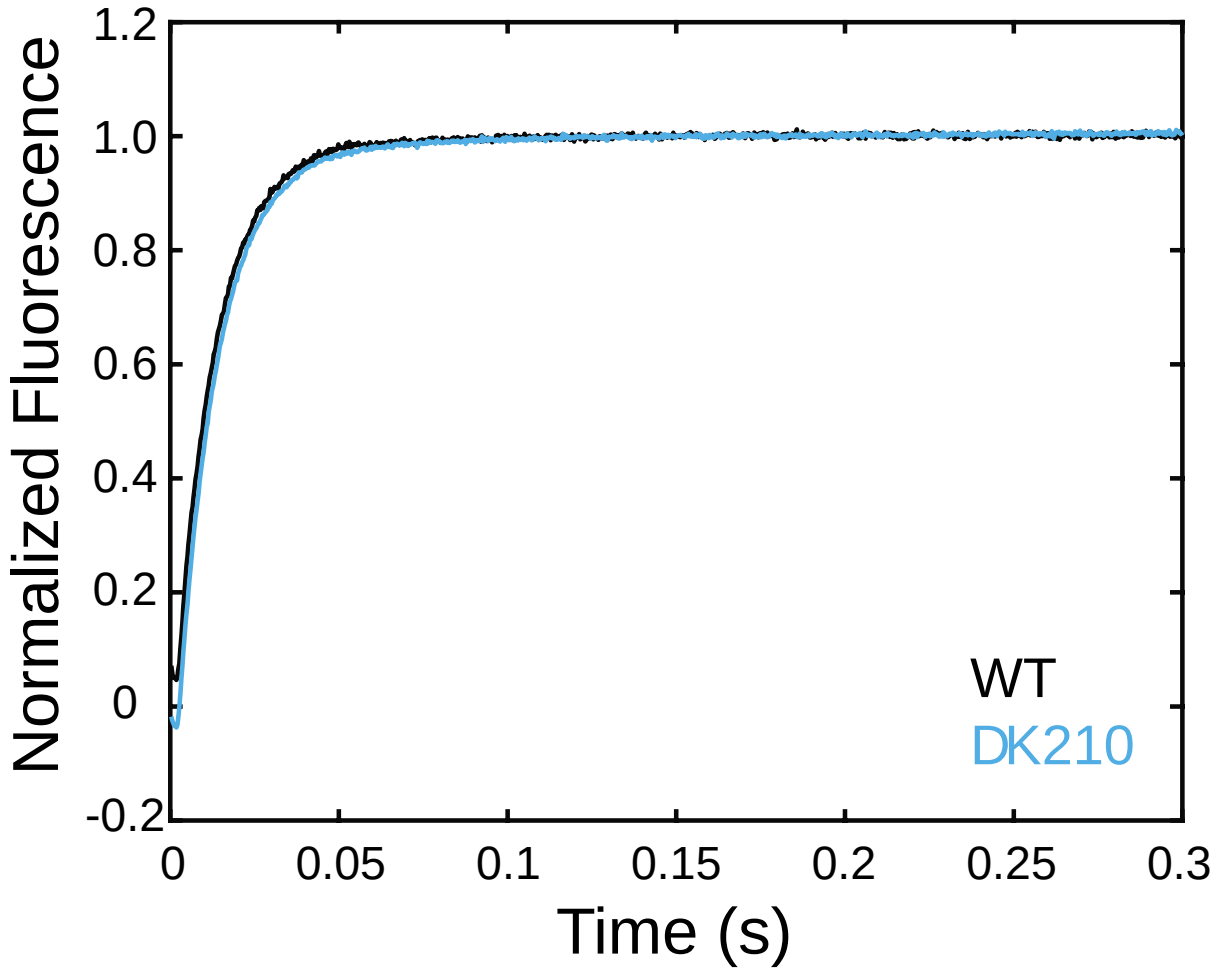

Figure 2 **Fig. S1.** ADP release rates from myosin bound to regulated thin filaments for WT and ΔK210 at 20°C. The data is the average of at least three individual experiments. The ADP release rate in the presence of the mutation (72 ± 6 s^{-1}) is not significantly different from the WT (76 ± 5 s^{-1}, p=0.344).

Chromosome	Position	ID	Gene	Change	CDS_position	Clinvar Annotation
1	78392446	rs1166698	NEXN	G/A	541	Benign
1	3328358	rs870124	PRDM16	C/C	1597	Benign
1	155880573	rs493446	RIT1	G/G	31	Benign
1	156107534	rs4641	LMNA	C/T	1698	Benign
2	73613031	rs61156725	ALMS1	T/T	36-41	Benign
2	179401740	rs55675869	TTN	C/T	73276	Benign
2	179411011	rs72648257	TTN	T/C	68227	Benign
2	179414992	rs72648244	TTN	T/C	64753	Benign
2	179421694	rs9808377	TTN	A/G	61367	Benign
2	179427536	rs3829746	TTN	T/C	56503	Benign
2	179431594	rs3731745	TTN	A/G	52445	Benign
2	179433221	rs56018860	TTN	T/C	50818	Benign
2	179433580	rs3813246	TTN	T/C	50459	Benign
2	179434139	rs3813245	TTN	A/G	49900	Benign
2	179437928	rs56201325	TTN	T/C	46111	Conflicting interpretations (benign (4) /likely benign (2) / unknown (1))
2	179444768	rs4145333	TTN	G/G	40426	Benign
2	179451420	rs2042996	TTN	G/A	37388	Benign
2	179464527	rs1001238	TTN	T/C	29281	Benign
2	179472292	rs2303832	TTN	T/A	26303	Benign
2	179498042	rs6723526	TTN	T/C	16138	Benign
2	179499530	rs2288563	TTN	T/C	15251	Benign
2	179518003	rs2562847	TTN	A/G	38753	Not found
2	179523514	rs200021871	TTN	T/A	37461	Benign
2	179528378	rs2163008	TTN	C/T	700	Benign
2	179554305	rs2244492	TTN	C/T	1498	Benign
2	179558366	rs2042995	TTN	T/C	1198	Benign
2	179581835	rs2562832	TTN	C/A	21894	Benign
2	179600648	rs2742347	TTN	C/T	10793	Benign
2	179604160	rs1883085	TTN	T/G	13086	Benign
2	179604366	rs2562829	TTN	T/G	12880	Benign
2	179606538	rs2627037	TTN	G/A	10708	Benign
2	179611711	rs66677602	TTN	C/A	15416	Benign
2	179615887	rs922984	TTN	T/C	11240	Benign
2	179615931	rs922985	TTN	G/G	11196	Benign
2	179621477	rs6433728	TTN	T/T	10213	Benign
2	179623758	rs2291310	TTN	C/T	10256	Benign
2	179629461	rs2291311	TTN	C/T	9781	Benign
2	179634936	rs2306636	TTN	C/T	8492	Benign
2	179637861	rs56142888	TTN	C/G	7830	Benign
2	179641975	rs12476289	TTN	C/T	4715	Benign
2	179644035	rs1552280	TTN	A/A	3884	Benign
2	179644855	rs10497520	TTN	T/C	3463	Benign
2	179658175	rs72647851	TTN	C/T	280	Benign
2	73716810	rs3820700	ALMS1	A/A	2555	Benign
2	73717103	rs2017116	ALMS1	C/C	2848	Benign
2	179582537	rs2627043	TTN	G/T	21332	Benign
2	179620951	rs7585334	TTN	C/T	10739	Benign
2	179444289	rs2288570	TTN	A/G	40815	Benign
4	186423637	rs4635850	PDLIM3	A/A	762	Benign
5	155935708	rs45559835	SGCD	G/A	287	Benign
6	7580285	rs138907450	DSP	A/C	3862	Likely benign (4) / unknown (4)
6	7581636	rs6929069	DSP	G/A	5213	Benign
6	112457383	rs1050349	LAMA4	G/C	3356	Benign
6	112457390	rs2032567	LAMA4	T/T	3349	Benign
6	112493872	rs1050348	LAMA4	A/G	1492	Benign
6	112508770	rs9400522	LAMA4	T/T	827	Benign
6	112471688	rs3734286	LAMA4	G/C	536	Not found
6	7576527	rs1016835	DSP	G/A	2631	Benign
9	108366734	rs34787999	FKTN	G/A	608	Benign
10	121429633	rs2234962	BAG3	C/C	277	Benign
10	69926334	rs10823148	MYPN	C/G	1884	Benign
10	69933921	rs10997975	MYPN	G/A	2072	Benign
10	69933969	rs7916821	MYPN	G/A	2120	Benign
10	69934258	rs3814182	MYPN	C/G	2409	Benign
10	69959242	rs7079481	MYPN	C/A	3403	Benign
10	112572458	rs1417635	RBM20	C/C	2303	Benign
10	112595719	rs942077	RBM20	C/C	3667	Benign
11	6630028	314683;rs7593	ILK	T/T	457	Not found
11	111781047	rs11603779	CRYAB	A/C	328	Benign
11	47371598	rs3729986	MYBPC3	C/T	472	Benign
12	21997457	rs182158174	ABCC9	A/C	3167	Not found
12	98927830	rs17459334	TMPO	C/G	1795	Benign
15	85401259	rs306197	ALPK3	C/T	3896	Benign
15	73660505	rs143090627	HCN4	C/T	107	Benign
17	39912145	rs1126821	JUP	A/A	2089	Benign
19	4102449	rs17851657	MAP2K2	G/A	162	Benign
22	19868218	rs1139793	TXNRD2	A/G	1040	Benign
22	19907099	rs5748469	TXNRD2	C/A	127	Benign
X	31496350	rs1800280	DMD	T/T	8810	Benign
X	31893307	rs1800275	DMD	G/G	7096	Benign

Figure 3 **Fig. S2. Variants identified from whole exome sequencing of BJFF.6 cells.** None of the identified variants in the BJFF.6 line are classified as pathogenic or likely pathogenic in the ClinVar database.

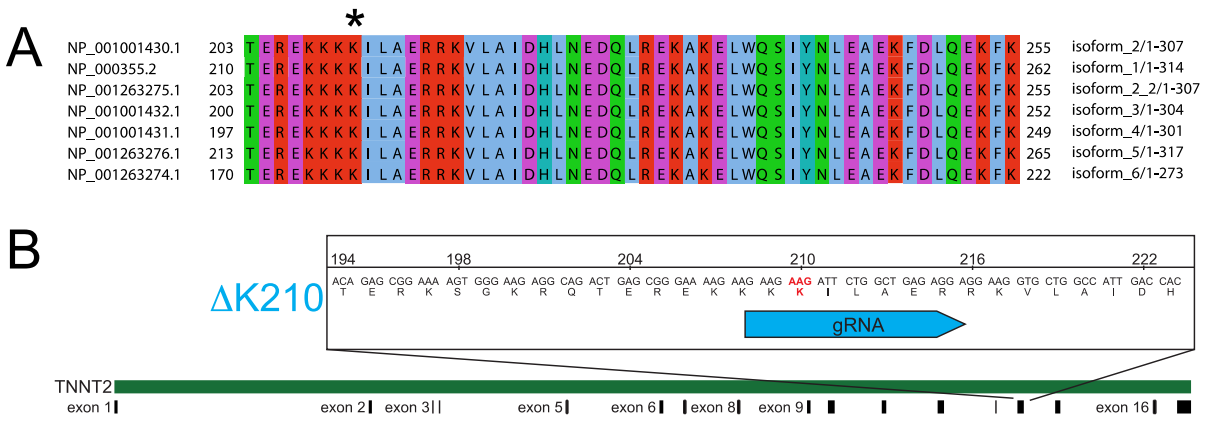

Figure 4 ***Fig. S3.*** *(A) Sequence alignment of all expressed human TNNT2 splice isoforms. K210 (*) is located in a conserved region of the protein. (B) CRISPR/Cas9 constructs for introducing the mutation into stem cells. This gRNA was chosen to minimize the risk of potential off-target effects. The AAG deletion was generated using a separate oligo for homology-directed repair, with an efficiency of ~10%. Two homozygous clones positive for the mutation were validated using Next Generation Sequencing.*

Figure 5 **Fig. S4. Karyotyping of gene edited cells.** Cytogenetic analysis was performed on 20 G-banded metaphase cells (Cell Line Genetics) and these cells had normal karyotypes.

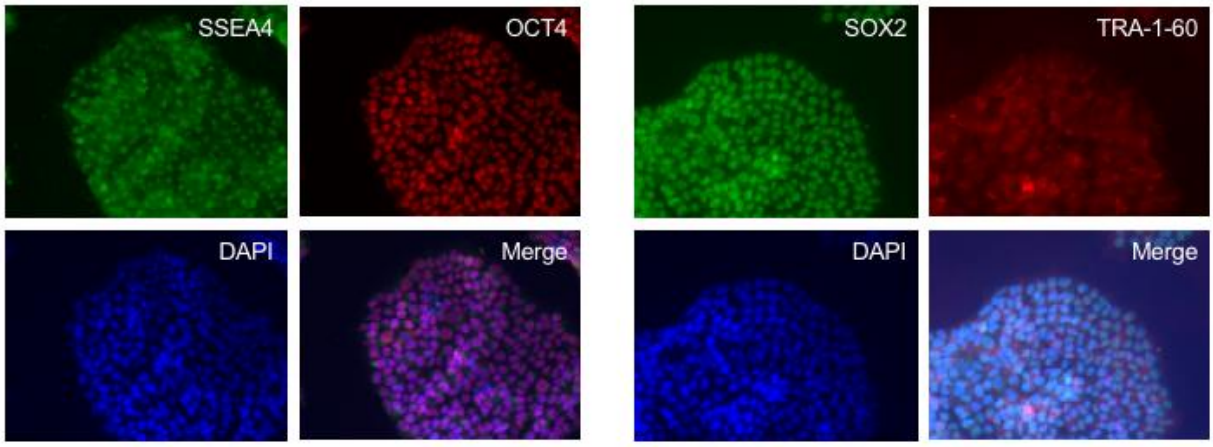

Figure 6 **Fig. S5.** Staining of gene-edited cells with markers of pluripotency demonstrates that stem cells retain pluripotency after gene editing.

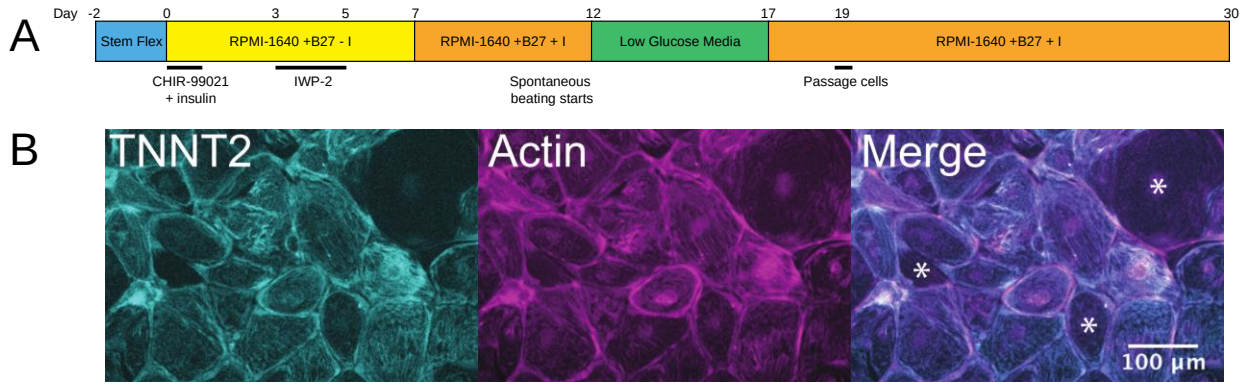

Figure 7 **Fig. S6.** (A) Differentiation protocol used to derive hiPSC-CMs from hiPSCs. I indicates insulin. (B) Cardiomyocyte purity was assessed by immunofluorescence. Cells were stained 30 days after differentiation to assess cardiomyocyte purity. Cells were stained using an antibody for cardiac troponin-T (TNNT2, cyan) and phalloidin which labels actin and acts as a marker of all cells (magenta). Cells were imaged using epifluorescence illumination. Non-cardiomyocytes contained actin, but not TNNT2 (denoted with *). 711 cells were examined, 652 of which were cardiomyocytes. This gives a cardiomyocyte differentiation efficiency of 92%.

	B	C	O	W	S	W/S
pCa >9	0.68	0.24	0.022	0.0026	0.046	0.049
pCa >9	0.72	0.26	0.01	0.001	0.015	0.016
pCa 6.25	0.033	0.67	0.094	0.011	0.20	0.21
pCa 6.25	0.042	0.84	0.034	0.0046	0.083	0.087
pCa 3	0.026	0.51	0.14	0.017	0.30	0.32
pCa 3	0.030	0.60	0.10	0.014	0.25	0.26

Figure 8 **Fig. S7.** Fractional occupancy of regulated thin filament states at different calcium concentrations. Values were calculated using the partition function and the percent change compared to WT (Fig. 3) was calculated by finding the difference between ΔK210 and WT thin filaments and dividing by the WT value. WT is shown in black and ΔK210 is shown in blue.

SI References

1. Greenberg MJ, Shuman H, & Ostap EM (2014) Inherent force-dependent properties of beta-cardiac myosin contribute to the force-velocity relationship of cardiac muscle. *Biophysical journal* 107(12):L41-L44.
2. Margossian SS & Lowey S (1982) Preparation of myosin and its subfragments from rabbit skeletal muscle. *Methods in enzymology* 85 Pt B:55-71.
3. Eads TM, Thomas DD, & Austin RH (1984) Microsecond rotational motions of eosin-labeled myosin measured by time-resolved anisotropy of absorption and phosphorescence. *Journal of molecular biology* 179(1):55-81.
4. Spudich JA & Watt S (1971) The regulation of rabbit skeletal muscle contraction. I. Biochemical studies of the interaction of the tropomyosin-troponin complex with actin and the proteolytic fragments of myosin. *The Journal of biological chemistry* 246(15):4866-4871.
5. Pollard TD (1984) Purification of a high molecular weight actin filament gelation protein from Acanthamoeba that shares antigenic determinants with vertebrate spectrins. *The Journal of cell biology* 99(6):1970-1980.
6. Greenberg MJ, Lin T, Goldman YE, Shuman H, & Ostap EM (2012) Myosin IC generates power over a range of loads via a new tension-sensing mechanism. *Proceedings of the National Academy of Sciences of the United States of America* 109(37):E2433-2440.
7. Kozaili JM, Leek D, & Tobacman LS (2010) Dual regulatory functions of the thin filament revealed by replacement of the troponin I inhibitory peptide with a linker. *The Journal of biological chemistry* 285(49):38034-38041.
8. Hitchcock-DeGregori SE & Heald RW (1987) Altered actin and troponin binding of amino-terminal variants of chicken striated muscle alpha-tropomyosin expressed in Escherichia coli. *The Journal of biological chemistry* 262(20):9730-9735.
9. McIntosh BB, Holzbaur EL, & Ostap EM (2015) Control of the initiation and termination of kinesin-1-driven transport by myosin-Ic and nonmuscle tropomyosin. *Current biology : CB* 25(4):523-529.
10. Schindelin J*, et al.* (2012) Fiji: an open-source platform for biological-image analysis. *Nature methods* 9(7):676-682.
11. McKillop DF & Geeves MA (1993) Regulation of the interaction between actin and myosin subfragment 1: evidence for three states of the thin filament. *Biophysical journal* 65(2):693-701.
12. De La Cruz EM & Ostap EM (2009) Kinetic and equilibrium analysis of the myosin ATPase. *Methods in enzymology* 455:157-192.
13. Barrick SK, Clippinger SR, Greenberg L, & Greenberg MJ (2019) Computational Tool to Study Perturbations in Muscle Regulation and Its Application to Heart Disease. *Biophysical journal* 116(12):2246-2252.
14. Campbell SG, Lionetti FV, Campbell KS, & McCulloch AD (2010) Coupling of adjacent tropomyosins enhances cross-bridge-mediated cooperative activation in

a markov model of the cardiac thin filament. *Biophysical journal* 98(10):2254-2264.
15. Dobrunz LE, Backx PH, & Yue DT (1995) Steady-state [Ca2+]i-force relationship in intact twitching cardiac muscle: direct evidence for modulation by isoproterenol and EMD 53998. *Biophysical journal* 69(1):189-201.
16. Jinek M*, et al.* (2012) A programmable dual-RNA-guided DNA endonuclease in adaptive bacterial immunity. *Science* 337(6096):816-821.
17. Hsu PD*, et al.* (2013) DNA targeting specificity of RNA-guided Cas9 nucleases. *Nature biotechnology* 31(9):827-832.
18. Chen YH & Pruett-Miller SM (2018) Improving single-cell cloning workflow for gene editing in human pluripotent stem cells. *Stem Cell Res* 31:186-192.
19. Sentmanat MF, Peters ST, Florian CP, Connelly JP, & Pruett-Miller SM (2018) A Survey of Validation Strategies for CRISPR-Cas9 Editing. *Sci Rep* 8(1):888.
20. Lian X*, et al.* (2013) Directed cardiomyocyte differentiation from human pluripotent stem cells by modulating Wnt/beta-catenin signaling under fully defined conditions. *Nature protocols* 8(1):162-175.
21. Sharma A*, et al.* (2015) Derivation of highly purified cardiomyocytes from human induced pluripotent stem cells using small molecule-modulated differentiation and subsequent glucose starvation. *J Vis Exp* (97).
22. Ribeiro AJ*, et al.* (2015) Contractility of single cardiomyocytes differentiated from pluripotent stem cells depends on physiological shape and substrate stiffness. *Proceedings of the National Academy of Sciences of the United States of America* 112(41):12705-12710.
23. Pasqualini FS, Sheehy SP, Agarwal A, Aratyn-Schaus Y, & Parker KK (2015) Structural phenotyping of stem cell-derived cardiomyocytes. *Stem Cell Reports* 4(3):340-347.
24. Tse JR & Engler AJ (2010) Preparation of hydrogel substrates with tunable mechanical properties. *Curr Protoc Cell Biol* Chapter 10:Unit 10 16.
25. Ribeiro AJS*, et al.* (2017) Multi-Imaging Method to Assay the Contractile Mechanical Output of Micropatterned Human iPSC-Derived Cardiac Myocytes. *Circulation research* 120(10):1572-1583.

Chapter 4: The variant R94C in TNNT2-encoded troponin T predisposes to pediatric restrictive cardiomyopathy and sudden death through impaired thin filament relaxation resulting in myocardial diastolic dysfunction

This chapter was published in the Journal of the American Heart Association as:

J. E. Ezekian, S.R. Clippinger, J.M. Garcia, Q. Yang, S. Denfield, A. Jeewa, W. J. Dreyer, W. Zou, Y. Fan, H. D. Allen, J. J. Kim, M. J. Greenberg, A. P. Landstrom, Variant r94c in tnnt2-encoded troponin t predisposes to pediatric restrictive cardiomyopathy and sudden death through impaired thin filament relaxation resulting in myocardial diastolic dysfunction. *J. Am. Heart Assoc.* **9** (2020).

Author contributions: JE and SC contributed equally to this work. SC purified proteins, performed the stopped-flow and fluorescence experiments, analyzed the data, and drafted the biochemistry sections of the manuscript. JE and the Landstrom lab performed the clinical work.

Abstract

Background: Pediatric-onset restrictive cardiomyopathy (RCM) is associated with high mortality, but underlying mechanisms of disease are under investigation. RCM-associated diastolic dysfunction secondary to variants in *TNNT2*-encoded cardiac troponin T (TNNT2) is poorly described.

Methods and Results: Genetic analysis of a proband and kindred with RCM identified TNNT2-R94C which co-segregated in a family with two generations of RCM, ventricular arrhythmias, and sudden death. TNNT2-R94C was absent among large population-based cohorts (gnomAD) and predicted pathologic by *in silico* modeling. Biophysical experiments using recombinant human TNNT2-R94C demonstrated impaired cardiac regulation at the molecular level due to reduced calcium-dependent blocking of myosin's interaction with the thin filament. Computational modeling predicted a shift in the force-calcium curve for the R94C mutant towards submaximal calcium activation compared to the WT, suggesting low levels of muscle activation even at resting calcium concentrations and hypercontractility following activation by calcium.

Conclusions: The pathogenic TNNT2-R94C variant activates thin filament-mediated sarcomeric contraction at submaximal calcium concentrations, likely resulting in increased muscle tension during diastole and hypercontractility during systole. This describes the proximal biophysical mechanism for the development of a restrictive cardiomyopathy.

Key Words: Restrictive Cardiomyopathy, Heart Failure, Pediatrics, Sudden Cardiac Death, Myocardial Biology

Clinical Perspective

1) What is new?

   TNNT2-R94C is a heritable cause of restrictive cardiomyopathy and sudden death. This pathologic mutation leads to initiation of cardiac muscle contraction at resting calcium

levels. Computational modeling predicts that this causes increased basal muscle tension and likely leads to diastolic cardiac dysfunction.

2) What are the clinical implications?

Pediatric restrictive cardiomyopathy is a rare cause of sudden cardiac death in children. This study demonstrates the pathologic mechanism of the variant. Patients with this mutation should be followed closely for development of cardiomyopathy and/or arrhythmias and familial screening should be performed when the variant is discovered in an individual.

4.1 Introduction

Restrictive cardiomyopathy (RCM) is a primary disorder of increased myocardial stiffness and diastolic dysfunction with often only normal to slightly hypertrophied ventricular wall thickness[1]. This disease typically manifests with marked atrial dilation, due to transmission of elevated pressures during ventricular relaxation, with preserved ventricular systolic function. The etiologies of RCM are broad, including inherited and acquired causes, and the prognosis is poor[2, 3]. RCM comprises one of a group of primary muscle diseases of the heart collectively called cardiomyopathies. Once thought to be separate entities, cardiomyopathies are now thought to be a spectrum of diseases with the presence of restrictive and hypertrophic features varying across the phenotypes. Hypertrophic cardiomyopathy (HCM) is common and is associated with mutations in sarcomere protein-encoding genes[4-7]. Restrictive and hypertrophic cardiomyopathy patients often share the feature of diastolic dysfunction, and a subset of patients with RCM demonstrate mild ventricular hypertrophy. The genetic mechanisms underlying RCM, the corresponding clinical phenotypes, and the sub-class of RCM with hypertrophic features have not been well described.

To date, more than 1000 variants associated with cardiomyopathy have been identified in sarcomeric genes, including *TNNT2*-encoded cardiac troponin T (TNNT2)[7, 8]. TNNT2 combines with the calcium-binding protein troponin C and troponin I to form the troponin complex. This

troponin complex is integrated into the thin filament of the sarcomere and, in combination with tropomyosin, it coordinates the contraction of the cardiac muscle by regulating the calcium-dependent interaction between myosin and the thin filament. *TNNT2*-specific gene variants are a known, rare cause of HCM, found in 3-5% of patients with HCM[9]. They have also been associated with the development of ventricular arrhythmias[10-13]. Recent studies have suggested that variants in *TNNT2* may also be associated with the development of RCM[14-16]. For example, the TNNT2 variant I79N has been shown to cause RCM and HCM within the same family[17]. Previous biochemical studies have suggested that *TNNT2* variants identified in patients with HCM and dilated cardiomyopathy result in alterations in calcium sensitivity leading to systolic dysfunction[18, 19]. Based on these findings, this molecular mechanism has been extrapolated to disorders of diastolic dysfunction. To confirm this hypothesis, variants known to produce a clinical phenotype of primary diastolic dysfunction and RCM should be studied to confirm the underlying molecular mechanisms.

Herein, we identify a *TNNT2* variant, TNNT2-R94C, in a family with multiple members affected with a range of clinical presentations including arrhythmias, cardiomyopathy with predominantly restrictive physiology, and sudden death. We used biochemical techniques and computational modeling to demonstrate that this variant is likely pathogenic, and we determined its molecular mechanism. We show that this variant causes activation of the thin filament at submaximal calcium concentrations, contributing to diastolic dysfunction as seen in this family.

4.2 Results

Clinical Evaluation

The proband is a 2-year-old Caucasian girl who was found to have RCM following an evaluation precipitated by the sudden death of her older brother. Her electrocardiogram (ECG) demonstrated criteria for right and left atrial enlargement with marked repolarization abnormality. Echocardiogram revealed mild right atrial and severe left atrial enlargement (left atrial volume

61.5 cc/m^2, normal 16-28 cc/m^2) with mildly increased left ventricular mass and otherwise normal ventricular dimensions. Right and left ventricular systolic function was preserved. These findings were consistent with a mild form of HCM with markedly restrictive physiology (**Figure 1A and 1B**). The proband suffered a cardiac arrest during phlebotomy and was unable to be resuscitated.

Her seemingly healthy 4-year-old brother presented with a sudden cardiac arrest while running on a soccer field and could not be resuscitated. Autopsy revealed mild cardiomegaly (heart weighed 147 g, normal 55-121 g) with mild biventricular hypertrophy (LV free wall 0.8 cm (echocardiographic Z-Score +3.53), interventricular septum 0.9 cm (echocardiographic Z-Score +4.78), and RV free wall (0.3 cm) with myocyte hypertrophy and disarray found on histopathologic examination[48, 49]. These findings were determined to be consistent with a diagnosis of hypertrophic cardiomyopathy which was identified as the cause of death. Significant left ventricular outflow tract obstruction was not present. No genetic testing was performed at the time of death. Due to this diagnosis, clinical evaluation of the family was conducted which included phenotypic screening and genetic testing.

The proband's father is a 35-year-old male who was found to have episodes of asymptomatic, non-sustained ventricular tachycardia and premature ventricular beats on event monitoring in the setting of normal biventricular size and systolic function. Cardiac MRI demonstrated normal myocardium and marked right and left atrial enlargement consistent with diastolic dysfunction and restrictive cardiomyopathy. (**Figure 1C-E**).

Genetic Evaluation

Cardiomyopathy-based panel testing (Familion) was conducted on the proband demonstrating a single, heterozygous, variant TNNT2-R94C (c.280C>T). No other variants were identified in other cardiomyopathy-associated genes. This variant was absent in gnomAD and localized to a highly conserved portion of the N-terminal domain near the tropomyosin binding site (**Figure 2 A-B**). To test whether this variant was found among all affected individuals, family

history was expanded, and a total of 8 kindred was consented and subjected for confirmatory genetic testing. In addition to the proband (IV.3), post-mortem genetic testing of the deceased brother (IV.2) also demonstrated presence of the heterozygous TNNT2-R94C variant. While a first trimester fetal death (IV.4) was also identified from the mother (III.4), no fetal tissue was available for genetic analysis. The father (III.3) was also found to carry the TNNT2-R94C which was absent in both paternal grandparents (II.1 and II.2) and paternal sibling (III.2), suggesting a *de novo* variant that was subsequently passed in an autosomal dominant fashion. This is summarized in **Figure 3**. *In silico* prediction modeling was performed and demonstrated a prediction of deleterious impact from 5/6 models and neutral from one model with an average confidence of 74.6% (**Table 1**). This variant was designated as pathologic in ClinVar and there is strong evidence of pathogenicity based on 2015 ACMG Criteria[21] for classifying pathogenic variants.

R94C destabilizes the blocked state of tropomyosin and increases the equilibrium constant for myosin weak binding to the thin filament

Cardiac troponin T is part of the machinery that regulates the calcium dependent interactions between myosin and the thin filament (**Figure 4A**). To determine the molecular consequences of the TNNT2-R94C variant on cardiac contractile regulation, we expressed human wild-type ($TNNT2^{WT}$) and mutant troponin ($TNNT2^{R94C}$) and determined the biochemical impacts on thin filament regulation.

The first step in muscle activation is the calcium-induced change in the positioning of tropomyosin along the thin filament, moving it from the blocked to the closed state. The equilibrium constant that defines this transition, K_B, was calculated by measuring the rate of myosin binding to reconstituted thin filaments containing pyrene-labeled actin at high and low calcium concentrations[42, 45]. The pyrene fluorescence is quenched upon myosin binding, and the rate of myosin binding to the thin filament can be calculated by fitting an exponential function to

the fluorescence transient **(Figure 4B).** In $TNNT2^{WT}$, the rate of binding at high calcium (pCa 4) is faster than at low calcium (pCa 9) since the blocked state is scarcely populated at high calcium. While the fluorescence transients collected at high calcium are similar for the $TNNT2^{WT}$ and $TNNT2^{R94C}$, at low calcium, $TNNT2^{R94C}$ binds faster than the $TNNT2^{WT}$, consistent with less inhibition at low calcium in $TNNT2^{R49C}$. Consistent with this notion, we found that K_B for $TNNT2^{R94C}$ (0.67 $\pm$ 0.17) is significantly larger than K_B for the WT (0.40 $\pm$ 0.15; P = 0.04). This result demonstrates that the inhibitory blocked state is less populated in $TNNT2^{R94C}$ at low calcium compared to the $TNNT2^{WT}$. This loss of inhibition at low calcium would lead to hypercontractility (i.e., increased population of force-generating states) and create a predisposition toward myocardial stiffness and ultimately diastolic dysfunction.

Next, we examined the effects of $TNNT2^{R94C}$ on the closed, open, and myosin-bound states of the thin filament (**Figure 4A**) by performing steady-state titrations of myosin binding to reconstituted pyrene-labeled thin filaments at high (pCa 3), low (2 mM EGTA), and intermediate calcium concentrations (pCa 6.25)[42, 45](**Figure 4C-D**). Qualitatively, the myosin binding isotherms for the $TNNT2^{WT}$ and $TNNT2^{R94C}$ thin filaments are similar at high and intermediate calcium concentrations; however, at low calcium, myosin binding to $TNNT2^{R94C}$ thin filaments is increased at low myosin concentrations compared to $TNNT2^{WT}$. These findings are consistent with the stopped flow data showing less inhibition to myosin binding at low calcium. Fitting of the data (see Supplement for details) demonstrates that $TNNT2^{R94C}$ has an increased equilibrium constant for myosin weak binding, K_W (0.20 -0.03/+0.16 for $TNNT2^{R94C}$ vs. 0.13 -0.01/+0.01 for the WT; P=0.002). The variant does not significantly change the equilibrium constant between the closed and open states. This includes K_T, (0.11 [-0.08, 0.12] for $TNNT2^{R94C}$ vs 0.06 [-0.03, 0.06] for the WT at low calcium, P=0.43; 0.07 [-0.04, 0.05] for $TNNT2^{R94C}$ vs 0.08 [-0.04, 0.04] for the WT at intermediate calcium, P=0.45; and 0.14 [-0.08, 0.09] for $TNNT2^{R94C}$ vs 0.18 [-0.07, 0.08] for the WT at high calcium, P=0.37). Further, the cooperativity of activation was unchanged between

$TNNT2^{R94C}$ vs. $TNNT2^{WT}$, *n* (4.47 [-1.66, 2.18] for $TNNT2^{R94C}$ vs. $TNNT2^{WT}$, *P*=0.18). These results are summarized in **Figure 5A-B**.

Computational modeling reveals hypercontractility in $TNNT2^{R94C}$

These biochemical experiments identified the primary effects of $TNNT2^{R94C}$ on thin filament regulation as 2-fold increases in the values for both K_B and K_W. Computational modeling was used to predict how these changes in the equilibrium constants would affect the force-calcium curve in cardiac muscle[47]. The modeling demonstrates a shift in the force-pCa curve for $TNNT2^{R94C}$ towards submaximal calcium activation compared to $TNNT2^{WT}$, consistent with molecular hypercontractility. The model also predicts that even at resting calcium concentrations (100-150 nM[50, 51]), there could be some basal level of activation with $TNNT2^{R94C}$ (**Figure 5C**). Taken together, these data demonstrate that $TNNT2^{R94C}$ would yield less calcium-induced inhibition to contraction, leading to hypercontractility and potentially an increase in basal muscle tension. These contractile defects could lead to diastolic dysfunction culminating in restrictive cardiac physiology.

4.3 Discussion

Spectrum of cardiomyopathy phenotypic presentation

Recent advances in high throughput sequencing have facilitated the identification of a number of novel cardiomyopathy-associated genes, with the number identified as pathogenic increasing significantly over the last few years[9]. Due to the increased utilization of this technology, it is now possible to identify shared genetic variants among phenotypically dissimilar individuals, whose clinical presentations have not previously been associated with specific genes[52]. This has increased understanding of the role of genetic variants in the predisposing pathophysiologic mechanisms of atypical forms of cardiomyopathy[53]. Here, we describe a variant associated with relatively mild hypertrophy and clear evidence of restrictive physiology consistent with RCM. It is

well established that cardiomyopathic diseases, including RCM, have variable expressivity of disease frequently yielding a wide spectrum of phenotypes[54, 55]. This study is supportive of these previous findings.

We report a family in which a single variant in *TNNT2* is associated with restrictive cardiomyopathy and sudden cardiac death. The TNNT2-R94C variant was not observed in control populations and was predicted to be deleterious by *in silico* modeling, ClinVar, and by current ACMG guidelines. Our biochemical data show a clear molecular phenotype that would be consistent with hypercontractility and diastolic dysfunction supporting the concept that this variant is causative for the disease. There are a total of five prior reports of the TNNT2-R94C variant (NCBI ClinVar database), all with the designation of "pathogenic" or "likely pathogenic" and associated with familial HCM[13, 56-59]. There has only been one prior report of a *TNNT2* variant causing restrictive physiology via autosomal dominant inheritance[13]. While the TNNT2-R94C variant has been previously associated with HCM, the spectrum of phenotypic features associated with TNNT2-R94C, including RCM, has not been well described.

Contractile defects caused by the R94C variant

Overall, the clinical phenotype of RCM consists of severe diastolic dysfunction leading to atrial enlargement and, at most, mild ventricular hypertrophy. The molecular mechanisms of contractile defects causing diastolic disease remain largely unknown. Reflecting this, genetic causes of pediatric RCM cases remain unexplained with only rare patients hosting variants within the thin filament. Here, we put forward TNNT2-R94C, as likely causative of disease. TNNT2 is part of the troponin complex that regulates the calcium-dependent interactions between the molecular motor myosin and the thin filament. R94 is located in the highly conserved region of the TNNT2 N-terminal segment, and it is located near other residues that have been associated with other forms of cardiomyopathy, such as R92[60-65]. Currently, there is no high-resolution molecular structure of the thin filament or this region of TNNT2, so it is not possible to determine

the exact structural basis of the biophysical changes that we see; however, it has been proposed that this region plays an important role in mediating the interaction between tropomyosin and the troponin complex. HCM variants in this region have been associated with reduced affinity of troponin for tropomyosin[66, 67], leading to the proposal that variant-induced changes in this affinity could reduce the ability of troponin to regulate the interactions between myosin and the thin filament[66]. Our data, showing destabilization of the blocked state, would be consistent with this concept.

Prior analyses of the biochemical effects of HCM-associated TNNT2 mutations at the R94 position have demonstrated that appropriate calcium regulation is critical to normal function of the troponin complex[18, 19]. Based on these findings, calcium sensitization is hypothesized to have a direct impact on cardiac systolic function with calcium desensitization likely leading to decreased systolic function, and calcium sensitization likely leading to increased systolic function. The described R94C variant is novel in that it produces a clinical phenotype of RCM and primarily diastolic dysfunction, making it an optimal variant for biochemical studies to investigate the interaction between calcium sensitivity and diastolic dysfunction.

Our computational modeling predicts that the R94C variant will lead to submaximal calcium activation and possibly an increase in the basal tension during diastole. Previous studies of many hypertrophic cardiomyopathy variants have demonstrated similar shifts towards submaximal calcium activation, leading to the proposal that these variants cause net hypercontractility and diastolic dysfunction. The phenotype seen in the R94C patients, consisting of a primarily restrictive phenotype with mild hypertrophy would be consistent with this hypothesis.

Limitations

While we illustrate a novel genetic cause of RCM, our findings are based around a single family and may limit study generalizability. Our classification of this variant as causative for the disease is supported by our biochemical studies demonstrating that the introduction of this single

point variant alone causes hypercontractility and features of diastolic dysfunction at the molecular scale. Further studies are warranted to determine how the findings presented here translate to the cellular and organ levels; however, our study clearly identifies the initial lesion that leads to downstream changes with the disease progression. Clinical genetic testing for patients with cardiomyopathic disease is routinely limited to genes of the sarcomere and metabolism which are known causes of cardiomyopathy. It is possible that another variant or variants may be contributing to the severe phenotype observed in the family. This is unlikely considering the results of our biochemical experiments clearly demonstrate a pathologic mechanism of disease.

Moreover, caution should be used when extrapolating the results here to the disease progression seen in human patients. Our biochemical experiments and modeling were performed using all mutant troponin; however, most patients with the disease are heterozygous for the variant, and the exact proportion of protein that is expressed and incorporated into the sarcomere can vary with the variant. Moreover, as the disease progresses, there are changes in gene expression, fibrosis, and cellular organization that occur over the course of years. While our modeling cannot capture the full complexity of the disease progression, it clearly demonstrates the initial contractile defects that lead to the disease phenotype. Future studies will be needed to identify the connection between the initial defect and the disease phenotype seen in patients in the later stages of the disease.

4.4 Conclusions

The R94C variant in TNNT2 is a novel genetic cause of RCM occurring in a conserved domain which causes dysfunction of calcium-based regulation of cardiac contraction and likely yields significant myocardial diastolic dysfunction. This variant, when compared to control cohorts, has a high likelihood of producing a malignant phenotype. Furthermore, this work demonstrates the power of using *in vitro* biochemical studies as well as computational modeling to support disease causality.

4.5 Methods

The data that support the findings of this study are available from the corresponding author upon reasonable request.

Clinical Evaluation

This study received approval from the Institutional Review Boards at Baylor College of Medicine and Duke University Health System. Available clinical data from the identified proband and relatives were collected, which included pertinent personal and family history, physical examination, standard 12-lead electrocardiogram (ECG) analysis, echocardiographic testing, cardiac catheterization data, and genetic testing. An autopsy was performed on the brother of the proband by the Medical Examiner Service of the Harris County, Texas Institute of Forensic Sciences (Houston, Texas) following his death. The family underwent a full evaluation by pediatric cardiomyopathy and heart failure specialists.

Genetic Analysis

The proband underwent clinical genetic testing using the Familion (New Haven, CT) hypertrophic cardiomyopathy panel test which involves sequencing 9 sarcomeric genes (*ACTC, MYBPC3, MYH7, MYL2, MYL3, TNNT2, TNNI3, TNNC1, and TPM1)* and 3 metabolic genes (*GLA*, *LAMP2*, and *PRKAG2*). Clinical genetic testing was performed on family members using the same hypertrophic cardiomyopathy panel test. Subsequently, Sanger Sequencing was utilized for confirmatory testing. For this, genomic DNA was isolated using Gentra Puregene Blood Kit (Qiagen, Valencia, CA) from peripheral whole blood as well as post-mortem blood spot. To confirm the absence of the identified presumed pathogenic variant in ostensibly healthy individuals, the publicly-available Genome Aggregation Database (gnomAD) was used as a control cohort which is comprised of a total of 15,708 genomes and 125,748 exomes from 141,456

individuals.[20] Though the gnomAD database is comprised partly of various disease-specific cohorts in addition to population genetics studies, it excludes individuals known to have severe pediatric disease or severe disease in their first-degree relatives. These individuals were therefore utilized as "control" or "reference" alleles. Variant pathogenicity classification was also assigned based on 2015 American College of Medical Genetics (ACMG) Criteria[21] and ClinVar (National Center for Biotechnology Information)[22].

Sequencing Conservation

Sequence conservation analysis was performed using the primary TNNT2 sequence obtained from the National Center for Biotechnology Information (NP_001001430.1)[23]. Multalign alignment algorithms were utilized to determine sequence conservation across species[24, 25].

In Silico Variant Pathogenicity Modeling

In silico variant pathogenicity prediction was performed using GenMAPP[26], PolyPhen-2[27], PredictSNP[28], SIFT[29], SNAP[30], and PANTHER[31] prediction tools. Variants were considered pathogenic if they carried the designation of "damaging or probably damaging," "deleterious," "disease-related," and/or "disease-associated." Variants were considered benign if they carried designation of "tolerated," "benign," or "neutral."

Purification of Cardiac Myosin and Actin

Porcine cardiac ventricular myosin and actin were purified from cryoground tissue as previously described[32-34]. Myosin subfragment 1 (S1) was prepared by chymotrypsic digestion as previously described[32], using standard techniques[35, 36], and the purity of the protein was assessed by SDS-PAGE. The concentration of myosin S1 was determined by absorbance at 280 and 320 nm. Pyrene-labeled actin was prepared from acetone powder[37] and labeled with the dye N-(1-pyrenyl)iodoacetamide (pyrene) as described previously[38, 39]. The concentration of pyrene actin

was determined by absorbance at 290 and 344 nm. Before use, all actin was stabilized by incubating with equimolar concentrations of phalloidin.

Preparation of Recombinant Human Troponin and Tropomyosin

Human cardiac tropomyosin was expressed in BL21-CodonPlus cells (Agilent) and purified using established protocols[33, 40-42]. On the day of the experiment, tropomyosin was reduced in 50 mM DTT at 56 °C for 5 minutes and aggregates were subsequently removed by ultracentrifugation at 436000 x g in an Optima MAX-TL Ultracentrifuge (Beckman Coulter)[43]. The R94C variant was introduced into *TNNT2* using the QuickChange Site-Directed Mutagenesis kid (Agilent). Human troponins I, T, and C were expressed in BL21-CodonPlus cells (Agilent), purified, and complexed using established protocols[44].

Determination of K_B Using Stopped Flow Transient Kinetics

To determine the equilibrium constant between the blocked and closed states, K_B, a stopped flow approach developed by McKillop and Geeves[42, 45] was utilized. This method analyzes the rate of myosin binding to reconstituted thin filaments in the presence and absence of calcium. Pyrene-actin was excited at 365 nm and fluorescence emission was detected using a 390 nm long-pass filter. Reconstituted thin filaments (5 µM phalloidin-stabilized pyrene actin, 2 µM tropomyosin, 2 µM troponin) and 0.04 U/mL apyrase were rapidly mixed with 0.5 µM S1 myosin and 0.04 U/mL apyrase at 20 °C in an SX-20 stopped flow apparatus (Applied Photophysics). The high calcium (pCa 4) buffer contained 200 mM KCl, 5mM $MgCl_2$, 60 mM MOPS, 2 mM EGTA, 1mM DTT, and 2.15 mM $CaCl_2$. The low calcium (pCa 9) buffer contained 200 mM KCl, 5mM $MgCl_2$, 60 mM MOPS, 2 mM EGTA, 1 mM DTT and 5.2 µM $CaCl_2$. Myosin strong binding to pyrene-labeled actin in reconstituted thin filaments quenches the pyrene fluorescence. Fluorescence transients were collected for at least 3 separate mixes, and a single

exponential function was fit to the transient. K_B is calculated from the ratio of the rates of myosin binding to the reconstituted thin filaments at high and low calcium [45]:

$$\frac{k_{obs}(-Ca^{2+})}{k_{obs}(+Ca^{2+})} \approx \frac{K_B}{1+K_B} \quad (Equation\ 1)$$

The average K_B was calculated from three different experiments and the *P*-value was calculated from a 2-tailed Student's t-test.

Determination of K_W, K_T, and n from fluorescence titrations

The values of the equilibrium constant between the open and weakly-bound myosin states, K_W, the equilibrium constant between the closed and open states K_T, and the size of the cooperative unit (i.e., the number of binding sites on the thin filament opened by myosin binding), *n,* were determined by measuring the steady-state binding of myosin to pyrene-labeled regulated thin filaments [45]. Fluorescence titrations were carried out at 20 °C in an Applied Photophysics SX-20. Myosin S1 was added at 1-minute intervals to a stirred cuvette containing 0.5 μM pyrene-actin, 0.27 μM troponin and tropomyosin up to a final concentration of 10 μM S1. The buffers contained 200 mM KCl, 5 mM free $MgCl_2$, 60 mM MOPS, 2 mM EGTA, 1 mM DTT, 2 mM ADP, and the desired free concentration of free calcium. Any contaminating ATP was eliminated by adding 50 μM P1,P5-di(adenosine-5')pentaphosphate (Ap5A), 2 mM glucose, and 1 μM hexokinase. Titrations were performed at 3 calcium concentrations: low (2 mM EGTA), intermediate (pCa 6.25), and high (pCa 3). Five technical replicates were performed. Data were analyzed as previously described[32].

To quantify differences in myosin binding of the WT and mutant proteins, titration curves were fit to the fractional change in the fluorescence, a, as a function of myosin, [M], given by:

$$a = \frac{F_0 - F}{F_0 - F_\infty} = \frac{K_W[M]P^{n-1}(K_T(1+K_S)^n + 1)}{(K_T P^n + Q^n + \frac{1}{K_B})(1+K_S)^{n-1}} \quad (Eq.2)$$

where F is the measured fluorescence, F_0 is the fluorescence of the pyrene in the absence of myosin binding, F_∞ is the fluorescence at saturating myosin concentrations, n is the size of the cooperative unit, $P=1+K_W[M](1+K_S)$, and $Q=1+K_W[M]$[45]. For the fitting, the equilibrium constant between the closed and open states (K_T), the equilibrium constant between the open and myosin weakly-bound state (K_W), and n were fitted parameters. Titration curves were globally fit to extract parameter values, 95% confidence intervals by bootstrapping simulations, and P-values were determined as described[42]. K_B was fixed based on stopped flow experiments. The equilibrium constant between the states in which myosin is weakly and strongly bound to the thin filament (K_S) was fixed based on previous studies[46].

Computational Modeling of the Variants on Thin Filament Regulation

To quantitatively model the impacts of the variant on overall calcium-force production relationship in the heart, we utilized a computational model developed by the McCulloch lab which uses the measured equilibrium constants to calculate the expected force per sarcomere as a function of calcium[47]. Model parameters for the mutant protein were adjusted to be proportional to our measured parameters and we used these parameters to simulate a force-calcium curve. For the WT protein, we used the default model parameters.

Statistical Analysis

A Student's t-test was performed to determine statistical significance between two groups. A p-value < 0.05 was considered significant unless otherwise noted.

Acknowledgements:

We acknowledge Lina Greenberg for technical support in generating and purifying the mutant proteins.

Sources of Funding:

J.E.E. is supported by the NIH Clinical and Translational Science Award (UL1TR00255).

S.R.C is supported by the NIH (T32EB018266).

M.J.G is supported by the NIH (R01HL141086), the March of Dimes Foundation (FY18-BOC-430198), and the Children's Discovery Institute of Washington University and St. Louis Children's Hospital (PM-LI-2019-829),

A.P.L is supported by the Phoebe Muzzy-McCrae Foundation and Duke University School of Medicine.

Conflict of Interest Disclosures

The authors declare no conflicts of interest.

4.6 Figures

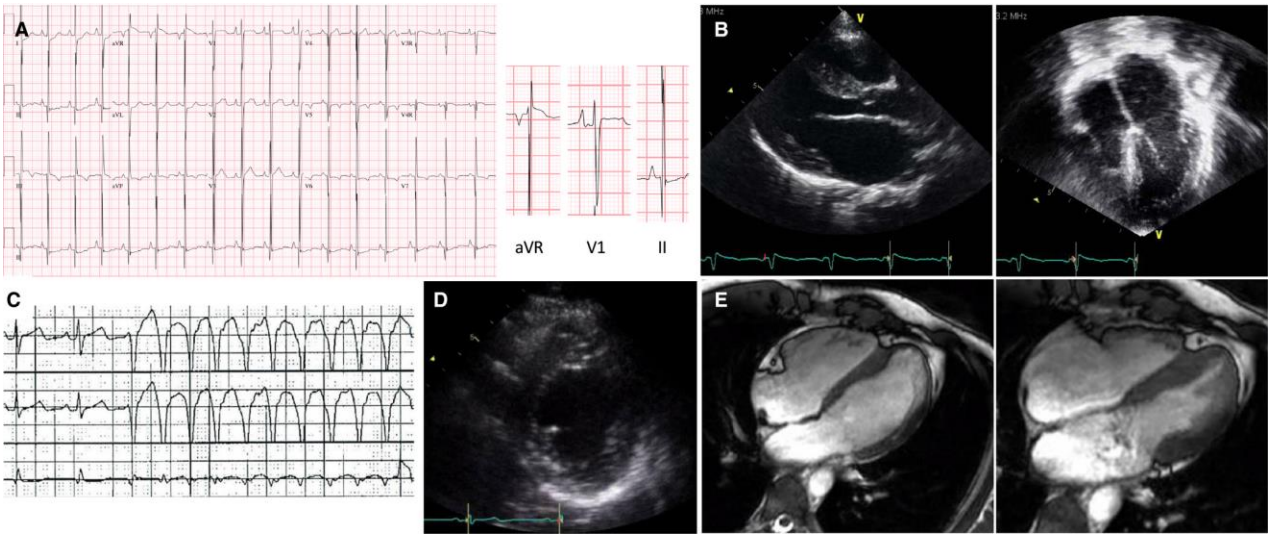

Figure 1. Clinical evaluation of TNNT2-R94C positive kindred. A) Representative ECG obtained from the proband demonstrating right and left atrial enlargement with nonspecific ST and T wave abnormalities and ST depression in the inferolateral leads. An enlarged representative ECG is shown. B) Representative echocardiographic images in the parasternal long axis and apical 4-chamber windows demonstrating severe left atrial enlargement. C) Cardiac telemetry demonstrating ventricular tachycardia overtaking sinus rhythm. D). Representative echocardiographic images

from the father of the proband in the parasternal short axis view demonstrating normal LV size and systolic function. E) Representative cardiac MRI images demonstrating right and left atrial enlargement with normal biventricular size and function. TNNT2, TNNT2-encoded cardiac troponin T; ECG, electrocardiogram; LV, left ventricular; MRI, magnetic resonance imaging.

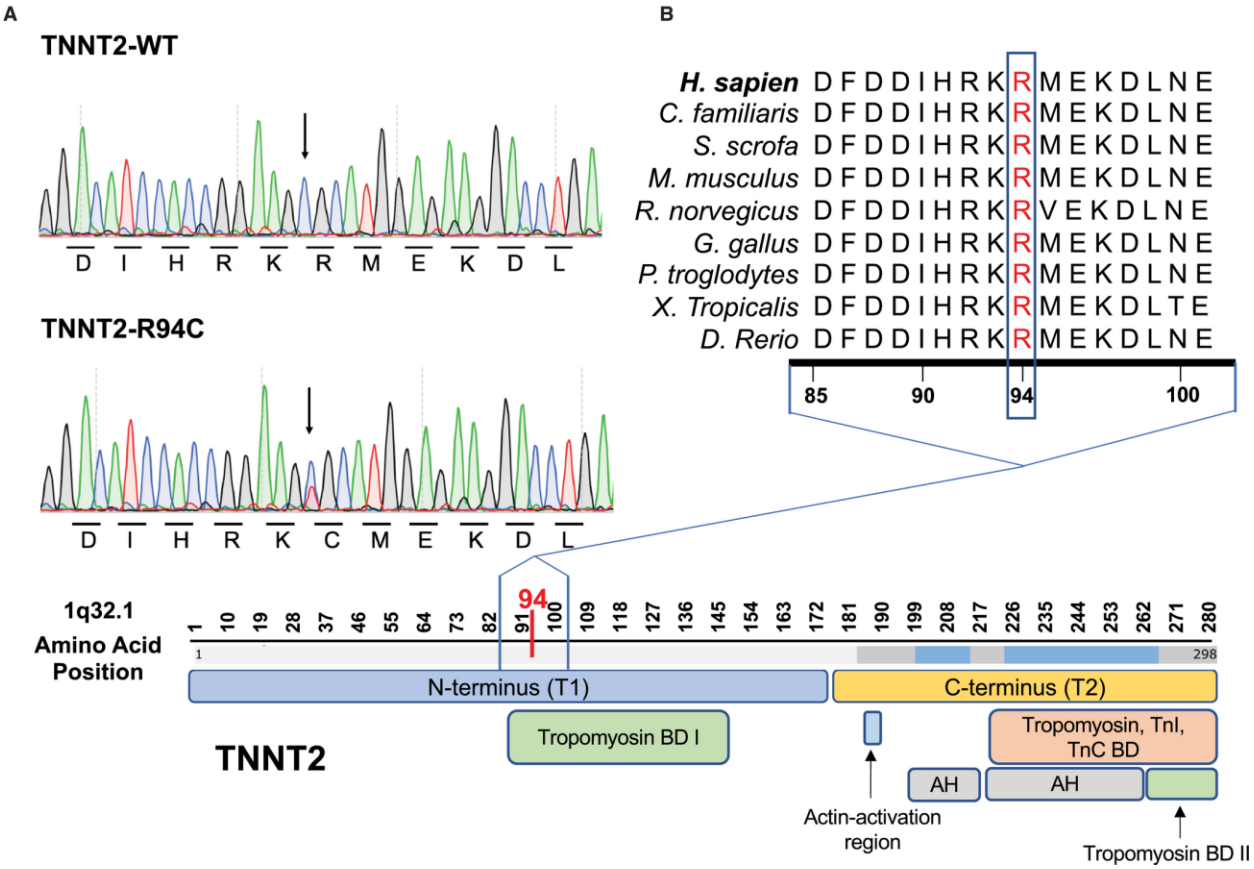

Figure 2. R94C localizes to a highly conserved region of TNNT2. A) Sanger sequencing chromatograms of heterozygous mutant TNNT2-R94C (obtained from subject III-3) and wild-type genotypes. B). The topological map of TNNT2 with primary sequence alignment from multiple divergent species are shown. The variant localizes to the N-terminal segment of TNNT2 in the tropomyosin binding domain I. This region is highly conserved across species. TNNT2, TNNT2-encoded cardiac troponin T; Tm, Tropomyosin; TnI, troponin I; TnC, troponin C; BD, binding domain; AH, actin helix

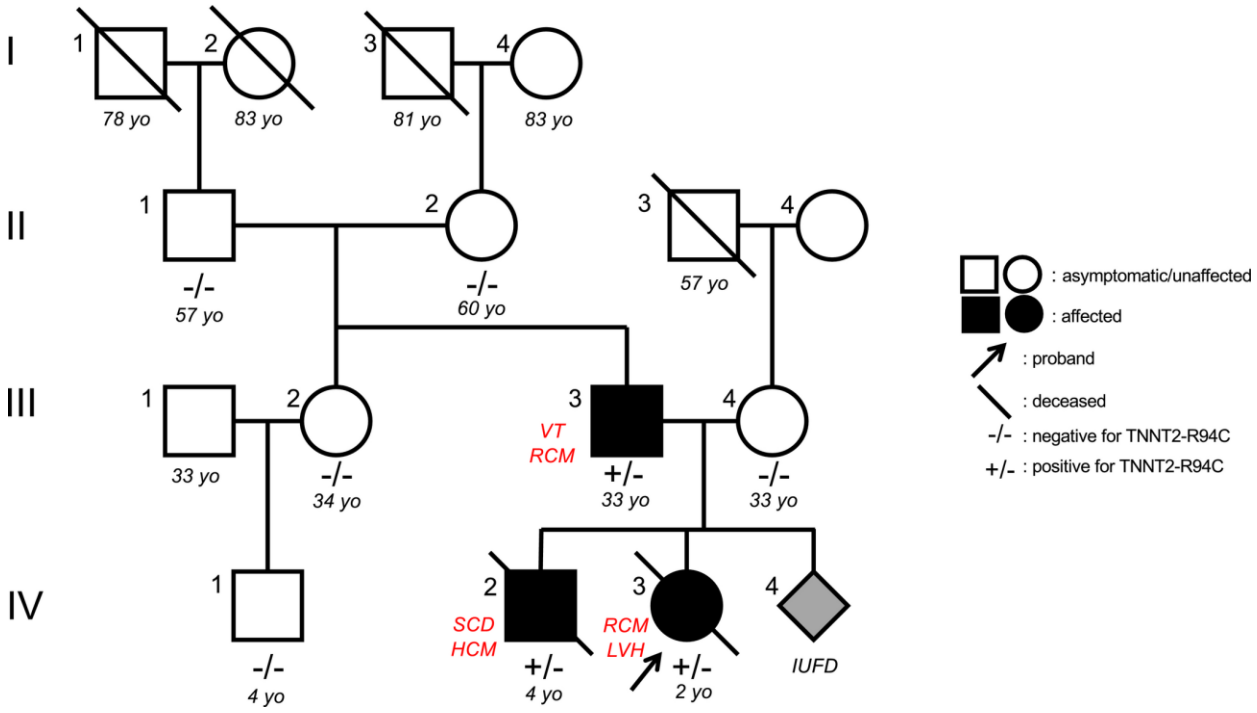

Figure 3. Pedigree of TNNT-R94C kindred. Four generations were evaluated (denoted by Roman numerals). The clinical presentations are noted in red. The predominant phenotype is a RCM with mild hypertrophic features. Arrow denotes the proband (IV.4). Circles denote female and squares denote male. Black fill denotes diagnosis of cardiomyopathy. Gray fill denotes fetal demise (IUFD). White fill denotes no cardiac diagnosis either following clinical evaluation or by reported history. +/- denotes heterozygosity for TNNT2-R94C variant while -/- denotes wild-type. Diagonal line denotes deceased. TNNT2, TNNT2-encoded cardiac troponin T; VT, ventricular tachycardia; RCM, restrictive cardiomyopathy; SCD, sudden cardiac death; LVH, left ventricular hypertrophy; IUFD, intrauterine fetal demise

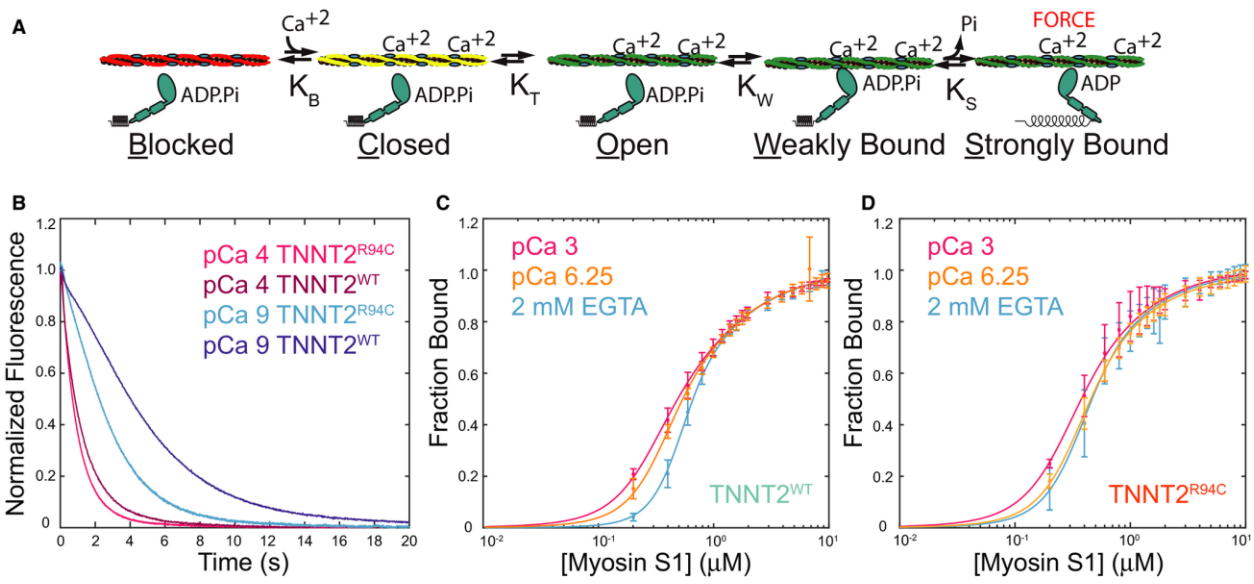

Figure 4: *Measurement of the biochemical steps involved in thin filament activation. A)* Kinetic scheme for thin filament activation. Tropomyosin lies along the thin filament in 3 positions, blocked (red), closed (yellow), and open (green). The positioning of the tropomyosin depends both on calcium and myosin binding. Myosin binds weakly to the thin filament before undergoing an isomerization to the strong-binding state, where force is generated. B) Measurement of K_B, the equilibrium constant between the blocked and closed states, was measured by rapidly mixing myosin with pyrene-labeled thin filaments at low (pCa 9) and high calcium (pCa 4). Myosin binding quenches the fluorescence. The ratio of the rates of binding in at high and low calcium can be used to calculate K_B (see Methods). There is significantly less blocking in the R94C mutant than the WT at low calcium, as evidenced by the faster binding of the mutant at low calcium. C-D) Equilibrium titrations of myosin with pyrene-labeled regulated thin filaments enables the calculation of several equilibrium constants (see Methods). Experiments were conducted with thin filaments containing either C) $TNNT2^{WT}$ and D) $TNNT2^{R94C}$. TNNT2, TNNT2-encoded cardiac troponin T

A

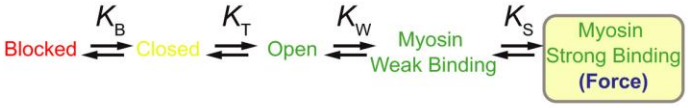

B

	WT	R94C	p
K_B	0.40 (-0.15/+0.15)	0.67 (-0.17/+0.17)	0.037
K_W	0.13 (-0.01/+0.01)	0.20 (-0.03/+0.16)	0.002
K_T 2mM EGTA	0.06 (-0.03/+0.06)	0.11 (-0.08/+0.12)	0.43
K_T pCa 6.25	0.08 (-0.04/+0.04)	0.07 (-0.04/+0.05)	0.45
K_T pCa 3	0.18 (-0.07/+0.08)	0.14 (-0.08/+0.09)	0.37
n	5.97 (-0.95/+1.23)	4.47 (-1.66/+2.18)	0.18

C

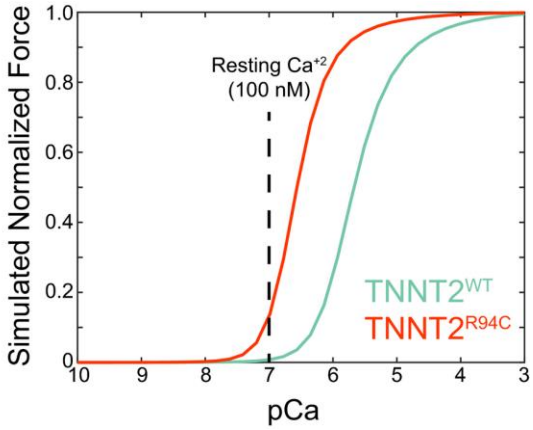

Figure 5: A) Simplified kinetic scheme for thin filament activation. B) Equilibrium constants measured for the thin filaments containing TNNT2^{WT} and TNNT2^{R94C}. The mutant causes statistically significant increases in K_B and K_W. C) Computational modeling of the effects of the variant on the force-calcium relationship. The variant causes a leftward shift in the curve, signifying hypercontractility at lower calcium and a basal level of tension, even at resting calcium concentrations. TNNT2, TNNT2-encoded cardiac troponin T; K_B, the equilibrium constant between the blocked and closed states; K_W, the equilibrium constant between the closed and open states.

Table 1: In silico variant prediction aggregate analysis of the TNNT2 Arg94Cys variant using variant prediction models.

Tool	Algorithm	Clinical Significance	Confidence (%)
GenMAPP	Pathway analysis tool	Deleterious	72%
PolyPhen-2	Naïve Bayes classification	Deleterious	81%
PredictSNP	Metaserver	Deleterious	76%
SIFT	Sequence conservation	Deleterious	79%
SNAP	Neural networks	Neutral	50%
PANTHER	Ontology association	Deleterious	65%

GenMAPP, Gene Map Annotator and Pathway Profiler; PolyPhen-2, Polymorphism Phenotyping v2; SIFT, Sorting Intolerant from Tolerant; PANTHER, Protein Analysis Through Evolutionary Relationships.

4.7 References

- 1. Elliott P, Andersson B, Arbustini E, Bilinska Z, Cecchi F, Charron P, Dubourg O, Kuhl U, Maisch B, McKenna WJ, Monserrat L, Pankuweit S, Rapezzi C, Seferovic P, Tavazzi L and Keren A. Classification of the cardiomyopathies: a position statement from the European Society Of Cardiology Working Group on Myocardial and Pericardial Diseases. *Eur Heart J*. 2008;29:270-6.
- 2. Anderson HN, Cetta F, Driscoll DJ, Olson TM, Ackerman MJ and Johnson JN. Idiopathic Restrictive Cardiomyopathy in Children and Young Adults. *Am J Cardiol*. 2018;121:1266-1270.
- 3. Cetta F, O'Leary PW, Seward JB and Driscoll DJ. Idiopathic restrictive cardiomyopathy in childhood: diagnostic features and clinical course. *Mayo Clin Proc*. 1995;70:634-40.
- 4. Harvey PA and Leinwand LA. The cell biology of disease: cellular mechanisms of cardiomyopathy. *J Cell Biol*. 2011;194:355-65.
- 5. Maron BJ, Haas TS, Ahluwalia A, Murphy CJ and Garberich RF. Demographics and Epidemiology of Sudden Deaths in Young Competitive Athletes: From the United States National Registry. *Am J Med*. 2016;129:1170-1177.
- 6. Maron MS, Hellawell JL, Lucove JC, Farzaneh-Far R and Olivotto I. Occurrence of Clinically Diagnosed Hypertrophic Cardiomyopathy in the United States. *Am J Cardiol*. 2016;117:1651-1654.
- 7. Van Driest SL, Ommen SR, Tajik AJ, Gersh BJ and Ackerman MJ. Sarcomeric Genotyping in Hypertrophic Cardiomyopathy. *Mayo Clinic Proceedings*. 2005;80:463-469.
- 8. Watkins H, Ashrafian H and Redwood C. Inherited Cardiomyopathies. *New England Journal of Medicine*. 2011;364:1643-1656.
- 9. Sabater-Molina M, Perez-Sanchez I, Hernandez Del Rincon JP and Gimeno JR. Genetics of hypertrophic cardiomyopathy: A review of current state. *Clin Genet*. 2018;93:3-14.
- 10. Wang L, Kim K, Parikh S, Cadar AG, Bersell KR, He H, Pinto JR, Kryshtal DO and Knollmann BC. Hypertrophic cardiomyopathy-linked mutation in troponin T causes myofibrillar disarray and pro-arrhythmic action potential changes in human iPSC cardiomyocytes. *J Mol Cell Cardiol*. 2018;114:320-327.
- 11. Wang L, Kryshtal DO, Kim K, Parikh S, Cadar AG, Bersell KR, He H, Pinto JR and Knollmann BC. Myofilament Calcium-Buffering Dependent Action Potential Triangulation in Human-Induced Pluripotent Stem Cell Model of Hypertrophic Cardiomyopathy. *Journal of the American College of Cardiology*. 2017;70:2600-2602.
- 12. Baudenbacher F, Schober T, Renato Pinto J, Sidorov VY, Hilliard F, Solaro RJ, Potter JD and Knollmann BC. Myofilament Ca2+ sensitization causes susceptibility to cardiac arrhythmia in mice. *Journal of Clinical Investigation*. 2008;118.
- 13. Varnava A, Baboonian C, Davison F, de Cruz L, Elliott PM, Davies MJ and McKenna WJ. A new mutation of the cardiac troponin T gene causing familial hypertrophic cardiomyopathy without left ventricular hypertrophy. *Heart*. 1999;82:621-624.
- 14. Parvatiyar MS and Pinto JR. Pathogenesis associated with a restrictive cardiomyopathy mutant in cardiac troponin T is due to reduced protein stability and

greatly increased myofilament Ca2+ sensitivity. *Biochim Biophys Acta*. 2015;1850:365-72.
- 15. Kaski JP, Syrris P, Burch M, Tome-Esteban MT, Fenton M, Christiansen M, Andersen PS, Sebire N, Ashworth M, Deanfield JE, McKenna WJ and Elliott PM. Idiopathic restrictive cardiomyopathy in children is caused by mutations in cardiac sarcomere protein genes. *Heart*. 2008;94:1478-84.
- 16. Gallego-Delgado M, Delgado JF, Brossa-Loidi V, Palomo J, Marzoa-Rivas R, Perez-Villa F, Salazar-Mendiguchia J, Ruiz-Cano MJ, Gonzalez-Lopez E, Padron-Barthe L, Bornstein B, Alonso-Pulpon L and Garcia-Pavia P. Idiopathic Restrictive Cardiomyopathy Is Primarily a Genetic Disease. *J Am Coll Cardiol*. 2016;67:3021-3.
- 17. Menon SC, Michels VV, Pellikka PA, Ballew JD, Karst ML, Herron KJ, Nelson SM, Rodeheffer RJ and Olson TM. Cardiac troponin T mutation in familial cardiomyopathy with variable remodeling and restrictive physiology. *Clin Genet*. 2008;74:445-54.
- 18. Lu QW, Morimoto S, Harada K, Du CK, Takahashi-Yanaga F, Miwa Y, Sasaguri T and Ohtsuki I. Cardiac troponin T mutation R141W found in dilated cardiomyopathy stabilizes the troponin T-tropomyosin interaction and causes a Ca2+ desensitization. *J Mol Cell Cardiol*. 2003;35:1421-7.
- 19. Mickelson AV and Chandra M. Hypertrophic cardiomyopathy mutation in cardiac troponin T (R95H) attenuates length-dependent activation in guinea pig cardiac muscle fibers. *Am J Physiol Heart Circ Physiol*. 2017;313:H1180-H1189.
- 20. Lek M, Karczewski KJ, Minikel EV, Samocha KE, Banks E, Fennell T, O'Donnell-Luria AH, Ware JS, Hill AJ, Cummings BB, Tukiainen T, Birnbaum DP, Kosmicki JA, Duncan LE, Estrada K, Zhao F, Zou J, Pierce-Hoffman E, Berghout J, Cooper DN, Deflaux N, DePristo M, Do R, Flannick J, Fromer M, Gauthier L, Goldstein J, Gupta N, Howrigan D, Kiezun A, Kurki MI, Moonshine AL, Natarajan P, Orozco L, Peloso GM, Poplin R, Rivas MA, Ruano-Rubio V, Rose SA, Ruderfer DM, Shakir K, Stenson PD, Stevens C, Thomas BP, Tiao G, Tusie-Luna MT, Weisburd B, Won HH, Yu D, Altshuler DM, Ardissino D, Boehnke M, Danesh J, Donnelly S, Elosua R, Florez JC, Gabriel SB, Getz G, Glatt SJ, Hultman CM, Kathiresan S, Laakso M, McCarroll S, McCarthy MI, McGovern D, McPherson R, Neale BM, Palotie A, Purcell SM, Saleheen D, Scharf JM, Sklar P, Sullivan PF, Tuomilehto J, Tsuang MT, Watkins HC, Wilson JG, Daly MJ, MacArthur DG and Exome Aggregation C. Analysis of protein-coding genetic variation in 60,706 humans. *Nature*. 2016;536:285-91.
- 21. Richards S, Aziz N, Bale S, Bick D, Das S, Gastier-Foster J, Grody WW, Hegde M, Lyon E, Spector E, Voelkerding K, Rehm HL and Committee ALQA. Standards and guidelines for the interpretation of sequence variants: a joint consensus recommendation of the American College of Medical Genetics and Genomics and the Association for Molecular Pathology. *Genet Med*. 2015;17:405-24.
- 22. Landrum MJ, Lee JM, Benson M, Brown GR, Chao C, Chitipiralla S, Gu B, Hart J, Hoffman D, Jang W, Karapetyan K, Katz K, Liu C, Maddipatla Z, Malheiro A, McDaniel K, Ovetsky M, Riley G, Zhou G, Holmes JB, Kattman BL and Maglott DR. ClinVar: improving access to variant interpretations and supporting evidence. *Nucleic Acids Res*. 2018;46:D1062-D1067.
- 23. NCBI. troponin T, cardiac muscle isoform 2 [Homo sapiens]. 2019:NCBI Reference Sequence: NP_001001430.1.

- 24. Corpet F. Multiple sequence alignment with heirarchical clustering. *Nucleic Acids Res*. 1988;16.
- 25. Corpet F, Gouzy J and Kahn D. Browsing protein families via the 'Rich Family Description' format. *Bioinformatics*. 1999;15:1020-1027.
- 26. Kam D. Dahlquist NS and Karen Vranizan SCL, Bruce R. Conklin. GenMAPP, a new tool for viewing and analyzing microarray data on biological pathways. *Nature Genetics*. 2002;31:19-20.
- 27. Adzhubei IA, Schmidt S, Peshkin L, Ramensky VE, Gerasimova A, Bork P, Kondrashov AS and Sunyaev SR. A method and server for predicting damaging missense mutations. *Nat Methods*. 2010;7:248-9.
- 28. Bendl J, Stourac J, Salanda O, Pavelka A, Wieben ED, Zendulka J, Brezovsky J and Damborsky J. PredictSNP: robust and accurate consensus classifier for prediction of disease-related mutations. *PLoS Comput Biol*. 2014;10:e1003440.
- 29. Sim NL, Kumar P, Hu J, Henikoff S, Schneider G and Ng PC. SIFT web server: predicting effects of amino acid substitutions on proteins. *Nucleic Acids Res*. 2012;40:W452-7.
- 30. Korf I. Gene finding in novel genomes. *BMC Bioinformatics*. 2004;5.
- 31. Mi H, Muruganujan A, Ebert D, Huang X and Thomas PD. PANTHER version 14: more genomes, a new PANTHER GO-slim and improvements in enrichment analysis tools. *Nucleic Acids Res*. 2019;47:D419-D426.
- 32. Barrick SK, Clippinger SR, Greenberg L and Greenberg MJ. Computational Tool to Study Perturbations in Muscle Regulation and its Application to Heart Disease. *Biorxiv*. 2019.
- 33. Clippinger SR, Cloonan PE, Greenberg L, Ernst M, Stump WT and Greenberg MJ. Disrupted mechanobiology links the molecular and cellular phenotypes in familial dilated cardiomyopathy. *Biorxiv*. 2019.
- 34. Greenberg MJ, Shuman H and Ostap EM. Inherent force-dependent properties of beta-cardiac myosin contribute to the force-velocity relationship of cardiac muscle. *Biophysical journal*. 2014;107:L41-4.
- 35. Eads TM, Thomas DD and Austin RH. Microsecond rotational motions of eosin-labeled myosin measured by time-resolved anisotropy of absorption and phosphorescence. *Journal of molecular biology*. 1984;179:55-81.
- 36. Margossian SS and Lowey S. Preparation of myosin and its subfragments from rabbit skeletal muscle. *Methods in enzymology*. 1982;85 Pt B:55-71.
- 37. Spudich JA and Watt S. The regulation of rabbit skeletal muscle contraction. I. Biochemical studies of the interaction of the tropomyosin-troponin complex with actin and the proteolytic fragments of myosin. *The Journal of biological chemistry*. 1971;246:4866-71.
- 38. Pollard TD. Purification of a high molecular weight actin filament gelation protein from Acanthamoeba that shares antigenic determinants with vertebrate spectrins. *The Journal of cell biology*. 1984;99:1970-80.
- 39. Greenberg MJ, Lin T, Goldman YE, Shuman H and Ostap EM. Myosin IC generates power over a range of loads via a new tension-sensing mechanism. *Proceedings of the National Academy of Sciences of the United States of America*. 2012;109:E2433-40.

- 40. Hitchcock-DeGregori SE and Heald RW. Altered actin and troponin binding of amino-terminal variants of chicken striated muscle alpha-tropomyosin expressed in Escherichia coli. *The Journal of biological chemistry*. 1987;262:9730-5.
- 41. Pan S, Sommese RF, Sallam KI, Nag S, Sutton S, Miller SM, Spudich JA, Ruppel KM and Ashley EA. Establishing disease causality for a novel gene variant in familial dilated cardiomyopathy using a functional in-vitro assay of regulated thin filaments and human cardiac myosin. *BMC Med Genet*. 2015;16:97.
- 42. Barrick SK, Clippinger SR, Greenberg L and Greenberg MJ. Computational Tool to Study Perturbations in Muscle Regulation and Its Application to Heart Disease. *Biophysical journal*. 2019;116:2246-2252.
- 43. McIntosh BB, Holzbaur EL and Ostap EM. Control of the initiation and termination of kinesin-1-driven transport by myosin-Ic and nonmuscle tropomyosin. *Current biology : CB*. 2015;25:523-9.
- 44. Kozaili JM, Leek D and Tobacman LS. Dual regulatory functions of the thin filament revealed by replacement of the troponin I inhibitory peptide with a linker. *The Journal of biological chemistry*. 2010;285:38034-41.
- 45. McKillop DF and Geeves MA. Regulation of the interaction between actin and myosin subfragment 1: evidence for three states of the thin filament. *Biophysical journal*. 1993;65:693-701.
- 46. Maytum R, Westerdorf B, Jaquet K and Geeves MA. Differential regulation of the actomyosin interaction by skeletal and cardiac troponin isoforms. *The Journal of biological chemistry*. 2003;278:6696-701.
- 47. Campbell SG, Lionetti FV, Campbell KS and McCulloch AD. Coupling of adjacent tropomyosins enhances cross-bridge-mediated cooperative activation in a markov model of the cardiac thin filament. *Biophysical journal*. 2010;98:2254-64.
- 48. Colan S. Normal echocardiographic values for cardiovascular structures. In: W. Lai, M. Cohen, T. Geva and L. Mertens, eds. *Echocardiography in Pediatric and Congenital Heart Disease* West Sussex, UK: Wiley-Blackwell; 2009: 765-785.
- 49. Molina DK, Pinneri K, Stash JA, Li L, Vance K and Cross C. Organ Weight Reference Ranges for Ages 0 to 12 Years. *Am J Forensic Med Pathol*. 2019.
- 50. Guatimosim S, Dilly K, Santana LF, Saleet Jafri M, Sobie EA and Lederer WJ. Local Ca(2+) signaling and EC coupling in heart: Ca(2+) sparks and the regulation of the [Ca(2+)](i) transient. *Journal of molecular and cellular cardiology*. 2002;34:941-50.
- 51. Bers DM. Cardiac excitation-contraction coupling. *Nature*. 2002;415:198-205.
- 52. Landstrom AP, Boczek NJ, Ye D, Miyake CY, De la Uz CM, Allen HD, Ackerman MJ and Kim JJ. Novel long QT syndrome-associated missense mutation, L762F, in CACNA1C-encoded L-type calcium channel imparts a slower inactivation tau and increased sustained and window current. *Int J Cardiol*. 2016;220:290-8.
- 53. Connell PS, Jeewa A, Kearney DL, Tunuguntla H, Denfield SW, Allen HD and Landstrom AP. A 14-year-old in heart failure with multiple cardiomyopathy variants illustrates a role for signal-to-noise analysis in gene test re-interpretation. *Clin Case Rep*. 2019;7:211-217.

- 54. Ho CY, Charron P, Richard P, Girolami F, Van Spaendonck-Zwarts KY and Pinto Y. Genetic advances in sarcomeric cardiomyopathies: state of the art. *Cardiovasc Res*. 2015;105:397-408.
- 55. Rindler TN, Hinton RB, Salomonis N and Ware SM. Molecular Characterization of Pediatric Restrictive Cardiomyopathy from Integrative Genomics. *Sci Rep*. 2017;7:39276.
- 56. Lopes LR, Syrris P, Guttmann OP, O'Mahony C, Tang HC, Dalageorgou C, Jenkins S, Hubank M, Monserrat L, McKenna WJ, Plagnol V and Elliott PM. Novel genotype-phenotype associations demonstrated by high-throughput sequencing in patients with hypertrophic cardiomyopathy. *Heart*. 2015;101:294-301.
- 57. Berge KE and Leren TP. Genetics of hypertrophic cardiomyopathy in Norway. *Clin Genet*. 2014;86:355-60.
- 58. Liu W, Liu W, Hu D, Zhu T, Ma Z, Yang J, Xie W, Li C, Li L, Yang J, Li T, Bian H and Tong Q. Mutation spectrum in a large cohort of unrelated Chinese patients with hypertrophic cardiomyopathy. *Am J Cardiol*. 2013;112:585-9.
- 59. Otsuka H, Arimura T, Abe T, Kawai H, Aizawa Y, Kubo T, Kitaoka H, Nakamura H, Nakamura K, Okamoto H, Ichida F, Ayusawa M, Nunoda S, Isobe M, Matsuzaki M, Doi YL, Fukuda K, Sasaoka T, Izumi T, Ashizawa N and Kimura A. Prevalence and Distribution of Sarcomeric Gene Mutations in Japanese Patients With Familial Hypertrophic Cardiomyopathy. *Circulation Journal*. 2012;76:453-461.
- 60. Chandra M, Tschirgi ML and Tardiff JC. Increase in tension-dependent ATP consumption induced by cardiac troponin T mutation. *American journal of physiology Heart and circulatory physiology*. 2005;289:H2112-9.
- 61. Ford SJ, Mamidi R, Jimenez J, Tardiff JC and Chandra M. Effects of R92 mutations in mouse cardiac troponin T are influenced by changes in myosin heavy chain isoform. *Journal of molecular and cellular cardiology*. 2012;53:542-51.
- 62. Robinson P, Mirza M, Knott A, Abdulrazzak H, Willott R, Marston S, Watkins H and Redwood C. Alterations in thin filament regulation induced by a human cardiac troponin T mutant that causes dilated cardiomyopathy are distinct from those induced by troponin T mutants that cause hypertrophic cardiomyopathy. *The Journal of biological chemistry*. 2002;277:40710-6.
- 63. Szczesna D, Zhang R, Zhao J, Jones M, Guzman G and Potter JD. Altered regulation of cardiac muscle contraction by troponin T mutations that cause familial hypertrophic cardiomyopathy. *The Journal of biological chemistry*. 2000;275:624-30.
- 64. Tobacman LS, Lin D, Butters C, Landis C, Back N, Pavlov D and Homsher E. Functional consequences of troponin T mutations found in hypertrophic cardiomyopathy. *The Journal of biological chemistry*. 1999;274:28363-70.
- 65. Williams MR, Lehman SJ, Tardiff JC and Schwartz SD. Atomic resolution probe for allostery in the regulatory thin filament. *Proceedings of the National Academy of Sciences of the United States of America*. 2016;113:3257-62.
- 66. Gangadharan B, Sunitha MS, Mukherjee S, Chowdhury RR, Haque F, Sekar N, Sowdhamini R, Spudich JA and Mercer JA. Molecular mechanisms and structural features of cardiomyopathy-causing troponin T mutants in the tropomyosin overlap region. *Proceedings of the National Academy of Sciences of the United States of America*. 2017;114:11115-11120.

- 67. Palm T, Graboski S, Hitchcock-DeGregori SE and Greenfield NJ. Disease-causing mutations in cardiac troponin T: identification of a critical tropomyosin-binding region. *Biophysical journal*. 2001;81:2827-37.

4.8 Supplemental Material

Supplemental Tables

Supplement Table 1: Clinical and genetic information for the multi-generational family

Individual	Age (years)	Sex	Status	TNNT2-R94C Status	Cardiovascular Phenotype
I.1	78	M	Deceased	Unknown	
I.2	83	F	Deceased	Unknown	
I.3	81	M	Deceased	Unknown	
I.4	83	F	Alive	Unknown	
II.1	59	M	Alive	-/-	Atrial fibrillation
II.2	60	F	Alive	-/-	
II.3	57	M	Deceased	Unknown	
II.4	Unknown	F	Alive	Unknown	
III.1	33	M	Alive	Unknown	
III.2	31	F	Alive	-/-	Supraventricular tachycardia
III.3	35	M	Alive	+/-	Ventricular tachycardia
III.4	36	F	Alive	-/-	
IV.1	4	M	Alive	-/-	
IV.2	4	M	Deceased	+/-	Hypertrophic cardiomyopathy with restrictive features, sudden cardiac arrest
IV.3	2	F	Deceased	+/-	Restrictive cardiomyopathy with mild hypertrophy, sudden cardiac arrest
IV.4	Fetus	Unknown	Deceased	Unknown	First trimester fetal death

Chapter 5: Mechanical dysfunction of the sarcomere induced by a pathogenic mutation in troponin T drives cellular adaptation

This chapter was published in the Journal of General Physiology as:

S. R. Clippinger, *et al.*, Mechanical dysfunction of the sarcomere induced by a pathogenic mutation in troponin T drives cellular adaptation. *J. Gen. Physiol.* **153** (2021).

Author Contributions: S.R.C. purified proteins and performed and analyzed the stopped flow and fluorescence experiments. P.E.C. performed and analyzed the traction force microscopy experiments with the stem cell derived cardiomyocytes. W.W. performed and analyzed electrophysiological experiments. L.G. purified proteins, implemented the cell-based assays, performed and analyzed experiments with stem cell derived cardiomyocytes, performed qPCR measurements, and performed calcium imaging experiments. W.T.S. designed tools for microcontact printing. P.A. performed *in vitro* motility assays. J.M.N. oversaw the electrophysiological experiments and analyzed data. M.J.G. oversaw the project, performed simulations, generated mutant proteins, implemented biochemical assays, analyzed data, and drafted the manuscript. All authors contributed to the writing and/or editing of the manuscript.

Abstract

Familial hypertrophic cardiomyopathy (HCM), a leading cause of sudden cardiac death, is primarily caused by mutations in sarcomeric proteins. The pathogenesis of HCM is complex, with functional changes that span scales, from molecules to tissues. This makes it challenging to deconvolve the biophysical molecular defect that drives the disease pathogenesis from downstream changes in cellular function. In this study, we examined a HCM mutation in troponin T, R92Q, for which several models explaining its effects in disease have been put forward. We demonstrate that the primary molecular insult driving disease pathogenesis are mutation-induced alterations in tropomyosin positioning, which cause increased molecular and cellular force generation during calcium-based activation. Computational modeling shows that the increased cellular force is consistent with the molecular mechanism. These changes in cellular contractility cause downstream alterations in gene expression, calcium handling, and electrophysiology. Taken together, our results demonstrate that molecularly-driven changes in mechanical tension drive the early disease pathogenesis of familial HCM, leading to activation of adaptive mechanobiological signaling pathways.

5.1 Introduction

Hypertrophic cardiomyopathy (HCM) is the leading cause of sudden cardiac death in people under age 30. HCM is characterized by hypertrophy of the left ventricular wall and interventricular septum, myocyte disarray, fibrosis, and diastolic dysfunction. HCM is also associated with marked alterations in cardiomyocyte function, including changes in electrophysiology, contractility and calcium handling (Harvey and Leinwand, 2011). Large

scale sequencing of families has revealed that HCM is caused by mutations in sarcomeric proteins involved in cardiac contraction, including troponin T (Watkins et al., 1995).

The disease presentation in HCM is quite complex, with functional differences seen at scales ranging from molecules to tissues; however, the molecular trigger that drives the disease pathogenesis is alterations in the abundance, stability, and/or functionality of mutant protein (Greenberg and Tardiff, 2021). This initial trigger activates downstream adaptive and maladaptive processes, some of which can take years to decades to manifest, including ventricular remodeling, and eventually symptomatic disease. Given the inherent complexity of HCM, it has been challenging to link the molecular and cellular phenotypes and to dissect the initial biophysical trigger from secondary adaptive processes.

To better understand the initial molecular insult and its connection to cellular dysfunction in early HCM disease pathogenesis, we examined a pathogenic mutation in troponin T, R92Q (**Fig. 1A**), identified in several unrelated families, that causes pronounced ventricular hypertrophy and a relatively high incidence of sudden cardiac death (Watkins et al., 1995). R92Q has been studied in model systems including feline (Marian et al., 1997) and rat (Rust et al., 1999) cardiomyocytes, rabbit skeletal myofibrils (Morimoto et al., 1998), quail myotubes (Sweeney et al., 1998), and transgenic mice (Tardiff et al., 1999). These studies have reached conflicting conclusions about the effects of the mutation, in part due to phenotypic differences between species. For example, the widely studied transgenic mouse model of R92Q (Tardiff et al., 1999) recapitulates some, but not all, aspects of the human disease phenotype. Elegant experiments by the Tardiff lab showed that the disease presentation in mice depends on the myosin heavy chain

isoform expressed, with different phenotypes seen when using the faster (*MYH6*) isoform found in mouse ventricles or the slower (*MYH7*) isoform found in human ventricles (Ford et al., 2012). This highlights the need to study the mutation in humanized systems.

Troponin T is part of the troponin complex, which, together with tropomyosin, regulates the calcium-dependent interactions between myosin and the thin filament that power muscle contraction. Biochemical (McKillop and Geeves, 1993) and structural (Lehman et al., 1994) measurements demonstrated that tropomyosin can lie in three states along the thin filament (**Fig. 1B**). In the absence of calcium, tropomyosin lies in the blocked position and inhibits the binding of force-generating actomyosin crossbridges. When calcium binds to troponin C, tropomyosin shifts to the closed position. The tropomyosin can then be pushed into the open position either by thermal fluctuations or myosin weak binding. Once weakly associated with the thin filament, myosin isomerizes into the strong binding state, generating force. The amount of force developed will be proportional to the number of strongly bound, force-generating myosin crossbridges.

Three models have been put forward to describe the initial molecular insult that drives the R92Q disease pathogenesis (**Fig. 1B**). 1) R92Q could affect the cycling kinetics of myosins bound to the thin filament (Ford et al., 2012). 2) R92Q could increase the calcium affinity of troponin, leading to altered calcium buffering by myofilaments that directly disrupts calcium homeostasis (Schober et al., 2012; Ferrantini et al., 2017; Robinson et al., 2018). 3) R92Q could alter the distribution of positions assumed by tropomyosin along the thin filament, changing the number of bound myosin crossbridges (McConnell et al., 2017). The mechanistic differences between these models have important implications for the design of therapeutic strategies.

Here, we set out to identify the initial molecular insult in troponin T caused by the R92Q mutation, and to link the molecular defect to observed derangements in cellular function. To do this, we developed a human R92Q model in gene-edited human induced pluripotent stem cell-derived cardiomyocytes (hiPSC-CMs). We show that the initial biophysical insult is altered positioning of tropomyosin along the thin filament, which directly affects cellular tension, leading to secondary adaptive changes in calcium homeostasis, gene expression, and electrophysiology. Our results implicate mechanobiological signaling as a primary driver of HCM disease pathogenesis.

5.2 Results

Determination of the molecular mechanism of R92Q

At the molecular scale, the initial insult that drives the disease pathogenesis is mutation-induced alterations in protein function. Therefore, we set out to determine the molecular mechanism of the R92Q mutation in troponin T. WT and R92Q human troponin T were expressed and reconstituted into functional troponin complexes for biochemical and biophysical measurements. All assays were conducted using recombinant human tropomyosin and troponin complex. β-cardiac ventricular myosin (*MYH7*) and cardiac actin were purified from porcine hearts. The porcine β-cardiac myosin isoform has 98% sequence identity with adult human β-cardiac ventricular myosin and similar biophysical properties, including indistinguishable ATPase kinetics and mechanics measured in the optical trap (Deacon et al., 2012; Greenberg et al., 2014; Sung et al., 2015).

We examined the effect of the R92Q mutation on thin filament regulation using an *in vitro* motility assay. In this assay, fluorescently labeled reconstituted regulated thin filaments are translocated over a bed of myosin in the presence of ATP and varying

concentrations of calcium. The speed of translocation was measured as a function of calcium concentration, and normalized data were fitted with the Hill equation, as previously described (Greenberg et al., 2010). R92Q-regulated thin filaments show a shift in the pCa_{50} towards activation at submaximal, but physiologically relevant, calcium concentrations ($p < 0.001$) (**Fig. 2A**). There is no change in cooperativity, as determined by the Hill coefficient ($p = 0.76$).

The R92Q mutation does not change myosin detachment kinetics or calcium binding affinity

The shift towards submaximal calcium activation observed for R92Q in the *in vitro* motility assay stems from changes in the function of the troponin-T protein. Given the role of troponin T in regulating calcium-dependent muscle contraction, three models have been proposed to explain the molecular mechanism of the R92Q mutation (**Fig. 1B**): 1) R92Q could affect the cycling kinetics of myosins that are bound to the thin filament (Ford et al., 2012). In this model, one would expect to observe a change in the amount of time that myosin remains bound to the thin filament during crossbridge cycling in the mutant. 2) R92Q could increase the calcium affinity of the troponin complex, leading to altered calcium buffering by myofilaments that directly disrupts calcium homeostasis (Schober et al., 2012; Ferrantini et al., 2017; Robinson et al., 2018). In this model, one would expect to observe an increased binding affinity for calcium in the troponin complex containing R92Q. 3) R92Q could alter the distribution of positions assumed by tropomyosin along the thin filament, leading to changes in the fraction of bound myosin crossbridges (McConnell et al., 2017). In this model, one would expect to see changes in the

equilibrium constants that define the positioning of tropomyosin along the thin filament. We set out to test these three models.

First, we tested whether the mutation affects the kinetics of myosin detachment from the thin filament by using stopped-flow kinetics to measure the rate of ADP release from actomyosin (i.e., the transition that limits actomyosin dissociation and unloaded sliding velocity) , as we have done previously (Clippinger et al., 2019). We found that the rate of ADP release from myosin bound to regulated thin filaments is not affected by the R92Q mutation ($p = 0.88$) (**Fig. 2B**). Therefore, changes in myosin detachment kinetics cannot explain the shift towards submaximal calcium activation seen in the *in vitro* motility assay.

We measured whether the calcium binding affinity to the troponin complex is affected by the mutation. We used an IAANS-labeled form of troponin C to characterize calcium binding to the troponin complex (Robinson et al., 2007; Liu et al., 2012). The fluorescence intensity of this probe changes upon calcium binding to troponin C (Davis et al., 2007; Robinson et al., 2007; Liu et al., 2012; Williams et al., 2016). We used it to spectroscopically measure the affinity of calcium binding to regulated thin filaments (**Fig. 2C**) (Liu et al., 2012). We saw that the calcium concentration required for half maximal activation, Ca_{50}, is not significantly different for the WT and R92Q mutant proteins ($p = 0.93$). Similar results were seen at 15°C (**Fig. 2C**), 20°C, and 37°C (**Fig. S1**). These results demonstrate that changes in the affinity of calcium binding to troponin C cannot explain the shift towards submaximal calcium activation seen in the *in vitro* motility assay (**Fig. 2A**). Our finding of no change in calcium affinity for troponin C is consistent with some (Liu et al., 2012), but not all (Robinson et al., 2007), previous studies. The difference

between our results and those obtained in previous studies showing changes in calcium affinity could come from differences in the calcium-sensing troponin constructs used, the actin proteins used (i.e., skeletal (Robinson et al., 2007) versus cardiac in the present study), or, possibly other experimental conditions, such as the buffer composition.

The initial biophysical insult of R92Q is increased thin filament activation due to repositioning of tropomyosin along the thin filament

To test whether the shift in calcium sensitivity can be explained by a change in the distribution of positions assumed by tropomyosin along the thin filament (**Fig. 3A**), we measured the equilibrium constants that define the fraction of thin filament regulatory units in each state (McKillop and Geeves, 1993; Barrick et al., 2019). The equilibrium constant between the blocked and closed states, K_B, was determined by rapidly mixing fluorescently labeled regulated thin filaments together with myosin and then measuring the rate of myosin binding (seen as quenching of the fluorescence signal) in the presence and absence of calcium (see Materials and Methods for details). At low calcium, when tropomyosin is primarily in the blocked state, the rate of myosin binding to the thin filament is slower than at high calcium, when the blocked state is less populated. The ratio of the rates of binding at low and high calcium were used to calculate K_B (Eq. 1, **Fig. 3B**). As can be seen from the fluorescence transients, the rate of myosin binding to regulated thin filaments is similar for the WT and R92Q mutant proteins at high calcium (pCa 4); however, at low calcium (pCa 9), the rate of binding for the mutant is much faster than for the WT, consistent with lower population of the blocked state. When we calculate K_B, we see that it is significantly larger in the mutant compared to the WT ($p=0.003$), meaning

that population of the more inhibitory blocked state is reduced while population of the closed state is increased. The increased K_B value means that, at low calcium levels, the thin filament will be more activated in the mutant, consistent with the *in vitro* motility measurements (**Fig. 2A**).

Next, we considered whether the mutation affects the equilibrium constant for the transitions between the closed and open states, K_T, or the equilibrium constant between the open and myosin weakly bound states, K_w. To do this, we performed titrations of fluorescently labeled regulated thin filaments with increasing concentrations of myosin and measured the quenching of the fluorescence as the myosin binds to the regulated thin filaments (**Fig. 3C**). These data, analyzed using a modification of the method of McKillop and Geeves (McKillop and Geeves, 1993; Barrick et al., 2019), show that there are no significant differences in K_T between WT and R92Q (**Fig. 3**). There is a small increase in K_w; however, its magnitude is insufficient to explain the shift in the *in vitro* motility assay. This demonstrates that the primary molecular defect in R92Q is partial activation of the thin filament at low calcium levels due to reduced population of the inhibitory blocked state. Taken together, our results demonstrate that the initial molecular insult resulting from the R92Q mutation is decreased population of the thin filament blocked state, leading to increased thin filament activation and myosin-driven force generation.

Computational modeling corroborates the assertion that altered tropomyosin positioning with R92Q is sufficient to explain the shift towards submaximal calcium activation

To model the effects of the initial molecular insult identified in our biochemical studies, we used a widely used computational model of thin filament activation that was originally developed by Campbell et al (Campbell et al., 2010). This model is based on the McKillop and Geeves three-state formalism that was also used to analyze our data (McKillop and Geeves, 1993). In this model, the equilibrium constants for transitions between thin filament states are inputted, and the model predicts several parameters, including the force per sarcomere as a function of calcium. When we used the default parameters of the model, but proportionally increase the value of K_B to match the fractional change seen in our biochemical experiments with the mutant (**Fig. 4A**), we find that this change alone is sufficient to produce the shift towards submaximal calcium activation observed in the *in vitro* motility experiments (**Fig. 2A**).

Generation of gene-edited stem cell-derived cardiomyocytes

To examine the effects of the R92Q mutation in human cells, we used CRISPR/Cas9 to generate two independent human induced pluripotent stem cell (hiPSC) lines that are homozygous for the R92Q mutation (**Fig. S2**). While there are several splice isoforms of troponin T expressed during development, the primary isoform expressed in hiPSC-CMs is the adult isoform (Cai et al., 2019). All of these isoforms contain R92, so all of the troponin T expressed in the cell has the mutation (**Fig. S2**). Homozygous lines were used to facilitate direct correlation of the molecular insult with alterations in cellular function. Heterozygous lines would better mimic the disease seen in humans but would contain complex mixtures of wild type (WT) and mutant proteins, confounding the correlation of the molecular and cellular results. Both WT and R92Q hiPSCs were derived

from the same parent line and are therefore isogenic except for the mutation. We previously showed, by whole exome sequencing of the parent line, that it has no known variants associated with cardiomyopathy (Clippinger et al., 2019). Gene-edited hiPSCs are pluripotent, as assessed by immunofluorescence (**Fig. S3A**) and have normal karyotypes (**Fig. S3B**). hiPSCs were differentiated to hiPSC-CMs through temporal modulation of WNT signaling (Lian et al., 2012), and our efficiency of differentiation using this procedure is >90% (Clippinger et al., 2019). Both WT and R92Q cells express similar ratios of fetal (slow skeletal) to adult (cardiac) troponin I isoforms (p=0.49; **Fig. S4)**.

R92Q hiPSC-CMs generate increased force, power, and contraction speed compared to WT cells

To test whether R92Q hiPSC-CMs show the altered contractility seen in some model systems, we measured the contractility of single hiPSC-CMs using traction force microscopy. hiPSC-CMs were seeded onto rectangular extracellular matrix (ECM) patterns on polyacrylamide hydrogels of physiological stiffness (10 kPa) (Clippinger et al., 2019). This patterning on physiological stiffness hydrogels promotes hiPSC-CM maturation and sarcomeric alignment (Ribeiro et al., 2015). Patterned hiPSC-CMs show sarcomeres that align preferentially along the long axis of the cell (**Fig. S3B**) and these cells contract primarily along that single axis (**Movie S1**). The force, speed of contraction, and power were calculated from the displacement of beads embedded in the hydrogel (**Fig. S5**) (Ribeiro et al., 2017). Data were plotted as cumulative distributions of single cells to account for cell-to-cell variability (Clippinger et al., 2019). R92Q hiPSC-CMs generate more force, power, and have a higher contractile speed compared to the WT

(**Fig. 5**). There were no significant differences observed between the two independently derived R92Q clones that we examined (**Fig. S6**).

Intracellular calcium transients are reduced in R92Q cells

While the initial molecular insult driving the disease pathogenesis is alterations in tropomyosin positioning which increases molecular contractility, changes in contractility can lead to downstream activation of adaptive and maladaptive pathways. Previous studies using transgenic mice with troponin T mutations also showed altered cardiomyocyte calcium handling (Rice et al., 2010; Schober et al., 2012; Coppini et al., 2017; Ferrantini et al., 2017; Robinson et al., 2018). To examine calcium dynamics in hiPSC-CMs, cells were patterned onto rectangular ECM patterns on 10 kPa hydrogels and loaded with the ratiometric fluorescent calcium indicator dye, Fura Red. Line scans of the fluorescence of spontaneously beating cells were collected at 1.9 ms intervals. As can be seen, hiPSC-CMs display well-defined calcium transients (**Fig. 6A**); however, the amplitudes of the transients are lower ($p < 0.002$) in R92Q (0.56 ± 0.13; n=18), compared to WT (0.84 ± 0.11; n=19), cells. Although the low signal-to-noise ratio of the dye on the hydrogel substrate precluded us from determining whether there were differences in diastolic calcium as has been reported previously (Schober et al., 2012; Robinson et al., 2018), the data presented demonstrate that, despite generating increased force, R92Q hiPSC-CMs have reduced calcium transient amplitudes compared to WT cells.

To see whether the reduced population of the blocked state, observed in our molecular studies (**Fig. 4B**), is sufficient to explain the hypercontractility seen in cells despite the reduction in calcium transient amplitude, we used the same computational

model described earlier to predict the force per sarcomere in response to a calcium transient. In the modeling, the amplitude of the calcium transient for R92Q was reduced to 67% of the value seen in the WT, as observed in our cellular measurements (**Fig. 6A**). As above, we proportionally increased K_B for the mutant to match the relative difference seen in our biochemical experiments. Consistent with our cellular experiments, the model predicts that the mutant will generate more force in response to a calcium transient than the WT, despite having a smaller amplitude calcium transient (**Fig. 4B**). It should be noted that hiPSC-CMs express complex mixtures of fetal and adult protein isoforms and that, as a result, there could be some subtle differences between the absolute forces predicted by the model, which is based on the equilibrium constants measured for the adult proteins, and the experimentally measured forces in hiPSC-CMs.

R92Q cells show alterations in expression of calcium-handling genes

The observed changes in calcium handling could come from a variety of sources, including changes in transcription, protein expression, and/or post-translational modifications of proteins that regulate calcium homeostasis. To explore a possible role for transcriptional remodeling downstream of the initial molecular insult, we performed RT-qPCR analyses of the expression of transcripts encoded by key genes involved in the regulation of calcium homeostasis in cardiomyocytes (**Fig. 6**). Specifically, we examined the expression levels of transcripts encoding phospholamban (*PLN*), sarcoendoplasmic reticulum calcium-ATPase (SERCA, *ATPA2*), voltage-gated calcium channel subunits (*CACNA1C*, *CACNA1G*, *CACNA1H*), inositol triphosphate receptor (*ITPR2*), calsequestrin (*CASQ2*), calcium-calmodulin dependent kinase 2 (C*AMK2D*), sodium-

calcium exchanger (*SLC8A1*), and the ryanodine receptor (*RYR2*). We found marked upregulation of *CASQ*, *CAMK2D*, and *SLC8A1* and downregulation of *CACNA1H* in R92Q, compared with WT, hiPSC-CMs (**Fig. 6B, Fig. S7-S8**), demonstrating that the expression levels of key genes associated with calcium handling are altered in R92Q hiPSC-CMs.

R92Q cells show altered action potentials and reduced inward calcium current densities

The observed reductions in the calcium transients observed in spontaneously beating R92Q cells could reflect changes in transmembrane calcium influx. To determine directly if membrane excitability is altered in R92Q cells, we obtained whole-cell current clamp recordings of spontaneous action potentials in WT and R92Q mutant hiPSC-CMs patterned onto rectangular ECM patterns on 10 kPa hydrogels (**Fig. 7A-B**). Analyses of the data obtained in these experiments revealed that the maximum diastolic potential (the most negative membrane potential achieved between action potentials in spontaneously firing cells) is more depolarized in R92Q hiPSC-CMs than in WT hiPSC-CMs (**Fig. 7B**). In addition, the frequency of spontaneous action potential firing is higher, upstroke velocities (i.e., the rate of membrane depolarization) are lower, and action potential durations, measured at 50% repolarization (APD_{50}), are shorter in R92Q hiPSC-CMs, compared with WT cells (**Fig. 7B, Fig. S9**).

To better understand the mechanism(s) contributing to the reductions in the APD_{50} seen in spontaneously beating R92Q cells, we examined the waveforms of evoked action potentials of hiPSC-CMs hyperpolarized to a membrane potential of -80 mV. Although similar hyperpolarizing currents were required to render R92Q and WT hiPSC-CMs

electrically silent and similar currents were required to evoke action potentials in WT and mutant cells, the durations of evoked action potentials are significantly shorter in R92Q, than in WT cells (**Fig. 7C-D**).

Additional voltage-clamp experiments were conducted to determine directly if voltage-gated inward calcium current densities were altered in R92Q compared with WT cells. With outward potassium currents blocked, we recorded whole-cell voltage-gated calcium currents evoked on membrane depolarization in WT and R92Q hiPSC-CMs. As illustrated in **Fig. 7E**, these experiments revealed that inward calcium current densities are markedly reduced in R92Q compared to WT hiPSC-CMs (**Fig. 7F**).

5.3 Discussion

Here, we elucidated the molecular and cellular consequences of the R92Q mutation in troponin T. We show that the initial molecular insult that drives disease pathogenesis is increased thin filament activation at physiologically relevant micromolar calcium levels due to destabilization of the tropomyosin blocked state. We demonstrate computationally and experimentally that this increased activation is consistent with the increased mechanical force produced by hiPSC-CMs. We show that altered mechanical forces leads to downstream changes in the expression of calcium handling genes, altered calcium transients, and alterations in cellular electrophysiology. Taken together, our results highlight the role of mechanobiology in driving the early disease pathogenesis.

Defining the primary molecular driver of the disease pathogenesis

Previous studies demonstrated that R92Q mutant protein is expressed and properly integrated into sarcomeres, suggesting that the driver of the disease is changes

in protein function, rather than haploinsufficiency (Marian et al., 1997; Sweeney et al., 1998; Tardiff et al., 1999; Yanaga et al., 1999). Our results demonstrating that R92Q causes a shift towards submaximal calcium activation (**Fig. 2A**) are consistent with some (Morimoto et al., 1998; Yanaga et al., 1999; Szczesna et al., 2000; Chandra et al., 2001; Robinson et al., 2002; Ford et al., 2012), but not all (Sweeney et al., 1998; Rust et al., 1999), previous measurements in muscle fibers and biochemical assays using non-cardiac protein isoforms. The shift towards submaximal calcium activation could come from changes in actomyosin dissociation kinetics, the affinity of calcium binding to troponin C, and/or the positioning of tropomyosin along the thin filament (**Fig. 1B**).

Our results demonstrate that R92Q does not affect the calcium binding affinity of troponin C or the kinetics of actomyosin dissociation (**Fig. 2**); however, the mutation increases the equilibrium constant between the blocked and closed states (**Fig. 3B**). This change favors the closed state over the blocked state, lowering the energy barrier for thin filament activation at physiologically relevant calcium concentrations (pCa 5-7). Our computational modeling (**Fig. 4**) demonstrates that the increase in this equilibrium constant is sufficient to explain the shift towards submaximal calcium activation seen in our *in vitro* motility measurements (**Fig. 2A**). Our data demonstrate that the initial insult that drives the early disease pathogenesis is reduced population of the inhibitory blocked position of tropomyosin at low calcium, which would lead to increased thin filament activation.

The R92Q mutation has been studied in many model systems, including quail myotubes (Sweeney et al., 1998), transfected rat cardiomyocytes (Rust et al., 1999), skinned rabbit muscle fibers (Morimoto et al., 1998), transgenic mice (Tardiff et al., 1999),

and transfected cat cardiomyocytes (Marian et al., 1997). While these studies have greatly advanced our understanding of the mutation, they also demonstrated that the effects of the mutation depend on the model system used. Studies using transgenic mice demonstrated that disease presentation depends on whether proteins with biophysical properties similar to human isoforms are used (Ford et al., 2012). The use of all cardiac proteins with biophysical properties similar to human proteins is important for studies of thin filament mutations, since the activation of the thin filament depends on both myosin and calcium binding (**Fig. 3A**). The most commonly used myosins in studies of R92Q mutation have been murine ventricular myosin (MYH6 - 92% sequence identity with human ventricular myosin) and rabbit fast skeletal muscle myosin (MYH2 - 82% sequence identity with human ventricular myosin), both of which have very different biophysical properties than human ventricular myosin (VanBuren et al., 1995; Malmqvist et al., 2004; Debold et al., 2007; Deacon et al., 2012). Our molecular studies used human cardiac troponin and tropomyosin and porcine cardiac myosin and actin. Porcine cardiac actin is identical in sequence to human cardiac actin. Porcine cardiac myosin (*MYH7*) is 98% identical in sequence to the human isoform, and displays biochemical kinetics, mechanical step sizes, and load-dependent kinetics that are indistinguishable from human cardiac myosin (Deacon et al., 2012; Greenberg et al., 2014; Sung et al., 2015).

Interestingly, the R92 residue is in the region of troponin T that interacts with tropomyosin (Yamada et al., 2020). Two other HCM mutations have been identified at R92, R92W and R92L, leading to the suggestion that R92 is a hotspot for HCM mutations. While there are no atomic-resolution structures of this region of the thin filament, structural studies have shown that troponin T plays a role in stabilizing the tropomyosin blocked

state (Tobacman et al., 2002; Johnson et al., 2019; Madan et al., 2020). Molecular dynamics simulations demonstrated that mutations at R92 can change the distance between troponin T and tropomyosin (Manning et al., 2011), and biochemical experiments showed that R92L decreases the affinity of troponin for tropomyosin (Gangadharan et al., 2017). These two mechanisms are not mutually exclusive, and we speculate that R92Q reduces the coupling between troponin conformation and tropomyosin positioning, leading to destabilization of the blocked state. It is worth noting that we have focused on the effects of a troponin T mutation on calcium-based activation, due to the central role of troponin in calcium-dependent thin filament regulation. Recent work has suggested that the N-terminal region of myosin binding protein C can play a role in activating the thin filament in the C-zone (Mun et al., 2014; Risi et al., 2018; Napierski et al., 2020). It will be interesting to investigate whether the R92Q mutation also affects the interactions of myosin binding protein C with the thin filament.

Recent studies of HCM-causing mutations in thick filament proteins, including β-cardiac myosin, myosin binding protein C, myosin regulatory light chain, and myosin essential light chain, have demonstrated that many of these mutations disrupt the autoinhibited super relaxed state of myosin, leading to the recruitment of more crossbridges and thus to hypercontractility (Spudich, 2015; McNamara et al., 2016; Alamo et al., 2017; Nag et al., 2017; Adhikari et al., 2019; Sitbon et al., 2020). It has been proposed that increased crossbridge recruitment correlates with the hyperdynamic cardiac function seen in HCM (Alamo et al., 2017). Our studies with R92Q, a thin filament mutation, demonstrate a similar net effect of increased crossbridge recruitment at

physiologically relevant calcium levels, suggesting that altered recruitment of crossbridges in HCM as a common theme for both some thin and thick filament mutations.

It has been proposed that R92Q causes an increase in troponin C's calcium affinity which would affect the buffering of calcium by myofilaments, disrupting calcium homeostasis (Schober et al., 2012; Robinson et al., 2018). While our cellular data reveal disrupted calcium homeostasis, our molecular experiments shows no change in the affinity of calcium for R92Q troponin, demonstrating that disrupted calcium homeostasis is a downstream consequence of the initial molecular insult. Our results are consistent with the notion that the development of HCM correlates with changes in tension, rather than calcium handling (Davis et al., 2016).

Connecting the molecular and cellular phenotypes in R92Q

R92Q hiPSC-CMs show both an increase in force production (**Fig. 5A**) and a reduction in the amplitude of the calcium transient (**Fig. 6A**). These seemingly conflicting findings can be reconciled by our computational modeling (**Fig. 4B**), which predicts that the shift towards submaximal calcium activation observed at the molecular scale can lead to cellular hypercontractility, despite the reduction in the amplitude of the calcium transient. This hypercontractility occurs at physiologically relevant (micromolar) concentrations of calcium (Bers, 2002). Therefore, the observed cellular hypercontractility is consistent with the proposed molecular mechanism.

At the cellular level, we see disrupted calcium homeostasis with R92Q, which is downstream of the initial contractile insult. Calcium homeostasis in the myocardium is a complicated process which depends on many factors, including gene expression and

post-translational modifications of signaling and contractile proteins (Bers, 2002). While a complete dissection of this mechanism is beyond the scope of the current study, our results provide insights into potential transcriptional mechanisms. We observed changes in the expression of several genes involved in calcium handling (**Fig. 6B**), including calsequestrin (*CASQ2*), calcium-calmodulin kinase (*CAMK2D*), the sodium-calcium exchanger (*SLC8A1*), and a voltage-gated calcium channel subunit (*CACNA1H*). Interestingly, overexpression of *CASQ2* or *CAMK2D* in transgenic mice causes heart failure and arrhythmogenesis (Sato et al., 1998; Zhang et al., 2003). While we recognize that changes in transcript expression do not always correlate with protein function, our data demonstrate that altered mechanics at the molecular level can drive changes in gene expression, showing a mechanobiological link between these processes in HCM. It is worth noting that some of the differentially expressed calcium handling genes observed here in human cells are different from observations in the R92Q mouse model, which may be due to species differences (Coppini et al., 2017; Chowdhury et al., 2020). Interestingly, in mice, ablation of *PLN* can rescue the HCM phenotype, and it will be interesting to see whether similar results are observed in human cells (Chowdhury et al., 2020).

Our single-cell electrophysiological experiments reveal that action potential durations are shorter in R92Q, compared with WT cells, due in part to reduced inward L-type calcium current densities (**Fig. 7**). These changes would be expected to be arrhythmogenic and could contribute to the increased incidence of arrhythmias and sudden death in individuals harboring the mutation. We observe normal expression levels of the transcripts encoding L-type channel subunits, and therefore, the reduced current density could be due to alterations in signaling pathways and/or post-translational

modifications of channel subunits. The reduced inward calcium current densities (**Fig. 7**) would be expected to reduce calcium-induced calcium release from intracellular calcium stores, potentially contributing to the reductions in calcium transient amplitudes (**Fig. 6A**).

Based on our observation that molecular hypercontractility drives downstream changes in cellular calcium handling and electrophysiology, we propose that mutation-induced changes in cellular tension alter mechanosensitive signaling pathways in cardiomyocytes (Saucerman et al., 2019). Consistent with this idea, we recently demonstrated that a dilated cardiomyopathy mutation in troponin T, ΔK210, affects molecular tension and mechanosensing, which helps to drive the disease progression (Clippinger et al., 2019). Similarly, increases in cardiac tension from external sources including hypertensive disease and aortic stenosis promotes pathological hypertrophy. Deciphering the mechanobiological pathways in cardiomyocytes is an active field of research (Prosser et al., 2011; Robison et al., 2016; Saucerman et al., 2019). Hypercontractility of cardiomyocytes can impose aberrant stretch on fibroblasts, activating the transition to myofibroblasts (Saucerman et al., 2019) and contributing to the diffuse myocardial fibrosis frequently seen with HCM.

Implications for modeling and treating HCM

Modeling HCM is challenging, since it is a complex disease where different adaptive and maladaptive pathways are activated as the disease progresses. Our goal was to connect the initial molecular insult with the early disease pathogenesis in human cells. We therefore used genome-edited hiPSC-CMs, which are excellent tools for dissecting the early disease pathogenesis (Lam and Wu, 2018). These experiments

utilized isogenic cells, making it easier to decipher the direct consequences of the mutation on a controlled genetic background. R92Q hiPSC-CMs recapitulate some important aspects of HCM-induced changes in contractility (Tardiff et al., 1999; Robinson et al., 2002; Ford et al., 2012), altered electrophysiology (Coppini et al., 2017; Robinson et al., 2018), and calcium dysfunction (Rice et al., 2010; Ferrantini et al., 2017; Robinson et al., 2018) seen in other model systems. It should be noted that hPSC-CMs have several important limitations (see limitations section below). Limitations aside, hiPSC-CMs are powerful tools for studying the connection between the initial molecular insult and the early disease pathogenesis in human cells.

Our identification of altered cellular mechanics and downstream mechanobiological signaling pathways as key drivers of the disease has important implications for therapeutics. There is currently an outstanding need to develop new strategies to treat HCM. Our results suggest that targeting mechanobiological signaling pathways in cardiomyocytes could be useful for treating some forms of HCM.

We believe that cardiomyopathies are excellent candidates for a precision medicine approach (McNally and Mestroni, 2017; Fatkin et al., 2019; Lavine and Greenberg, 2020; Greenberg and Tardiff, 2021). Recently, there was a report of a HCM mutation in α-actinin linked to action potential prolongation attributed to increased calcium current density (Prondzynski et al., 2019), and the patient harboring this mutation was successfully treated with the L-type calcium channel blocker, diltiazem. In R92Q, we observed a reduction in the calcium current density (**Fig. 7**), and therefore, a different therapeutic strategy would be necessary. Similarly, hiPSC-CMs harboring a HCM-linked mutation in troponin T, I79N, display changes in the action potential durations due to

altered sodium-calcium exchanger function. Again, the cellular mechanism is distinct from that observed for R92Q, which is associated with changes in the inward calcium current density, potentially suggesting different therapeutic strategies (Wang et al., 2017; Wang et al., 2018). The marked differences between the functional effects of different HCM mutations highlight the need to understand the underlying derangements in molecular and cellular function when designing therapies.

Limitations

In our molecular studies, we were interested in uncovering the initial molecular insult of the R92Q mutation in troponin T that drives the early disease pathogenesis. As such, we focused on the effects of the mutation on calcium-dependent thin filament activation. Our experiments and computational modeling utilized well established methods (McKillop and Geeves, 1993; Campbell et al., 2010) that are tailored to capture the effects of changes in thin filament function. It is important to note that other models exist which incorporate higher order sarcomeric structures beyond the thin filament, including thick filament-based regulation of contractility (e.g., the super relaxed state of myosin in the thick filament which modulates the number of available crossbridges, mutation-induced alterations in the force per crossbridge, and myosin binding protein C's role in thin filament activation). However, the potential impacts of the mutation on thick filament function, if present, are downstream of the initial molecular insult. That said, to a first order approximation, our proposed molecular mechanism of mutation-induced changes in tropomyosin positioning is sufficient to explain the observed change in the calcium sensitivity of thin filament activation that we and others have observed.

Moreover, while our R92Q hiPSC-CMs recapitulate aspects of the early disease pathogenesis, they cannot fully capture the clinical phenotype for several reasons. First, hiPSC-CMs are developmentally immature, and they lack many of the physiological cues present in the myocardium (Lam and Wu, 2018; Musunuru et al., 2018). This immaturity includes expression of fetal genes (**Fig. S4**), spontaneous beating (**Fig. 6**), less negative resting membrane potentials (**Fig. 7**), and metabolic differences. As such, they do not capture aspects of clinical HCM including fibrosis, myocyte disarray, and ventricular arrhythmias. While we employ several techniques to promote hiPSC-CM maturation including plating the cells on physiological stiffness hydrogels, providing rectangular patterns to promote sarcomeric alignment, and aging cells at least 30 days before using them, these cells are still immature compared to adult cardiomyocytes (Ribeiro et al., 2015). Moreover, while patients are typically heterozygous for R92Q, our studies used homozygous cell lines to facilitate connecting the molecular and cellular phenotypes. It will be interesting to see how heterozygous cells differ from the homozygous cells used here. Despite these limitations, our gene edited hPSC-CMs captured several aspects of the disease phenotype and helped to enable us to decipher the initial molecular insult from the activation of downstream adaptive and maladaptive signaling pathways.

5.4 Conclusions

We demonstrate that the initial insult of the R92Q mutation in troponin T is molecular hypercontractility at physiologically relevant calcium concentrations, which leads to alterations in mechanobiological signaling pathways that regulate calcium

homeostasis, gene expression, and cellular electrophysiology. Taken together, our results demonstrate that mechanobiological adaptations are important in the early disease pathogenesis, and they suggest that targeting these pathways could open new avenues for treating HCM.

5.5 Methods

Protein modification and purification

Cardiac myosin and actin were purified from cryoground porcine ventricles (Pelfreez) as previously described (Clippinger et al., 2019). S1 myosin was prepared by chymotrypsin digestion as previously described (Clippinger et al., 2019). Recombinant human cardiac tropomyosin, troponin I, troponin T, and troponin C were expressed in *E. coli* and purified from BL21-CodonPlus cells (Agilent) as described previously (Clippinger et al., 2019). Purified tropomyosin was reduced in 50 mM DTT at 56°C for 5 minutes and ultracentrifuged to remove aggregates immediately before being used in each assay. The R92Q mutation was introduced into troponin T using QuickChange Site-Directed Mutagenesis (Agilent) and the presence of the mutation was verified by sequencing.

For the studies of calcium binding, we used IAANS (6-((4-((2-iodoacetyl)amino)phenyl)amino)-2-naphthalenesulfonic acid)-labeled troponin C (Davis et al., 2007). IAANS was custom synthesized by Toronto Research Chemicals. Troponin C^{T53C} was labeled with five-fold molar excess IAANS dye overnight, and the reaction was quenched with DTT. Excess dye was dialyzed out with 4 dialysis buffer changes of 1 mM DTT, 0.01% NaN_3, 50 μM $CaCl_2$, 1 mM $MgCl_2$, 3 M Urea, 1 M KCl, 5 mg/L TPCK, 5 mg/L TLCK, 0.3 mM PMSF (Davis et al., 2007). The IAANS-labeled troponin C^{T53C} was then

purified over a MonoQ column and complexed with the troponin T and I as done previously (Clippinger et al., 2019).

In vitro motility assays

In vitro motility assays were conducted using thin filaments containing R92Q troponin T as previously described (Clippinger et al., 2019). Data for WT troponin T are from (Clippinger et al., 2019). Briefly, enzymatically inactive full-length porcine cardiac myosin was removed by cosedimentation with phalloidin-stabilized F-actin in the presence of ATP. Flow cells were loaded with 1 volume (50 µL) of 200 nM myosin, 2 volumes of 1 mg/mL BSA, 1 volume of 1 µM F-actin, 2 volumes of KMg25 (25 mM KCl, 4 mM $MgCl_2$,1 mM EGTA, 1 mM DTT, 60 mM MOPS pH 7.0) + 1 mM MgATP, 4 volumes of KMg25, and 1 volume of 40 nM rhodamine-phalloidin-labeled thin filaments. After loading 2 volumes of activation buffer (KMg25 with 4 mM MgATP, 1 mg/mL glucose, 192 U/mL glucose oxidase, 48 µg/mL catalase, 2 µM troponin and tropomyosin, 0.5% methyl cellulose), flow cells were imaged for 20 frames. Each buffer was balanced to give the desired free calcium, free magnesium, and ionic strength using MaxChelator (Bers et al., 2010). Individual motile filaments were manually tracked using the MTrackJ plugin in Fiji ImageJ (Schindelin et al., 2012), and each point shows the average and standard deviation of the speed from 3 separate experiments.

Stopped-flow transient kinetic measurement of K_B and ADP release

An SX-20 stopped flow apparatus (Applied Photophysics) was used. K_B was determined as previously described (Barrick et al., 2019; Clippinger et al., 2019). WT data are from (Clippinger et al., 2019). At both low (pCa 9) and high calcium (pCa 4), 5 μM phalloidin-stabilized pyrene actin, 2 μM tropomyosin, 2 μM troponin, and 0.04 U/mL apyrase were rapidly mixed with 0.5 μM S1 myosin and 0.04 U/mL apyrase. Performed at 20°C, each experiment was the average of at least 3 separate mixes and the data were fit by a single exponential curve. K_B was calculated from:

$$\frac{k_{obs}(-Ca^{2+})}{k_{obs}(+Ca^{2+})} = \frac{K_B}{1+K_B} \qquad \text{Equation 1}$$

The reported K_B is the average of at least three different experiments. The p-value was calculated from a 2-tailed Student's t-test.

The rate of ADP release from myosin bound to regulated thin filaments (20°C) was measured as previously described. (Clippinger et al., 2019) The average and standard deviation of the rate of at least four experiments was calculated and the p-value was derived using a two-tailed Student's t-test.

Fluorescence titrations to measure K_W, K_T, and n

A SX-20 stopped flow fluorometer was used for all fluorescence titrations. The values of K_W, K_T, and n (the cooperativity) were determined for R92Q and WT using fluorescence titrations as previously described (Barrick et al., 2019; Clippinger et al., 2019). The WT data is from (Clippinger et al., 2019). Hypothesis testing and uncertainty estimation were

done using established techniques (Efron, 1979; Press, 1992; Martin, 2007). Briefly, the data were resampled using a bootstrapping algorithm, resampled data were fit to calculate 95% confidence intervals, and p-values were calculated from the overlap regions between the distributions of bootstraps (Efron, 1979; Press, 1992; Martin, 2007; Barrick et al., 2019).

Measurement of calcium binding to troponin C

The calcium affinity for the troponin complex (Tn^{IAANS}) was determined by titrating regulated thin filaments with increasing calcium concentrations and measuring the change in fluorescence in IAANS-labeled troponin C upon calcium binding (Davis et al., 2007). Tn^{IAANS} was excited at 330 nm and fluorescence emission was detected using a 395 nm long-pass filter. 0.15 μM Tn^{IAANS} complex, 0.45 μM tropomyosin, and 2 μM actin were mixed with increasing concentrations of calcium in 10 mM MOPS pH 7.0, 150 mM KCl, 3 mM $MgCl_2$, and 1 mM DTT. Each buffer was balanced to give the desired free calcium, free magnesium, and ionic strengths using MaxChelator (Bers et al., 2010). The solution was allowed to equilibrate for 1 minute after mixing with constant stirring before the fluorescence intensity was measured. The titration curve was fit by the logistic sigmoid function, which is mathematically equivalent to the Hill equation:

$$Y = Y_{min} + \frac{Y_{max} - Y_{min}}{1 + \exp\left[(-H(X - pCa_{50})\right]} \qquad \text{Equation 2}$$

where Y_{max} and Y_{min} are the maximum and minimum IAANS fluorescence, X is the negative logarithm of $[Ca^{2+}]_{free}$, pCa_{50} is the negative log of the concentration of free calcium producing half-maximal fluorescence, and H is the cooperativity (proportional to

the Hill coefficient) (Tikunova et al., 2002). Titrations were performed at both 15°C and 20°C to facilitate comparison with previous measurements using different proteins (Liu et al., 2012). For the measurements at 37°C (**Fig. S1**), we used a Horiba fluorometer. We excited the fluorophore at 330 nm and integrated the fluorescence >500 nm (Davis et al., 2007). Data were analyzed with the same methodology.

Computational modeling of sarcomeric contractility

To simulate the effects of the experimentally determined changes in equilibrium constants on force production, we used the computational model developed by Campbell et al. (Campbell et al., 2010) based on McKillop and Geeves (McKillop and Geeves, 1993), as we have done previously (Clippinger et al., 2019). Briefly, in this model, 9 sarcomeres are simulated, where the equilibrium constants between states and a coupling constant describing cooperativity define the probability of switching between biochemical states. The steady-state force is calculated from the equilibrium distribution of states at a given calcium concentration. Our biochemical experiments demonstrated that the primary change at the molecular scale with the mutation is an increase in K_B, such that K_B (R92Q) = 2.56 * K_B (WT). To simulate the WT, we used the default model parameters. To simulate the mutant, we decreased the reverse rate constant that defines K_B, so that K_B (R92Q) = 2.56 * K_B (WT). To simulate the force per sarcomere in response to a calcium transient for the WT, we used the default calcium transient. To simulate the response of R92Q, we changed K_B as described above and we reduced the amplitude of the default calcium transient to 67% of its value to match our measurements in hiPSC-CMs.

Stem cell line derivation

R92Q stem cells were derived and the quality control was performed using procedures described in depth previously (Clippinger et al., 2019). Briefly, the parent human BJ fibroblast stem cell line (BJFF.6, ATCC) was reprogrammed to stem cells by the Genome Engineering and iPSC Center (GEiC) at Washington University in St. Louis. Two independent isogenic stem cell lines with the R92Q hTNNT2 point mutation were also generated at the GEiC using the CRISPR/Cas9 system (Jinek et al., 2012) (**Fig. S2**). The oligo used to generate the gRNA was CCTTCTCCATGCGCTTCCGGNGG and the mutation was introduced by homology directed repair. This gRNA was selected to minimize off target effects. The presence of the homozygous mutation was verified by sequencing. Karyotype (G-banding) analysis was performed by Cell Line Genetics (**Fig. S2**). Mycoplasma testing and immunofluorescence staining for pluripotency markers were performed by the GEiC (**Fig. S3**).

Stem cell and hiPSC-CMs culture

Stem cell culture and differentiation to hiPSC-CMs were done as previously described (Clippinger et al., 2019). Briefly, stem cells were maintained in feeder-free culture. To differentiate the stem cells to hiPSC-CMs, we used small-molecule manipulation of WNT signaling (Lian et al., 2012; Lian et al., 2013). hiPSC-CMs were enriched using metabolic selection (Sharma et al., 2015). All functional experiments were conducted at least 30 days after the initiation of differentiation. Experiments were conducted using 2

independently derived cell lines for the R92Q mutant. All experiments were repeated using at least two independent differentiations.

Microcontact patterning of hiPSC-CMs on glass and hydrogels

Fabrication of rectangular (7:1 aspect ratio) polydimethylsiloxane (PDMS) stamps for micropatterning of hiPSC-CMs on both glass and 10 kPa hydrogels was done as previously described (Ribeiro et al., 2015; Clippinger et al., 2019). Cells were patterned onto 10 kPa polyacrylamide hydrogels containing stamped Geltrex (Thermo Fisher) in rectangular patterns as in (Clippinger et al., 2019) (**Fig. S3**).

Quantification of troponin I isoform expression by Western blotting

Cell lysates from multiple differentiations were extracted from wild type and mutant hiPSC-CMs using protein lysis buffer containing 20 mM HEPES pH 7.0, 150 mM NaCl, 0.5% CHAPS, and 1 protease inhibitor cocktail tablet (Roche complete mini EDTA-free tablets). 30 µg of each protein lysate was loaded per well of an Any kD Mini-PROTEAN TGX Precast Protein Gel (BioRad), separated by electrophoresis, and transferred to PVDF membranes (Sigma). Membranes were blocked with 5% milk and incubated overnight with primary antibodies. One membrane was incubated with mouse anti-GAPDH antibody (DSHB; DSHB-hGAPDH-2G7; 3 µg/mL) and mouse anti-slow skeletal troponin I antibody (Santa Cruz; sc-514899; 1:700). The other membrane was incubated with mouse anti-GAPDH antibody (DSHB; DSHB-hGAPDH-2G7; 3 µg/mL) and rabbit anti-cardiac troponin I (Santa Cruz; sc-15368; 1:500). After washing off the primary antibodies, the membranes were incubated with either anti-rabbit IgG, HRP-linked

antibody (Cell Signaling; 7074S; 1:2000) and/or anti-mouse IgG, HRP-linked Antibody (Cell Signaling; 7076S; 1:2000). The proteins were detected using the SuperSignal West Dura Extended Duration Substrate (ThermoFisher Scientific) and imaged on a MyECL Imager (ThermoFisher Scientific). Blot intensity was quantified by densitometry using ImageJ (Schindelin et al., 2012) (**Fig. S4**). P-values were calculated using a Mann-Whitney U-test.

Traction force microscopy

Traction force microscopy was conducted on 10 kPa hydrogels with cells patterned on rectangular patterns as previously described (Clippinger et al., 2019) and analyzed using the computational tool developed in (Ribeiro et al., 2017). Data were analyzed and 95% confidence intervals of the mean were calculated as described previously (Barrick et al., 2019; Clippinger et al., 2019). Briefly, the data were resampled using a bootstrapping algorithm to calculate 95% confidence intervals and p-values were calculated from the overlap regions between the distributions of bootstraps (Efron, 1979; Press, 1992; Martin, 2007; Barrick et al., 2019). Videos of contracting cells (**Movie S1**) and sample traces derived from those videos (**Fig. S5**) are provided. Two independently derived cell lines were examined (**Fig. S6**).

Measurement of calcium transients in live cells

Live-cell imaging was conducted using the ratiometric fluorescent calcium indicator dye Fura Red AM (Thermo Fisher). The use of a ratiometric dye is important since the mutation could affect the uptake of dye into the cells, and the ratiometric dye normalizes the calcium-induced

changes in fluorescence to the total amount of dye taken up by the cell. hiPSC-CMs were patterned on hydrogels as described above. After 5-7 days on the patterns, the cells were loaded with 10 μM Fura Red AM dye and 0.01% Pluronic F-127 (Invitrogen/ThermoFisher) in RPMI-B27 with insulin media for 20 min at room temperature. The cells were washed twice and incubated with Tyrode's solution (1.8 mM CaCl2, 135 mM NaCl, 4 mM KCl, 1 mM MgCl2, 5 mM glucose and 10 mM HEPES, pH 7) for 15-20 minutes at 37°C to allow de-esterification of the dye. Calcium transients were recorded with a Nikon A1Rsi confocal microscope in line scan mode using a 40X objective and the Ex2Em1 microscope setting. Fura Red AM loaded cells were excited at both 405 nm and 488 nm, and the emission fluorescence signal was collected at 595nm. Line scans were acquired at a sampling rate of 512 pixels x 1.9 ms per line (total 10,000 lines per recording). Each cell was recorded along with a line scan of the background fluorescence outside the cell area.

Analysis of calcium transients

The calcium transient fluorescence counts were converted to ratios using Fiji software (Schindelin et al., 2012). The averaged background fluorescence was subtracted from each recording and a montage was created from the image stacks. The ratio of fluorescence at 405 nm / 488 nm was then calculated in Excel. The resulting ratiometric calcium fluorescence traces were then analyzed using a custom MATLAB script to calculate the amplitude of the calcium transient. Traces with fewer than 3 peaks were not analyzed. Briefly, the data were smoothed over a 100-point sliding window using a Savitsky-Golay filter. The locations of peaks and minima in the fluorescence signal

were determined using a peak-finding algorithm. Statistical significance was tested using a 2-tailed Student's t-test.

Measurement of the expression of transcripts encoding key calcium-handling proteins

hiPSC-CMs were grown on Matrigel-coated (Corning) 10 kPa PrimeCoat elastic substrate culture dishes (35 mm) (ExCellness Biotech SA, Lausanne, Switzerland) for 10 days. Total RNA was isolated using RNeasy Mini Kit (Qiagen) with on-column DNase I treatment according to the manufacturer's instructions. cDNA was generated using iScript Reverse Transcription Supermix (Biorad) according to the manufacturer's instructions. qPCR reactions were performed in triplicate using iTaq Universal SYBRGreen Supermix (Biorad) and using the ViiA 7 System (Applied Biosystems). Primers for all genes were obtained from IDT PrimeTime qPCR Primers. Primer product numbers from IDT are listed in **Fig. S7**. Three separate biological samples were evaluated for both WT and R92Q homozygous hiPSC-CMs. The relative levels of mRNA were calculated using the comparative threshold cycle (ΔCt) method (Livak and Schmittgen, 2001). GAPDH and HPRT1 were used as endogenous controls, and Rox dye present in the master mix was used to normalize background fluorescence. ΔCt values are presented in **Fig. S8**. The statistical significance of differences in ΔCt values was evaluated using a Mann-Whitney U-test.

Cellular electrophysiological studies

Whole-cell current- and voltage-clamp recordings were obtained at room temperature (22~24°C) from hiPSC-CMs plated on hydrogel-coated coverslips using a Dagan 3900A (Dagan Corporation) amplifier interfaced to a Digidata 1332A A/D converter (Axon) and

the pClamp 10.3 software (Axon). For current-clamp recordings, recording pipettes contained 135 mM KCl, 5 mM K_2ATP, 10 mM EGTA, 10 mM HEPES and 5 mM glucose (pH 7.2; 310 mOsm). The bath solution contained 136 mM NaCl, 4 mM KCl, 2 mM $MgCl_2$, 1 mM $CaCl_2$, 10 mM HEPES and 10 mM glucose (pH 7.4; 300 mOsm). For recordings of voltage-gated Ca^{2+} currents (I_{Ca}), pipettes contained 5 mM NaCl, 90 mM Cs CH_3SO_3, 20 mM CsCl, 4 mM MgATP, 0.4 mM Tris-GTP, 10 mM EGTA, 10 mM HEPES and 3 mM $CaCl_2$ (pH 7.2; 310 mOsm), and the bath solution contained 20 mM NaCl, 110 mM TEA-Cl, 10 mM CsCl, 1 mM $MgCl_2$, 1 mM $CaCl_2$, 10 mM HEPES and 10 mM glucose (pH 7.4; 300 mOsm). In all experiments, pipette resistances were 2-3 MΩ.

Electrophysiological data were acquired at 10 or 100 kHz, and signals were low pass filtered at 5 kHz before digitization and storage. After the formation of a gigaohm seal (>1GΩ) and establishment of the whole-cell configuration, brief (10 ms) ± 5 mV voltage steps from a holding potential (HP) of -70 mV were presented to allow measurements of whole-cell membrane capacitances (C_m), input resistances (R_{in}), and series resistances (R_s). Mean ± SEM C_m values were 32 ± 2 pF and 47 ± 2 pF ($P < 0.001$) in WT (n = 96) and R92Q (n = 67), hiPSC-CMs, respectively; mean ± SEM R_{in} values were 1665 ± 125 MΩ and 1551 ± 162 MΩ ($P > 0.05$) in WT (n = 96) and R92Q (n = 67), hiPSC-CMs, respectively. Whole-cell C_m and R_s were electronically compensated by 85%. Voltage errors resulting from the uncompensated R_s were always <2 mV and were not corrected. Leak currents were always <50 pA and also were not corrected.

In current-clamp recordings, spontaneous action potentials were recorded on establishing the whole-cell configuration. To record evoked action potentials, small (-10 ~ -100 pA) current injections were made to hyperpolarize the membrane potential to -80 mV and to

stop spontaneous firing. Individual action potentials were then evoked by brief (4 ms) depolarizing current (600 pA) injections. In voltage-clamp experiments, whole-cell I_{Ca}, evoked in response to depolarizing (300 ms) voltage steps to test potentials between -45 and +15 mV (in 5 mV increments at 1 s intervals) from a holding potential of -50 mV, were recorded.

Analysis of electrophysiological data

Electrophysiological data were compiled and analyzed using Clampfit 10.3 (Axon) and GraphPad (Prism). C_m values were determined by integration of the capacitive transients recorded during ± 5 mV voltage steps from -70 mV. Current amplitudes in each cell were normalized to the C_m and current densities are reported (pA/pF). All data are presented as means ± SEM. The statistical significance of observed differences between WT and R92Q hiPSC-CMs was evaluated using two-tailed Student's t-test or two-way ANOVA; p-values are presented in **Fig. S9**.

Online supplemental material

Online supplemental materials include 9 figures (**Fig. S1-S9**). Also included is **Movie S1** showing the displacement of beads by WT (gray) and R92Q (red) hiPSC-CMs contracting on a 10 kPa polyacrylamide gel. Videos were recorded at 30 frames per second using a spinning disc confocal microscope (Nikon). The cell, which is not visible, is on a rectangular pattern of Matrigel with a 7:1 aspect ratio. The displacement of the beads was tracked as a function of time. Note that the two cells shown are not on the same

slide/hydrogel; rather, we have merged two videos to facilitate direct visual comparison of the contractility in WT and mutant cells. As is evident in the video, force is generated primarily along the long axis of the cells. These videos were used to generate the representative traces in **Fig. S5**.

Funding Acknowledgements: This work was supported by the National Institutes of Health (R01 HL141086 to M.J.G., R01 HL034161 and R01 HL142520 to J.M.N.), the March of Dimes Foundation (FY18-BOC-430198 to M.J.G.), the Children's Discovery Institute of Washington University and St. Louis Children's Hospital (PM-LI-2019-829 M.J.G.), the Washington University Institute of Materials Science, and the Washington University Center for Cellular Imaging (WUCCI) (CDI-CORE-2015-505 to M.J.G.). S.R.C. was supported through an institutional training grant (T32 EB018266).

Conflict of interest:

All experiments were conducted in the absence of any financial relationships that could be construed as potential conflicts of interest.

5.6 Figures

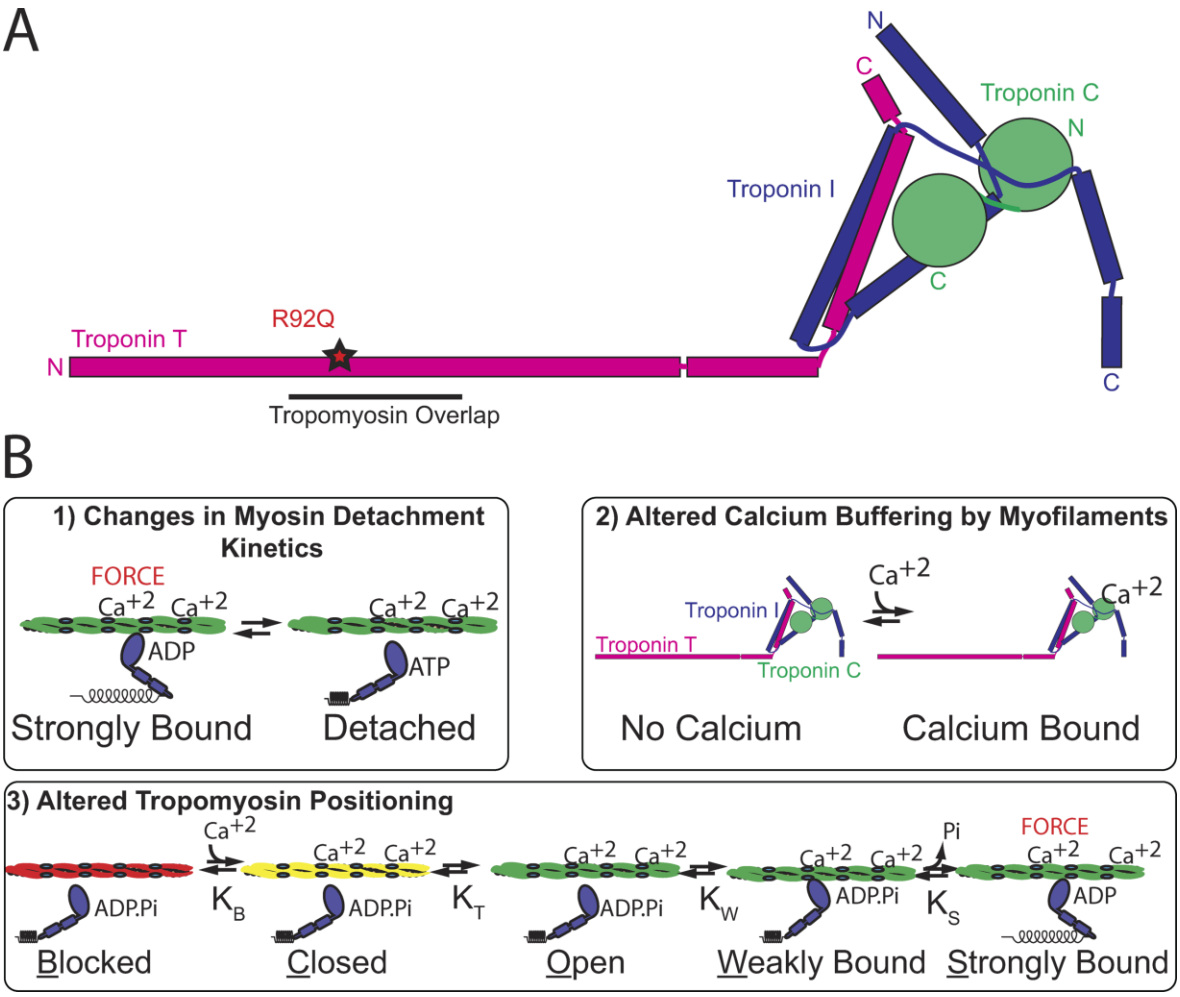

Figure 1. R92Q mutation in troponin T causes hypertrophic cardiomyopathy. (**A**) Cartoon of the troponin complex based on (Sheng and Jin, 2014). R92Q is located in the region of troponin T that interacts with tropomyosin, near the tropomyosin overlap region. (**B**) Models for the molecular mechanism of R92Q.

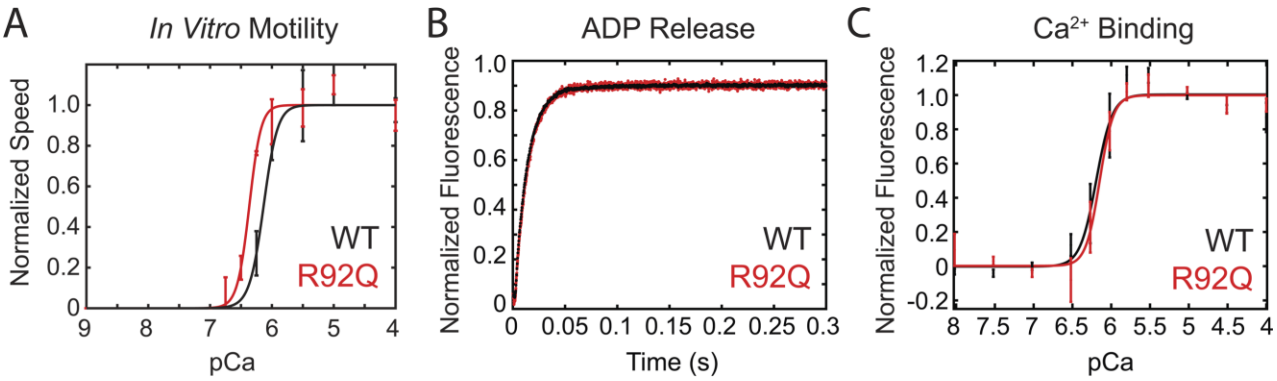

	WT	R92Q	p
Motility pCa50 (n=3)	6.12 (±0.02)	6.37 (±0.03)	<0.001
Motility Hill (n=3)	3.8 (±0.6)	3.4 (±0.7)	0.75
ADP release (s^{-1}) (n=4)	76.3 (±5.0)	75.8 (±3.9)	0.88
IAANs Ca50 (μM) (n=5)	0.66 (±0.18)	0.67 (±0.19)	0.93
IAANs Hill (n=5)	2.69 (±0.40)	3.50 (±0.39)	0.01

Figure 2. R92Q does not change the rate of unloaded actomyosin dissociation or calcium binding affinity to troponin C. (**A**) In vitro motility assays using cardiac myosin and reconstituted regulated thin filaments. The speed of motility was measured as a function of calcium. R92Q shows a shift towards submaximal calcium activation. WT data are from (Clippinger et al., 2019). Error bars are standard deviations from 3 separate experiments. (**B**) The rate of ADP release from myosin attached to regulated thin filaments was measured using stopped-flow kinetics (fluorescence transients are shown). Myosin bound to ADP and pyrene-labeled regulated thin filaments was rapidly mixed with ATP and the fluorescence increases as myosin dissociates from the thin filament. The rate of actomyosin dissociation was unchanged by the R92Q mutation. WT data are from (Clippinger et al., 2019). Curves show the average of 5 technical repeats. (**C**) The affinity of calcium binding to the troponin complex. IAANS-labeled troponin C was reconstituted into regulated thin filaments. Titrations with increasing calcium were conducted, and there is no difference in calcium binding affinity between the WT and R92Q. Error bars show the standard deviation of 5 experiments. Values derived from fits, standard errors in the fits, and p-values are shown. P-values were calculated using a 2-tailed student's t-test.

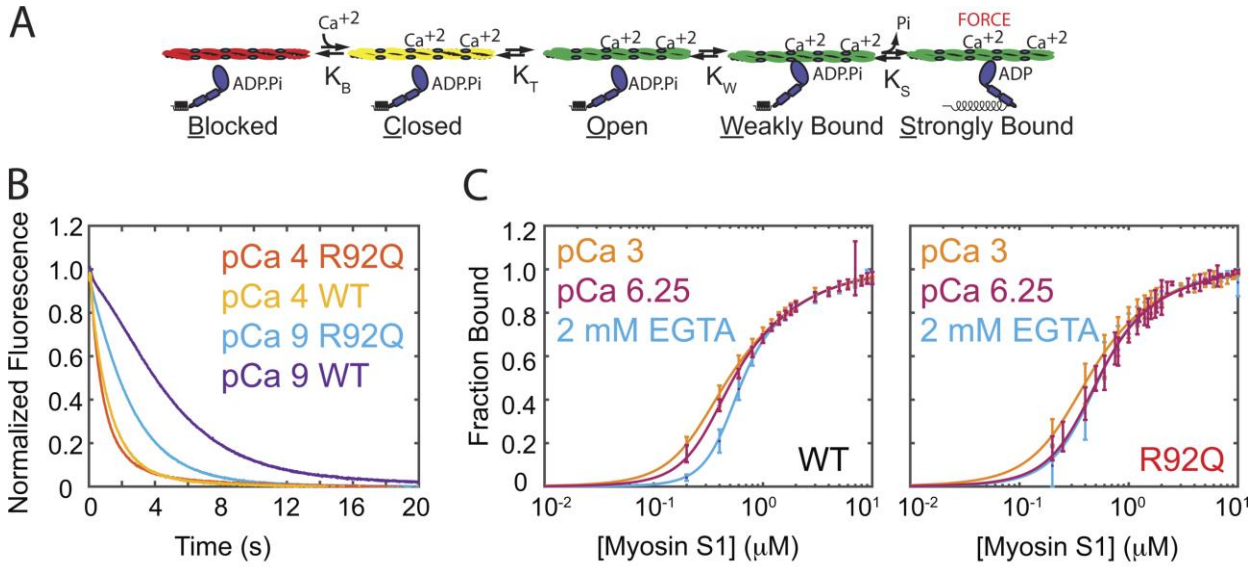

	WT	R92Q	p
K_B	0.40 (-0.15/+0.15)	1.02 (-0.26/+0.26)	0.003
K_W	0.13 (-0.01/+0.01)	0.18 (-0.04/+0.22)	0.014
K_T 2mM EGTA	0.06 (-0.03/+0.06)	0.13 (-0.10/+0.10)	0.39
K_T pCa 6.25	0.08 (-0.04/+0.04)	0.08 (-0.06/+0.05)	0.75
K_T pCa 3	0.18 (-0.07/+0.08)	0.21 (-0.15/+0.16)	0.94
Cooperativity (n)	5.97 (-0.95/+1.35)	4.01 (-1.69/+3.20)	0.20

Figure 3. R92Q alters the positioning of tropomyosin along the thin filament. (A) Kinetic scheme for thin filament activation. (**B**) Measurement of the equilibrium constant K_B using stopped-flow kinetics methods (fluorescence transients are shown). Pyrene-labeled regulated thin filaments were rapidly mixed with myosin at high (pCa 4) or low (pCa 9) calcium, and the rate of myosin binding was measured by quenching of the fluorescence. K_B is calculated as described in the methods. The rate of myosin binding is similar for the WT and R92Q at pCa 4, but much faster for R92Q at pCa 9, consistent with destabilization of the blocked state. K_B for R92Q is significantly larger than the WT. (**C**) Measurement of the parameters K_T and K_W using equilibrium titrations of myosin with regulated thin filaments. Fitting reveals no significant differences for R92Q for either K_T or K_W compared to the WT. WT data are from (Clippinger et al., 2019). Error bars show the standard deviation of 5 experiments. The average value, 95% confidence intervals calculated from bootstrapping, and p-values derived from distribution of bootstrapped values are shown in the table.

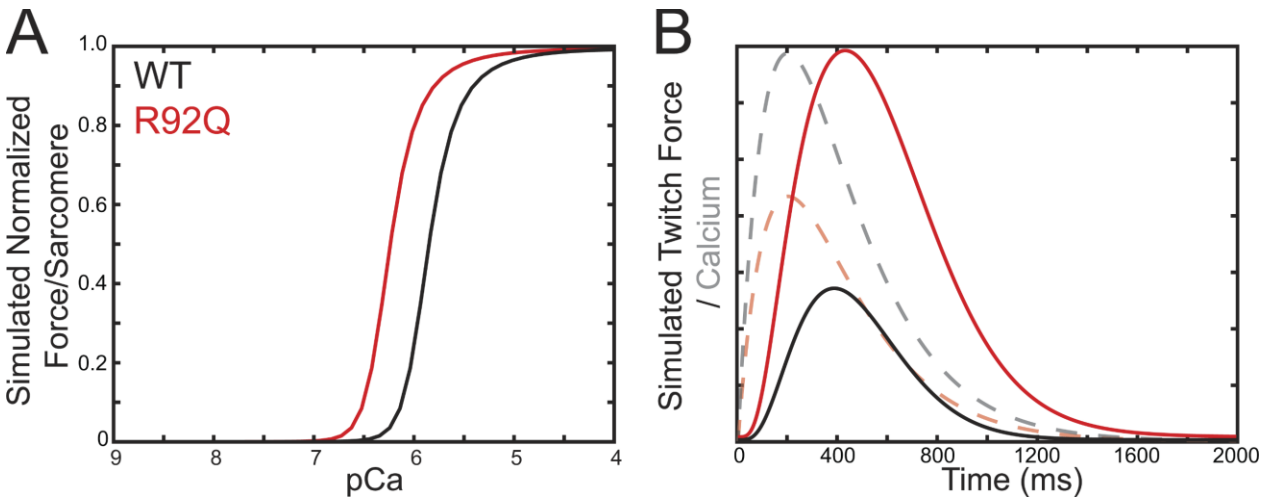

Figure 4. Computational modeling reveals that altered tropomyosin positioning is sufficient to explain the hypercontractility seen with R92Q. (**A**) Using the computational model developed by (Campbell et al., 2010) and the measured equilibrium constants for thin filament activation, the steady state force per sarcomere was calculated. Changing K_B alone is sufficient to reproduce the shift towards submaximal calcium activation seen in the in vitro motility experiments (**Fig. 2A**). (**B**) Using the same model, the equilibrium constants measured in vitro, and the calcium transients measured in hiPSC-CMs (**Fig, 6A**), the twitch force (solid line) in response to a calcium transient (dashed line) was calculated. Consistent with our cellular measurements, the simulations demonstrate that despite having a reduced calcium transient, R92Q produces a larger force in a twitch due to changes in tropomyosin positioning.

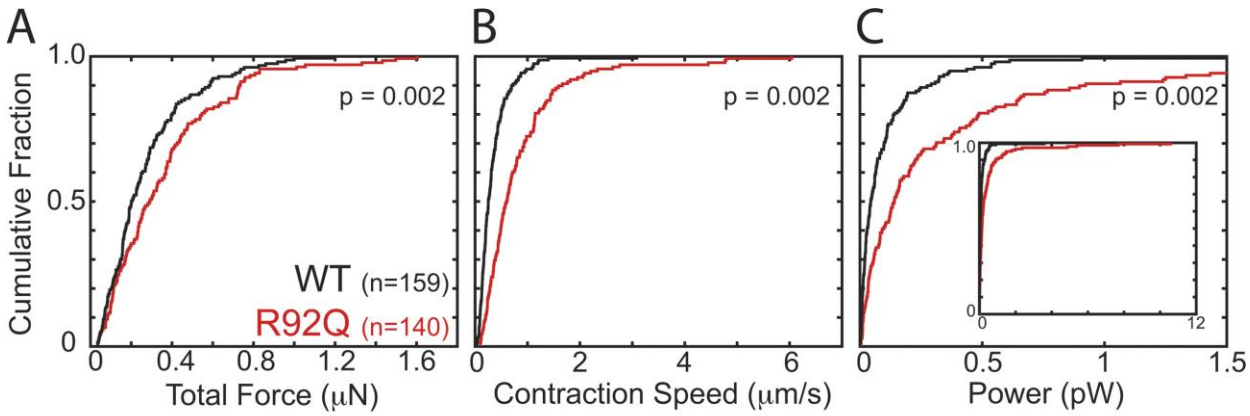

	WT (n=159)	R92Q (n=140)	p
Total force (μN)	0.27 (-0.03/+0.04)	0.36 (-0.04/+0.05)	0.002
Contraction speed (μm/s)	0.35 (-0.05/+0.06)	0.84 (-0.22/+0.23)	0.002
Contraction power (pW)	0.12 (-0.04/+0.06)	0.47 (-0.3/+0.3)	0.002

Figure 5. R92Q causes cellular hypercontractility in hiPSC-CMs. Single hiPSC-CMs were seeded on rectangular patterns on 10 kPa hydrogels for traction force microscopy. Cumulative distributions reveal that R92Q hiPSC-CMs have a (**A**) greater total force, (**B**) contraction speed, and (**C**) contraction power compared to the WT. WT data are from (Clippinger et al., 2019). Values from the analysis, number of cells examined, 95% confidence intervals obtained from bootstrapping, and p-values derived from the distributions of bootstrapped values are listed in the table.

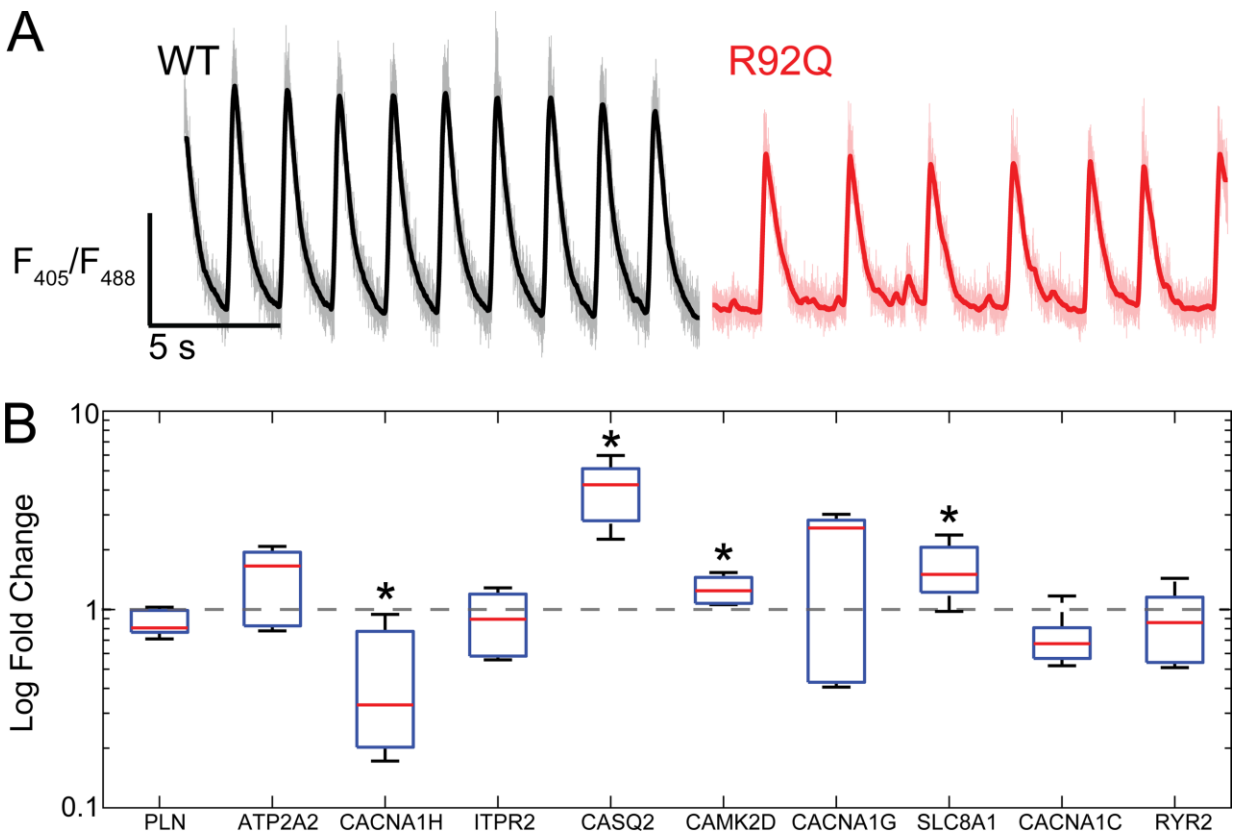

Figure 6. R92Q hiPSC-CMs show altered calcium transients and gene expression. (**A**) Representative fluorescence ratio traces showing calcium transients. Single hiPSC-CMs were seeded on rectangular patterns on 10 kPa hydrogels and loaded with the ratiometric calcium dye, Fura Red. R92Q hiPSC-CMs calcium transients have lower amplitudes than the WT cells. (**B**) Expression of key calcium-handling genes measured using qPCR. Data show significant increases in the expression of CASQ2, CAMK2D, and SLC8A1, and a decrease in CACNA1H. ΔCt values are shown in **Fig. S8**. Statistics were performed on the ΔCt values; however, we show the log-fold changes. Red lines show the means, boxes show the quartiles, and error bars show the standard deviations. Data shown reflect 3 biological replicates, each of which included 3 technical replicates. * denotes ΔCt values with $p<0.05$ compared to the WT. P-values were calculated using a Mann-Whitney test.

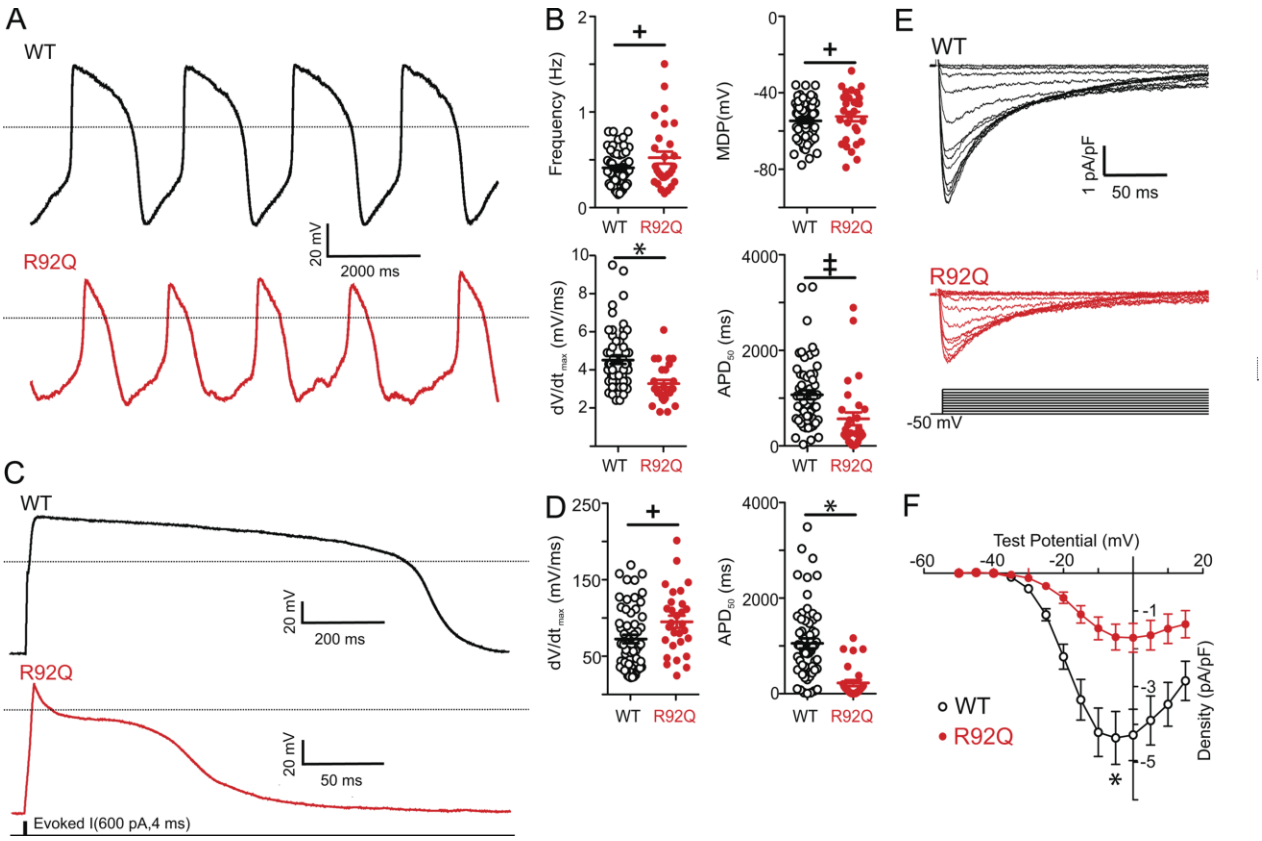

Figure 7. Spontaneous and evoked action potentials are altered in R92Q hiPSC-CMs and I_{Ca} densities are reduced. (**A**) Representative whole-cell spontaneous action potentials recorded from WT and R92Q hiPSC-CMs are illustrated; dotted black lines indicate 0 mV. (**B**) Firing frequencies, maximum diastolic potentials (MDP), maximum upstroke velocities (dV/dt_{max}) and action potential durations at 50% repolarization (APD_{50}), measured in individual WT (n = 58) and R92Q (n = 29) hiPSC-CMs are plotted; mean values are also indicated and are provided in **Fig. S9**. (**C**) Representative whole-cell action potential waveforms evoked from a hyperpolarized membrane potential, as described in Materials and Methods, in WT and R92Q cells are shown; dotted black lines indicate 0 mV. (**D**) dV/dt_{max} and APD_{50} values measured in individual WT (n = 58) and R92Q (n = 29) cells are plotted; mean values are also indicated and are provided in **Fig. S9**. (**E**) Representative voltage-gated Ca^{2+} current (I_{Ca}) waveforms, elicited by voltage steps to test potentials between -40 and +15 mV (in 5 mV increments) from a holding potential (HP) of -50 mV, in WT and R92Q hiPSC-CMs are shown. (**F**) Mean ± SEM peak I_{Ca} densities in R92Q (n = 12) and WT (n = 15) hiPSC-CMs are plotted as a function of the test potential. $^{+, ‡, *}$ Values in R92Q mutant cells are significantly different from those in WT cells at the $^{+}p < 0.05$, $‡p < 0.01$ and $*p < 0.001$ levels. P-values were calculated using a two-tailed Student's t-test.

5.7 References

Adhikari, A.S., D.V. Trivedi, S.S. Sarkar, D. Song, K.B. Kooiker, D. Bernstein, J.A. Spudich, and K.M. Ruppel. 2019. beta-Cardiac myosin hypertrophic cardiomyopathy mutations release sequestered heads and increase enzymatic activity. *Nat Commun*. 10:2685.

Alamo, L., J.S. Ware, A. Pinto, R.E. Gillilan, J.G. Seidman, C.E. Seidman, and R. Padron. 2017. Effects of myosin variants on interacting-heads motif explain distinct hypertrophic and dilated cardiomyopathy phenotypes. *eLife*. 6.

Barrick, S.K., S.R. Clippinger, L. Greenberg, and M.J. Greenberg. 2019. Computational Tool to Study Perturbations in Muscle Regulation and Its Application to Heart Disease. *Biophysical journal*. 116:2246-2252.

Bers, D.M. 2002. Cardiac excitation-contraction coupling. *Nature*. 415:198-205.

Bers, D.M., C.W. Patton, and R. Nuccitelli. 2010. A practical guide to the preparation of Ca(2+) buffers. *Methods in cell biology*. 99:1-26.

Cai, W., J. Zhang, W.J. de Lange, Z.R. Gregorich, H. Karp, E.T. Farrell, S.D. Mitchell, T. Tucholski, Z. Lin, M. Biermann, S.J. McIlwain, J.C. Ralphe, T.J. Kamp, and Y. Ge. 2019. An Unbiased Proteomics Method to Assess the Maturation of Human Pluripotent Stem Cell-Derived Cardiomyocytes. *Circulation research*. 125:936-953.

Campbell, S.G., F.V. Lionetti, K.S. Campbell, and A.D. McCulloch. 2010. Coupling of adjacent tropomyosins enhances cross-bridge-mediated cooperative activation in a markov model of the cardiac thin filament. *Biophysical journal*. 98:2254-2264.

Chandra, M., V.L. Rundell, J.C. Tardiff, L.A. Leinwand, P.P. De Tombe, and R.J. Solaro. 2001. Ca(2+) activation of myofilaments from transgenic mouse hearts expressing R92Q mutant cardiac troponin T. *American journal of physiology. Heart and circulatory physiology*. 280:H705-713.

Chowdhury, S.A.K., C.M. Warren, J.N. Simon, D.M. Ryba, A. Batra, P. Varga, E.G. Kranias, J.C. Tardiff, R.J. Solaro, and B.M. Wolska. 2020. Modifications of Sarcoplasmic Reticulum Function Prevent Progression of Sarcomere-Linked Hypertrophic Cardiomyopathy Despite a Persistent Increase in Myofilament Calcium Response. *Front Physiol*. 11:107.

Clippinger, S.R., P.E. Cloonan, L. Greenberg, M. Ernst, W.T. Stump, and M.J. Greenberg. 2019. Disrupted mechanobiology links the molecular and cellular phenotypes in familial dilated cardiomyopathy. *Proceedings of the National Academy of Sciences of the United States of America*. 116:17831-17840.

Coppini, R., L. Mazzoni, C. Ferrantini, F. Gentile, J.M. Pioner, A. Laurino, L. Santini, V. Bargelli, M. Rotellini, G. Bartolucci, C. Crocini, L. Sacconi, C. Tesi, L. Belardinelli, J. Tardiff, A. Mugelli, I. Olivotto, E. Cerbai, and C. Poggesi. 2017. Ranolazine Prevents Phenotype Development in a Mouse Model of Hypertrophic Cardiomyopathy. *Circulation. Heart failure*. 10.

Davis, J., L.C. Davis, R.N. Correll, C.A. Makarewich, J.A. Schwanekamp, F. Moussavi-Harami, D. Wang, A.J. York, H. Wu, S.R. Houser, C.E. Seidman, J.G. Seidman, M. Regnier, J.M. Metzger, J.C. Wu, and J.D. Molkentin. 2016. A Tension-Based Model Distinguishes Hypertrophic versus Dilated Cardiomyopathy. *Cell*. 165:1147-1159.

Davis, J.P., C. Norman, T. Kobayashi, R.J. Solaro, D.R. Swartz, and S.B. Tikunova. 2007. Effects of thin and thick filament proteins on calcium binding and exchange with cardiac troponin C. *Biophysical journal*. 92:3195-3206.

Deacon, J.C., M.J. Bloemink, H. Rezavandi, M.A. Geeves, and L.A. Leinwand. 2012. Identification of functional differences between recombinant human alpha and beta cardiac myosin motors. *Cellular and molecular life sciences : CMLS*. 69:2261-2277.

Debold, E.P., J.P. Schmitt, J.B. Patlak, S.E. Beck, J.R. Moore, J.G. Seidman, C. Seidman, and D.M. Warshaw. 2007. Hypertrophic and dilated cardiomyopathy mutations differentially affect the molecular force generation of mouse alpha-cardiac myosin in the laser trap assay. *American journal of physiology. Heart and circulatory physiology*. 293:H284-291.

Efron, B. 1979. Bootstrap Methods: Another Look at the Jackknife. *The Annals of Statistics*. 7:1-26.

Fatkin, D., I.G. Huttner, J.C. Kovacic, J.G. Seidman, and C.E. Seidman. 2019. Precision Medicine in the Management of Dilated Cardiomyopathy: JACC State-of-the-Art Review. *Journal of the American College of Cardiology*. 74:2921-2938.

Ferrantini, C., R. Coppini, J.M. Pioner, F. Gentile, B. Tosi, L. Mazzoni, B. Scellini, N. Piroddi, A. Laurino, L. Santini, V. Spinelli, L. Sacconi, P. De Tombe, R. Moore, J. Tardiff, A. Mugelli, I. Olivotto, E. Cerbai, C. Tesi, and C. Poggesi. 2017. Pathogenesis of Hypertrophic Cardiomyopathy is Mutation Rather Than Disease Specific: A Comparison of the Cardiac Troponin T E163R and R92Q Mouse Models. *J Am Heart Assoc*. 6.

Ford, S.J., R. Mamidi, J. Jimenez, J.C. Tardiff, and M. Chandra. 2012. Effects of R92 mutations in mouse cardiac troponin T are influenced by changes in myosin heavy chain isoform. *Journal of molecular and cellular cardiology*. 53:542-551.

Gangadharan, B., M.S. Sunitha, S. Mukherjee, R.R. Chowdhury, F. Haque, N. Sekar, R. Sowdhamini, J.A. Spudich, and J.A. Mercer. 2017. Molecular mechanisms and structural features of cardiomyopathy-causing troponin T mutants in the tropomyosin overlap region. *Proceedings of the National Academy of Sciences of the United States of America*. 114:11115-11120.

Greenberg, M.J., K. Kazmierczak, D. Szczesna-Cordary, and J.R. Moore. 2010. Cardiomyopathy-linked myosin regulatory light chain mutations disrupt myosin strain-dependent biochemistry. *Proceedings of the National Academy of Sciences of the United States of America*. 107:17403-17408.

Greenberg, M.J., H. Shuman, and E.M. Ostap. 2014. Inherent force-dependent properties of beta-cardiac myosin contribute to the force-velocity relationship of cardiac muscle. *Biophysical journal*. 107:L41-L44.

Greenberg, M.J., and J.C. Tardiff. 2021. Complexity in genetic cardiomyopathies and new approaches for mechanism-based precision medicine. *The Journal of general physiology*. 153.

Harvey, P.A., and L.A. Leinwand. 2011. The cell biology of disease: cellular mechanisms of cardiomyopathy. *The Journal of cell biology*. 194:355-365.

Jinek, M., K. Chylinski, I. Fonfara, M. Hauer, J.A. Doudna, and E. Charpentier. 2012. A programmable dual-RNA-guided DNA endonuclease in adaptive bacterial immunity. *Science*. 337:816-821.

Johnson, D., L. Zhu, M. Landim-Vieira, J.R. Pinto, and J.M. Chalovich. 2019. Basic residues within the cardiac troponin T C terminus are required for full inhibition of muscle contraction and limit activation by calcium. *The Journal of biological chemistry*. 294:19535-19545.

Lam, C.K., and J.C. Wu. 2018. Disease modelling and drug discovery for hypertrophic cardiomyopathy using pluripotent stem cells: how far have we come? *Eur Heart J*. 39:3893-3895.

Lavine, K.J., and M.J. Greenberg. 2020. Beyond genomics-technological advances improving the molecular characterization and precision treatment of heart failure. *Heart Fail Rev*.

Lehman, W., R. Craig, and P. Vibert. 1994. Ca(2+)-induced tropomyosin movement in Limulus thin filaments revealed by three-dimensional reconstruction. *Nature*. 368:65-67.

Lian, X., C. Hsiao, G. Wilson, K. Zhu, L.B. Hazeltine, S.M. Azarin, K.K. Raval, J. Zhang, T.J. Kamp, and S.P. Palecek. 2012. Robust cardiomyocyte differentiation from human pluripotent stem cells via temporal modulation of canonical Wnt signaling. *Proceedings of the National Academy of Sciences of the United States of America*. 109:E1848-1857.

Lian, X., J. Zhang, S.M. Azarin, K. Zhu, L.B. Hazeltine, X. Bao, C. Hsiao, T.J. Kamp, and S.P. Palecek. 2013. Directed cardiomyocyte differentiation from human pluripotent stem cells by modulating Wnt/beta-catenin signaling under fully defined conditions. *Nature protocols*. 8:162-175.

Liu, B., S.B. Tikunova, K.P. Kline, J.K. Siddiqui, and J.P. Davis. 2012. Disease-related cardiac troponins alter thin filament Ca2+ association and dissociation rates. *PloS one*. 7:e38259.

Livak, K.J., and T.D. Schmittgen. 2001. Analysis of relative gene expression data using real-time quantitative PCR and the 2(-Delta Delta C(T)) Method. *Methods*. 25:402-408.

Madan, A., M.C. Viswanathan, K.C. Woulfe, W. Schmidt, A. Sidor, T. Liu, T.H. Nguyen, B. Trinh, C. Wilson, S. Madathil, G. Vogler, B. O'Rourke, B.J. Biesiadecki, L.S. Tobacman, and A. Cammarato. 2020. TNNT2 mutations in the tropomyosin binding region of TNT1 disrupt its role in contractile inhibition and stimulate cardiac dysfunction. *Proceedings of the National Academy of Sciences of the United States of America*. 117:18822-18831.

Malmqvist, U.P., A. Aronshtam, and S. Lowey. 2004. Cardiac myosin isoforms from different species have unique enzymatic and mechanical properties. *Biochemistry*. 43:15058-15065.

Manning, E.P., J.C. Tardiff, and S.D. Schwartz. 2011. A model of calcium activation of the cardiac thin filament. *Biochemistry*. 50:7405-7413.

Marian, A.J., G. Zhao, Y. Seta, R. Roberts, and Q.T. Yu. 1997. Expression of a mutant (Arg92Gln) human cardiac troponin T, known to cause hypertrophic cardiomyopathy, impairs adult cardiac myocyte contractility. *Circulation research*. 81:76-85.

Martin, M.A. 2007. Bootstrap hypothesis testing for some common statistical problems: A critical evaluation of size and power properties. *Comput Stat Data An*. 51:6321-6342.

McConnell, M., L. Tal Grinspan, M.R. Williams, M.L. Lynn, B.A. Schwartz, O.Z. Fass, S.D. Schwartz, and J.C. Tardiff. 2017. Clinically Divergent Mutation Effects on the Structure and Function of the Human Cardiac Tropomyosin Overlap. *Biochemistry*. 56:3403-3413.

McKillop, D.F., and M.A. Geeves. 1993. Regulation of the interaction between actin and myosin subfragment 1: evidence for three states of the thin filament. *Biophysical journal*. 65:693-701.

McNally, E.M., and L. Mestroni. 2017. Dilated Cardiomyopathy: Genetic Determinants and Mechanisms. *Circulation research*. 121:731-748.

McNamara, J.W., A. Li, N.J. Smith, S. Lal, R.M. Graham, K.B. Kooiker, S.J. van Dijk, C.G.D. Remedios, S.P. Harris, and R. Cooke. 2016. Ablation of cardiac myosin binding protein-C disrupts the super-relaxed state of myosin in murine cardiomyocytes. *Journal of molecular and cellular cardiology*. 94:65-71.

Morimoto, S., F. Yanaga, R. Minakami, and I. Ohtsuki. 1998. Ca2+-sensitizing effects of the mutations at Ile-79 and Arg-92 of troponin T in hypertrophic cardiomyopathy. *The American journal of physiology*. 275:C200-207.

Mun, J.Y., M.J. Previs, H.Y. Yu, J. Gulick, L.S. Tobacman, S. Beck Previs, J. Robbins, D.M. Warshaw, and R. Craig. 2014. Myosin-binding protein C displaces tropomyosin to activate cardiac thin filaments and governs their speed by an independent mechanism. *Proceedings of the National Academy of Sciences of the United States of America*. 111:2170-2175.

Musunuru, K., F. Sheikh, R.M. Gupta, S.R. Houser, K.O. Maher, D.J. Milan, A. Terzic, J.C. Wu, G. American Heart Association Council on Functional, B. Translational, Y. Council on Cardiovascular Disease in the, C. Council on, and N. Stroke. 2018. Induced Pluripotent Stem Cells for Cardiovascular Disease Modeling and Precision Medicine: A Scientific Statement From the American Heart Association. *Circ Genom Precis Med*. 11:e000043.

Nag, S., D.V. Trivedi, S.S. Sarkar, A.S. Adhikari, M.S. Sunitha, S. Sutton, K.M. Ruppel, and J.A. Spudich. 2017. The myosin mesa and the basis of hypercontractility caused by hypertrophic cardiomyopathy mutations. *Nature structural & molecular biology*. 24:525-533.

Napierski, N.C., K. Granger, P.R. Langlais, H.R. Moran, J. Strom, K. Touma, and S.P. Harris. 2020. A Novel "Cut and Paste" Method for In Situ Replacement of cMyBP-C Reveals a New Role for cMyBP-C in the Regulation of Contractile Oscillations. *Circulation research*. 126:737-749.

Press, W.H. 1992. Numerical recipes in C : the art of scientific computing. 2nd.ed. Cambridge University Press, Cambridge England ; New York. xxvi, 994 p. pp.

Prondzynski, M., M.D. Lemoine, A.T. Zech, A. Horvath, V. Di Mauro, J.T. Koivumaki, N. Kresin, J. Busch, T. Krause, E. Kramer, S. Schlossarek, M. Spohn, F.W. Friedrich, J. Munch, S.D. Laufer, C. Redwood, A.E. Volk, A. Hansen, G. Mearini, D. Catalucci, C. Meyer, T. Christ, M. Patten, T. Eschenhagen, and L. Carrier. 2019. Disease modeling of a mutation in alpha-actinin 2 guides clinical therapy in hypertrophic cardiomyopathy. *EMBO Mol Med*. 11:e11115.

Prosser, B.L., C.W. Ward, and W.J. Lederer. 2011. X-ROS signaling: rapid mechano-chemo transduction in heart. *Science*. 333:1440-1445.

Ribeiro, A.J., Y.S. Ang, J.D. Fu, R.N. Rivas, T.M. Mohamed, G.C. Higgs, D. Srivastava, and B.L. Pruitt. 2015. Contractility of single cardiomyocytes differentiated from pluripotent stem cells depends on physiological shape and substrate stiffness. *Proceedings of the National Academy of Sciences of the United States of America*. 112:12705-12710.

Ribeiro, A.J.S., O. Schwab, M.A. Mandegar, Y.S. Ang, B.R. Conklin, D. Srivastava, and B.L. Pruitt. 2017. Multi-Imaging Method to Assay the Contractile Mechanical Output of Micropatterned Human iPSC-Derived Cardiac Myocytes. *Circulation research*. 120:1572-1583.

Rice, R., P. Guinto, C. Dowell-Martino, H. He, K. Hoyer, M. Krenz, J. Robbins, J.S. Ingwall, and J.C. Tardiff. 2010. Cardiac myosin heavy chain isoform exchange alters the phenotype of cTnT-related cardiomyopathies in mouse hearts. *Journal of molecular and cellular cardiology*. 48:979-988.

Risi, C., B. Belknap, E. Forgacs-Lonart, S.P. Harris, G.F. Schroder, H.D. White, and V.E. Galkin. 2018. N-Terminal Domains of Cardiac Myosin Binding Protein C Cooperatively Activate the Thin Filament. *Structure*. 26:1604-1611 e1604.

Robinson, P., P.J. Griffiths, H. Watkins, and C.S. Redwood. 2007. Dilated and hypertrophic cardiomyopathy mutations in troponin and alpha-tropomyosin have opposing effects on the calcium affinity of cardiac thin filaments. *Circulation research*. 101:1266-1273.

Robinson, P., X. Liu, A. Sparrow, S. Patel, Y.H. Zhang, B. Casadei, H. Watkins, and C. Redwood. 2018. Hypertrophic cardiomyopathy mutations increase myofilament Ca(2+) buffering, alter intracellular Ca(2+) handling, and stimulate Ca(2+)-dependent signaling. *The Journal of biological chemistry*. 293:10487-10499.

Robinson, P., M. Mirza, A. Knott, H. Abdulrazzak, R. Willott, S. Marston, H. Watkins, and C. Redwood. 2002. Alterations in thin filament regulation induced by a human cardiac troponin T mutant that causes dilated cardiomyopathy are distinct from those induced by troponin T mutants that cause hypertrophic cardiomyopathy. *The Journal of biological chemistry*. 277:40710-40716.

Robison, P., M.A. Caporizzo, H. Ahmadzadeh, A.I. Bogush, C.Y. Chen, K.B. Margulies, V.B. Shenoy, and B.L. Prosser. 2016. Detyrosinated microtubules buckle and bear load in contracting cardiomyocytes. *Science*. 352:aaf0659.

Rust, E.M., F.P. Albayya, and J.M. Metzger. 1999. Identification of a contractile deficit in adult cardiac myocytes expressing hypertrophic cardiomyopathy-associated mutant troponin T proteins. *The Journal of clinical investigation*. 103:1459-1467.

Sato, Y., D.G. Ferguson, H. Sako, G.W. Dorn, 2nd, V.J. Kadambi, A. Yatani, B.D. Hoit, R.A. Walsh, and E.G. Kranias. 1998. Cardiac-specific overexpression of mouse cardiac calsequestrin is associated with depressed cardiovascular function and hypertrophy in transgenic mice. *The Journal of biological chemistry*. 273:28470-28477.

Saucerman, J.J., P.M. Tan, K.S. Buchholz, A.D. McCulloch, and J.H. Omens. 2019. Mechanical regulation of gene expression in cardiac myocytes and fibroblasts. *Nat Rev Cardiol*. 16:361-378.

Schindelin, J., I. Arganda-Carreras, E. Frise, V. Kaynig, M. Longair, T. Pietzsch, S. Preibisch, C. Rueden, S. Saalfeld, B. Schmid, J.Y. Tinevez, D.J. White, V.

Hartenstein, K. Eliceiri, P. Tomancak, and A. Cardona. 2012. Fiji: an open-source platform for biological-image analysis. *Nature methods*. 9:676-682.
Schober, T., S. Huke, R. Venkataraman, O. Gryshchenko, D. Kryshtal, H.S. Hwang, F.J. Baudenbacher, and B.C. Knollmann. 2012. Myofilament Ca sensitization increases cytosolic Ca binding affinity, alters intracellular Ca homeostasis, and causes pause-dependent Ca-triggered arrhythmia. *Circulation research*. 111:170-179.
Sharma, A., G. Li, K. Rajarajan, R. Hamaguchi, P.W. Burridge, and S.M. Wu. 2015. Derivation of highly purified cardiomyocytes from human induced pluripotent stem cells using small molecule-modulated differentiation and subsequent glucose starvation. *J Vis Exp*.
Sheng, J.J., and J.P. Jin. 2014. Gene regulation, alternative splicing, and posttranslational modification of troponin subunits in cardiac development and adaptation: a focused review. *Front Physiol*. 5:165.
Sitbon, Y.H., K. Kazmierczak, J. Liang, S. Yadav, M. Veerasammy, R.M. Kanashiro-Takeuchi, and D. Szczesna-Cordary. 2020. Ablation of the N terminus of cardiac essential light chain promotes the super-relaxed state of myosin and counteracts hypercontractility in hypertrophic cardiomyopathy mutant mice. *FEBS J*.
Spudich, J.A. 2015. The myosin mesa and a possible unifying hypothesis for the molecular basis of human hypertrophic cardiomyopathy. *Biochemical Society transactions*. 43:64-72.
Sung, J., S. Nag, K.I. Mortensen, C.L. Vestergaard, S. Sutton, K. Ruppel, H. Flyvbjerg, and J.A. Spudich. 2015. Harmonic force spectroscopy measures load-dependent kinetics of individual human beta-cardiac myosin molecules. *Nat Commun*. 6:7931.
Sweeney, H.L., H.S. Feng, Z. Yang, and H. Watkins. 1998. Functional analyses of troponin T mutations that cause hypertrophic cardiomyopathy: insights into disease pathogenesis and troponin function. *Proceedings of the National Academy of Sciences of the United States of America*. 95:14406-14410.
Szczesna, D., R. Zhang, J. Zhao, M. Jones, G. Guzman, and J.D. Potter. 2000. Altered regulation of cardiac muscle contraction by troponin T mutations that cause familial hypertrophic cardiomyopathy. *The Journal of biological chemistry*. 275:624-630.
Tardiff, J.C., T.E. Hewett, B.M. Palmer, C. Olsson, S.M. Factor, R.L. Moore, J. Robbins, and L.A. Leinwand. 1999. Cardiac troponin T mutations result in allele-specific phenotypes in a mouse model for hypertrophic cardiomyopathy. *The Journal of clinical investigation*. 104:469-481.
Tikunova, S.B., J.A. Rall, and J.P. Davis. 2002. Effect of hydrophobic residue substitutions with glutamine on Ca(2+) binding and exchange with the N-domain of troponin C. *Biochemistry*. 41:6697-6705.
Tobacman, L.S., M. Nihli, C. Butters, M. Heller, V. Hatch, R. Craig, W. Lehman, and E. Homsher. 2002. The troponin tail domain promotes a conformational state of the thin filament that suppresses myosin activity. *The Journal of biological chemistry*. 277:27636-27642.

VanBuren, P., D.E. Harris, N.R. Alpert, and D.M. Warshaw. 1995. Cardiac V1 and V3 myosins differ in their hydrolytic and mechanical activities in vitro. *Circulation research*. 77:439-444.

Wang, L., K. Kim, S. Parikh, A.G. Cadar, K.R. Bersell, H. He, J.R. Pinto, D.O. Kryshtal, and B.C. Knollmann. 2018. Hypertrophic cardiomyopathy-linked mutation in troponin T causes myofibrillar disarray and pro-arrhythmic action potential changes in human iPSC cardiomyocytes. *Journal of molecular and cellular cardiology*. 114:320-327.

Wang, L., D.O. Kryshtal, K. Kim, S. Parikh, A.G. Cadar, K.R. Bersell, H. He, J.R. Pinto, and B.C. Knollmann. 2017. Myofilament Calcium-Buffering Dependent Action Potential Triangulation in Human-Induced Pluripotent Stem Cell Model of Hypertrophic Cardiomyopathy. *Journal of the American College of Cardiology*. 70:2600-2602.

Watkins, H., W.J. McKenna, L. Thierfelder, H.J. Suk, R. Anan, A. O'Donoghue, P. Spirito, A. Matsumori, C.S. Moravec, J.G. Seidman, and et al. 1995. Mutations in the genes for cardiac troponin T and alpha-tropomyosin in hypertrophic cardiomyopathy. *The New England journal of medicine*. 332:1058-1064.

Williams, M.R., S.J. Lehman, J.C. Tardiff, and S.D. Schwartz. 2016. Atomic resolution probe for allostery in the regulatory thin filament. *Proceedings of the National Academy of Sciences of the United States of America*. 113:3257-3262.

Yamada, Y., K. Namba, and T. Fujii. 2020. Cardiac muscle thin filament structures reveal calcium regulatory mechanism. *Nat Commun*. 11:153.

Yanaga, F., S. Morimoto, and I. Ohtsuki. 1999. Ca2+ sensitization and potentiation of the maximum level of myofibrillar ATPase activity caused by mutations of troponin T found in familial hypertrophic cardiomyopathy. *The Journal of biological chemistry*. 274:8806-8812.

Zhang, T., L.S. Maier, N.D. Dalton, S. Miyamoto, J. Ross, Jr., D.M. Bers, and J.H. Brown. 2003. The deltaC isoform of CaMKII is activated in cardiac hypertrophy and induces dilated cardiomyopathy and heart failure. *Circulation research*. 92:912-919.

5.8 Supplemental Materials

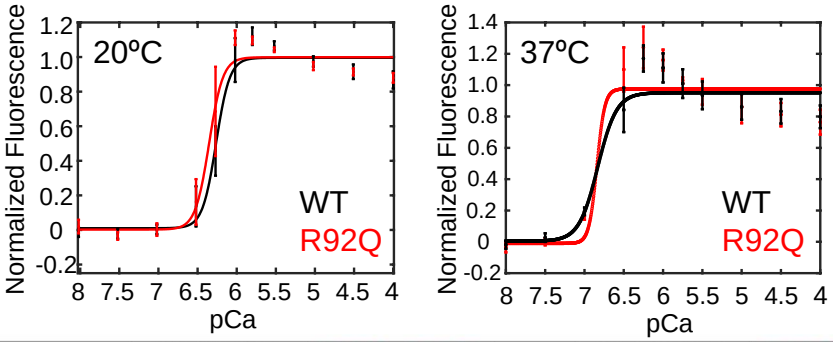

	WT (20°C)	R92Q (20°C)	p	WT (37°C)	R92Q (37°C)	p
IAANs Ca50 (μM) (n≥3)	0.55 (±0.10)	0.49 (±0.09)	0.36	0.14 (±0.11)	0.12(±0.07)	0.44
IAANs Hill (n≥3)	3.60 (±1.16)	6.59 (±2.20)	0.04	4.51 (±2.32)	8.94 (±4.33)	0.21

Fig. S1. The affinity of calcium binding to the troponin complex at 20°C and 37°C. IAANS-labeled troponin C was reconstituted into regulated thin filaments. Titrations with increasing calcium were conducted. Error bars show the standard deviation of greater than or equal to 3 experiments. Values derived from fits, standard errors in the fits, and p-values are shown. P-values were calculated using a two-tailed Student's t-test.

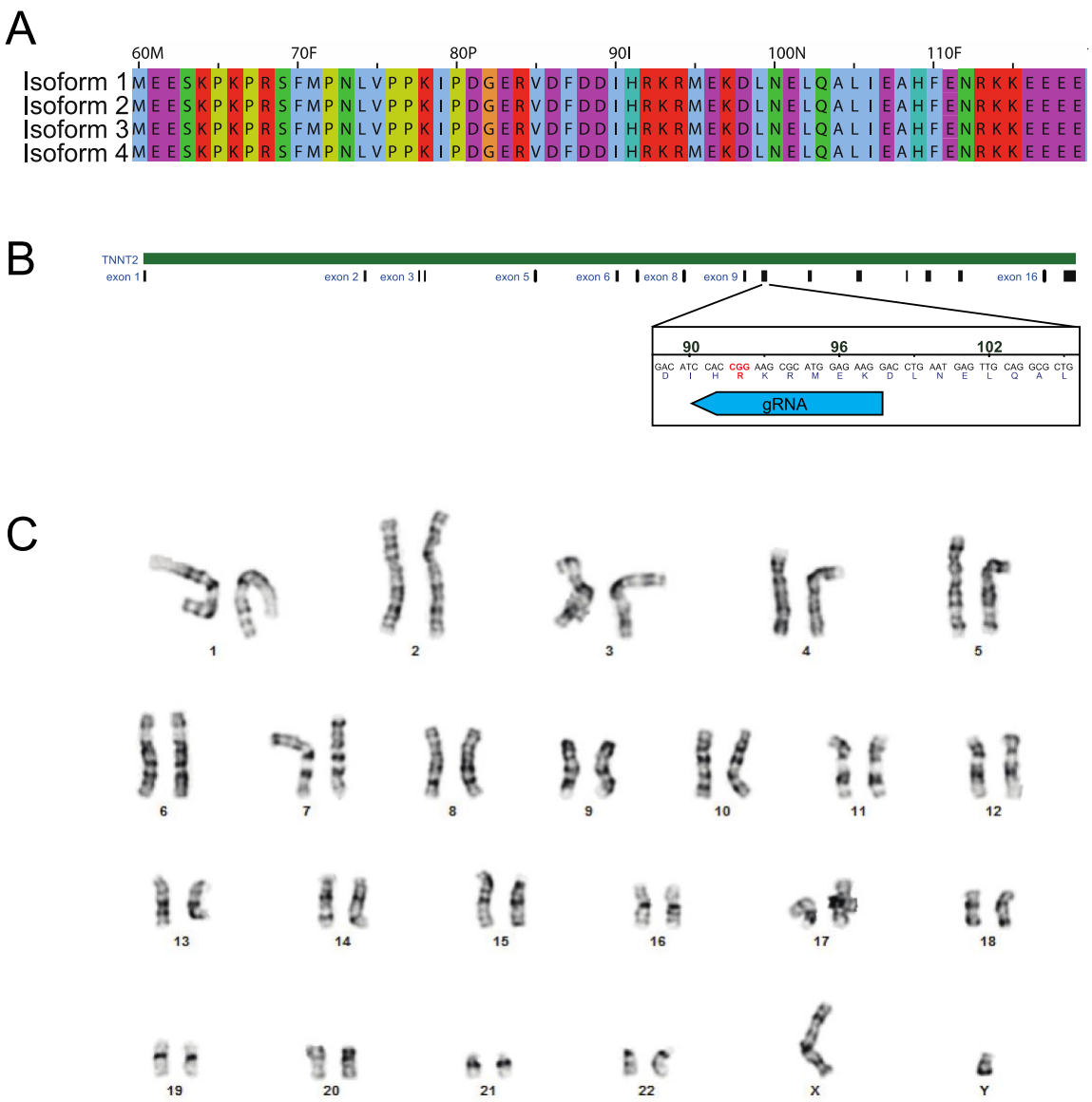

Fig. S2. Generation of gene edited hiPSC-CMs. (**A**) Sequence alignment of troponin T splice isoforms expressed in humans reveals that all isoforms contain the R92 residue. (**B**) CRISPR/Cas9 targeting of R92Q in troponin T. The R92Q mutation was added via homology directed repair. The guide RNA sequence for targeting was CCTTCTCCATGCGCTTCCGGNGG. From our screen, 21% of the cells were homozygous for the R92Q mutation (CGG -> CAA). (**C**) Karyotyping of R92Q gene edited cells reveals a normal karyotype.

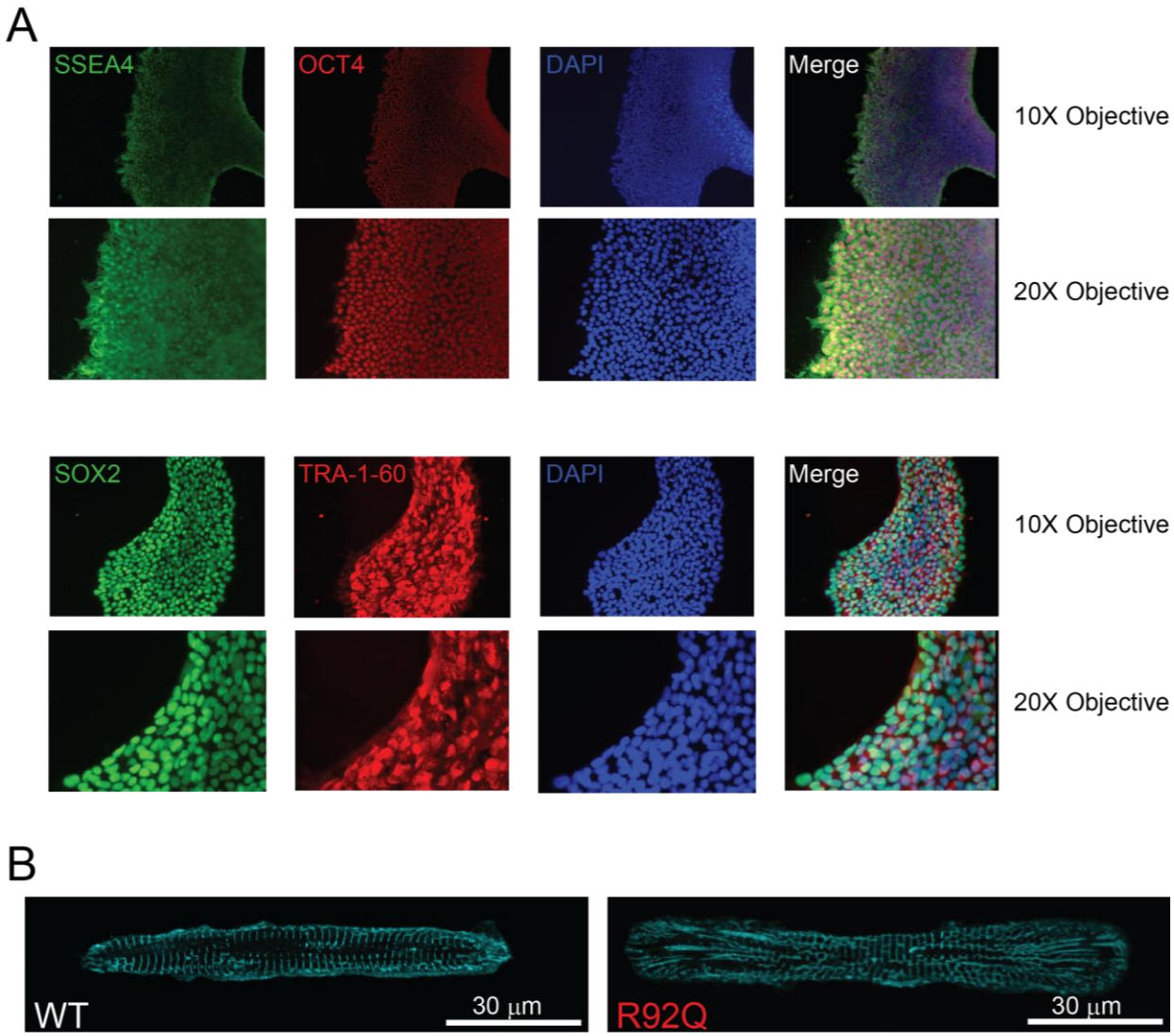

Fig. S3. Immunofluorescence images of stem cells and hiPSC-CMs. (**A**) Pluripotency staining of R92Q cells. R92Q gene edited cells are pluripotent as assessed by immunofluorescence staining for the markers SSEA4, OCT4, SOX2, and TRA-1-60. (**B**) Projections of hiPSC-CMs on glass stained for alpha actinin to mark the sarcomeric Z-discs.

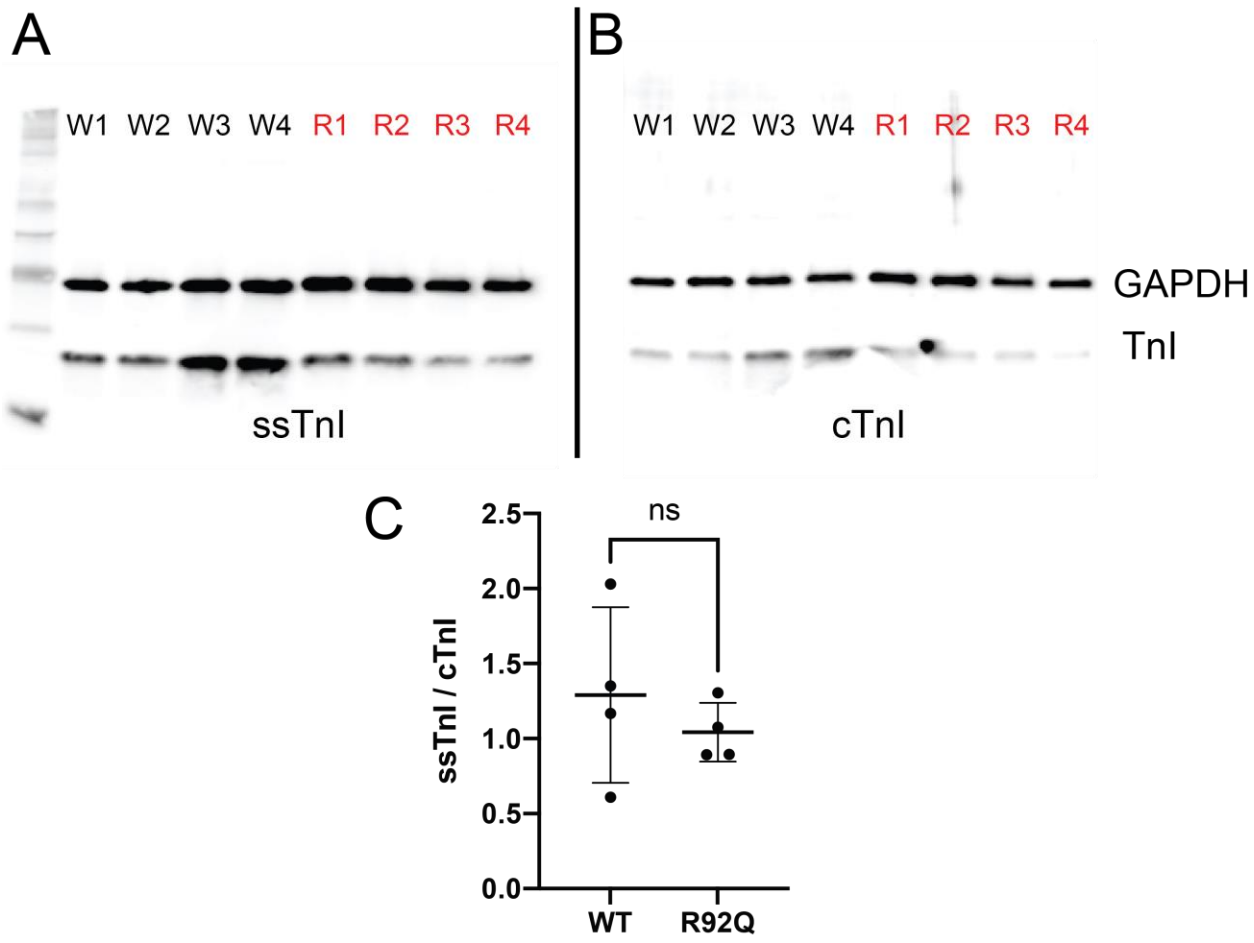

Fig. S4. The relative expression of fetal (slow skeletal) and adult (cardiac) troponin I isoforms in hiPSC-CMs. (**A**) Western blot showing the expression of the fetal isoform of troponin I (slow skeletal troponin I, ssTnI). Shown are 4 lysates from WT cells (W1, W2, W3, W4) and 4 lysates from R92Q cells (R1, R2, R3, R4). GAPDH is used as a loading control. (**B**) Western blot on a separate membrane showing the expression of the adult isoform of troponin I (cardiac troponin I, cTnI). Shown are 4 lysates from WT cells (W1, W2, W3, W4) and 4 lysates from R92Q cells (R1, R2, R3, R4). GAPDH is used as a loading control. (**C**) Quantification of the ratio of ssTnI / cTnI was determined by densitometry. The ratio of TnI / GAPDH was calculated for both ssTnI and cTnI and then divided to get the ratio. These is no difference in the ratio (p=0.49 by Mann-Whitney test).

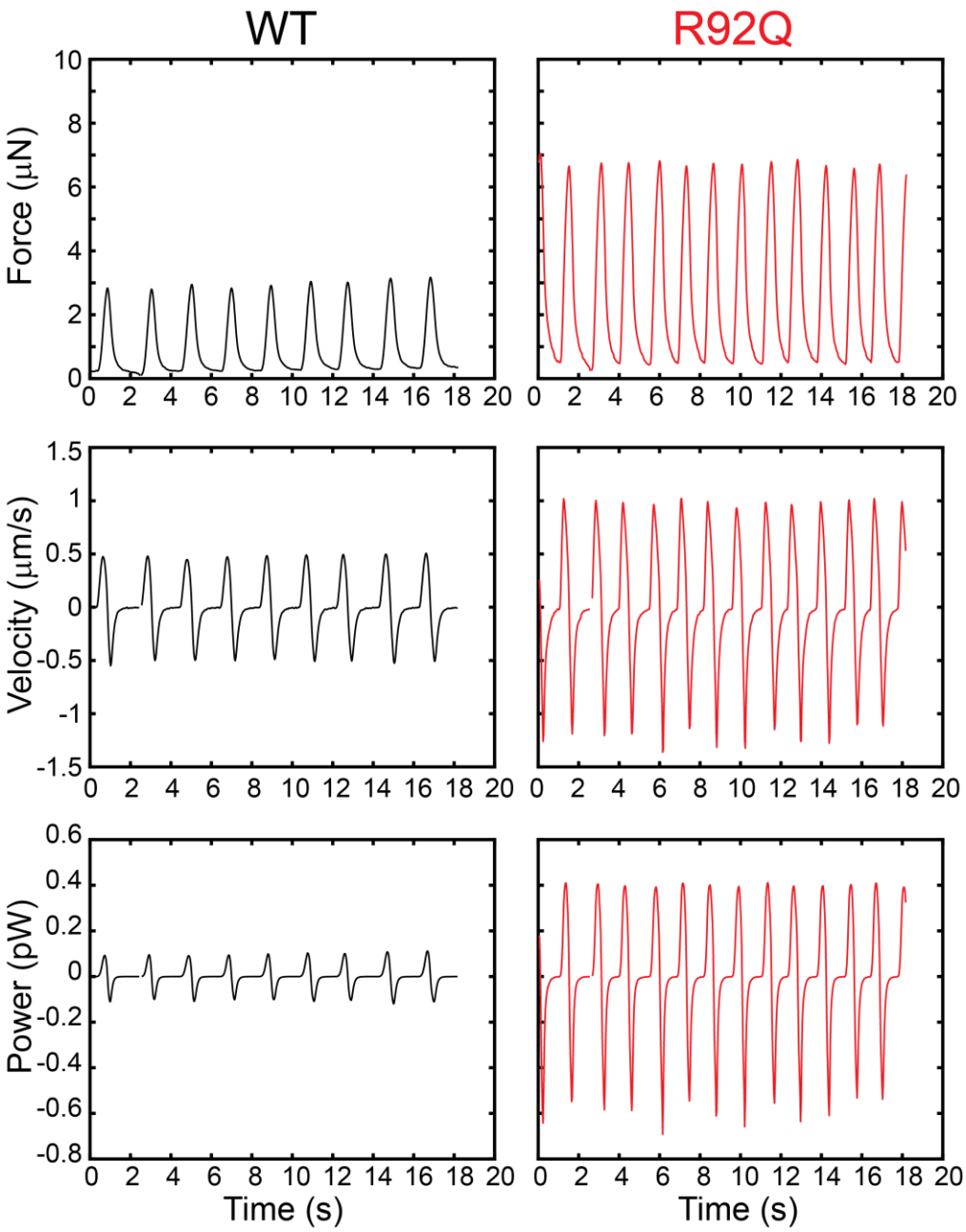

Fig. S5. Representative traces of hiPSC-CMs spontaneously beating on 10 kPa polyacrylamide gels measured by traction force microscopy. Plotted are the force of contraction, the velocity, and the power output. Positive values denote shortening and negative values denote lengthening.

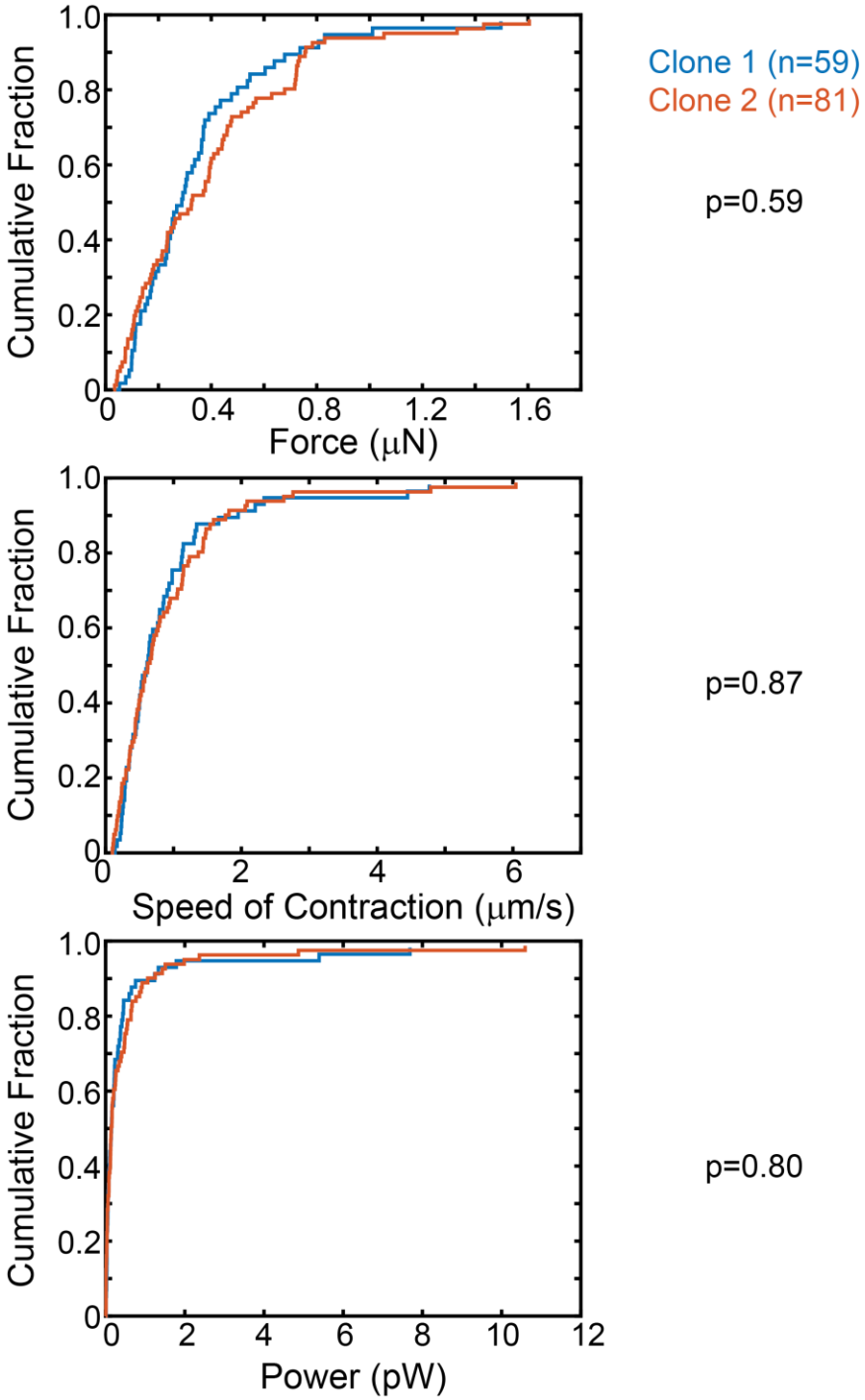

Fig. S6. Comparison of the two independently derived R92Q clones examined using traction force microscopy reveals no significant differences between the clones. Cumulative distributions showing the force, speed, and power of contraction. P-values are calculated from a Mann-Whitney U-test.

Gene Symbol	Gene Name	Product Number
PLN	Phospholamban	Hs.PT.58.23189767
ITPR2	Inositol 1,4,5-trisphosphate receptor type 2	Hs.PT.58.3479603
RYR2	Ryanodine receptor 2	Hs.PT.58.502763
CACNA1C	Calcium voltage-gated channel subunit alpha1 C	Hs.PT.58.14979004
CACNA1G	Calcium voltage-gated channel subunit alpha1 G	Hs.PT.58.4441520
CACNA1H	Calcium voltage-gated channel subunit alpha1 H	Hs.PT.58.814570
CASQ2	Calsequestrin 2	Hs.PT.56a.219158
ATP2A2	ATPase sarcoplasmic/endoplasmic reticulum Ca2+ transporting 2	Hs.PT.56a.39859858.g
SLC8A1	Solute carrier family 8 member A1	Hs.PT.58.40534466
CAMK2D	Calcium/calmodulin dependent protein kinase II delta	Hs.PT.56a.25723872.g
HPRT1	Hypoxanthine phosphoribosyltransferase 1	Hs.PT.58v.45621572
GAPDH	Glyceraldehyde-3-phosphate dehydrogenase	Hs.PT.39a.22214836

Fig. S7. RT-qPCR gene names and primers.

Gene	WT ΔCt	WT ΔCt S.D.	R92Q ΔCt	R92Q ΔCt S.D.	Fold Change	p-value
PLN	-4.83	0.27	-4.59	0.20	0.85	0.04
ATP2A2	-1.18	0.26	-1.65	0.60	1.39	0.09
CACNA1H	6.69	1.28	8.15	0.96	0.36	0.01
ITPR2	6.48	0.36	6.73	0.50	0.84	0.34
CASQ2	2.87	0.09	0.92	0.51	3.86	4.1E-5
CAMK2D	-0.10	0.26	-0.43	0.21	1.25	0.02
CACNA1G	8.86	1.36	8.32	1.35	1.46	0.19
SLC8A1	4.97	0.31	4.36	0.45	1.54	0.01
CACNA1C	1.91	0.67	2.45	0.37	0.69	0.11
RYR2	1.34	0.92	1.60	0.57	0.83	0.39

Fig S8. RT-qPCR measurements of the expression of key calcium handling genes. Three biological replicates were conducted for each experiment. Statistics were conducted on the ΔCt values, not fold-changes, and the p-value was calculated from a Mann-Whitney U test.

Action Potentials	Cells	dV/dt_{max} (mV/ms)	APD_{50} (ms)	Frequency (Hz)	MDP (mV)
Spontaneous	WT	4.5 ± 0.2	1076 ± 93	0.41 ± 0.02	-55 ± 1
	R92Q	3.3 ± 0.2*	571 ± 134‡	0.52 ± 0.06+	-50 ± 2+
Evoked	WT	73 ± 5	1053 ± 103	na	na
	R92Q	95 ± 8+	230 ± 61*	na	na

Fig. S9. Table of values from electrophysiological experiments. Values are means ± standard error of the means determined in WT (n = 58) and R92Q (n = 29) cells, where n = number of cells; dV/dt_{max} = maximal rate of change of the membrane voltage during the rising phase of the action potential; APD_{50} = action potential duration at 50% repolarization; MDP= maximum diastolic potential; na = not applicable. +, ‡, * Values in R92Q mutant cells are significantly different from those in WT cells at the +$p < 0.05$, ‡$p < 0.01$ and *$p < 0.001$ levels.

Movie S1: Displacement of beads by WT (gray) and R92Q (red) hiPSC-CMs contracting on a 10 kPa polyacrylamide gel. Videos were recorded at 30 frames per second using a spinning disc confocal microscope (Nikkon). The cell, which is not visible, is on a rectangular pattern of Matrigel with a 7:1 aspect ratio. The displacement of the beads was tracked as a function of time. Note that the two cells shown are not on the same slide/hydrogel; rather, we have merged two videos to facilitate direct visual comparison of the contractility in WT and mutant cells. As is evident in the video, force is generated primarily along the long axis of the cells. These videos were used to generate the representative traces in **Fig. S5**.

Chapter 6: Analysis of single-molecule data from optical trapping experiments

6.1 Introduction

Molecular motors like β-cardiac myosin have complex and finely tuned kinetics and mechanics, which allow them to perform their specific functions. Even minor changes in β-cardiac myosin can lead to devastating diseases (1). The development of single-molecule optical trapping techniques has given scientists the ability to study the piconewton forces and nanometer steps produced by these motors. However, analyzing the single-molecule data in an unbiased and consistent manner is challenging, and multiple different methods were used in the past. Here I present a brief history of the analysis of single-molecule data as it relates to the three-bead assay, as well as the rationale behind the software Precise Analysis of Single Molecules (SPASM), developed by the Greenberg lab and used to analyze all the data presented in Chapter 7. Finally, I will discuss the four parameters that can be manipulated in SPASM and how I performed simulations to ensure that data was being analyzed with minimal false positives and false negatives.

6.2 Overview of the three-bead assay and data analysis techniques

In the three-bead assay a dual-beam optical trap is used to trap two beads and hold them in place while the motor's track (an actin filament) is strung between the two beads forming a bead-actin-bead dumbbell. This dumbbell is then lowered unto a third bead attached to the surface of the flow cell; the bead has been coated with myosin in such a way that only a single

motor interacts with the actin at a time (2). Due to Brownian motion in solution, the trapped beads experience positional variance, and this is decreased when myosin binds to actin. This reduction in variance and displacement of the beads as myosin undergoes its powerstroke can be used to detect binding events. However, thermal diffusion of the dumbbell is often larger than that of myosin binding events making some binding events indistinguishable from baseline fluctuations (3). Thus, the method of identifying events by eye is not only extremely time consuming but can also significantly bias the data (4). In order to have unbiased analyses, the technique of mean variance was applied to data traces where sample points within a defined sliding window were used to estimate the mean variance. These mean variance estimates are then used to generate histograms which show two distinct populations where the population with the lower variance corresponds to the myosin-bound state and the population with the higher variance corresponds to the unbound state (4). This same principle can be applied to the three-bead assay except that instead of only measuring the variance of one bead, we are examining the covariance of both beads. When myosin binds to actin the mechanical coupling between the two beads is reduced and this lower covariance corresponds to the bound state.

Generation of a covariance histogram with good separation between the two peaks depends on selection of the sliding window length and smoothing of the covariance (discussed more below). Once a covariance histogram has been generated, two different thresholding techniques can be used to identify binding events. The first is “single threshold,” where the minimal value between the two peaks is used to distinguish the beginning of the event (covariance drops below this value) and the end of the event (covariance rises above this value). However, this method can have false positives. The second technique is “peak-to-peak”

in which the values of the two peaks are both used as thresholds. A binding event is selected when the covariance drops below the threshold of the unbound peak to the peak of the bound peak and vice versa for the end of the event. This method misses more true events than the single threshold method, but it does not introduce as many false positives (5).

The noise introduced by Brownian motion can obscure the second substep of the myosin working stroke (6). In order to extract this information from our data, a method called ensemble averaging is used. In ensemble averaging, the beginnings of all the binding events are synchronized and averaged forward in time, while the endings of all the binding events are synchronized and averaged backwards in time (7)(8)(9). One important challenge when generating ensemble averages is determining the exact point where the transitions from unbound to bound and bound to unbound takes place. The MATLAB program SPASM developed by the Greenberg lab uses a change-point algorithm that identifies the most likely times when there was a change in both the mean and the variance of the bead positions. Thus each individual binding event is identified by the covariance peak-to-peak method, and the two points corresponding to the transitions of myosin binding and detaching are found from the mean and variance by the change point algorithm and used to generate the ensemble average (5).

6.3 Manipulation of Window Size, covariance smoothing, minimum event duration and minimum event separation in SPASM

One goal of the data analysis performed in Chapter 7 was to minimize false-positive and false-negative events. In general this depends on the signal to noise of the data. In SPASM, there are four parameters that determine the detection of binding events, which are as follows:

1. The moving average window size, which calculates the covariance

2. The 2nd order Savitzky-Golay filter window size, which smooths the covariance
3. The minimum event duration, which removes events that are too short and most likely not true events
4. The minimum event separation which removes events that are too close together

One limitation of this approach is that ideally one already has some information about the kinetics of the motor one is studying and how the motor responds to different conditions, such as ATP concentration. Becuase we are studying β-cardiac myosin, we can simulate data based on rates previously measured in stopped-flow experiments. For analysis of force feedback data described in Chapter 7, I generated simulated data for myosin binding to actin at saturating ATP concentration (4mM ATP). The simulated data were analyzed using SPASM, and for a given set of the four parameters, true events are distinguishable from false positives or false negatives. These data were simulated for saturating ATP concentration, but the original default parameters of SPASM were optimized for lower ATP concentrations. Therefore, I wanted to test whether lowering the minimum duration and minimum separation (so as to catch more of the short-lived binding events) increased the number of missed true events without increasing the number of picked false events. The results are shown in Table 1, where the minimum duration and minimum separation were gradually decreased and the number of missed true events, picked false events and picked true events were quantified.

Table 1.

Window Size	2nd order SG filter	Minimum Duration	Minimum Separation	Missed True Events	Picked False Events	Picked True Events	Total True Events
175	73	150	173	46	2	54	100
175	73	100	123	45	2	55	100
175	73	50	73	45	2	55	100
175	73	0	23	45	2	55	100
175	73	0	0	45	2	55	100

Decreasing the minimum duration and minimum separation did not increase the number of picked false events, and it also did not significantly increase the number of picked true events. Therefore, we concluded that the data should be analyzed according to the Nyquist principle, where the minimum duration/separation should not be lower than half of the window size value. While almost half of the true events were not selected by SPASM, the number of false events was very low, showing that SPASM succeeded at minimizing false events at different ATP concentrations.

6.4 Conclusions

In summary, the SPASM program is successful at analysis of single-molecule myosin data at both low and high ATP making SPASM a powerful tool for ensemble average analysis. SPASM not only helps to eliminate bias from single-molecule analysis but accurately identifies binding/unbinding transitions and limits the number of false positive and false negative events.

6.5 References

1. J. A. Spudich, Hypertrophic and Dilated Cardiomyopathy: Four Decades of Basic Research on Muscle Lead to Potential Therapeutic Approaches to These Devastating Genetic Diseases. *Biophys. J.* **106**, 1236–1249 (2014).

2. J. A. Finer, Jeffrey T., Simmons, Robert M., Spudich, Single myosin molecule mechanics: piconewton forces and nanometre steps. *Nature* **368**, 113–119 (1994).
3. A. D. Mehta, J. T. Finer, J. A. Spudich, Detection of single-molecule interactions using correlated thermal diffusion. *Proc. Natl. Acad. Sci.* **94**, 7927 LP – 7931 (1997).
4. W. H. Guilford, *et al.*, Smooth muscle and skeletal muscle myosins produce similar unitary forces and displacements in the laser trap. *Biophys. J.* **72**, 1006–1021 (1997).
5. T. Blackwell, W. T. Stump, S. R. Clippinger, M. J. Greenberg, Computational Tool for Ensemble Averaging of Single-Molecule Data. *Biophys. J.* **120**, 10–20 (2021).
6. M. J. Greenberg, H. Shuman, E. M. Ostap, Inherent force-dependent properties of β-cardiac myosin contribute to the force-velocity relationship of cardiac muscle. *Biophys. J.* **107**, L41–L44 (2014).
7. C. Veigel, F. Wang, M. L. Bartoo, J. R. Sellers, J. E. Molloy, The gated gait of the processive molecular motor, myosin V. *Nat. Cell Biol.* **4**, 59–65 (2002).
8. C. Veigel, J. E. Molloy, S. Schmitz, J. Kendrick-Jones, Load-dependent kinetics of force production by smooth muscle myosin measured with optical tweezers. *Nat. Cell Biol.* **5**, 980–986 (2003).
9. C. Chen, *et al.*, Kinetic schemes for post-synchronized single molecule dynamics. *Biophys. J.* **102**, L23–L25 (2012).

Chapter 7: Step size and kinetics of cardiac myosin crossbridges are not affected by troponin and tropomyosin (first draft)

Sarah R Clippinger Schulte, W. Tom Stump, Thomas Blackwell, Michael J. Greenberg

Author contributions: SCS purified proteins, performed optical trapping experiments, analyzed data, and drafted the manuscript. WTS built the optical trap and wrote software for data acquisition. TB wrote the computational tool used for data analysis.

7.1 Introduction

The human heart is finely tuned to generate the appropriate power necessary to pump blood against cardiac afterload. The cardiac regulatory proteins tropomyosin (Tm) and troponin (Tn) have been studied extensively in their role of controlling myosin's ability to bind to actin and produce force in a calcium-dependent manner. Experimental (1) and structural (2)(3)(4) evidence now shows that Tm and Tn exist in three different states of the thin filament (TF), termed the blocked, closed and open states. In the absence of calcium, the TF is in the blocked state, where the myosin binding site on actin is completely occluded by Tm. Upon calcium binding to Tn, tropomyosin undergoes a conformational shift leading to the closed position where myosin can weakly bind to actin. However, only in the open state can myosin strongly bind and produce force (5). The role of mutations in both β-cardiac myosin (βCM) (6) (7) and thin filament (8) (9) (10) (11) (12) proteins in familial cardiomyopathies has been studied extensively by us and others in recombinant systems, animal models, cells and modeled computationally (13). Elegant single-molecule experiments have determined the mechanics and kinetics of βCM's interaction with actin. However, at a single-molecule level we do not yet understand the impact of cardiac Tm and Tn on the step size and mechanics of βCM, as well as how these regulatory proteins affect myosin function under load. In this work, we determined that the presence of Tm and Tn do not affect the step size of βCM or the force sensitivity. The changes we observed in kinetics may not be biologically relevant. These parameters we determined will serve as important tools for modeling the heart's force velocity relationship in the case of disease.

The role of regulatory proteins in modulating myosin function

At the single-molecule level, the ways in which regulatory proteins like Tm and Tn affect myosin's ability to bind and produce force are not well understood. Optical trapping and the three-bead assay have allowed parameters such as step size, kinetics of myosin binding and detaching and force sensitivity to be determined with high spatial and temporal resolution (14). The importance of these assays lies in the fact that myosins function as mechanosensors and respond to forces they experience at the cellular and tissue level (15). However, the number of applications of these techniques to study regulatory proteins remains few. One of the first was performed by the Warshaw lab where they argued that Tm and Tn affect the step size of skeletal muscle myosin by decreasing the total step size by half; however, not all cardiac proteins were used (16). The Trybus lab found that Myosin V in yeast is only processive on actin decorated with Tpm1p (17), and work from the Manstein lab showed that Tm4.2 (prominent in growth cones of developing neurons) increased the force sensitivity of non-muscle myosin-2A (18). These few studies are all of the single-molecule studies that have examined regulatory proteins, but the potential complexity is far greater. For example, tropomyosin exists in more than 40 different isoforms generated by alternative splicing from four genes which display distinct cellular functions (19). It is widely assumed that myosin's interaction with regulatory proteins depends on the specific isoforms of the proteins. Therefore, in this work cardiac forms of actin, myosin (βCM) and Tm and Tn were used for all experiments.

7.2 Results

Unloaded kinetics

In order to determine whether cardiac Tm and Tn effect the unloaded kinetics of the actomyosin interaction, we first measured the rate of ADP release from myosin which limits how fast ATP can bind and therefore limits actomyosin dissociation at saturating ATP. The presence of regulatory proteins did not alter the kinetics of ADP release from myosin (Fig 1A). To determine if regulatory proteins affect ATP-induced dissociation of myosin from actin at lower ATP concentrations (where ADP release it not rate-limiting), we rapidly mixed varying concentrations of ATP with pyrene-labeled actin, S1 and regulatory proteins. The data at each ATP concentration was best described by a two exponential fit with a fast phase (Fig 1C) and a slow phase (Fig 1D) with Fig 1B showing the ratio of the fast amplitude to the slow amplitude. (20)(21) For the fast phase, the initial linear increase (shown in inset) corresponds to the rate of ATP binding while the k_{max} corresponds to k_{+2} in Scheme 1. Consistent with previous work k_{+2} for unregulated was 1220 s^{-1} (-55/+56), however regulated was significantly slower at 1084 s^{-1} (-49/+49, p-value=0.01) (21). The slow phase k_{obs} ($k_{+\alpha}$ in scheme 1) which is mostly ATP independent is consistent with that rate of ADP release measured by us and others but slightly faster for regulated (Fig 1D). Where the ratio of the fast to slow amplitudes plateaus, this corresponds to the equilibrium constant (K_a) describing the transition between actin-bound myosin from a state unable to bind nucleotide (AM*) to an isomerized state (AM) that can bind ATP. Our measurements show that the addition of regulatory proteins shifts the equilibrium to favor the ATP-insensitive state (AM*) compared to the state without regulatory proteins (Fig 1B). Overall, these data show that regulatory proteins do not affect actomyosin dissociation at

saturating ATP but do slow ATP binding at lower ATP concentrations.

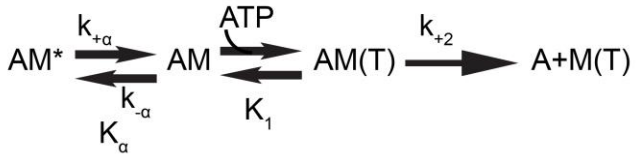

Achieving regulation with biotinylated actin

For optical trapping experiments, we form an actin-filament dumbbell through a biotin streptavidin linkage. To ensure that biotinylated actin does not interfere with the regulation of Tm and Tn on the actin surface, we performed *in vitro* motility experiments at both low (pCa9) and high (pCa 4) calcium. Calcium-based regulation was observed, and there was no significant difference in average speed between bare actin (0.26 ± 0.08 μm/sec) and biotinylated actin (0.25 ± 0.08 μm/sec) at pCa 4 (p-value = 0.19) (Fig 2A). At pCa 9 there was no motility for either bare actin or biotinylated actin (data not shown). Next, using the three-bead assay (14) in the optical trap, we showed that, in the presence of Tm and Tn, myosin binding is very rare at pCa 9 but frequent at pCa 4 (Fig 2B). This result indicates that in the presence of low concentrations of biotin actin (10%), the regulation of Tm and Tn is not significantly affected at either pCa 4 or pCa 9.

The step size of myosin is not affected by Tm and Tn

While the step size and the kinetics of β-cardiac myosin has been previously reported, these parameters have not been measured in the presence of the cardiac regulatory proteins Tm and

Tn. (22)(23) We therefore compared unregulated actin to regulated actin at pCa 4 in the presence of low ATP (1uM ATP) to help resolve the two-step working stroke of myosin (22). Individual traces (Fig 3A) were analyzed using the Matlab program SPASM (24), and the combined data were used to generate ensemble averages showing the rate of the time forward average (k_f) and the rate of the time reverse average (k_r) (25)(26)(27). The k_f (corresponding to the rate of ADP release) was 32.1 s^{-1} for unregulated and 30.4 s^{-1} for regulated while k_r (corresponding to the rate of ATP-induced myosin dissociation from actin) was 5.7 s^{-1} for unregulated and 5.1 s^{-1} for regulated (p-values 0.52 and 0.16 respectively Fig 3B). While the rates of k_f were lower than that measured in the stopped flow (Fig 1A) these values are consistent with previous measurements (28). Therefore, at low ATP the mechanics of the two-step working stroke are unaffected by Tm and Tn. This result contrasts with previous work finding that the presence of Tm and Tn decreased the total step size by half (16); however, not all the proteins used in this study were cardiac ones, which may explain the discrepancy. The cumulative distributions of step 1, step 2, and the total step size also show that unregulated and regulated actin thin filaments are almost identical (Fig 3C-E). On the other hand, the cumulative distributions of event duration showed a significant difference, consistent with Tm and Tn slowing ATP binding (Fig 3F).

Tm and Tn do not affect detachment kinetics under load

It had been shown that force slows the rate of actomyosin detachment by inhibiting the mechanical transition of myosin associated with ADP release (22). However, how cardiac Tm and Tn affect this force dependence has not been studied. Using a positional feedback optical

clamp, the actin dumbbell is kept at a fixed position by movement of the motor bead (Fig 4A), thereby applying a dynamic load to myosin in response to myosin's working stroke (29). Binding events for unregulated and regulated actin were collected at saturating (4mM) Mg.ATP to ensure that ATP binding was not rate-limiting for detachment and that the force-dependent transition of ADP release was being examined. Individual traces were also analyzed using SPASM and used to generate the force dependence of the attachment duration (Fig 4B). Data were fit to the bell equation using the maximum likelihood estimation fitting tool MEMLET (30) where k(F) is the force-dependent actin detachment rate, k_0 is the rate of the force-sensitive transition (ADP release) at zero force, F is the force exerted on myosin, d is the measurement of force sensitivity, k_B is Boltzmann's constant, and T is the temperature (31). There was no significant difference in k_0 between unregulated (31.8 s^{-1} (-4.9/+7.3)) and regulated (30.9 s^{-1} (-5.8/+8.1)) actin (p-value=0.75). These rates are slightly slower than those from previous measurements (50-70 s^{-1}), however they are consistent with results from other studies (28), and they are consistent with the rate of ADP release obtained from the ensemble averages in this study (Fig 3B). The force sensitivity (d) was also not significantly different (0.5 nm -0.3/+0.2 for unregulated and 0.6 nm -0.4/+0.4 for regulated, p-value=0.6), and the values were similar to previous measurements for bare actin (0.97 nm), indicating that cardiac myosin in the presence of Tm and Tn still has a relatively mild slowing of the ADP release transition compared to other myosins (32).

7.3 Discussion

In this work we used our custom-built optical trap to determine the effect of the cardiac

regulatory proteins Tm and Tn on the mechanics and kinetics of βCM. We found that at low ATP the step size and ensemble average rates of k_f and k_r are unaffected by the presence of regulatory proteins (Fig 3). The difference in detachment rate between regulated and unregulated TF was significant, and this is consistent with our ATP-binding experiments showing that regulatory proteins slow ATP binding (Fig 1). These results differ from the results of the Warshaw lab in which the myosin step size decreased from ~10 nm to 5 nm in the presence of regulatory proteins.

There are a few potential explanations for this discrepancy. One is the use of non-cardiac isoforms in the Warshaw study. The Warshaw study argued that the decrease in step size was caused by only one of myosin's heads being able to bind in the presence of Tm and Tn. While it is certainly true that at low calcium Tm and Tn prevents optimal interaction with actin, it is well established that βCM is a low-duty motor meaning it does not spend the majority of its cycle strongly bound to actin (21). And while the presence of force does slightly increase the time that βCM is strongly bound by slowing the rate of ADP release (22) , this increase is small when compared to what is observed for other myosin isoforms (15). Therefore, it is very unlikely that both of βCM's heads would be attached to actin at the same time. In addition, multiple groups have independently determined that the step size of βCM is closer to 6 nm (23) (33). However, while it has been shown that the two heads of a single myosin do not interact cooperatively, there is evidence that when one myosin binds and helps to push Tm into the open position, this subsequently makes it easier for neighboring myosins to bind to actin and produce force. This work only examined single binding events, and it would be interesting to investigate how Tm and Tn affect cooperative binding of multiple myosins. In previous work we found that

cardiomyopathy-causing mutations increase or decrease the population of thin filament in the open state, thereby increasing or decreasing force production. Based on the results presented here, we predict that in the optical trap, this would translate to either an increase or decrease in the number of binding events.

7.4 Conclusions

The recent development of computational models to examine potential effects of cardiomyopathy causing mutations have given great insight into mechanisms that are viable targets for therapeutics (13)(34)(35). The parameters measured here will serve as crucial tools for accurate modeling of the heart's force velocity relationship in the case of disease.

7.5 Material and Methods

Recombinant Proteins

Cardiac actin and myosin were purified from porcine ventricles and human troponin and tropomyosin were expressed recombinantly in E. coli as described previously (10).

ADP release and ATP binding

Stopped-flow experiments were performed in a SX-20 apparatus (Applied Photophysics). ADP release experiments were performed as described previously. (10) ATP binding experiments were performed by rapidly mixing either regulated (1.5 μM Tm and Tn) or unregulated pyrene-labeled actin (1 μM) and myosin S1 (1 μM) with varying concentrations of ATP. Myosin dissociation from pyrene actin upon binding of ATP caused an increase in fluorescence signal which was fit with a double exponential. The exact concentration of each ATP solution was

measured spectroscopically and the parameters from scheme 1 were determined as described previously (20).

In Vitro Motility

In vitro motility was performed as described previously except that 10% biotin-actin (Cytoskeleton) was added to 2 μM G-actin stabilized with tetramethylrhodamine isothiocyanate-labeled phalloidin in KMg25 buffer (60 mM MOPS pH 7.0, 25 mM KCl, 2mM EGTA, 4 mM $MgCl_2$, 1 mM DTT) (10).

Optical trapping experiments

Experiments were performed on a custom-built, microscope free dual beam optical trap described previously (24). Tm was dialyzed into KMg25 buffer before being used in experiments. Experiments at low ATP (1 μM ATP) were performed as described previously except that data was acquired at 20 kHz for all experiments (24). Briefly, all experiments were performed in KMg25 buffer and all buffers and dilutions were prepared fresh each day. Flow cells were loaded with myosin (3-7 nM in KMg25 with 200 mM KCl) for 5 minutes and the blocked with 1mg/mL BSA for 5 minutes. For low ATP experiments, the activation buffer contained KMg25 with 1 μM ATP, 192 U/mL glucose oxidase, 48 ug/mL catalase, 1 mg/mL glucose and ~25 pM Biotin-rhodamine-phalloidin actin with 200 nM Tm and Tn at pCa 4 (calculated using WebmaxC Standard) for regulated actin. For high ATP experiments 4 mM ATP and 4 mM $MgCl_2$ were used in the activation buffer with 200 nM Tm and Tn at pCa 4 for regulated actin. This was followed with a small amount (3-4 μL) of streptavidin beads. Trapping experiments were conducted as previously described (36) (24). For force feedback experiments,

once binding interactions were detected feedback was turned on and data was collected at 20 kHz. However, due to the short duration of the binding events at saturating ATP it was sometimes beneficial to search surface beads for myosin binding in the feedback mode.

Design of isometric optical clamp feedback

In an isometric optical clamp feedback experiment, one bead (the "transducer") is continuously sampled for position changes, and deviations from its original "setpoint" position are compensated for by moving the second ("motor") bead. Briefly, the positions of the beads are monitored using quadrant photodiodes, the feedback calculations are digitally performed on a field programmable gate array (FPGA) board (National Instruments PCIe-7852), and the laser controlling the motor bead is translated using acoustic optical deflectors.

The error signal used for the feedback, V_t, is the time filtered positional error for the current sample period given by:

$$V_t = K_p E_t + K_i \sum_{k=t}^{t-W} E_k$$

where K_p is the user defined proportional gain, K_i is the user defined integral gain, E_t is the current sample's absolute error from the setpoint, and W is the user defined integration window (up to a 255-sample memory). The compensating position for the motor bead in frequency units is then calculated by the FPGA and transmitted to the parallel port interface of the Digital Frequency Synthesizer (Analog Devices AD9912A/PCBZ) which controls the beam deflection angle from the AOD crystal (Gooch and Housego). The feedback loop can run at a maximal speed of 50 kHz, limited by parallel port cable capacitance.

The time constant for the feedback response time was set as previously described. Briefly, a bead-actin-bead dumbbell was held in the dual beam traps, a square wave was injected into the transducer bead channel, and then movement of the motor bead by the feedback system was monitored. The proportional and integral gains were empirically adjusted to give a response time of 5 ms without introducing oscillations into the system.

Analysis of single-molecule data

All data from optical trapping experiments was analyzed using the MATLAB program SPASM using the peak-to-peak method (36) (24). For low ATP experiments, individual traces with detachment rates greater than 10 s^{-1} were excluded due to the low probability of having myosin bound longer at 1 μM ATP. At saturating ATP, individual traces with detachment rates lower than 13 s^{-1} were excluded due to the low probability of having myosin bound for a shorter time at 4 mM ATP.$MgCl_2$. Data was also excluded if the separation between the bound and unbound populations of the covariance histogram was not well defined as the analysis becomes more susceptible to false and/or missed binding interactions (24). Data from ensemble averages were fit in MATLAB until the signal plateaued (200 milliseconds for the k_f and 400 milliseconds for k_r). Mean Step 1, mean step 2 and mean total step were calculated from the average of bead A and bead B for each event. P-values were derived using a two-tailed Student's t-test. P-values of kf and kr were derived from 95% confidence intervals of the fit. The p-value of the detachment rates was derived from a Mann-Whitney test.

For force feedback experiments the relationship between the detachment rate and force was modeled as a single step process as done previously (22) and fit to the data using the maximum

likelihood estimation (MLE) MATLAB tool MEMLET (30). 95 % confidence intervals for the MLE fitting were determined using bootstrapping simulations and the bootstrap data was used to generate p-values using our previously published hypothesis testing tool (37).

7.6 Figures

Fig 1

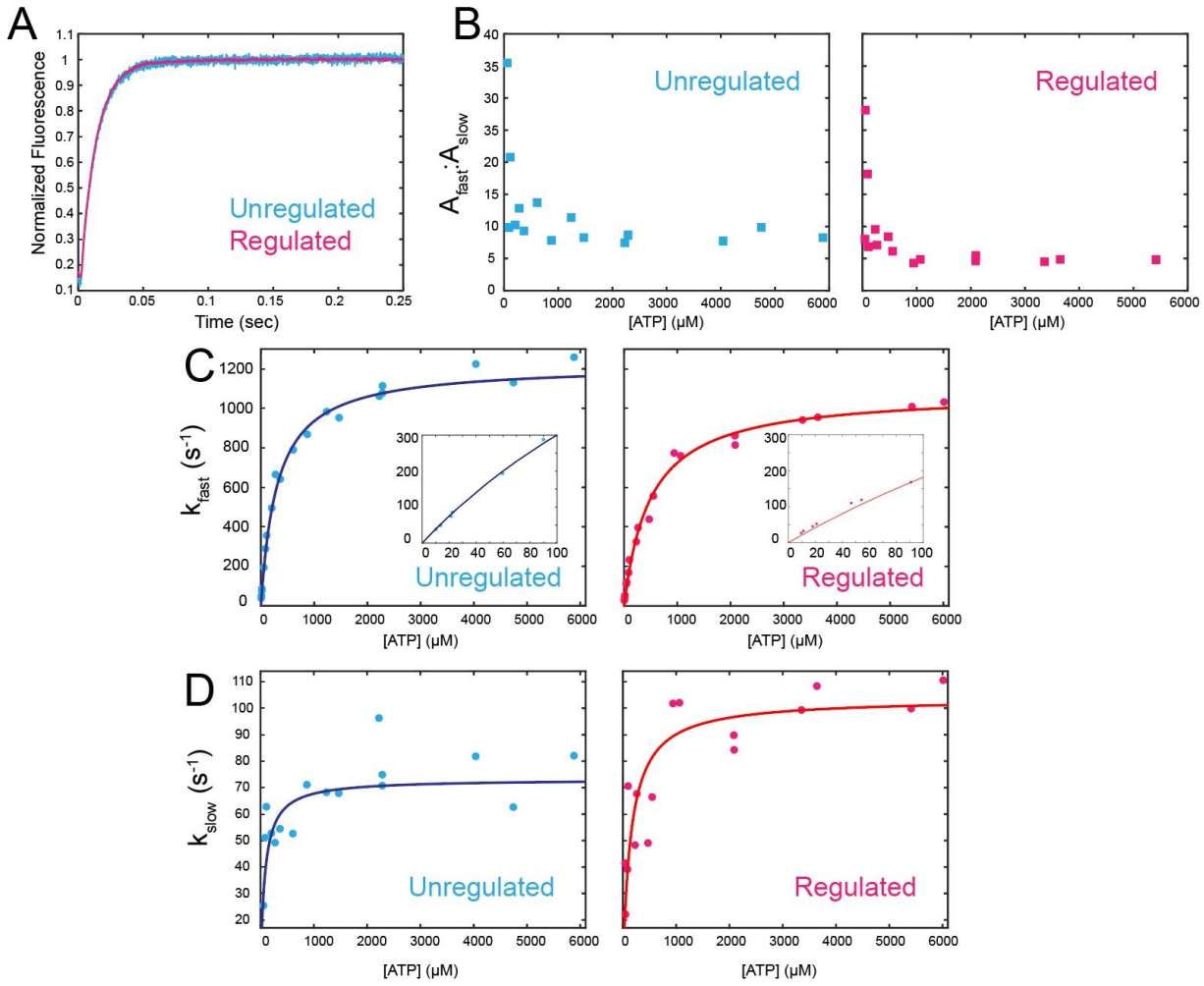

	Unregulated	Regulated	P-Value
K_α	8.4 (-0.8/+0.8)	4.9 (-0.3/+0.3)	<0.00001
$k_{+\alpha}$ (s^{-1})	73.2 (-9.8/+9.4)	103.7 (-14/+14)	0.01
$k_{-\alpha}$ (s^{-1})	8.7	21.2	
$1/K_1$	305.8 (-59/+59.1)	496.3 (-82/+82)	0.008
k_{+2} (s^{-1})	1220 (-55/+56)	1084 (-49/+49)	0.01

Figure 1. Stopped-flow assays to compare regulated and unregulated thin filaments. **A.** Measurement of ADP release showed no difference between regulated and unregulated. **B-D.** Measurement of ATP-induced dissociation of myosin from actin was best described by a two exponential fit with a fast phase (C) and a slow phase (D). The inset in (C) shows the initial linearincrease corresponding to the rate of ATP binding. (B) shows the ratio of the fast amplitude to the slow amplitude.

Fig 2

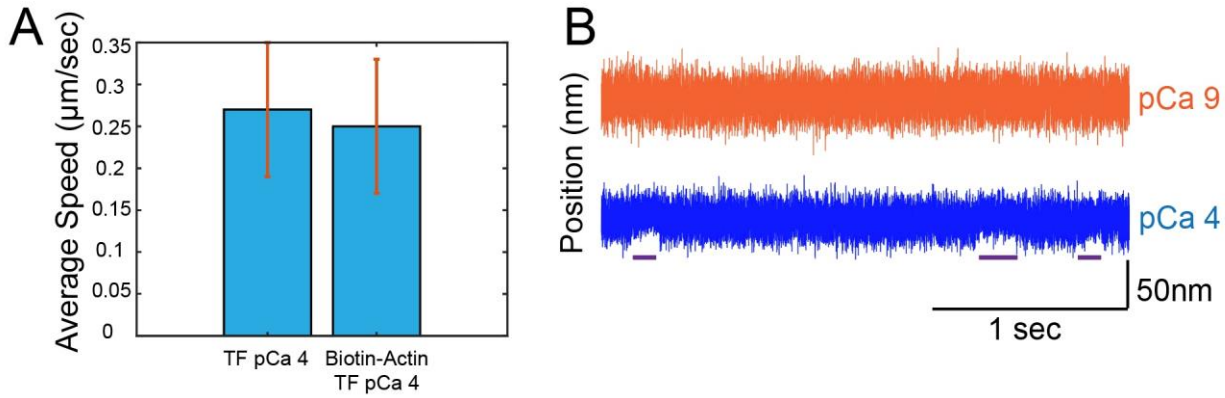

Figure 2. A. in vitro motility showed no significant difference in average speed between regulated thin filaments with and without biotin-labeled actin at pCa 4. **B.** To ensure regulation was being achieved in the three-bead optical trap assay experiments were performed at pCa 9 and pCa 4. At pCa 9 binding events were very rare and at pCa 4 binding events were frequent (purple lines indicate binding event).

Fig 3

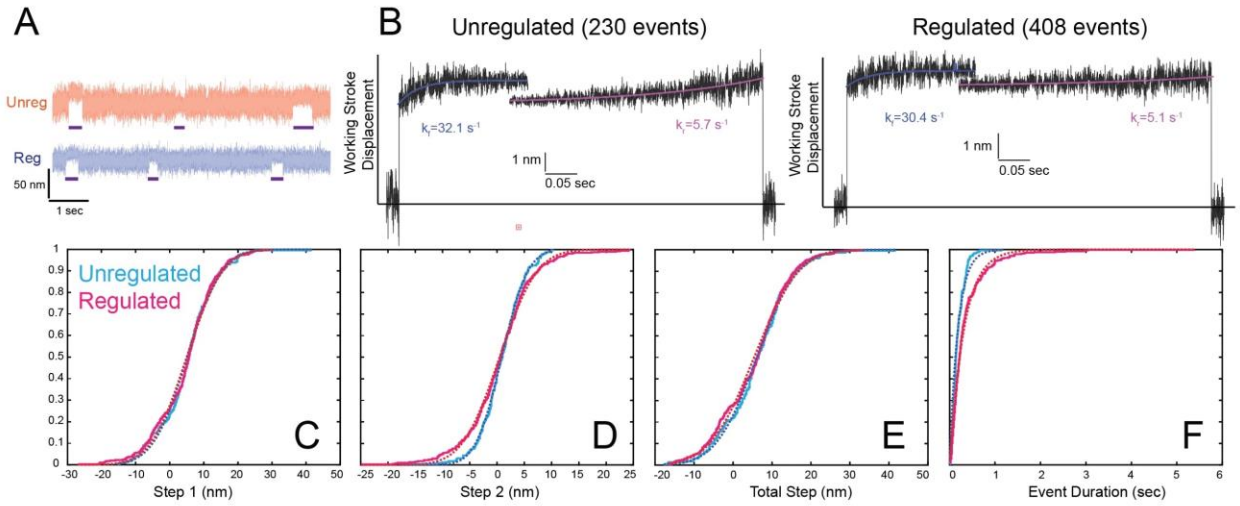

	Unregulated (230 events)	Regulated (408 events)	P-Value
Mean Step 1 Size (nm)	5.4 (±8.3)	4.8(±8.7)	0.40
Mean Step 2 Size (nm)	0.9(±4.0)	0.6(±6.2)	0.39
Mean Total Step Size (nm)	6.3 (±8.7)	5.4 (±8.9)	0.19
kf (s^{-1})	32.1 (-1.2/+1.2)	30.4 (-3.9/+3.9)	0.52
kr (s^{-1})	5.7 (-0.2/+0.3	5.1 (-0.6/+0.5)	0.16
Detachment rate (s^{-1})	5.4	2.8	<0.00001

Figure 3. A. Representative traces from the three-bead assay for regulated and unregulated thin filament. **B-C.** Ensemble averages of all collected data where k_f is a measure of the rate of ADP release and k_r is a measure of the rate of ATP induced myosin dissociation from actin. **D-G.** Cumulative distributions of the first step (D), second step (E), total step (F) and event duration.

Fig 4

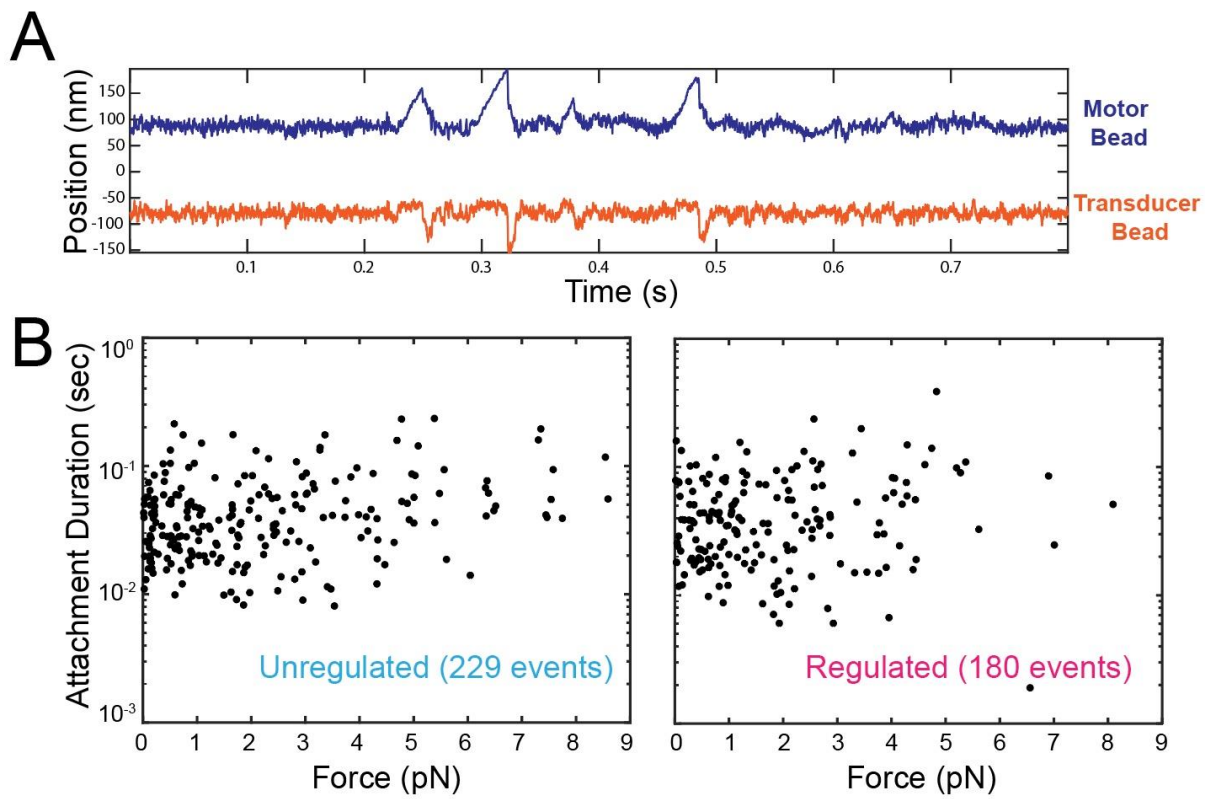

	Unregulated (229 events)	Regulated (180 events)	P-Value
k_0 (s^{-1})	31.8 (-4.9/+7.3)	30.9 (-5.8/+8.1)	0.75
d (nm)	0.5 (-0.3/+0.2)	0.6 (-0.4/+0.4)	0.60

Figure 4. A. Representative traces using a positional feedback optical clamp where the motor bead moves to compensate for the force being exerted by myosin while the position of the transducer bead stays constant. **B.** Attachment durations as a function of force for unregulated and regulated binding events. Data was fit in the MATLAB program MEMLET using Bell's equation (not shown) to obtain k_0 and d.

7.7 References

1. D. F. McKillop, M. A. Geeves, Regulation of the interaction between actin and myosin subfragment 1: evidence for three states of the thin filament. *Biophys. J.* **65**, 693–701 (1993).
2. S. Takeda, A. Yamashita, K. Maeda, Y. Maéda, Structure of the core domain of human cardiac troponin in the Ca2+-saturated form. *Nature* **424**, 35–41 (2003).
3. K. J. V. Poole, *et al.*, A comparison of muscle thin filament models obtained from electron microscopy reconstructions and low-angle X-ray fibre diagrams from non-overlap muscle. *J. Struct. Biol.* **155**, 273–284 (2006).
4. Y. Yamada, K. Namba, T. Fujii, Cardiac muscle thin filament structures reveal calcium regulatory mechanism. *Nat. Commun.* **11**, 1–3 (2020).
5. R. Craig, W. Lehman, Crossbridge and tropomyosin positions observed in native, interacting thick and thin filaments11Edited by W. Baumeister. *J. Mol. Biol.* **311**, 1027–1036 (2001).
6. J. A. Spudich, The myosin mesa and a possible unifying hypothesis for the molecular basis of human hypertrophic cardiomyopathy. *Biochem. Soc. Trans.* **43**, 64–72 (2015).
7. J. A. Spudich, *et al.*, Effects of hypertrophic and dilated cardiomyopathy mutations on power output by human β-cardiac myosin. *J. Exp. Biol.* **219**, 161–167 (2016).
8. R. Coppini, *et al.*, Clinical Phenotype and Outcome of Hypertrophic Cardiomyopathy Associated With Thin-Filament Gene Mutations. *J. Am. Coll. Cardiol.* **64**, 2589–2600 (2014).
9. J. G. Seidman, C. Seidman, The Genetic Basis for Cardiomyopathy: from Mutation Identification to Mechanistic Paradigms. *Cell* **104**, 557–567 (2001).
10. S. R. Clippinger, *et al.*, Disrupted mechanobiology links the molecular and cellular phenotypes in familial dilated cardiomyopathy. *Proc. Natl. Acad. Sci. U. S. A.* **116**, 17831–17840 (2019).
11. S. R. Clippinger, *et al.*, Mechanical dysfunction of the sarcomere induced by a pathogenic mutation in troponin T drives cellular adaptation. *J. Gen. Physiol.* **153** (2021).
12. J. E. Ezekian, *et al.*, Variant r94c in tnnt2-encoded troponin t predisposes to pediatric restrictive cardiomyopathy and sudden death through impaired thin filament relaxation resulting in myocardial diastolic dysfunction. *J. Am. Heart Assoc.* **9** (2020).
13. J. Davis, *et al.*, A Tension-Based Model Distinguishes Hypertrophic versus Dilated Cardiomyopathy. *Cell* **165**, 1147–1159 (2016).
14. J. A. Finer, Jeffrey T., Simmons, Robert M., Spudich, Single myosin molecule mechanics: piconewton forces and nanometre steps. *Nature* **368**, 113–119 (1994).
15. M. J. Greenberg, G. Arpağ, E. Tüzel, E. M. Ostap, A Perspective on the Role of Myosins as Mechanosensors. *Biophys. J.* **110**, 2568–2576 (2016).
16. N. M. Kad, S. Kim, D. M. Warshaw, P. VanBuren, J. E. Baker, Single-myosin crossbridge interactions with actin filaments regulated by troponin-tropomyosin. *Proc. Natl. Acad. Sci. U. S. A.* **102**, 16990–16995 (2005).
17. A. R. Hodges, *et al.*, Tropomyosin is essential for processive movement of a class V myosin from budding yeast. *Curr. Biol.* **22**, 1410–1416 (2012).
18. N. Hundt, W. Steffen, S. Pathan-Chhatbar, M. H. Taft, D. J. Manstein, Load-dependent

modulation of non-muscle myosin-2A function by tropomyosin 4.2. *Sci. Rep.* **6**, 1–12 (2016).
19. H. Vindin, P. Gunning, Cytoskeletal tropomyosins: choreographers of actin filament functional diversity. *J. Muscle Res. Cell Motil.* **34**, 261–274 (2013).
20. M. J. Greenberg, T. Lin, Y. E. Goldman, H. Shuman, E. M. Ostap, Myosin IC generates power over a range of loads via a new tension-sensing mechanism. *Proc. Natl. Acad. Sci. U. S. A.* **109** (2012).
21. J. C. Deacon, M. J. Bloemink, H. Rezavandi, M. A. Geeves, L. A. Leinwand, Identification of functional differences between recombinant human α and β cardiac myosin motors. *Cell. Mol. Life Sci.* **69**, 2261–2277 (2012).
22. M. J. Greenberg, H. Shuman, E. M. Ostap, Inherent force-dependent properties of β-cardiac myosin contribute to the force-velocity relationship of cardiac muscle. *Biophys. J.* **107**, L41–L44 (2014).
23. M. S. Woody, *et al.*, Positive cardiac inotrope omecamtiv mecarbil activates muscle despite suppressing the myosin working stroke. *Nat. Commun.* **9**, 1–11 (2018).
24. T. Blackwell, W. T. Stump, S. R. Clippinger, M. J. Greenberg, Computational Tool for Ensemble Averaging of Single-Molecule Data. *Biophys. J.* **120**, 10–20 (2021).
25. C. Veigel, F. Wang, M. L. Bartoo, J. R. Sellers, J. E. Molloy, The gated gait of the processive molecular motor, myosin V. *Nat. Cell Biol.* **4**, 59–65 (2002).
26. C. Veigel, J. E. Molloy, S. Schmitz, J. Kendrick-Jones, Load-dependent kinetics of force production by smooth muscle myosin measured with optical tweezers. *Nat. Cell Biol.* **5**, 980–986 (2003).
27. C. Chen, *et al.*, Kinetic schemes for post-synchronized single molecule dynamics. *Biophys. J.* **102**, L23–L25 (2012).
28. M. S. Woody, D. A. Winkelmann, M. Capitanio, E. M. Ostap, Y. E. Goldman, Single molecule mechanics resolves the earliest events in force generation by cardiac myosin. *Elife* **8**, 1–19 (2019).
29. Y. Takagi, E. E. Homsher, Y. E. Goldman, H. Shuman, Force generation in single conventional actomyosin complexes under high dynamic load. *Biophys. J.* **90**, 1295–1307 (2006).
30. M. S. Woody, J. H. Lewis, M. J. Greenberg, Y. E. Goldman, E. M. Ostap, MEMLET: An Easy-to-Use Tool for Data Fitting and Model Comparison Using Maximum-Likelihood Estimation. *Biophys. J.* **111**, 273–282 (2016).
31. G. I. Bell, Models for the specific adhesion of cells to cells. *Science (80-.).* **200**, 618–627 (1978).
32. M. J. Greenberg, E. M. Ostap, Regulation and control of myosin-I by the motor and light chain-binding domains. *Trends Cell Biol.* **23**, 81–89 (2013).
33. J. Sung, *et al.*, Harmonic force spectroscopy measures load-dependent kinetics of individual human β-cardiac myosin molecules. *Nat. Commun.* **6**, 1–9 (2015).
34. E. P. Manning, P. J. Guinto, J. C. Tardiff, Correlation of molecular and functional effects of mutations in cardiac troponin T linked to familial hypertrophic cardiomyopathy: an integrative in silico/in vitro approach. *J. Biol. Chem.* **287**, 14515–14523 (2012).
35. P. J. Guinto, E. P. Manning, S. D. Schwartz, J. C. Tardiff, Computational Characterization of Mutations in Cardiac Troponin T Known to Cause Familial Hypertrophic Cardiomyopathy.

J. Theor. Comput. Chem. **6**, 413 (2007).
36. M. J. Greenberg, H. Shuman, E. M. Ostap, “Measuring the Kinetic and Mechanical Properties of Non-processive Myosins Using Optical Tweezers” in *Optical Tweezers: Methods and Protocols*, A. Gennerich, Ed. (Springer New York, 2017), pp. 483–509.
37. S. K. Barrick, S. R. Clippinger, L. Greenberg, M. J. Greenberg, Computational Tool to Study Perturbations in Muscle Regulation and Its Application to Heart Disease. *Biophys. J.* **116**, 2246–2252 (2019).

Chapter 8: Conclusions and Future Directions

In this thesis, I show that while Tm and Tn do not significantly affect the step size, the kinetics, or the force sensitivity of βCM, mutations in Tn-T that cause familial cardiomyopathies alter the ability of βCM to bind to actin and produce force. Using the three-state model of thin filament activation, I was able to pinpoint the molecular transition being affected by a DCM, HCM and RCM mutation. Here, I will consider the overarching implications of this work with a focus on the importance of understanding the initial insult and molecular mechanism of cardiomyopathy-causing mutations, as well as mechanosensing and adaptive/maladaptive changes in heart tissue. I will also discuss future directions of the work presented here.

8.1 Diversity of genetic cardiomyopathies and importance of studying molecular effects

While this work focused on mutations in Tn-T, it is important to understand that HCM and DCM arise from nearly 1,500 distinct mutations in genes that encode proteins of the sarcomere, as well as proteins such as lamin A/C and desmin, which play no direct role in contractility (1). In general, the molecular effects of these mutations can be grouped into three broad categories with effects on protein abundance, stability or function (2). The mutations studied here do not affect protein abundance (e.g. they do not lead to net haploinsufficiency), which is an important consideration for therapeutics. However, within these three groups there are mutations that may lead to direct or indirect effects on phosphorylation, calcium homeostasis, protein flexibility, sarcomere assembly, protein turnover, contractility and others, each of which would most likely require a different therapeutic approach (3). As stated previously, classifying mutations based on the gene affected is also not effective. For example, some mutations

identified in βCM cause HCM or DCM, and some are benign (4). As another example, the three Tn-T mutations described here produce different disease phenotypes. It is therefore becoming more apparent that the key to treating patients lies in mechanistic understanding of the mutation in question.

8.2 Mechanosensing and adaptive/maladaptive changes in heart tissue

The work presented here shows the power of studying these diseases across multiple scales of organization as there were insights gained at the molecular scale that would not have been possible at the cellular level and vice versa. In Chapter 3 we provided evidence that the ΔK210 Tn-T mutation not only affects contractility but also the ability of hiPSC-CMs to sense and respond to their environment, known as mechanosensing. This finding is significant because, as mentioned above, not all genes that cause cardiomyopathies have known roles in contractility but some have roles in mechanosensing pathways (5) (6). At birth, patients with HCM, DCM or RCM usually do not yet show signs of cardiac remodeling or symptoms, but over time (spanning from pediatric onset to onset late in adult life) signs of heart tissue remodeling and symptomatic cardiomyopathy become apparent. This progressive behavior suggests that the initial insult caused by the mutation causes downstream effects leading to changes in gene expression via mechanosensing pathways. These changes in gene expression may initially serve as an adaptation to help the cell compensate for molecular defects, but over time these changes appear to become maladaptive.

8.3 Future Directions for *in vivo* modeling of Tn-T mutations

The next logical step up the scale of organization from hiPSC-CMs is to use human engineered heart tissues (EHT's) to ask how the effects we see at the single cell level translate to remodeling/difference in force and power production in tissue. This work is already underway by others in the lab and serves as a powerful method for how large groups of cardiomyocytes as well as other cell types present in heart tissue respond to applied forces (7). This work is crucial in order to deepen our understanding of the early disease progression, because tissue obtained from patients has usually already undergone severe remodeling and fibrosis.

8.4 Future Directions for optical trapping experiments

In Chapter 7 I present evidence that the step size of βCM is not affected by the presence of Tm and Tn, which is contrary to previously published work (8). I also found that changes in βCM kinetics are not necessarily biologically relevant, and that the force sensitivity of βCM was not changed by Tm and Tn. If Tm and Tn have little effect on these parameters at saturating calcium, the question remains whether Tn-T mutations have an effect. Based on the stopped-flow experiments and fluorescence titrations I performed for all three Tn-T mutations, the overarching theme is that these mutations do not affect the force produced by βCM once bound to actin, but they alter βCM's ability to bind, by increasing or decreasing the population of thin filament in the open position. I would therefore predict that in optical trapping experiments these mutations would increase or decrease the frequency of βCM binding events. However, it is possible that the presence of force would alter this anticipated behavior. These

experiments would help to inform the recent use of computational models to expand our understanding of these disease-causing mutations (9)(10)(11).

8.5 Summary

Much work remains to be done to understand how these single familial cardiomyopathy mutations cause such devastating disease phenotypes, but the first step is understanding the molecular mechanism. Through this thesis I have contributed to the growing understanding of mechanisms that serve as potential targets for precision-based medicine.

8.6 References

1. E. M. Mcnally, J. R. Golbus, M. J. Puckelwartz, Review series Genetic mutations and mechanisms in dilated cardiomyopathy. *J Clin Invest.* **123**, 19–26 (2013).
2. M. J. Greenberg, J. C. Tardiff, Complexity in genetic cardiomyopathies and new approaches for mechanism-based precision medicine. *J. Gen. Physiol.* **153** (2021).
3. M. L. Lynn, S. J. Lehman, J. C. Tardiff, Biophysical Derangements in Genetic Cardiomyopathies. *Heart Fail. Clin.* **14**, 147–159 (2018).
4. L. Alamo, *et al.*, Effects of myosin variants on interacting-heads motif explain distinct hypertrophic and dilated cardiomyopathy phenotypes. *Elife* **6**, e24634 (2017).
5. C. Uhler, G. V Shivashankar, Regulation of genome organization and gene expression by nuclear mechanotransduction. *Nat. Rev. Mol. Cell Biol.* **18**, 717–727 (2017).
6. T. Iskratsch, H. Wolfenson, M. P. Sheetz, Appreciating force and shape — the rise of mechanotransduction in cell biology. *Nat. Rev. Mol. Cell Biol.* **15**, 825–833 (2014).
7. A. L. Bailey, *et al.*, SARS-CoV-2 Infects Human Engineered Heart Tissues and Models COVID-19 Myocarditis. *JACC Basic to Transl. Sci.* **6**, 331–345 (2021).
8. N. M. Kad, S. Kim, D. M. Warshaw, P. VanBuren, J. E. Baker, Single-myosin crossbridge interactions with actin filaments regulated by troponin-tropomyosin. *Proc. Natl. Acad. Sci. U. S. A.* **102**, 16990–16995 (2005).
9. P. J. Guinto, E. P. Manning, S. D. Schwartz, J. C. Tardiff, Computational Characterization of Mutations in Cardiac Troponin T Known to Cause Familial Hypertrophic Cardiomyopathy. *J. Theor. Comput. Chem.* **6**, 413 (2007).
10. E. P. Manning, P. J. Guinto, J. C. Tardiff, Correlation of molecular and functional effects of mutations in cardiac troponin T linked to familial hypertrophic cardiomyopathy: an integrative in silico/in vitro approach. *J. Biol. Chem.* **287**, 14515–14523 (2012).
11. J. Davis, *et al.*, A Tension-Based Model Distinguishes Hypertrophic versus Dilated Cardiomyopathy. *Cell* **165**, 1147–1159 (2016).